

Computational Techniques for Efficient Solution of Discretized Biot's Theory
for Fluid Flow in Deformable Porous Media

by

Im Soo Lee

Dissertation submitted to the Faculty of the
Virginia Polytechnic Institute and State University
in partial fulfillment of the requirements for the degree of

Doctor of Philosophy

in

Civil and Environmental Engineering

M. S. Gutierrez (Chair)
J. M. Duncan
G. M. Filz
L. Chin

June 24, 2008
Blacksburg, Virginia

Keywords: Biot's theory, fully-coupled solution, finite elements

Computational Techniques for Efficient Solution of Discretized Biot's Theory for Fluid Flow in Deformable Porous Media

Im Soo Lee

ABSTRACT

In soil and rock mechanics, coupling effects between geomechanics field and fluid-flow field are important to understand many physical phenomena. Coupling effects in fluid-saturated porous media comes from the interaction between the geomechanics field and the fluid flow. Stresses subjected on the porous material result volumetric strains and fluid diffusion in the pores. In turn, pore pressure change cause effective stresses change that leads to the deformation of the geomechanics field. Coupling effects have been neglected in traditional geotechnical engineering and petroleum engineering however, it should not be ignored or simplified to increases reliability of the results. The coupling effect in porous media was theoretically established in the poroelasticity theory developed by Biot, and it has become a powerful theory for modeling three-dimensional consolidation type of problem.

The analysis of the porous media with fully-coupled simulations based on the Biot's theory requires intensive computational effort due to the large number of interacting fields. Therefore, advanced computational techniques need to be exploited to reduce computational time. In order to solve the coupled problem, several techniques are currently available such as one-way coupling, partial-coupling, and full-coupling. The fully-coupled approach is the most rigorous approach and produces the most correct results. However, it needs large computational efforts because it solves the geomechanics and the fluid-flow

unknowns simultaneously and monolithically. In order to overcome this limitation, staggered solution based on the Biot's theory is proposed and implemented using a modular approach. In this thesis, Biot's equations are implemented using a Finite Element method and/or Finite Difference method with expansion of nonlinear stress-strain constitutive relation and multi-phase fluid flow. Fully-coupled effects are achieved by updating the compressibility matrix and by using an additional source term in the conventional fluid flow equation. The proposed method is tested in multi-phase FE and FD fluid flow codes coupled with a FE geomechanical code and numerical results are compared with analytical solutions and published results.

ACKNOWLEDGEMENTS

I am indebted to many people for their help during my graduate studies and completion of this dissertation. I wish to record my gratitude to my supervisor, Professor Marte Gutierrez for his guidance and constructive ideas throughout the period of the present study. His handling of both research and consultancy works have motivated me in the present work and will inspire me in my career in the future. I am also grateful for the help of committee members Prof. James Michael Duncan, Prof. George Filz, and Dr. Lee Chin for their review of and suggestions to improve the dissertation.

I have been very fortunate to have made the many friendships during my stay at Virginia Tech. Many people have positively influenced my life during these days. It is not possible to name here everyone who has made my life more gratifying, but a few special people must be noted: Soonkie Nam, Jeremy Decker, Youngjin Park, Sotirios Vardakos, and Kyusang Kim.

This study was funded by the American Chemical Society and I gratefully acknowledge their financial support.

Finally, and most of all, I am very thankful to my wife, Yujin Chun, for the support, strength, encouragement, and understanding during my graduate study and beyond. I cannot express my debt I owe to her for caring our precious daughter, Tricia Lee.

Im Soo Lee
June 2008

TABLE OF CONTENTS

1	INTRODUCTION	1
1.1	Background.....	1
1.2	Problems involving Fluid Flow in Deformable Porous Media.....	4
1.2.1	Consolidation.....	4
1.2.2	Water aquifers and hydrogeology.....	4
1.2.3	Hydrocarbon production	6
1.3	Motivation and Objective	8
1.4	Organization of the Thesis.....	11
	REFERENCES	12
2	BIOT'S THEORY OF POREOELASTICITY	15
2.1	Introduction	15
2.2	Biot's theory	15
2.3	Equilibrium Equation	17
2.4	Continuity Equation.....	19
2.5	Finite Element Implementation of Biot's theory	21
2.5.1	Equilibrium equation using FE method.....	21
2.5.2	Continuity equation using FE method	24
2.5.3	Complete set of FE Biot's equation.....	26
2.6	Validation of the Finite Element Discretization	27
2.6.1	Original Mandel's problem	27
2.6.2	Rigidity effects on Mandel's problem	35
	REFERENCES	49
3	BIOT'S THEORY FOR MULTI-PHASE FLUID FLOW.....	51
3.1	Introduction	51
3.2	Fluid Flow Properties	52
3.2.1	Capillary pressure	52
3.2.2	Relative permeability.....	55
3.3	Governing Equations	56
3.3.1	Continuity equation in the fully-coupled theory.....	57
3.3.2	Continuity equation in the conventional multi-phase fluid flow formulation	59
3.4	Discretization of the Governing Equations	61
3.4.1	Equilibrium equation	61
3.4.2	Continuity equation based on the fully-coupled theory.....	62
3.4.3	Complete set of FE Biot's equation with two-phase fluid flow	63
3.4.4	Conventional fluid flow equation	63
3.5	Numerical procedures for multi-phase flow equations.....	64
3.5.1	Treatment of nonlinear terms	65
3.5.2	Simultaneous Solutions (SS)	66
3.5.3	Implicit Pressure – Explicit Saturation method (IMPES)	69

3.5.4	The Sequential Solution Method (SEQ)	69
3.6	Validation of the Finite Element Formulations	69
	REFERENCES	79
4	NONLINEARITY OF THE CONSTITUTIVE RELATION	81
4.1	Introduction	81
4.2	Stress and Strain Invariants	81
4.3	Linear Elastic Model	87
4.4	Nonlinear Elastic Models	89
4.5	Elasto-Plastic Models	90
4.5.1	Coincidence of axes.....	91
4.5.2	Yield surface and yield function.....	91
4.5.3	Plastic potential function	93
4.5.4	Incremental Elasticity	96
4.5.5	Strain additivity	96
4.5.6	Plastic hardening/softening rule	96
4.6	Simple Critical State Model	97
4.6.1	Elastic material properties for the Cam Clay and modified Cam Clay models	102
4.7	FE Solution Procedure for Nonlinear Materials	103
4.7.1	Tangent stiffness method.....	104
4.7.2	Visco-plastic method.....	104
4.7.3	Newton-Raphson method	105
4.8	Uniform Compression Test for the Modified Cam Clay Soils.....	112
	REFERENCES	117
5	SOLUTION TECHNIQUES FOR THE DISCRETIZED BIOT'S EQUATIONS	119
5.1	Introduction	119
5.2	Monolithic Solution.....	120
5.3	Partitioned Solution Methods	124
5.3.1	Partitioned approach with direct solution method.....	124
5.3.2	Partitioned approach with iterative solution method.....	127
5.4	Modular Approaches	128
5.4.1	Updating of the compressibility matrix	128
5.4.2	Geomechanics (FE) – Fluid Flow (FD) coupling	134
5.4.3	Porosity coupling.....	140
5.5	Code Validations and Applications	147
5.5.1	Simplified model of the Ekofisk Field subsidence	147
5.5.2	Mandel's problem.....	152
5.5.3	Linear elastic consolidation by Schiffman et al.....	157
5.5.4	Borja's example consolidation problem	161
5.5.5	Liakopoulos's drainage test	170
	REFERENCES	174

6 APPLICATION OF THE MODEL	177
6.1 Ekofisk Hydrocarbon Field	177
REFFRENCE.....	199
7 CONCLUSIONS AND RECOMMENDATIONS	200
Summary.....	200
Conclusions	203
Recommendations for Future Work	204
APPENDIX-A	207
Analytical Solution of Mandel's Problem.....	207
APPENDIX-B	210
Incremental formulations of the modified Cam clay	210
APPENDIX-C	213
The numerical iteration algorithms of the different strategies for the staggered solution of the fully-coupled Biot's equation	213

LIST OF FIGURES

Figure 2-1 Mandel's Problem	28
Figure 2-2 Mechanical boundary conditions for FE model.....	30
Figure 2-3 4-node element (Q4) and 9-node element (Q9)	31
Figure 2-4 Pore pressure profiles vs. time	33
Figure 2-5 Pore pressure profile (FEM Q9Q4)	33
Figure 2-6 Degree of consolidation profile	34
Figure 2-7 Pore pressure profiles with various Poisson's ratio	35
Figure 2-8 Full size model and quarter of the model with mechanical boundary conditions	36
Figure 2-9 FE mesh for the impervious material located on the top of porous media ($h_1/a = 0.2$, and $h_2/a = 0.1$)	38
Figure 2-10 Pore pressure profiles for different Young's modulus ratio	40
Figure 2-11 Vertical displacements of top of the poroelastic sample with different Young's modulus ratio ($t^*=0.065$)	40
Figure 2-12 Normalized pore pressures for different rigidity of impervious material	41
Figure 2-13 A quarter of the sample with mechanical boundary conditions of the different thickness of impervious layer	42
Figure 2-14 Maximum pore pressures for various thickness of impervious layer	43
Figure 2-15 Maximum pore pressures for various thickness of impervious layer after normalization	43
Figure 2-16 A quarter of the sample with mechanical boundary conditions of the different thickness of the porous layer	44
Figure 2-17 Maximum pore pressures for various thicknesses of the porous layer	45
Figure 2-18 Max. pore pressures for various thicknesses of the porous layer after normalization	46
Figure 2-19 Maximum pore pressure profile after normalization ($v=0$)	47
Figure 2-20 Maximum normalized pore pressure profile after normalization ($v=0$)	48
Figure 2-21 Maximum normalized pore pressure profile after normalization	48
Figure 3-1 Typical capillary pressure vs. saturation curve.....	54
Figure 3-2 Typical relative permeability curve	56
Figure 3-3 A schematic process of SS method	68
Figure 3-4 Mechanical boundary conditions of the Liakopoulos [16] test problem	72
Figure 3-5 Saturation vs. capillary pressure	73
Figure 3-6 Relative permeability vs. saturation	74
Figure 3-7 Comparison of water pressure profiles from numerical simulation and experimental results	76
Figure 3-8 Gas pressure profiles.....	76
Figure 3-9 Capillary pressure profiles from numerical simulations	77
Figure 3-10 Saturation profiles from numerical simulations.....	77

Figure 3-11 Vertical displacements profiles from numerical simulations	78
Figure 4-1 Stress invariants in the principal stress space: (a) stress point in the principal stress space; (b) projection on the deviatoric plane (π -plane)	84
Figure 4-2 Yield surface presentation; (a) two dimensional example; (b) segment of yield surface for three dimensional stress space.....	93
Figure 4-3 Plastic potential surface and plastic flow direction in two-dimensional stress space, for (a) associated flow; (b) non-associated flow.....	95
Figure 4-4 Behavior of soft soil under isotropic compression	99
Figure 4-5 Location of CSL relative to virgin compression line.....	99
Figure 4-6 Yield surface	100
Figure 4-7 Projection of yield surface of modified Cam clay onto q - p' plane	101
Figure 4-8 Examples of Newton-Raphson method for the uniaxial loading of nonlinear material in a) load-displacement space; and b) stress-strain space	106
Figure 4-9 Illustration of elastic predictor-plastic corrector (implicit method).....	109
Figure 4-10 Illustration of elastic predictor-plastic corrector (explicit method)	110
Figure 4-11 Illustration of sub-stepping method	111
Figure 4-12 Idealized drained triaxial test for N.C. clay in (a) q vs. ϵ_a ,and (b) ϵ_v vs. ϵ_a ..	114
Figure 4-13 Idealized drained triaxial test for O.C. clay in (a) q vs. ϵ_a , and (b) ϵ_v vs. ϵ_a ..	115
Figure 5-1 A schematic flow chart for the monolithic method with incorporation of nonlinear stress-strain analysis	123
Figure 5-2 A schematic flow chart of the partitioned Method with incorporation of nonlinear stress-strain analysis	126
Figure 5-3 A simple scheme of updating fluid flow equation based on the Biot's theory .	130
Figure 5-4 A schematic flow charts for modular approach: geomechanics (FE) – fluid-flow (FE) coupling with incorporation of nonlinear stress-strain analysis.....	132
Figure 5-5 A simple scheme of updating compressibility matrix on FD equation.....	135
Figure 5-6 A schematic flow charts of geomechanics (FE) – fluid-flow (FD) coupling with incorporation of nonlinear stress-strain analysis	136
Figure 5-7 Details of block-centered grid for 2D case	137
Figure 5-8 Details of point-distributed grid for 2D case	138
Figure 5-9 Element sharing grid (left) and node sharing grid (right)	139
Figure 5-10 Flow chart of partially-coupled analysis.....	144
Figure 5-11 Simplified 2D FE model of West-East section of the Ekofisk Field	149
Figure 5-12 Rock deformations after 14 years production magnified 20 times	150
Figure 5-13 Reservoir pressures profile after 14 years.....	150
Figure 5-14 FE mesh for the geomechanical domain of a partitioned solution method and the full domain of a monolithic solution method	153
Figure 5-15 Meshes for the fluid-flow domain (i.e., permeable porous media); (a) Finite Element, and (b) Finite Difference	153
Figure 5-16 Pore pressure profile at point 'A'	155

Figure 5-17 Pore pressure distributions along horizontal line; (a) $T=0.01$, (b) $T=0.05$, and (c) $T=0.5$	156
Figure 5-18 Plane strain linear elastic consolidation; (a) Normally loaded half-plane, and (b) Numerical model with boundary conditions.....	158
Figure 5-19 Meshes for numerical analysis; (a) FEM, and (b) FDM.....	159
Figure 5-20 Excess pore pressure variation of center line at depth $z=a$ with time	160
Figure 5-21 Isochrones of excess pore pressure along center line	160
Figure 5-22 Illustration of consolidation problem in Borja's paper; (a) Geometry for linear elastic and elasto-plastic consolidation problem, and (b) Load application scheme	161
Figure 5-23 Meshes for numerical analysis; (a) FE, and (b) FD	162
Figure 5-24 Pore pressure profiles of various depths; (a) $z/H=0.32$, (b) $z/H =0.56$, and (c) $z/H=1$	165
Figure 5-25 Settlement profile at point A.....	166
Figure 5-26 Final deformation of linear elastic consolidation problem	166
Figure 5-27 Excess pore pressure profiles at point B for nonlinear consolidation problem	169
Figure 5-28 Settlement profile at point A for nonlinear consolidation problem	169
Figure 5-29 Isochrones of pore pressure along depth.....	170
Figure 5-30 Water pressure profiles	171
Figure 5-31 Gas pressure profiles.....	171
Figure 5-32 Capillary pressure profiles	172
Figure 5-33 Saturation profiles.....	172
Figure 5-34 Vertical displacement profiles	173
 Figure 6-1 Location of the Ekofisk field in the North Sea (from Conocophillips.com http://www.conocophillips.com/about/worldwide_ops/country/europe/norway.htm).....	180
Figure 6-2 Ekofisk Field: depth map of the top of the Ekofisk Formation (by Spencer et al. [7])	181
Figure 6-3 Plan view of the numerical modeled region for the Ekofisk field	182
Figure 6-4 Cross section (North-South) of the numerical modeled region for the Ekofisk field	183
Figure 6-5 Cross section of the Ekofisk reservoir showing porosity and initial water saturation (by Spencer et. al [7])	187
Figure 6-6 Saturation vs. relative permeabilities in the oil-water system (similar to Ghafouri [2])	188
Figure 6-7 Capillary pressure vs. water saturation in the oil-water system (similar to Ghafouri [2]).....	188
Figure 6-8 Stress-strain curves for Low-Quartz-Content reservoir chalk	189
Figure 6-9 Stress-strain curves for High-Quartz-Content reservoir chalk	189
Figure 6-10 Ekofisk water production (by Hermansen, H. et al. [9])	191
Figure 6-11 Ekofisk oil production (by Hermansen, H. et al. [9])	191
Figure 6-12 Average pressure history on the well point	192

Figure 6-13 Initial FE mesh with surrounding area (shaded area represents reservoir field)	195
Figure 6-14 Final displacements profile after 14 years production with magnified 10 times (shaded area represents reservoir field)	195
Figure 6-15 Final subsidence and compaction profiles along the North-South cross-section	196
Figure 6-16 Subsidence and compaction profiles at the center along the production time	196
Figure 6-17 Water pressure profiles in the Ekofisk reservoir region along the mid depth	197
Figure 6-18 Oil pressure profiles in the Ekofisk reservoir region along the mid depth	197
Figure 6-19 Water saturation profiles in the Ekofisk reservoir region along the mid depth	198

LIST OF TABLES

Table 2-1 Properties and other input data for the FE model	31
Table 3-1 Material properties	71
Table 4-1 Stress/strain invariants	82
Table 4-2 Soil parameters for the modified Cam clay model.....	113
Table 4-3 Results and CPU times for the idealized drained triaxial test analyses (N.C. clay)	116
Table 4-4 Results and CPU times for the idealized drained triaxial test analyses (O.C. clay)	116
Table 5-1 Published porosity expressions	141
Table 5-2 Summary of test problems	147
Table 5-3 Material properties of simplified Ekofisk problem.....	149
Table 5-4 Comparison among different solution techniques for the simplified Ekofisk case	151
Table 5-5 Numerical input for the linear elastic consolidation problem.....	158
Table 5-6 Model parameters for the linear elastic consolidation problem.....	163
Table 5-7 Material properties for the nonlinear elasto-plastic (Modified Cam Clay) consolidation problem	167
Table 6-1 Fluids properties of reservoir	186
Table 6-2 Linear elastic parameters of surrounding materials	186
Table 6-3 Modified Cam Clay parameters of reservoir materials	186

1 INTRODUCTION

1.1 *Background*

Coupling effects in porous media containing interconnected fluid-saturated pores stem from the interaction between the geomechanical behavior and the pore fluid flow. When a fluid-saturated porous material is subjected to load, the resulting matrix deformation leads to volumetric changes in the pores and reduces in volume of the materials but also cause fluid diffusion between regions of higher and lower pore pressures. The three-dimensional coupling effect in fluid-saturated porous media was theoretically established in the Poroelasticity Theory which was developed by Biot [1]. Following Biot's work, fluid pressure effects on volumetric changes of porous rocks were explained by Geertsma [2] using compressibility terms, and Zimmerman [3] expanded the derivations of the equations in the theory.

Biot's Poroelasticity Theory was originally motivated by problems in soil mechanics such as consolidation, however, many applications are also associated with Biot's equations. Selvadurai [4] cited publications on different applications of poroelasticity such as offshore geotechniques [5], hydraulic fracturing for energy resource exploration, and estimation of ground subsidence or heave. In recent years, Biot's theory has found extensive applications in other areas such as biomechanics of soft tissues, mechanics of bone, transport of multi-phase fluids in porous media with special reference to applications in environmental geomechanics and energy resources recovery, etc.

In the original Biot's theory, the simplest mathematical description of the two basic forms of coupling between solid and fluid involves a set of linear constitutive equations. The equations relate strain and fluid-mass changes to stress and fluid-pressure changes. The poroelastic constitutive equations are generalizations of linear elasticity whereby the fluid pressure field is incorporated in the stress-strain relation in an analogous manner in which the temperature field is incorporated in thermoelasticity. Change of fluid mass or fluid pressure in a porous material produce strains in the bulk porous solid. A uniform change in fluid pressure throughout a porous body subjected to boundary constraints causes poroelastic stresses within the body. These poroelastic stresses cause a non-uniform pore pressure distribution leading to the time-dependent fluid flow according to Darcy's law. In turn, changes in the pore fluid pressures affect the effective stress which induces deformation in the porous material.

Coupling effects between geomechanics and fluid flow have been seen in actual field case histories. King [6] reported the water level fluctuation in a well near the train station at Whitewater, Wisconsin as caused by a train passing by the station. Meinzer [7] explained the water-level oscillations in wells in Atlantic City, New Jersey with the pore pressure caused by the high tide and the compression of underlying rock. Pratt and Johnson [8] showed that the subsidence of the Goose Creek oil field in Texas could be attributed to the extraction of the oil from the reservoir. Verruijt [9] explained the water level rise when large pumps were turned on the nearby wells in Noordbergum in northern Friesland (Netherlands) due to instant compression of the aquifer, which forced the water level up the well.

The above historical events show that geomechanics and fluid pressure coupling phenomena have two basic components. One is that solid-to-fluid coupling which occurs when a change in applied stresses produce a change in fluid pressures. The other is that fluid-to-solid coupling which occurs when a change in fluid pressure or fluid mass produces a change in the volume of the porous material. The solid-to-fluid and fluid-to-solid couplings occur instantaneously.

The importance of three-dimensional coupling effects has often been neglected in soil/rock mechanics, petroleum engineering, and hydrogeology. In soil/rock mechanics, uncoupled solution techniques have been commonly used to calculate subsidence. The techniques consist of a two-step procedure such that land subsidence was calculated assuming one-dimensional consolidation and calculated pore pressure distribution [10]. In petroleum engineering, geomechanics has been considered as a separate aspect of hydrocarbon reservoir behavior, and rock mechanical response has been oversimplified by the use of the *rock compressibility* term in reservoir simulations [11]. In hydrogeology, most of phenomena have been explained only by fluid flow behavior in which geomechanical effects are oversimplified through the use of the storativity coefficient.

There are three categories of strategies for implementing the coupling effects between fluid flow and geomechanics, as pointed out by Minkoff [12]. These are: as one-way coupling, partial-coupling, and full-coupling. In one-way coupling, the fluid pressure changes are used as applied loads in geomechanics field but geomechanical effects on the fluid flow profiles are ignored. In partial-coupling, some of the interactions between geomechanics fields and fluid flow are accounted in the strategy, however, it does not account for full

feedback mechanisms between two fields. One example of the partially coupled simulation technique is to model the impacts of stress-induced permeability changes on fluid flow behavior [13-16]. Full-coupling rigorously takes into account the interaction between geomechanics fields and fluid flow field according to Biot's theory [13, 14].

1.2 *Problems involving Fluid Flow in Deformable Porous Media*

1.2.1 Consolidation

Consolidation is a process in which soil decreases in volume as time proceeds with drainage and it plays an important role in many soil mechanics problems. Seepage or dissipation of excess pore pressure causes the effective stress to increase, which, in turn, results in the soil particles being packed more tightly together (i.e., reducing bulk volume). The magnitude of consolidation and rate of consolidation can be predicted by many different methods and one of the classical methods is developed by Terzaghi [15]. He proposed a one-dimensional consolidation theory, where the amounts of the consolidation were predicted by using a compression index obtained from an oedometer test.

1.2.2 Water aquifers and hydrogeology

In a general definition, aquifers are fully-saturated subsurface layer of permeable porous materials (e.g., rock, gravel, sand, silt, or clay). Groundwater can be usefully extracted from aquifers using water wells and the study of water flow in aquifers and/or the characterization of aquifers is called *hydrogeology*. Water aquifers can be exploited as a groundwater resource, however, water extraction can lead several problems. For example, lowering water table near a coastal line can cause the subsequent contamination of

groundwater by saltwater from sea (i.e., saline intrusion). Also, significant amount of subsidence due to the pore pressure decrease (i.e., effective stress increase) may cause structural damages near the aquifer (e.g., San Joaquin valley in California [16], Galveston in Mexico City [17], and Venice in Italy [18]). Aquifers can be categorized into two types in accordance with end members such as confined and unconfined aquifer. Unconfined aquifers (i.e., phreatic aquifers) has upper boundary with phreatic surface or water table and typically located closer to the surface. Confined aquifers have the water table above their upper boundary and are typically located below unconfined aquifers.

The process of compaction of aquifers is well known from the fact that the removal of groundwater from an aquifer leads to a decrease of the pore pressure in the porous medium (i.e., the aquifer). The reduction of pore pressure causes the effective stresses to increase in the skeleton in the aquifer matrix. Due to the effective stresses change, deformation may occur especially if the formation of the aquifer is unconsolidated. The vertical compaction of the aquifer system leads to the subsidence of the land surface. In accordance with types of aquifer material, compaction can be partially recoverable or non-recoverable. For example, rock or coarse-grained materials show relatively elastic behavior which deformation can be recovered after load removal, on the other hand fine-grained materials behave more plastic way such that non-recoverable deformation exists after load removal. Compaction in unconfined aquifers is usually of relatively small magnitude because most of effective stress changes are led by insignificant groundwater table changes due to surface repressurization and recharge. In case of confined aquifer system, more significant effective

stress changes may be caused by extraction of groundwater which leads to the decrease of pore pressure.

1.2.3 Hydrocarbon production

Hydrocarbons are mainly located in subsurface porous rock formations (e.g., hydrocarbon reservoirs), and exist as crude oil or gas. The essential properties required for rocks to be a hydrocarbon reservoir are porosity and permeability. The naturally occurring hydrocarbons are typically trapped by overlying rock formations with lower permeability (i.e., cap rocks) or by barriers by low permeability healed faults. Sandstone and limestone are the most common hydrocarbon reservoir rocks in the world. The characteristics of the reservoir formation can be classified in to structural and stratigraphic trap. Structural traps are formed by a deformation in the rock layer that contains the hydrocarbons in the formation of domes, anticlines, and folds shape. Also, fault related features may be classified as a structure trap as well. Stratigraphic traps are formed when other beds seal a reservoir bed or in case the permeability changes within the reservoir bed itself.

When oil or gas is exploited, the fluid pressure declines and it induces compaction of the hydrocarbon reservoir rock. This reservoir compaction may then be transferred to the ground surface as subsidence. Reservoir compaction and surface subsidence are of major concern in hydrocarbon reservoirs with weak and poorly consolidated rock formations. Pressure depletion due to hydrocarbon production can also cause significant deformation and shear failure in weak reservoir formation. In case where a subsidence is experienced, it may have caused serious consequences and subsidence problems have received many

attentions for several decades (e.g., Wilmington oil field in California [19], Goose Creek in Texas [20], and Po Delta in Italy [21]). The degree of compaction of a reservoir is dependent of the mechanical properties of the rock and the pressure profiles. Also, to extent the subsidence from compaction requires information of overburden rocks and geometrical factors such as reservoir dimension compared to depth.

1.2.3.1 Subsidence in the Ekofisk hydrocarbon field

After 25 years of production, the Ekofisk field has experienced subsidence involving 150 km³ of rock overburden in an area of 50 km². The seabed continued to subside about 38 centimeters per year, and the operator resolved in 1994 to redevelop the field. Designed to cope with 20 meters of subsidence, this Ekofisk II project came on stream in 1998. The seabed has so far subsided by 8.5 meters and the process is continuing [22, 23].

Seabed subsidence on Ekofisk was first observed in 1984 when reservoir pressure had halved as a result of oil and gas production from an initial reservoir of 48 MPa down to 24 MPa. The pressure depletion caused the 3 km of overlying sediments to compress the weak formation rocks.

In order to mitigate the potential impact of the seabed subsidence, Phillips Petroleum Company, the main operator of the Ekofisk field, found a temporary solution by jacking up six of the offshore platforms, and breakwater wall around the main Ekofisk tank. However, the temporary solution is now deemed insufficient as the subsidence has now exceeded the value used in jacking up the platform and in the design of the height of the Ekofisk tank protective wall.

Likewise, subsidence has led to significant pipeline concerns due to excess compressional or tensional strain. Reservoir compaction itself has led to numerous casing deformations and poses a notable challenge for well completion. However, reservoir compaction also provides significant drive energy and greatly contributes to increased hydrocarbon production and reserves.

1.3 Motivation and Objective

The coupled nature of fluid flow in deformable porous media should not be neglected by simplifying the physics of the problem, otherwise the simplifications can seriously affect the reliability of predicted results. For instance, one important coupling effect predicted by fully-coupled simulation of hydrocarbon reservoirs is the possibility for reservoir fluid pressure to increase above initial value even during production [24]. This unusual reservoir response is analogous to the so-called Mandel-Cryer and Noordbergum effects [9, 25, 26] that cannot be predicted by the conventional fluid flow simulators which are not coupled with geomechanical simulator. Lewis [27] indicated the need for coupled solution in single aquifer pumping and real subsidence problem. Lewis [14], and Gutierrez [13] showed the inadequacy of the one-way and partial coupling strategies and discussed the needs of the fully-coupled techniques. These studies have emphasized that analysis of fluid flow in deformable porous and fractured media should follow strictly Biot's theory.

In the analysis for the porous media with fully-coupled simulations, the number of interacting fields and the problem itself could be very large. Therefore, advanced computational techniques need to be exploited to reduce computational time and required

computation resources. The most direct procedure to rigorously solve the fully-coupled equations from Biot's theory is the monolithic approach in which the discretized coupled system of equations is solved simultaneously for both the fluid flow and geomechanical fields [14, 28]. This monolithic approach has limitations that: 1) it is a cumbersome and time consuming in particular for large problems, 2) there is a need to develop special software which directly solves the coupled problem, and 3) the resulting system of equations are often ill-conditioned due to the differences in the magnitudes of the variables involved in each of the subsystems.

Due to the difficulties in the monolithic solution of Biot's equation, other solution techniques have been developed. Partitioned solution of the discretized Biot's equation subdivides the resulting equations into geomechanics and fluid flow components within a time step. These include the partitioned approach of Park [29], the staggered drained-undrained technique of Zienkiewicz [30], the iterative staggered solutions of Schreffler [31], Chin [32, 33], and Longuemare [34]. The staggered solutions show that modular approaches can be implemented and that they enable the use of separate pre-developed fluid flow simulations and geomechanical simulations. For example, calculated permeability in a geomechanics simulator can be used in reservoir simulation to implement geomechanics effects on fluid flow field. Thus, a similar strategy can be implemented in a fully coupled system.

The main objective for the project is to develop efficient and effective techniques for the numerical solution of Biot's fully-coupled equations. To achieve this goal, Finite Element and/or Finite Difference codes are developed for the 2D plane strain case. The

codes will have the ability to analyze nonlinear constitutive models for geomaterial and the multi-phase fluid flow model. The performance and validity of the solution techniques will be studied and demonstrated by simulating and studying cases of the behavior of fluid-saturated porous media. The specific objectives of the proposed research are as follows:

- Develop a computer code for the Biot's couple equations using Finite Element and/or Finite Difference methods or combinations or these methods
- Validate the code using analytical solutions and/or published results
- Develop efficient solutions technique for the Biot's equations
- Apply the model to obtain better understanding of the behavior of fluid-saturated deformable porous media

Two-dimensional plane strain condition Finite Element code is developed based on the linear stress-strain condition of Biot's theory. The code is then expanded to cover more complex material models such as elasto-plastic constitutive model and two-phase fluid flow models. Validations of the code are performed by comparing with numerical results with available analytical solutions, experimental results, and published numerical results in case where analytical solution or experimental data are not available.

To develop efficient and effective partitioned solutions for the Biot's equation, different solution techniques are surveyed. It is envisioned that the research will lead to efficient solution techniques which will enable one to exploit existing computer codes with less computational efforts.

1.4 Organization of the Thesis

The arrangement of this dissertation is as follows: Chapter 2 describes the basic formulations of Biot's theory and its Finite Element discretization. Also, the study of rigidity effects on the Mandel's problem [35] is presented based on the monolithic finite solution of Biot's coupled equations to demonstrate the use of Biot's theory and to demonstrate the predicted of fluid flow and geomechanical coupling. Chapter 3 contains a description of the multi-phase fluid flow in porous media with their governing equations and their implementation into the continuity equation part of the Biot's fully-coupled equations. Chapter 4 consists of a review of nonlinear stress-strain constitutive models and schemes for their numerical integration and Finite Element implementation. Numerical schemes for rigorous and efficient implementation of the elasto-plastic Modified Cam Clay model into the equilibrium part of the Biot's equations are presented. Chapter 5 contains various solution strategies of Biot's fully-coupled equations. A new coupling scheme is proposed and validated by comparing numerical results with analytical solutions and other numerical published results. The performance of the proposed scheme is compared to other published numerical solution of Biot's coupled equations. Chapter 6 is devoted to verification of the code developed in the study. The Ekofisk oil field is analyzed as an actual application of the numerical models. Chapter 7 presents the main conclusions and future recommendations of the study.

REFERENCES

1. Biot, M.A. 1941. General theory of three-dimensional consolidation. *Journal of Applied Physics*. 12: 155-164.
2. Geertsma, J. 1957. The Effect of Fluid Pressure Decline on Volumetric Changes of Porous Rocks. *Transactions of the Society of Petroleum Engineers of the American Institute of Mining, Metallurgical, and Petroleum Engineers, Inc.* 210: 331-340.
3. Zimmerman, R.W. 2000. Coupling in Poroelasticity and Thermoelasticity. *International Journal of Rock Mechanics and Mining Sciences*. 27: 79-87.
4. Selvadurai, A.P.S. 1996. *Mechanics of Poroelastic Media*, in *Solid Mechanics and Its Application*. Kluwer Academic Publications: Dordrecht/Boston.
5. Sabin, G.C.W. and W. Raman-Nair 1996. The Effect of a Time-Dependent Load on a Poroelastic Seabed Over a Region with Moving Boundaries. *Solid Mechanics and Its Applications*. 35: 197-214.
6. King, F.H. 1892. *Fluctuations in the Level and Rate of Movement of Ground Water on the Wisconsin Agricultural Experiment Station Farm and at Whitewater, Wisconsin*. Vol. 5. Washington, D. C.: U. S. Department of Agriculture.
7. Meinzer, O.E. 1928. Compressibility and elasticity of artesian aquifers. *Economic Geology*. 23: 263-291.
8. Pratt, W.E. and D.W. Johnson 1926. Local subsidence of the Goose Creek oil field. *J. Geology*. 34: 577-590.
9. Verruijt, A. 1969. Elastic storage of aquifers. in *Flow Through Porous Media* New York: Academic Press.
10. Gambolati, G. and R.A. Freeze 1973. Mathematical Simulation of the Subsidence of Venice. 1. Theory. *Water Resources Research*. 9: 721-733.
11. Zheng, Z. 1993. Compressibility of porous rocks under different stress conditions. *International Journal of Rock Mechanics and Mining Sciences & Geomechanics Abstracts*. 30: 1181-1184.
12. Minkoff, S., C.M. Stone, J. Guadalupe-Arguello, S. Bryant, J. Eaton, M. Peszynska and M. Wheeler 1999. Staggered in Time Coupling of Reservoir Flow Simulation

and Geomechanical Deformation: Step 1 - One-Way Coupling. in *Proc. 15th SPE Symp. Reservoir Simulation*. Houston, Texas.

13. Gutierrez, M. and R.L. Lewis 2002. Coupling of Fluid Flow and Deformation in Underground Formations. *Journal of Engineering Mechanics*. 128.
14. Lewis, R.W. and Y. Sukirman 1993. Finite Element Modelling of Three-Phase Flow in Deforming Saturated Oil Reservoirs. *International journal for Numerical and Analytical Methods in Geomechanics*. 17: 577-598.
15. Terzaghi, K. 1943. *Theoretical Soil Mechanics*. New York: Wiley.
16. Lofgren, B.E. 1960. Near-surface land subsidence in Western San Joaquin valley, California. *Journal of Geophysical Research*. 65: 1053-1062.
17. Callaway, R., *Harris-Galveston Coastal Subsidence District*, in *Water Resources Symposium*. 1985: San Antonio, TX. p. 225-235.
18. Lewis, R.W. and B. Schrefler 1978. A fully coupled consolidated model of the subsidence of Venice. *Water Resources Research*. 14: 223-230.
19. Bartosh, E.J. 1938. Wilmington oil field. *American Institute of Mining and Metallurgical Engineers -Transactions - Petroleum Development and Technology*. 127.
20. Perkins, J., J.A. 1950. Completion and production techniques in unconsolidated sands. *Oil and Gas Journal*. 49: 113-119.
21. Yerkes, R.F. and R.O. Castle 1976. Seismicity and Faulting Attributable to Fluid Extraction. *Engineering Geology*. 10: 151-167.
22. Rhett, D.W. 1998. Ekofisk Revisited; A New Model of Ekofisk Reservoir Geomechanical Behavior. in *SPE/ISRM Rock Mechanics in Petroleum Engineering*. Trondheim, Norway.
23. Broughton, P. 1997. Geotechnical Aspects of Subsidence Related to the Foundation Design of Ekofisk. *Proceedings of the Institution of Civil Engineers. Geotechnical Engineering*. 125: 129.
24. Gutierrez, M. and R.L. Lewis 2001. Petroleum Reservoir Simulation Coupling Fluid Flow and Geomechanics. *SPE Reservoir Evaluation & Engineering*. 4: 164-171.
25. Cryer, C.W. 1963. A comparison of the three-dimensional consolidation theories of Biot and Terzaghi. *Quarterly Journal of Mechanics & Applied Mathematics*. 16: 401-412.

26. Mandel, J. 1953. Consolidation des sols. *Geotechnique*. 3: 287-299.
27. Lewis, R.W., B.A. Schrefler and L. Simoni 1991. Coupling versus uncoupling in soil consolidation. *International Journal for Numerical and Analytical Methods in Geomechanics*. 15: 533-548.
28. Wang, Y. and S. Xue 2002. Coupled Reservoir-Geomechanics Model with Sand Erosion for Sand Rate and Enhanced Production Prediction. in *SPE Int. Symp. and Exhibition Formation Damage Control*. Lafayette, Los Angeles.
29. Park, K.C. and C.A. Felippa 1980. Partitioned Transient Analysis Procedures for Coupled Field Problems: Accuracy Analysis. *J. Appl. Mech.* 47: 919-926.
30. Zienkiewicz, O.C., D.K. Paul and A.H.C. Chan 1988. Unconditionally Stable Staggered Solution Procedure for Soil-Pore Fluid Interaction Problems. *Int. J. Num. Meth. Eng.* 26: 1039-1055.
31. Schreffler, B.A., L. Simoni and E. Turska 1997. Standard and Staggered Newton Schemes in Thermo-Hydro-Mechanical PRoblems. *Com. Meth. Appl. Mech. Eng.* 144: 93-109.
32. Chin, L.Y. and L.K. Thomas 1999. Fully Coupled Analysis of Improved Oil Recovery by Reservoir Compaction. in *SPE Annual Technical Conference and Exhibition*. Houston, Texas.
33. Chin, L.Y., L.K. Thomas, J.E. Sylte and R.G. Pierson 2002. Iterative Coupled Analysis of Geomechanics and Fluid Flow for Rock Compaction in Reservoir Simulation. *Oil & Gas Science and Technology*. 57: 485-497.
34. Longuemare, P., M. Mainguy, P. Lemonnier, A. Onaisi, C. Gerard and N. Kotsabeloulis 2002. Geomechanics in Reservoir Simulation: Overview of Coupling Methods and Field Case Study. *Oil & Gas Science and Technology*. 57: 471-483.
35. Lee, I. and M.S. Gutierrez 2005. Mandel-Cryer Effect for Non-Perfectly Rigid Motion. in *American Rock Mechanis Associsation*. Golden, CO.

2 BIOT'S THEORY OF POREOELASTICITY

2.1 *Introduction*

The initial interest in the coupled diffusion-deformation mechanisms was motivated by the problem of *consolidation* that is the progressive settlement of a soil under surface surcharge. The earliest theory of consolidation was developed by Terzaghi [1] who proposed a model of one-dimensional consolidation and the theory was generalized to three-dimensions by Rendulic [2]. Later, a linear theory of three-dimensional poroelasticity of fluid saturated porous media which consists of fluid pressure effects on deformation and vice versa was developed by Biot [3]. In this chapter, the poroelasticity theory of Biot is revisited, and its Finite Element (FE) discretization is derived. Mandel's problem [4] is analyzed for the FE computer code validation and rigidity effects of Mandel-Cryer effect are investigated via a parametric study.

2.2 *Biot's theory*

The general three-dimensional theory of poroelasticity was first formulated by Biot in 1941 [3]. Since then, it has become a powerful theory for modeling three-dimensional fluid flow in deformable porous media in soil and rock mechanics. The original Biot's theory consists of the equilibrium equation with a linear elastic stress-strain relation and the continuity equation with fully-saturated single-phase fluid flow (i.e., diffusion) condition. The earlier theory of poroelasticity has been reformulated by Biot himself [5, 6] and others [7-10].

Biot's theory addresses the coupling effects between the deformation of fluid saturated porous media and the transient pore fluid flow based on a linear stress-strain relation. Biot introduced the new variable the *increment of fluid content*, ζ , which is defined as the increment of water volume per unit volume of soil. He also introduced two additional poroelastic moduli to relate the strains and the increment of fluid volume to stresses and pore pressure. The first modulus is the *specific storage coefficient*, $1/R$, which is the ratio of the change in increment of fluid volume to the change in pore pressure for a stress-free sample. The second modulus is the poroelastic expansion coefficient $1/H$, which relates the volumetric strain to pore pressure changes for conditions of constant total stress.

The constitutive relations from the original Biot's theory are given as:

$$\varepsilon_{ij} = \frac{1}{2G} \left[\sigma_{ij} - \frac{\nu}{1+\nu} \sigma_{kk} \delta_{ij} \right] + \frac{\alpha}{3K} p \delta_{ij} \quad (2.1)$$

$$\zeta = \frac{1}{H} \frac{\sigma_{kk}}{3} + \frac{p}{R} \quad \text{or} \quad \zeta = \frac{\alpha}{K} \frac{\sigma_{kk}}{3} + \frac{\alpha}{KB} p \quad (2.2)$$

where G is a shear modulus, ν is a drained Poisson's ratio, δ_{ij} is a Kronecker delta, K is a bulk modulus, $1/H$ is a poroelastic expansion coefficient, $1/R$ is a specific storage coefficient, α is a Biot-Willis coefficient ($\alpha \equiv K/H$), B is a Skempton's coefficient. In the above equations, tensorial notations are used and repeated indices imply summation.

It can be noted that for an isotropic poroelastic material, the deviatoric response is purely elastic and the coupled effects appear only in the volumetric stress-strain relation (e.g., H and R are both constant). One of the key features of the behavior of the fluid saturated

porous media is the difference between undrained and drained deformation. The undrained behavior characterizes the condition where the fluid is trapped in the porous media and no fluid flow occurs (i.e., $\zeta = 0$) on the other hand, the drained behavior corresponds to zero pore pressure (i.e., $p = 0$).

The original Biot's theory had been extended to more general cases, such as non-linear stress-strain relation and multi-phase fluid flow [11-14]. For simplicity, the original Biot's theory is considered in this chapter and the more general cases will be considered in other chapters. The complete set of Biot's theory based on the linear isotropic poroelastic theory is discussed in the following.

2.3 Equilibrium Equation

In order to describe the deformation of porous media in three-dimensional consolidation, the equilibrium equation which takes into account the stress-strain relation needs to be considered. The fundamental relation of the interaction between the solid deformation and the fluid flow can be explained by the Terzaghi's *effective stress principle* [1]. Equilibrium equation for the Biot's theory includes the following equations:

- Terzaghi-Biot's effective stress principle

$$\sigma'_{ij} = \sigma_{ij} + \alpha \delta_{ij} p \quad (2.3)$$

where σ'_{ij} and σ_{ij} are the effective and total stress tensors, respectively, δ_{ij} is the Kronecker delta tensor, α is the Biot's coefficient, and p is the fluid pressure. In

equation (2.3), the positive sign indicates tension and negative sign indicates compression.

- The stress-strain constitutive relation with pore pressure effects on the solid particles

$$d\sigma'_{ij} = D_{ijkl} (d\varepsilon_{kl} - d\varepsilon_{kl,p}) \quad (2.4)$$

where $d\varepsilon_{kl}$ is the strain increment tensor, D_{ijkl} is the constitutive tensor, and $d\varepsilon_{kl,p}$ is the overall volumetric strain caused by uniform compression of the material solid particle, i.e.,:

$$d\varepsilon_{lk,p} = -\delta_{kl} \frac{dp}{3K_s} \quad (2.5)$$

where K_s is the bulk modulus of the solid particle.

It should be noted that the strain of the medium caused by effective stress and pore pressure only and all other components of strains, such as swelling, thermal strain and chemical strain are not associated with stress changes and excluded in equation (2.4 – 2.5).

- The strain-displacement compatibility relation

$$d\varepsilon_{ij} = \frac{1}{2} \left(\frac{\partial u_i}{\partial x_j} + \frac{\partial u_j}{\partial x_i} \right) \quad (2.6)$$

where u_i is the displacement along the direction x_i .

2.4 Continuity Equation

The single-phase fluid diffusion equation in the fully-coupled system consists of the combination of mass balance relation and Darcy's law. The rate of fluid accumulation term in the mass balance equation contains more complex expression than uncoupled fluid transient diffusion equation which is a basis of the Terzaghi's consolidation theory. Mass balance equation for the Biot's theory can be written as:

$$\nabla \cdot \left[\frac{K_{ij}\rho}{\mu} (\nabla p - \rho g h) \right] + q = \rho \left(\delta_{kl} - \frac{\delta_{ij}D_{ijkl}}{3K_s} \right) \frac{\partial \varepsilon_{kl}}{\partial t} + \rho \left(\frac{\phi}{K_f} + \frac{1-\phi}{K_s} - \frac{\delta_{ij}D_{ijkl}\delta_{kl}}{(3K_s)^2} \right) \frac{\partial p}{\partial t} \quad (2.7)$$

where K_{ij} is the permeability tensor, μ is the dynamic viscosity of the fluid, g is the gravity acceleration, h is the height from the reference point, ϕ is the porosity, ρ is the fluid mass density, and K_f is the bulk modulus of the fluid.

Details of the components of the rate of fluid accumulation term are as given below:

- The rate of the soil matrix volume change due to the change of total strain

$$\frac{\partial \varepsilon_v}{\partial t} = \delta_{kl} \frac{\partial \varepsilon_{kl}}{\partial t} \quad (2.8)$$

- The rate of fluid volume change due to pore pressure change

$$\phi \frac{\partial \rho}{\partial t} = \phi \frac{\partial \rho}{\partial p} \frac{\partial p}{\partial t} = \frac{\phi}{K_f} \frac{\partial p}{\partial t} \quad (2.9)$$

and the bulk modulus of the fluid, K_f , can be written as:

$$K_f = \frac{\partial p}{\partial \rho} = \frac{1}{\rho} \frac{1}{c_f} \quad (2.10)$$

and c_f is the fluid compressibility

- The rate of solid grain volume change due to pore pressure changes

$$\frac{(1-\phi)}{K_s} \frac{\partial p}{\partial t} \quad (2.11)$$

- The change of solid grain size due to effective stress changes

$$-\frac{\delta_{ij}}{3K_s} \frac{\partial \sigma'_{ij}}{\partial t} \quad (2.12)$$

Equation (2.5) can be expressed using the stress-strain constitutive relation. Substituting for σ'_{ij} from equation (2.4) into equation (2.5) results in the following expression:

$$-\frac{\delta_{ij}}{3K_s} \frac{\partial \sigma'_{ij}}{\partial t} = -\frac{\delta_{ij}}{3K_s} D_{ijkl} \left(\frac{\partial \varepsilon_{kl}}{\partial t} + \frac{\delta_{kl}}{3K_s} \frac{\partial p}{\partial t} \right) \quad (2.13)$$

The above equations relate the applied loads from the static equilibrium condition and the pore pressures from the effective stress equation to the deformation of the fluid-saturated medium. Equation (2.7) consists of the volume changes of bulk medium, fluid, and solid grain due to pore pressure and effective stress changes. It can be noted that the fluid flow equation (2.7) involves not only the fluid pressure p but also the strain tensor ε_{kl} resulting in the coupling of the geomechanics field and fluid flow field. This is different from the fluid flow equation from the uncoupled fluid diffusion equation in which the compressibility is the only factor that accounts for the deformation of the porous medium. Also the compressibility in the traditional fluid flow equation is oversimplified (e.g., only limited cases of stress path can be represented) that it is a scalar parameter which is only a function

of the fluid pressure, and the effects of effective stress changes cannot be rigorously incorporated.

2.5 Finite Element Implementation of Biot's theory

2.5.1 Equilibrium equation using FE method

The equilibrium equation relates the total stress to the body force and the boundary traction which is specified at the boundary of the domain. Those relations are formulated in terms of the unknown displacements. The general equilibrium statement can be written using the principle of virtual work as;

$$\int_{\Omega} \sigma_{ij} \delta \varepsilon_{ij} d\Omega - \int_{\Omega} f_i \delta u_i d\Omega - \int_{\Gamma} \hat{t}_i \delta u_i d\Gamma = 0 \quad (2.14)$$

where σ_{ij} , and ε_{ij} are the stress and strain tensors, respectively, and f_i and \hat{t}_i are the body forces and boundary tractions, respectively. Ω is the elemental volume and the Γ is the boundary surface.

The first term in equation (2.14) corresponds to the virtual strain energy stored in the body, the second represents the virtual work done by the body forces, and the third represents the virtual work done by the surface tractions. This equilibrium statement (2.14) is also valid in incremental form,

$$\int_{\Omega} d\sigma_{ij} \delta \varepsilon_{ij} d\Omega - \int_{\Omega} df_i \delta u_i d\Omega - \int_{\Gamma} d\hat{t}_i \delta u_i d\Gamma = 0 \quad (2.15)$$

Incorporating the effective stress law from equation (2.4) into equation (2.15) results in the following:

$$\int_{\Omega} d\sigma'_{ij} \delta \varepsilon_{ij} d\Omega - \int_{\Omega} \delta_{ij} dp \delta \varepsilon_{ij} d\Omega - \int_{\Omega} df_i \delta u_i d\Omega - \int_{\Gamma} d\hat{f}_i \delta u_i d\Gamma = 0 \quad (2.16)$$

Equation (2.16) can be rewritten using the matrix notation as:

$$\int_{\Omega} \delta \boldsymbol{\varepsilon}^T d\boldsymbol{\sigma}' d\Omega - \int_{\Omega} \delta \boldsymbol{\varepsilon}^T \mathbf{m} dp d\Omega - d\hat{\mathbf{f}} = 0 \quad (2.17)$$

where

$$d\hat{\mathbf{f}} = \int_{\Omega} \delta \mathbf{u}^T d\mathbf{f} d\Omega - \int_{\Gamma} \delta \mathbf{u}^T d\hat{\mathbf{f}} d\Gamma \quad (2.18)$$

is the change in external force due to boundary and body force loadings.

After introducing the constitutive relationship from equation (2.4) into equation (2.17), the following equation is obtained:

$$\int_{\Omega} \delta \boldsymbol{\varepsilon}^T \mathbf{D} d\boldsymbol{\varepsilon} d\Omega - \int_{\Omega} \delta \boldsymbol{\varepsilon}^T \mathbf{m} dp d\Omega + \int_{\Omega} \delta \boldsymbol{\varepsilon}^T \mathbf{D} \mathbf{m} \frac{1}{3K_s} dp d\Omega - d\hat{\mathbf{f}} = 0 \quad (2.19)$$

where \mathbf{m} is the identity matrix.

It can be noted that the displacements and stresses within the equation (2.19) can be calculated with the fluid pressure value. However, the fluid pressure field is coupled with the volumetric strain changes and another fluid flow equation is needed to set the fully-coupled system.

In the process of finite element approximation, the displacements and pore pressure are expressed in terms of the vectors of the nodal values of the displacement \mathbf{u} , and the pore pressure \mathbf{p} at a finite number of points in space. In order to ensure continuity of displacements, shape function \mathbf{N} is used to express the variation of the displacements within

an element. The expressions for the fluid pressure, p is identical as in equation (2.7). The shape functions used for the pressure variables used in the equations are not necessarily the same. Hence, the two different types are distinguished by \mathbf{N} and \mathbf{N}_p . The expressions for \mathbf{u} , \mathbf{p} , and $\boldsymbol{\epsilon}$ take the form

$$\begin{aligned}\mathbf{u} &= \mathbf{N}\mathbf{u} \\ \mathbf{p} &= \mathbf{N}_p\mathbf{p} \\ \boldsymbol{\epsilon} &= \mathbf{S}\mathbf{N}\mathbf{u} = \mathbf{B}\mathbf{u}\end{aligned}\tag{2.20}$$

where \mathbf{S} is the operator matrix relating the displacement \mathbf{u} to the strain $\boldsymbol{\epsilon}$, and is defined as follows:

$$\mathbf{S} = \begin{bmatrix} \partial/\partial x & 0 & 0 \\ 0 & \partial/\partial y & 0 \\ 0 & 0 & \partial/\partial z \\ \partial/\partial y & \partial/\partial x & 0 \\ 0 & \partial/\partial z & \partial/\partial y \\ \partial/\partial z & 0 & \partial/\partial x \end{bmatrix}\tag{2.21}$$

Substituting the expression given in equation (2.20) and (2.21) into the weak form of the equilibrium equation (2.19) results in:

$$\begin{aligned}\delta\mathbf{u}^T \left\{ \int_{\Omega} \mathbf{B}^T \mathbf{D} \mathbf{B} d\Omega \mathbf{u} - \int_{\Omega} \mathbf{B}^T \mathbf{m} \mathbf{N}_p d\Omega \mathbf{p} + \int_{\Omega} \mathbf{B}^T \mathbf{D} \frac{\mathbf{m}}{3K_s} \mathbf{N} d\Omega \mathbf{p} \right\} \\ - \delta\mathbf{u}^T \left\{ \int_{\Omega} \mathbf{N}^T \mathbf{f} d\Omega + \int_{\Gamma} \mathbf{N}^T \hat{\mathbf{t}} d\Gamma \right\} = 0\end{aligned}\tag{2.22}$$

Equation (2.22) is valid for any value of the virtual displacements $\delta\mathbf{u}$ and the above equation can be further simplified as:

$$\mathbf{K}_m \mathbf{u} + \mathbf{L} \mathbf{p} = \mathbf{F}_u\tag{2.23}$$

where \mathbf{K}_m is the stiffness matrix, \mathbf{L} is the coupling matrix, and \mathbf{F}_u is the load matrix. These matrices are defined as follows:

$$\begin{aligned}\mathbf{K}_m &= \int_{\Omega} \mathbf{B}^T \mathbf{D} \mathbf{B} d\Omega \\ \mathbf{L} &= \int_{\Omega} \mathbf{B}^T \left(\mathbf{m} - \frac{\mathbf{Dm}}{3K_s} \right) \mathbf{N}_p d\Omega \\ \mathbf{F}_u &= \int_{\Omega} \mathbf{N}^T \mathbf{f} d\Omega + \int_{\Gamma} \mathbf{N}^T \hat{\mathbf{t}} d\Gamma\end{aligned}\quad (2.24)$$

The integration of the above equations usually requires the use of numerical techniques, and one of popular methods is Gaussian integration method, where integrals are evaluated at specific points, called Gaussian points, of the element and boundary surfaces. The evaluated values at all Gaussian points are then weighted and summed. The discretized equilibrium equation (2.23) is one of the pair of the complete set of the fully-coupled equations, and the other pair is the continuity equation which will be shown in the following section.

2.5.2 Continuity equation using FE method

Finite element discretization of fluid flow equation for the fully coupled system is similar to the uncoupled fluid flow. The approximate function for the fully-coupled fluid flow equation can be expressed as;

$$\mathbf{A}(p) \equiv -\nabla^T \left[\frac{K_{ij}\rho}{\mu} \nabla(p - \rho gh) \right] + \left(\delta_{kl} - \frac{\delta_{ij} D_{ijkl}}{3K_s} \right) \frac{\partial \epsilon_{kl}}{\partial t} + \left(\frac{\phi}{K_f} + \frac{1-\phi}{K_s} - \frac{\delta_{ij} D_{ijkl} \delta_{kl}}{(3K_s)^2} \right) \frac{\partial p}{\partial t} = 0 \quad (2.25)$$

with boundary conditions satisfying the continuity of flow across the boundary:

$$B(p) \equiv -(\mathbf{n}^T) \left[\frac{K_{ij}\rho}{\mu} \nabla(p - \rho gh) \right] + q = 0 \quad (2.26)$$

The weak formulation for the fluid flow equation can be obtained using Green's theorem:

$$\begin{aligned} & -\int_{\Omega} \left\{ (\nabla \mathbf{a}^T) \left[\frac{K_{ij}\rho}{\mu} \nabla(p - \rho gh) \right] + (\mathbf{a}^T) \left[\left(\delta_{kl} - \frac{\delta_{ij}D_{ijkl}}{3K_s} \right) \frac{\partial \epsilon_{kl}}{\partial t} + \left(\frac{\phi}{K_f} + \frac{1-\phi}{K_s} - \frac{\delta_{ij}D_{ijkl}\delta_{kl}}{(3K_s)^2} \right) \frac{\partial p}{\partial t} \right] \right\} d\Omega \\ & -\int_{\Gamma} \left\{ (\mathbf{a}^T) \mathbf{n}^T \left[\frac{K_{ij}\rho}{\mu} \nabla(p - \rho gh) \right] + (\mathbf{b}^T) \mathbf{n}^T \left[\frac{K_{ij}\rho}{\mu} \nabla(p - \rho gh) \right] + (\mathbf{b}^T) q \right\} d\Gamma = 0 \end{aligned} \quad (2.27)$$

After following same finite element discretization procedure as in the previous, and making the weight function equal to the shape function used to interpolate the pressure distribution, the final matrix formation of the fluid flow equation is obtained as:

$$\mathbf{L}^T \frac{d\mathbf{u}}{dt} - \mathbf{K}_c \mathbf{p} + \mathbf{S} \frac{d\mathbf{p}}{dt} = \mathbf{f}_p \quad (2.28)$$

where \mathbf{K}_c is the permeability matrix, \mathbf{S} is the combined fluid and solid compressibility matrix due to the pore pressure. The matrices in Eq. (2.28) are defined as:

$$\begin{aligned} \mathbf{m} &= [1, 1, 1, 0, 0, 0]^T \\ \mathbf{K}_c &= \int_{\Omega} (\nabla \mathbf{N}_p)^T \frac{\mathbf{k}\rho}{\mu} \nabla \mathbf{N}_p d\Omega \\ \mathbf{L}^T &= \int_{\Omega} \mathbf{N}_p^T \left(\mathbf{m} - \frac{\mathbf{Dm}}{3K_s} \right) \mathbf{B} d\Omega \\ \mathbf{S} &= \int_{\Omega} \mathbf{N}_p \left(\frac{\phi}{K_f} + \frac{1-\phi}{K_s} - \frac{\mathbf{m}^T \mathbf{Dm}}{(3K_s)^2} \right) \mathbf{N}_p \\ \mathbf{f}_p &= \int_{\Omega} (\nabla \mathbf{N}_p^T) \frac{K_{ij}\rho}{\mu} (\rho gh) d\Omega - \int_{\Gamma} (\mathbf{N}_p^T) q d\Gamma \end{aligned} \quad (2.29)$$

In a similar manner, linear interpolation is used for the time discretization. A weighted average of the time derivative of a variable, which is assumed to vary linearly over a small time step Δt is approximated at two consecutive times. For the simplicity, continuity equation (2.28) after applying fully implicit time integration scheme is given as:

$$\mathbf{L}^T \Delta \mathbf{u} + [\mathbf{S} - \Delta t \mathbf{K}_c] \Delta \mathbf{p} = \mathbf{F}_p \quad (2.30)$$

where

$$\begin{aligned} \Delta \mathbf{u} &= \mathbf{u}_{n+1} - \mathbf{u}_n \\ \Delta \mathbf{p} &= \mathbf{p}_{n+1} - \mathbf{p}_n \\ \mathbf{F}_p &= \Delta t \mathbf{K}_c \mathbf{p}_n + \Delta t \mathbf{f}_p \end{aligned} \quad (2.31)$$

The subscript **n** refers to the time step.

2.5.3 Complete set of FE Biot's equation

The complete set of fully coupled equation consists of equilibrium equation (2.23), and continuity equation (2.30). On the right hand side of the equilibrium equation, the total force vector, \mathbf{F}_u , is used and these equations are appropriate to linear system. In order to incorporate non-linear system, it is desirable to use incremental loads and allow plastic redistribution to equilibrate at each time step. If $\Delta \mathbf{F}_u$ is the change in load between successive times, the incremental form of the equation is

$$\mathbf{K}_m \Delta \mathbf{u} + \mathbf{L} \Delta \mathbf{p} = \Delta \mathbf{F}_u \quad (2.32)$$

Combining equation (2.30) and equation (2.32) results the incremental form of the discretized fully-coupled Biot's equations:

$$\begin{bmatrix} \mathbf{K}_m & \mathbf{L} \\ \mathbf{L}^T & \mathbf{S} - \Delta t \mathbf{K}_c \end{bmatrix} \begin{Bmatrix} \Delta \mathbf{u} \\ \Delta \mathbf{p} \end{Bmatrix} = \begin{Bmatrix} \Delta \mathbf{F}_u \\ \mathbf{F}_p \end{Bmatrix} \quad (2.33)$$

2.6 Validation of the Finite Element Discretization

2.6.1 Original Mandel's problem

Mandel [4] presented one of the first solutions for the three-dimensional consolidation theory of Biot, and it has been most popular problem for validating fully-coupled numerical codes [15-17]. In Mandel's problem, an infinitely long rectangular vertical cross-section of saturated poroelastic material is placed between two rigid frictionless plates under plan-strain condition as shown in Figure 2-1. The rigid motion of the plate simplifies the problem and leads to the solution independent of the y -axis. The lateral sides are free from normal and shear stress, and pore pressure. An instantaneous load, $2F$ is applied at $t=0$ at the top and bottom of the plates without allowing drainage on the lateral sides. Therefore, a uniform total vertical stress and a uniform excess pore pressure across the sample is initially generated by virtue of the Skempton effect [18] at $t=0^+$. Then drainage is allowed at the lateral sides and the pore pressure is allowed to dissipate as time progresses. As drainage proceeds at the lateral sides, non-uniform dissipation of induced pore pressure causes softening of the material near the sides and load transfer from the compressive total stress takes place towards center region. After a long time as $t \rightarrow \infty$, all excess pore pressure in the sample vanishes.

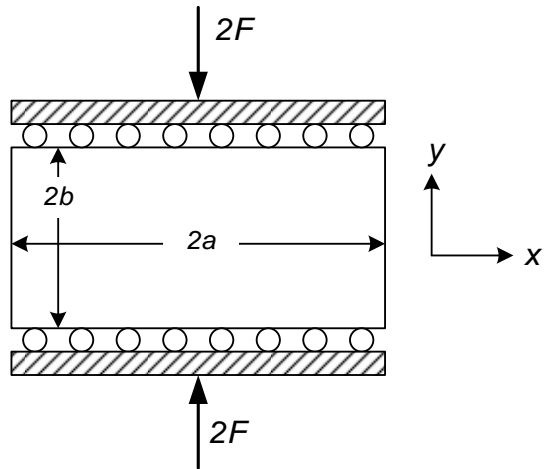


Figure 2-1 Mandel's Problem

An interesting phenomenon associated with Mandel's problem is that the pore pressure increases higher than the initial value in the central region of the porous layer at the early time of the drainage. Cryer [19] obtained similar results at the center of a spherical body consolidating under hydrostatic pressure. This type of non-monotonic pore pressure response has been referred to as the Mandel-Cryer effect which cannot be observed in a simple diffusion solution such as Terzaghi's theory [1]. The physical phenomena has been confirmed in the laboratory as well as in the field [9, 20].

In original solution by Mandel, exact solution with pore pressure expression was presented, and Cheng and Detournay [16] expanded the analytical solution to account for all field quantities such as total stresses, vertical/horizontal displacements, and flux. The expressions for the displacements, total stresses, and pore pressure are given by Cheng and Detournay [16] are presented in the Appendix-A. Abousleiman [21] extended Mandel's problem to account for the transverse anisotropy of the porous media.

2.6.1.1 FE model for Mandel's problem

Biot's FE equations based on linear stress-strain relation with 2D plane strain condition are developed and the FE implementation was carried out using MATLAB. Incompressible fluid and solid grains are assumed and that leads to $K_f \approx \infty$, and $K_s \approx \infty$, in the compressibility matrix \mathbf{S} in equation (2.29). Body force and source/sink of the fluid are ignored, and consequently the additional source term, \mathbf{f}_p , in equation (2.30) disappears. Mandel's problem is solved with FE simulation based on the prescribed equations with 80 elements. Only a quarter of the problem geometry is considered in the FE model due to the symmetry, and the geometry is shown in Figure 2-2. The aspect ratio of the poroelastic sample, h_2/a , is 0.2. The mechanical boundary conditions for symmetry correspond to roller boundaries along the bottom and the left side. After the vertical load $2F$ is applied, the pore pressures are allowed dissipate by reducing the nodal pore pressures to zero at the right side boundary of the model. Rigid body motion is enforced by locating weightless Euler-beam on the top and bottom of the elastic porous material with high rigidity (high EI , where E = Young's modulus and I = moment of inertia of the beam), and a uniformly distributed load is applied at the top of the rigid beam.

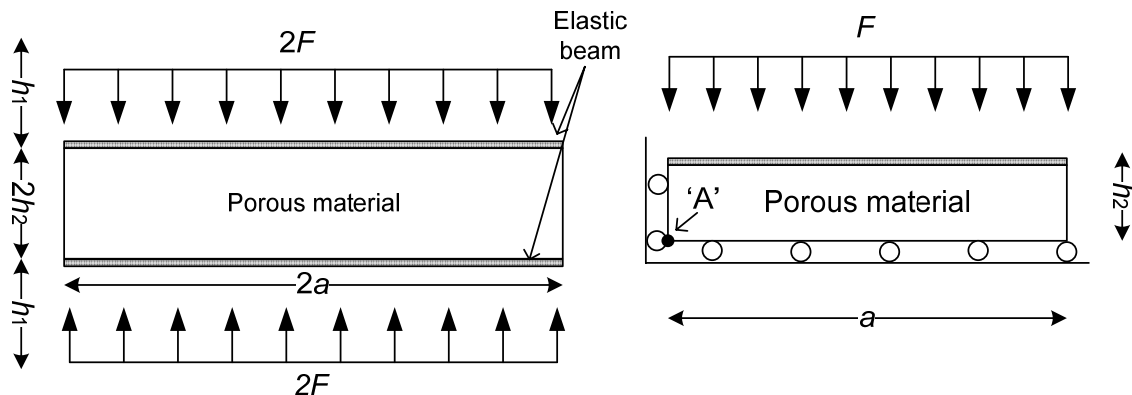


Figure 2-2 Mechanical boundary conditions for FE model

In the FE model, two types of isoparametric elements with different shape functions are introduced for the displacements field. One is Q4, which has four nodes per element (i.e., the element degree of freedom is 8 for the two dimensional case) and the other is Q9 which has nine nodes per element (i.e., the element degree of freedoms is 18) as shown in Figure 2-3. For the pore pressure field, only Q4 elements are used because it is a common technique to use lower ordered shape function for the pore pressure than the displacement field. The reason for this is that the discretized equations involve first derivatives for the fluid pressure, and second derivatives for the displacements. The element degree of freedom for the pore pressure is 4. The porous material and fluid properties and other input values used for each case are shown in Table 2-1.

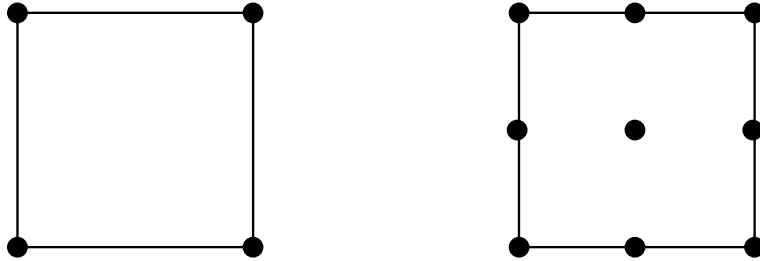


Figure 2-3 4-node element (Q4) and 9-node element (Q9)

Table 2-1 Properties and other input data for the FE model

Parameter	Case 1 (Q4Q4)	Case 2 (Q9Q4)
Poisson's ratio, ν	0.2	
Young's modulus, E		1 KPa
Permeability, $k_x=k_y$ ($k_{xy}=k_{yx}=0$)	0.1 m/s	
External Force, F		1 KN
Number of time steps	2000	
Number of node per element	displacement : 4 pore pressure : 4	displacement : 9 pore pressure : 4

Figure 2-4 shows pore pressure profiles from analytical and FE solutions at the center of the porous material (i.e., point 'A') as function of time. The load generates a uniform excess pore pressure which is a half of the amount of applied load due to Skempton's effect, that is:

$$\frac{ap(0^+)}{F} = \frac{1}{3} B(1 + \nu_u) \quad (2.34)$$

According to equation (2.34), the dimensionless pore pressure value is 0.5 with given undrained Poisson's ratio and Skempton's coefficient (i.e., $\nu_u=0.5$, $B=1$). Figure 2-4 shows that the pore pressure rises above the initial value for small time period because non-uniform dissipation of pore pressure during the short time cause compression near the lateral side where drainage take place. The resulting stress concentration in the central region then causes an additional rise in excess pore pressure as the load carried by fluid in the central carry region increases. Figure 2-5 shows pore pressure profiles along the horizontal distance, x/a at various normalized times, $t^* = ct/a^2$ (where c is a *generalized consolidation coefficient*), for both the FE solution and the analytical solution. Details of mathematical expression of a generalized consolidation are presented in Appendix-A. As can be seen, good agreement between the two solutions is obtained. Also, calculated pore pressures are not strongly dependent on the type of the finite element used.

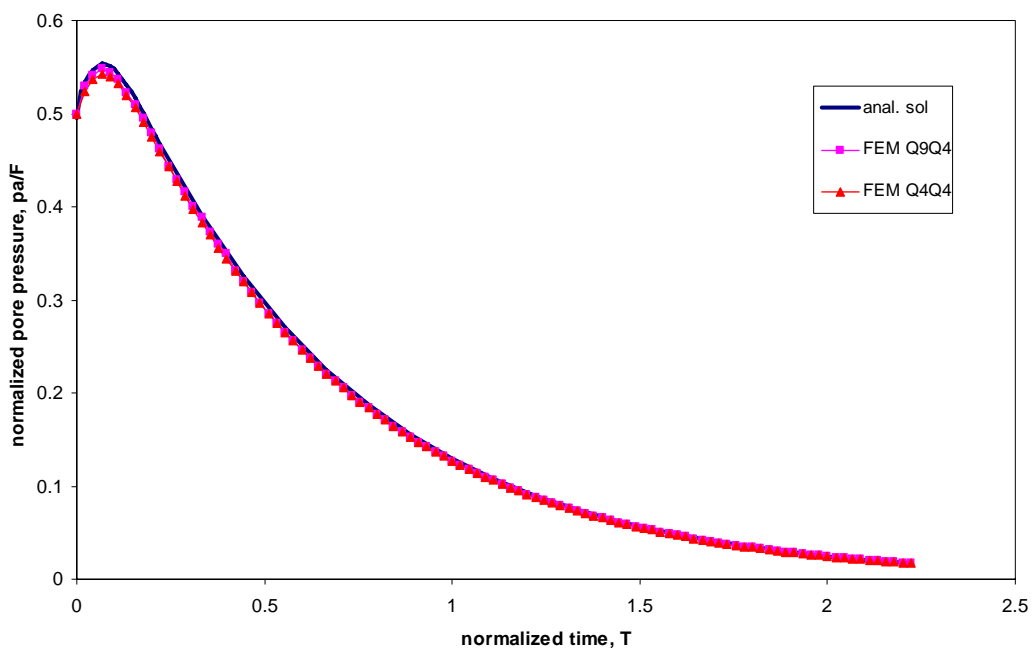


Figure 2-4 Pore pressure profiles vs. time

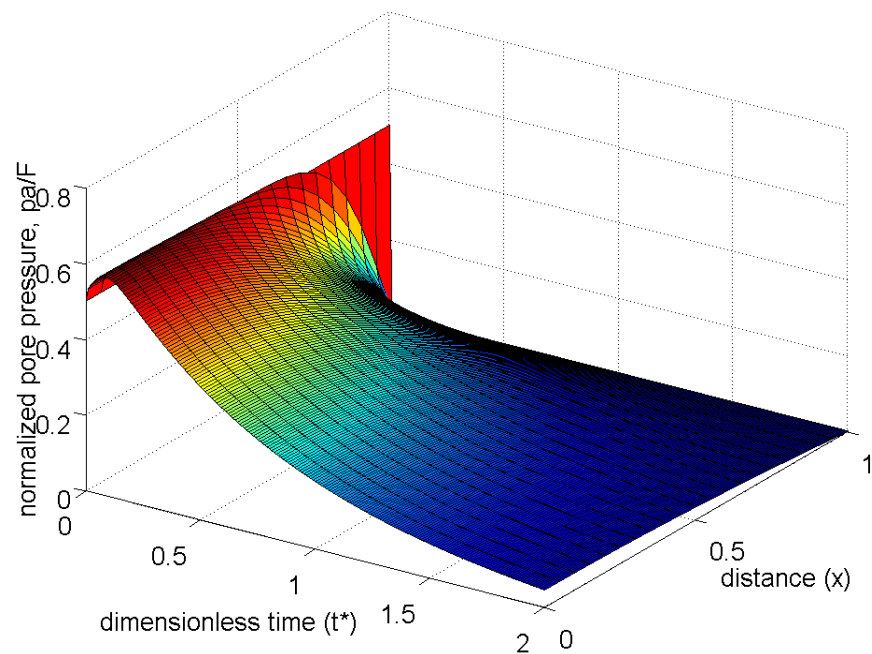


Figure 2-5 Pore pressure profile (FEM Q9Q4)

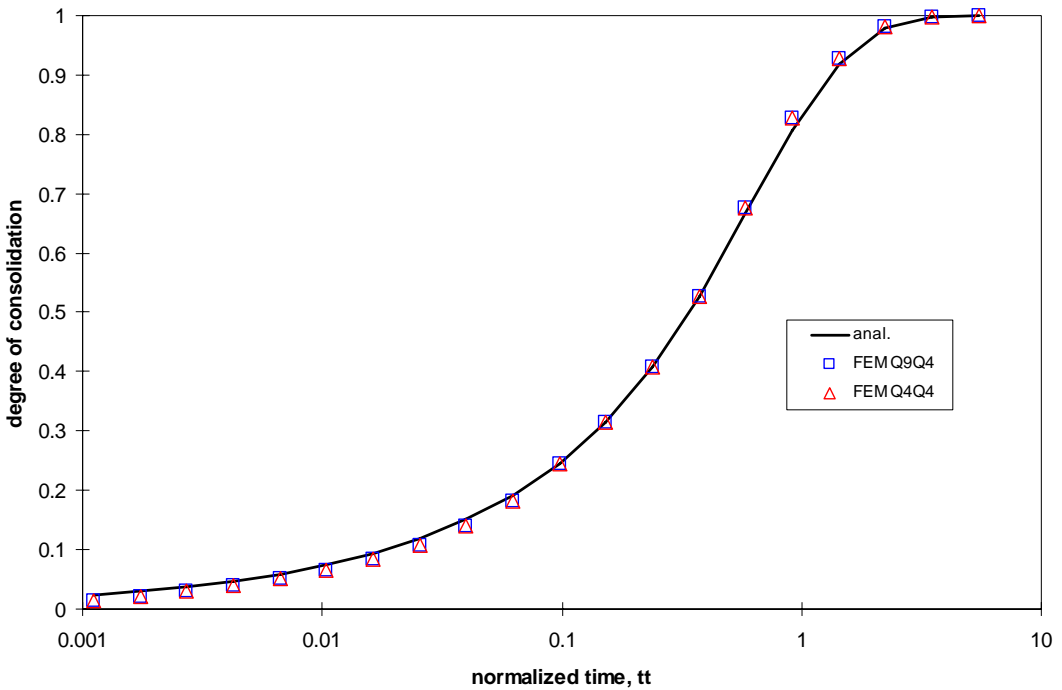


Figure 2-6 Degree of consolidation profile

Figure 2-6 presents the *degree of consolidation* based on the displacements and as can be seen, good agreement between the FE and analytical solutions are obtained. Detailed mathematical expression of the *degree of consolidation* for this specific problem is presented in Appendix-A. Although it is common technique to use higher order of shape function for displacement field than the pore pressure field, the difference of results between Q4Q4 (case1) and Q9Q4 (case2) are insignificant for this specific case.

2.6.1.2 Effects of Poisson's ratio

Four numerical simulations were performed to analyze the effect of drained Poisson's ratio, v. Sample dimensions, properties, loading, and boundary conditions are identical to Case 2 from the FE model in previous section, except the Poisson's ratio which varies from 0 to

0.4. Figure 2-7 shows the pore pressure profiles at point ‘A’ with normalized time as function of Poisson’s ratio from the analytical and finite element solutions.

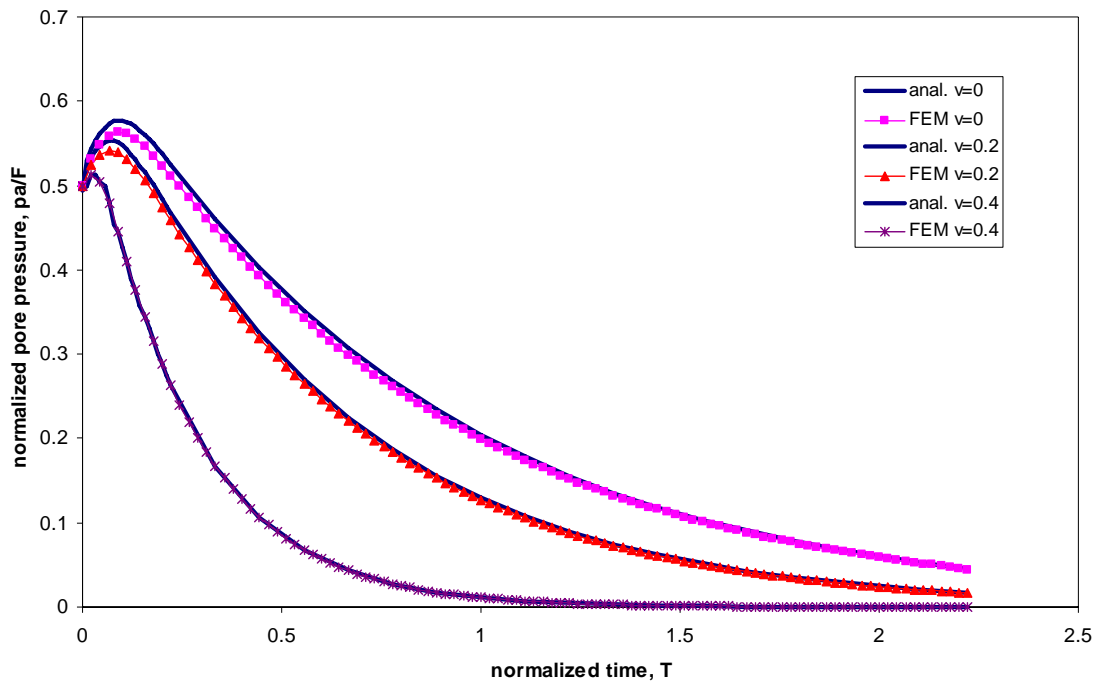


Figure 2-7 Pore pressure profiles with various Poisson’s ratio

As can be seen from the figure above, more pronounced Mandel-Cryer effect as indicated by the higher normalized pore pressure can be predicted from lower values of Poisson’s ratio.

2.6.2 Rigidity effects on Mandel’s problem

To represent more realistic situations, such as aquifers and reservoirs, and impervious deformable material with finite thickness and stiffness is placed on top of the porous material instead of elastic beam. Relatively rigid top platen movement is simulated by using

different values of the Young's modulus of the impervious elastic layer. In case of flexible top layer, stresses are not only function of the x -direction but also of the y -direction. In the simulations, a region of saturated poroelastic material is sandwiched between two impervious elastic layers and a quarter of the sample is analyzed in the FE simulations as shown in Figure 2-8.

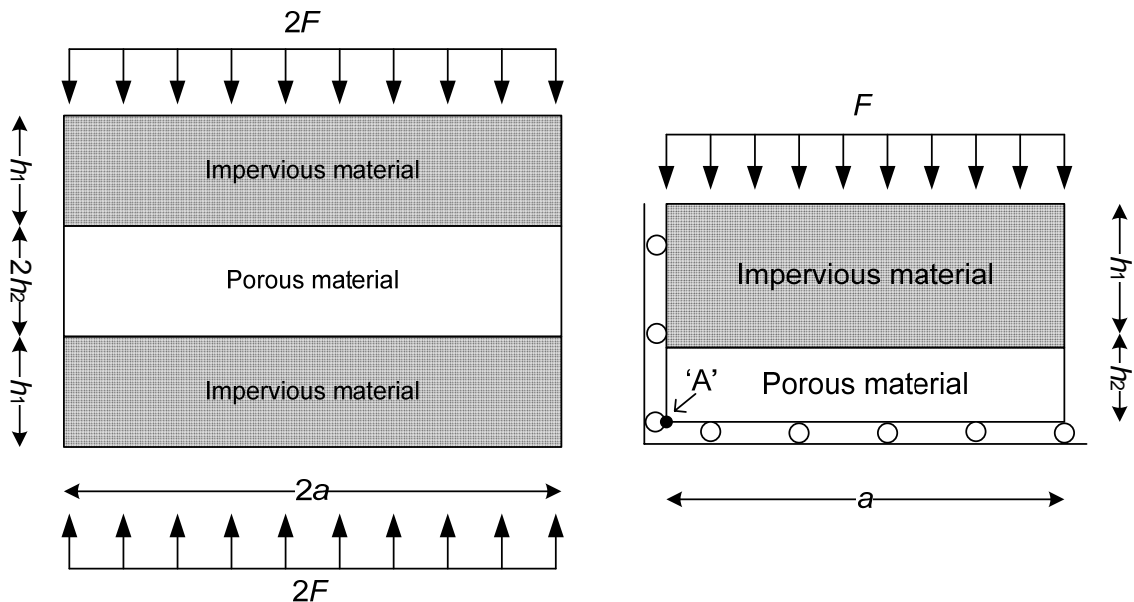


Figure 2-8 Full size model and quarter of the model with mechanical boundary conditions

In the FE analysis, frictionless condition is assumed to represent roller boundary between impervious layer and poroelastic layer. The thin-layer elements developed by Desai [22] are used as interface elements between the layers. Interface elements have very small thicknesses compared to the width and has same constitutive matrix as elastic materials.

The stiffness characteristics of the thin-layer interface elements are identical to solid elastic elements and the stiffness matrix \mathbf{K}_{int} is given as follows:

$$\mathbf{K}_{\text{int}} = \int_v \mathbf{B}^T \mathbf{D}^e \mathbf{B} dV \quad (2.35)$$

The shear stiffness of the thin-layer element can be determined from special laboratory tests and the normal stiffness is assumed to be same as the adjoining solid elements. To simulate frictionless condition, very small shear stiffness value is introduced in the interface element.

The thickness of the impervious layer, h_1/a , and the poroelastic layer, h_2/a , are 0.2 and 0.1 respectively. Drained Poisson's ratio is set to 0.2 and a Young's modulus ratio, which is ratio between Young's modulus of the impervious and porous material (E_1/E_2), varies from 1 to 10^7 . Fully implicit time scheme is introduced and dimensionless time interval, Δt^* , is 0.001. Figure 2-9 presents the discretized FE mesh of the model, and the shaded area represents an impervious elastic overburden.

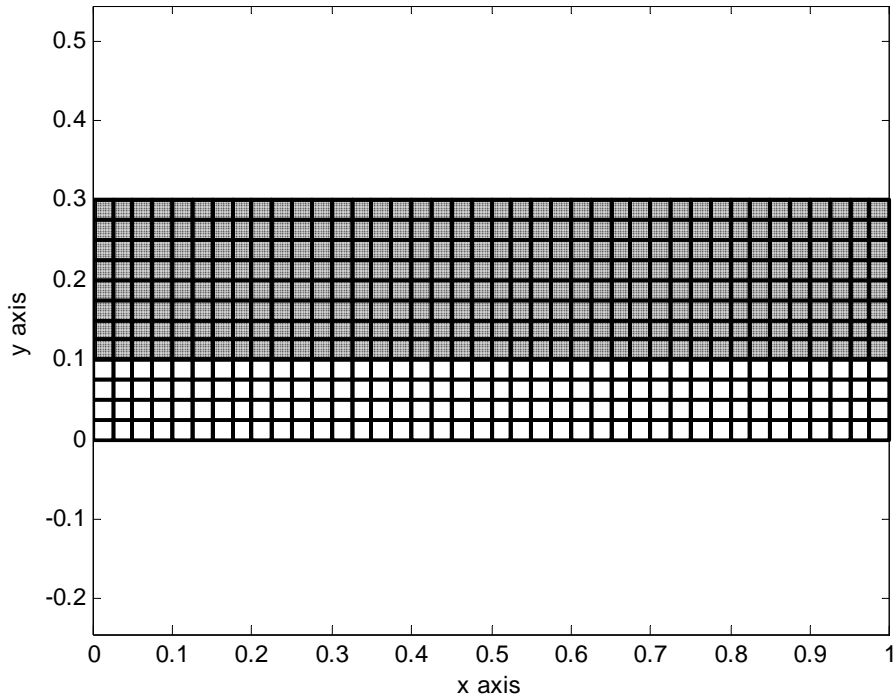


Figure 2-9 FE mesh for the impervious material located on the top of porous media ($h_1/a = 0.2$, and $h_2/a = 0.1$)

The results are presented in Figure 2-10. In this figure, pore pressures at the center of the poroelastic material (i.e., point ‘A’) are plotted for the different Young’s modulus ratio. As can be seen from the figure, a relatively flexible overburden, $E_1/E_2 = 1$, does not produce a Mandel-Cryer effect and more pronounced Mandel-Cryer effect is obtained with increasing rigidity of the impervious overburden layer. Because the edge of the model consolidates faster than central region due to the lateral drainage and as rigidity of overburden increases, larger forces are exerted to the central area. Vertical displacements on the top of poroelastic layer for the various Young’s modulus ratio at the dimensionless time, $t^*=0.65$ are shown

in Figure 2-11. As can be seen in the figure, the increased rigidity of top layer causes less vertical displacements at the edge and more displacements at the central area than a flexible top layer with a Young's modulus ratio of $E_1/E_2=1$. However, rigidity is not enough to cause larger vertical displacements at the central area for relatively low rigidity of $E_1/E_2=10^3$ and the vertical displacements are even less than flexible case. In case of high rigidity of $E_1/E_2=10^7$, the pore pressure profile is similar to the Mandel-Cryer analytical solution. Maximum pore pressures for various stiffness values of the overburden layer are shown in Figure 2-12 and as stiffness increases in terms of Young's modulus ratio, more significant Mandel-Cryer effect can be observed. Uncoupled solution is from the conventional fluid flow solution (e.g., single-phase transient problem solution). It only solves fluid flow equation and it cannot take into account the rigorous geomechanical effects, thus, normalized maximum pore pressure values are 0.5 (see equation (2.34)) regardless of the rigidity of the overburden layer in this particular case. Analytical Mandel's solution and uncoupled solution provides upper and lower boundary, respectively. FE solution may reach close to the upper boundary by increasing degree of freedom of elements, and/or using finer discretized mesh.

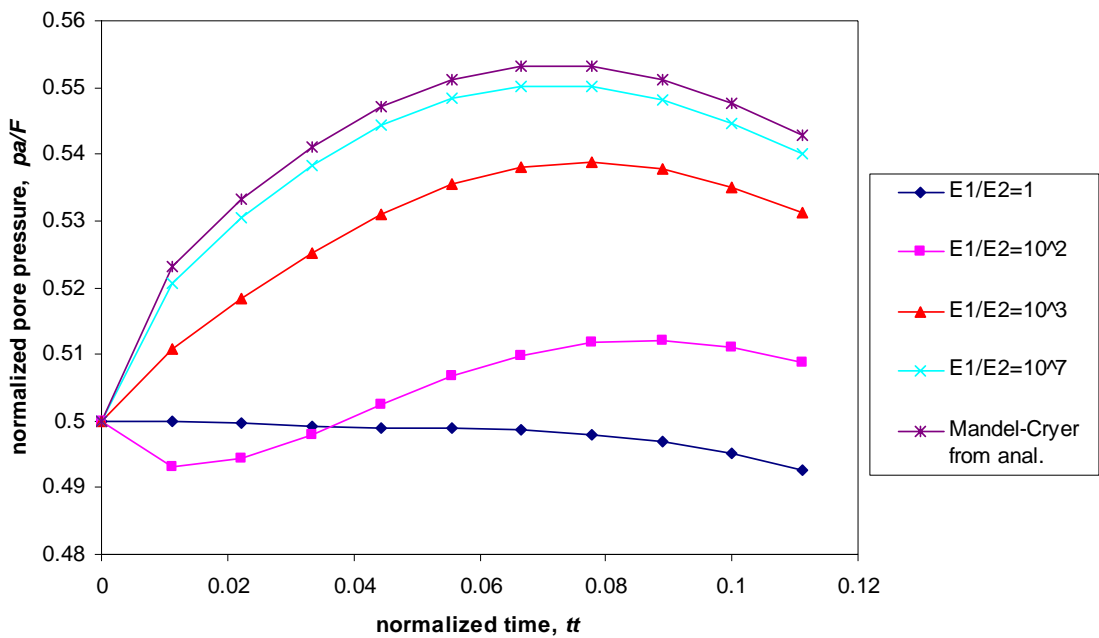


Figure 2-10 Pore pressure profiles for different Young's modulus ratio

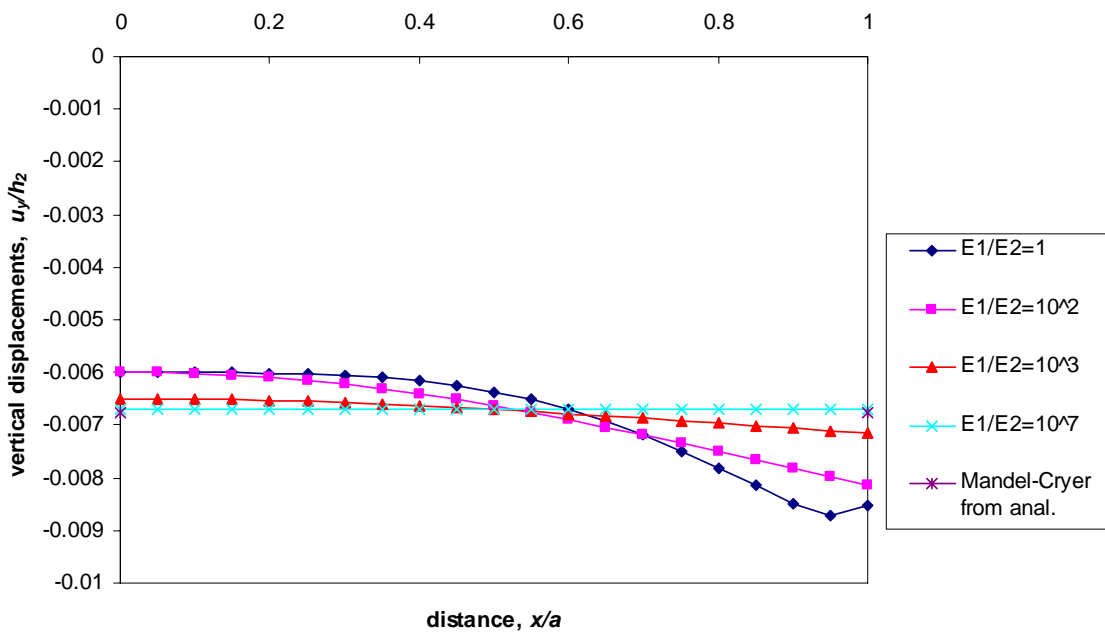


Figure 2-11 Vertical displacements of top of the poroelastic sample with different Young's modulus ratio ($t^*=0.065$)

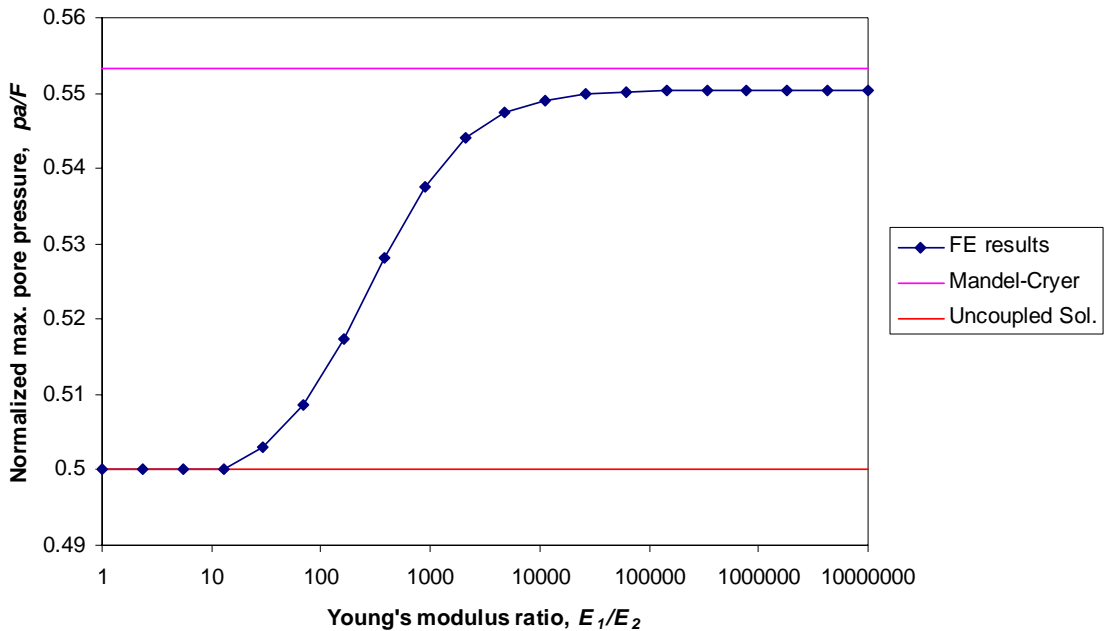


Figure 2-12 Normalized pore pressures for different rigidity of impervious material

2.6.2.1 Effect of thickness of overburden layer

The thickness of the impervious overburden layer affects the rigidity because thickness increases bending stiffness. However, it is not known what the relationship is between rigidity of the overburden and pore pressure profiles for Mandel's problem. In order to analyze the thickness effect, five FE simulations have been performed with different thickness ratios, h_1/a , varying from 0.05 to 0.8. Figure 2-13 shows the FE model with mechanical boundary conditions for two cases with $h_1/a=0.05$ and 0.8. Poisson's ratio for the elastic materials is set to zero to amplify the Mandel-Cryer effects.

Figure 2-14 presents the maximum pore pressure profile for the various Young's modulus ratios with different thickness ratios. As can be seen from the figure, higher maximum pore

pressures are obtained for the higher thickness ratio with same Young's modulus ratio. More interestingly, maximum pore pressure profiles have similar patterns with various thicknesses ratio. Therefore, it appears that a normalizing factor can be found by a trial and error method. For the various thicknesses of the overburden material, maximum pore pressure can be normalized with:

$$\frac{E_1}{E_2} \left(\frac{h_1}{a} \right)^{2.83} / \exp \left[\left(\frac{h_1}{a} \right)^3 \right] \quad (2.36)$$

Results after applying the normalization factors are shown in Figure 2-15. The case of $h_1/a > 0.8$ with fine refinement mesh cannot be simulated due to the large contrast in stiffness values. However, it is found that the normalization can be applied to the case until h_1/a equals 1.0 using a coarser mesh.

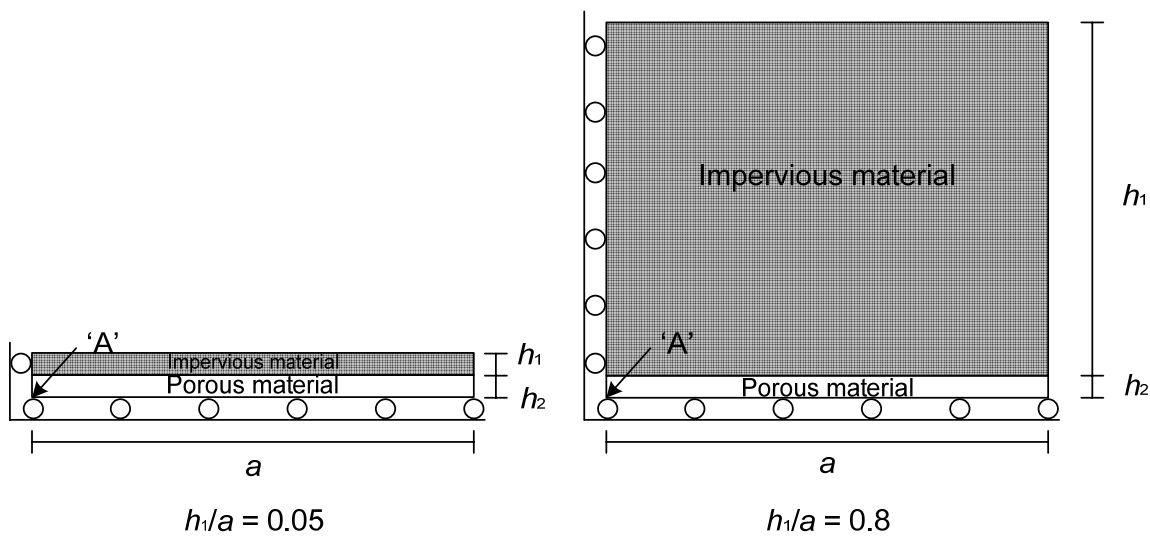


Figure 2-13 A quarter of the sample with mechanical boundary conditions of the different thickness of impervious layer

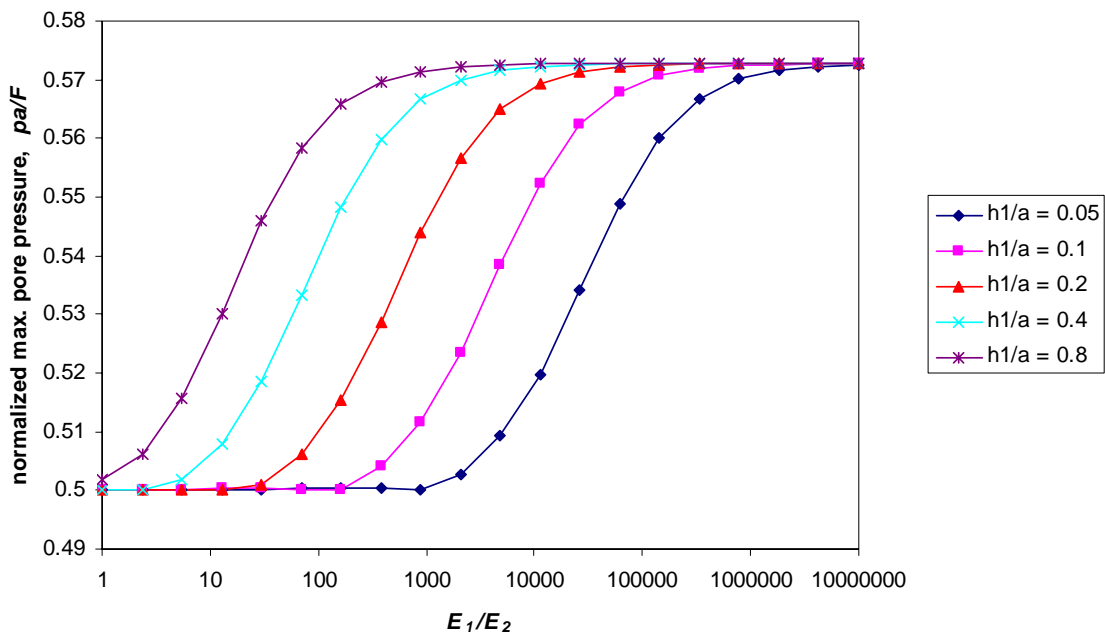


Figure 2-14 Maximum pore pressures for various thickness of impervious layer

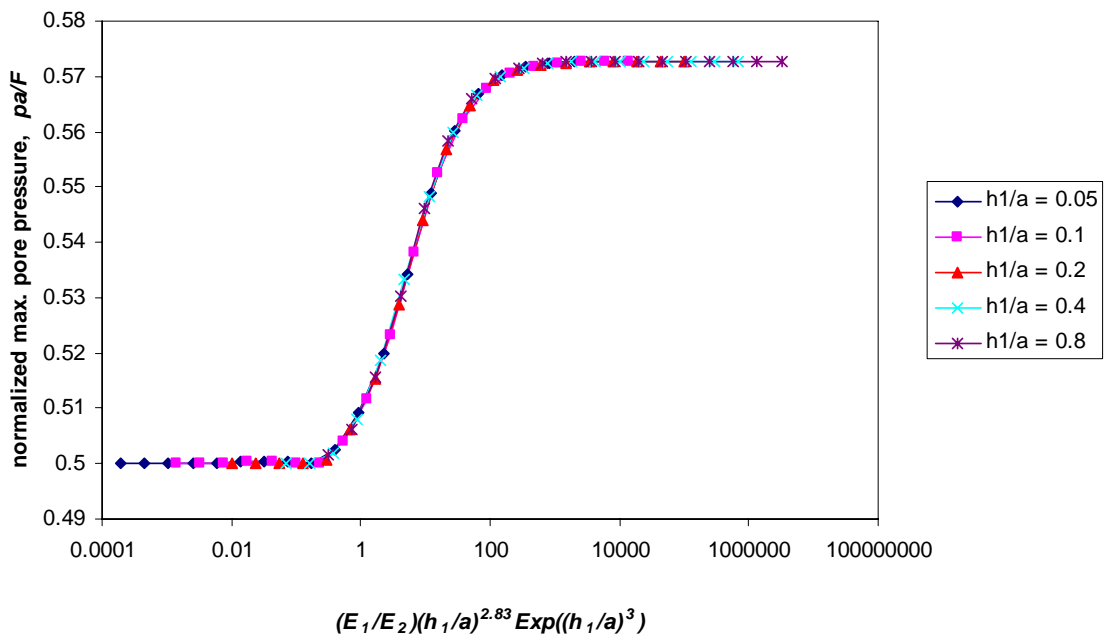


Figure 2-15 Maximum pore pressures for various thickness of impervious layer after normalization

2.6.2.2 Effect of thickness of porous material

Six numerical simulations were performed to analyze the effect of thickness of the fully saturated porous layer. The thickness of porous media h_2/a , varies from 0.05 to 0.5 and two cases with different thickness with $h_2/a = 0.05$ and 0.5 are presented in the Figure 2-16 with mechanical boundary conditions. Elements size and other properties are identical to those used in the previous section.

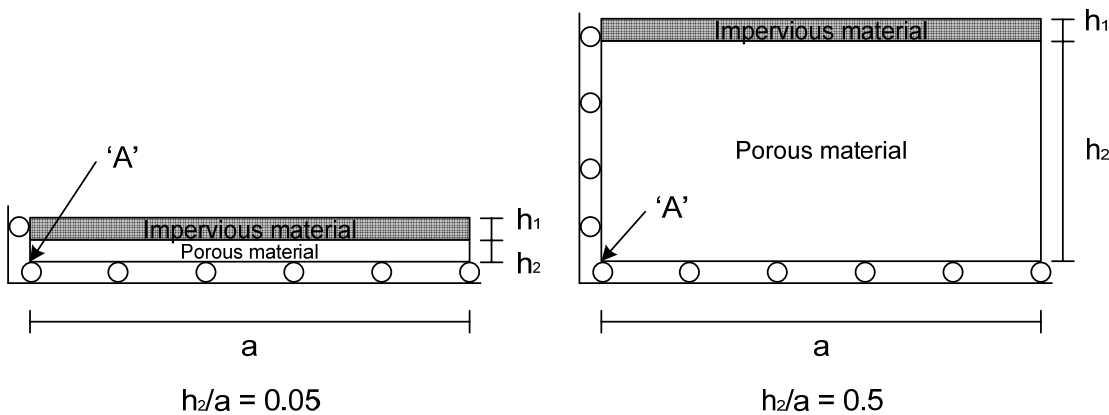


Figure 2-16 A quarter of the sample with mechanical boundary conditions of the different thickness of the porous layer

Maximum pore pressures profiles are shown in the Figure 2-17 for various Young's modulus ratio with various thickness of porous layer. It can be seen that higher maximum pore pressure is measured at the center of the porous layer (i.e., point 'A') with increasing thickness of porous layer. In other words, when the thickness of the porous layer increases, the porous layer above the measuring point behaves like an additional overburden. Therefore, Mandel-Cryer effect always can be found for the relatively high thickness (in

this case for $h_2/a > 0.4$) even though the rigidity of the top layer is not enough to cause Mandel-Cryer effect for a thin porous layer. For various thicknesses, h_2/a , within the range from 0.05 to 0.5, the maximum pore pressures can be normalized with;

$$\left[\frac{E_1}{E_2} \left(\frac{h_1}{a} \right)^{2.83} + \left(\frac{h_2}{a} \right)^{3.75} \right] \left(\frac{h_2}{a} \right) / \exp \left[\left(\frac{h_1}{a} \right)^3 \right] \quad (2.37)$$

As it can be seen in equation (2.37), it includes the thickness effects of impervious layer. As it can be seen from Figure 2-18, the normalization factor is applicable for the various thicknesses of porous material.

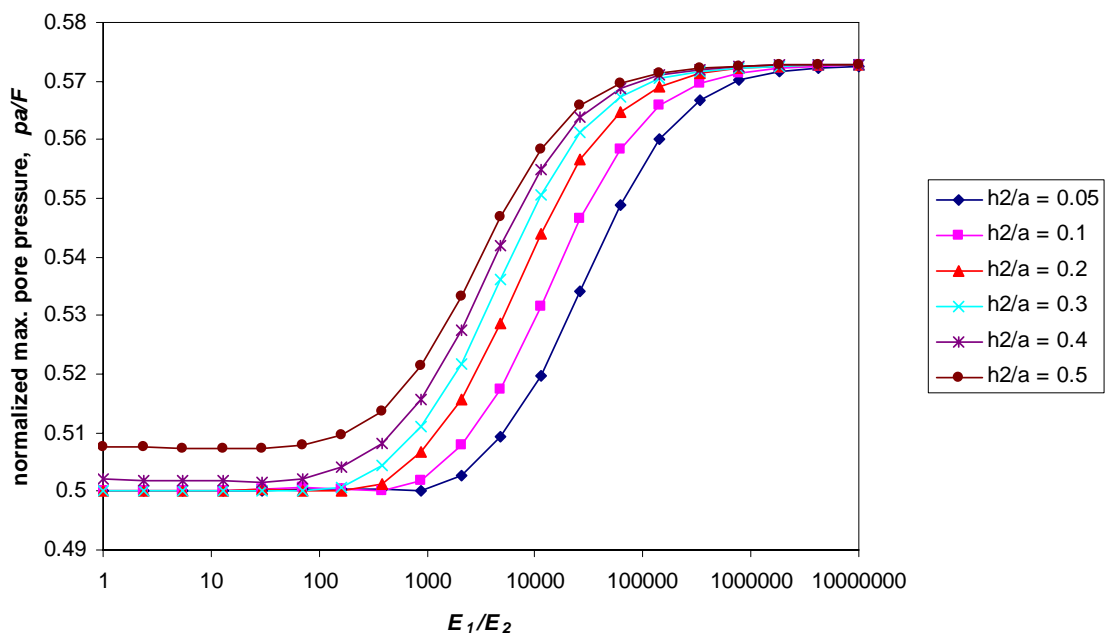


Figure 2-17 Maximum pore pressures for various thicknesses of the porous layer

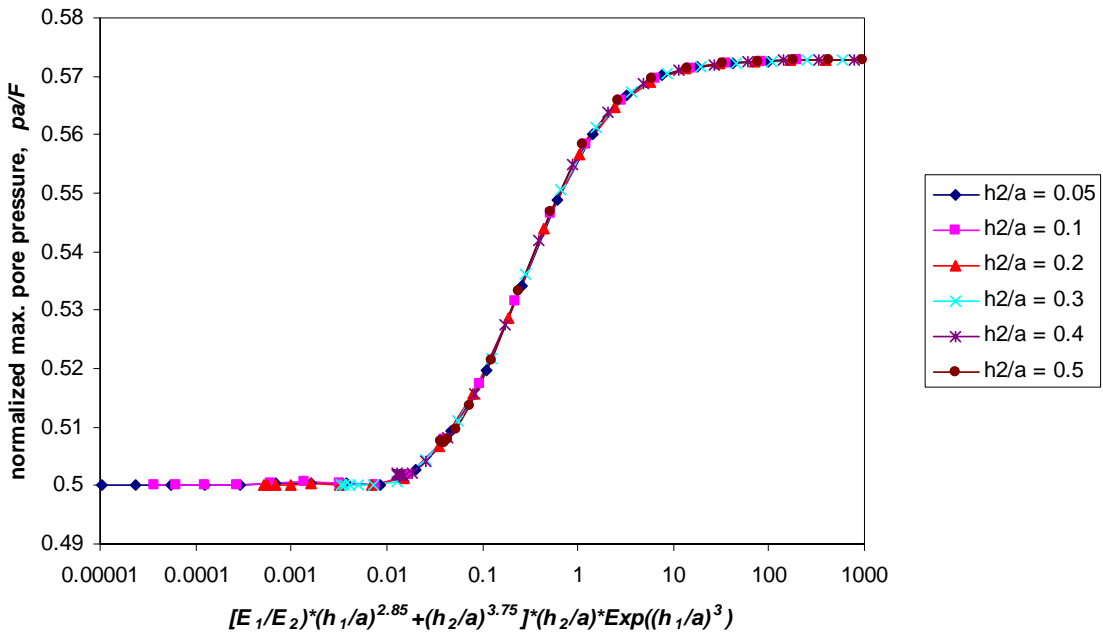


Figure 2-18 Max. pore pressures for various thicknesses of the porous layer after normalization

Dimensionless maximum pore pressure results from 14 FE simulations with zero drained Poisson's ratio are normalized and plotted in the Figure 2-19. A continuous trend line is obtained from non-linear regression of the FE simulations results. The applicable dimension ranges of the equation are $0.005 \leq h_1/a \leq 1.0$ for the impervious top layer and $0.005 \leq h_2/a \leq 0.5$ for the porous material. Coefficients for the equation are $a_1=0.573$, $a_2=0.074$, $a_3=0.306$ and $a_4=1.047$. However, results from the equation are from numerical analyses and equation is not fitted perfectly in the relatively low range of x -coordinate in the graph.

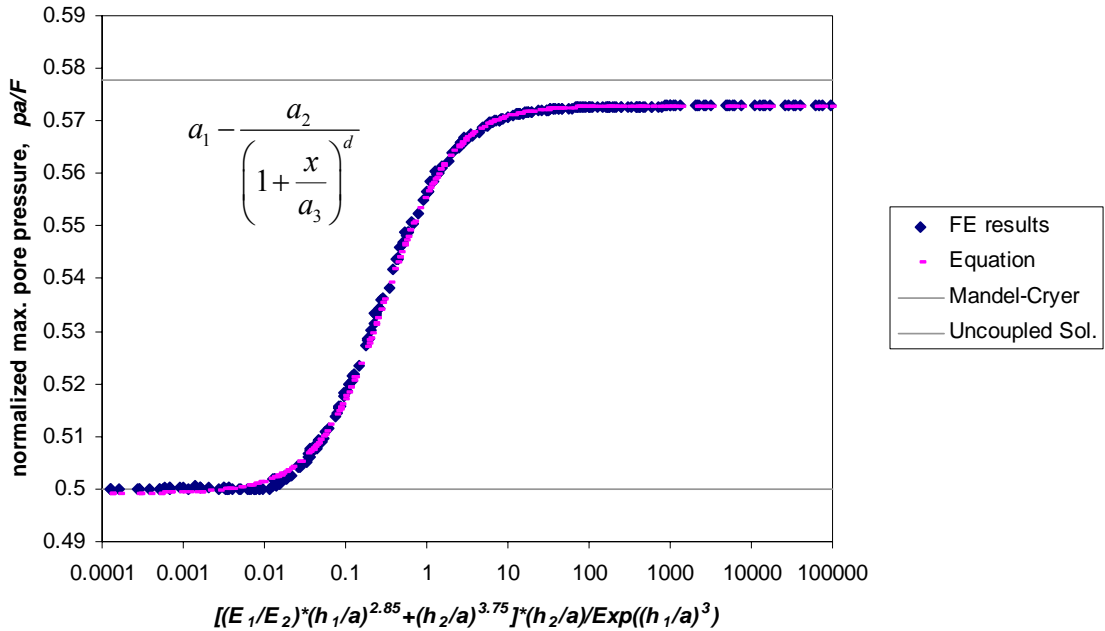


Figure 2-19 Maximum pore pressure profile after normalization ($\nu=0$)

Figure 2-20 shows maximum pore pressure results using the normalization of the pore pressure which vary from 0 from uncoupled solution to 1 from the full Mandel-Cryer effect. Result from the equation is free from discretization effects but it produces higher pore pressure values than FE results in the low range of x -coordinate in the graph. Best-fit values for the equation are 0.339 and 1.092 for b_1 and b_2 , respectively. These normalized graphs enable one to predict maximum pore pressure at the center of the poroelastic material as function of geometry and Young's modulus ratio. Normalized pore pressure profiles with various values of Poisson's ratio are presented in Figure 2-21. In this figure, the maximum and minimum pore pressure correspond to the ones from Mandel's solution, and uncoupled solution, respectively

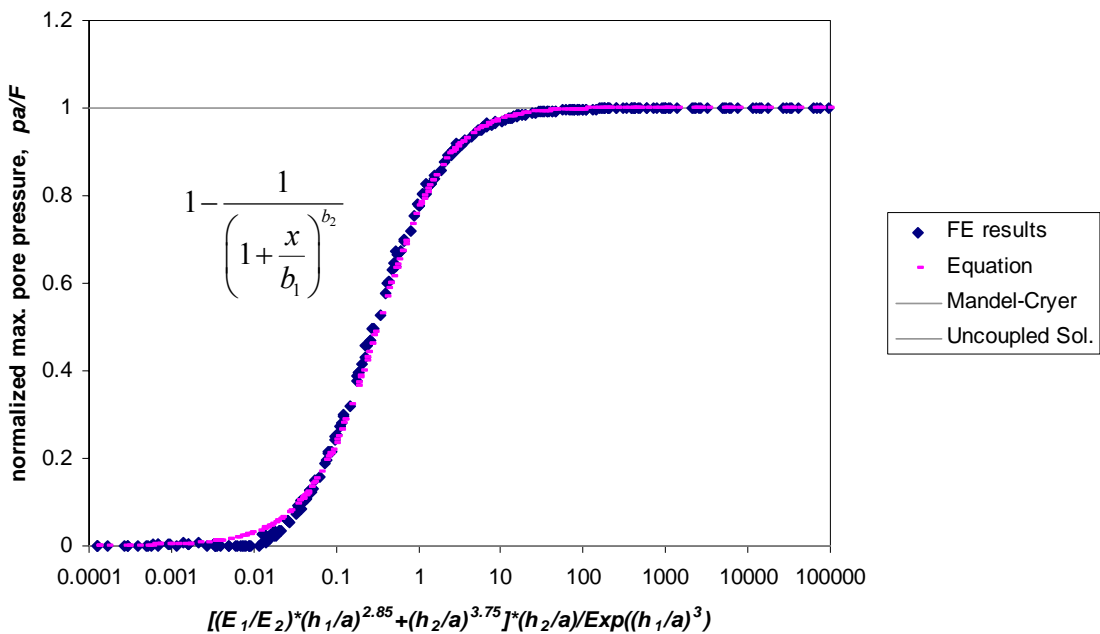


Figure 2-20 Maximum normalized pore pressure profile after normalization ($v=0$)

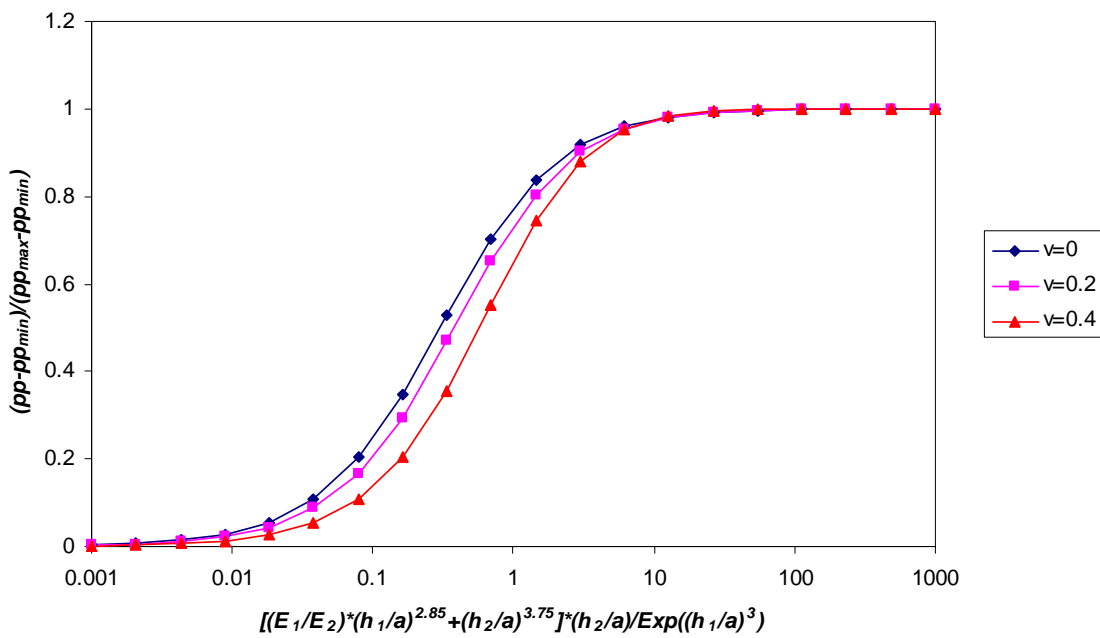


Figure 2-21 Maximum normalized pore pressure profile after normalization

REFERENCES

1. Terzaghi, K. 1943. *Theoretical Soil Mechanics*. New York: Wiley.
2. Rendulic, L. 1936. Porenziffer und Porenwasserdruck in Tonen. *Der Bauingenieur*. 17: 559-564.
3. Biot, M.A. 1941. General theory of three-dimensional consolidation. *Journal of Applied Physics*. 12: 155-164.
4. Mandel, J. 1953. Consolidation des sols. *Geotechnique*. 3: 287-299.
5. Biot, M.A. 1955. Theory of elasticity and consolidation for a porous anisotropic solid. *Journal of Applied Physics*. 26: 182-185.
6. Biot, M.A. 1956. General solutions of the equations of elasticity and consolidation for a porous material. *Journal of Applied Mechanics*. 78: 91-96.
7. Detournay, E. and A.H.D. Cheng 1993. *Fundamentals of poroelasticity*, In in *Comprehensive rock engineering: principles, practice, projects, Vol. II, Analysis and design method*, C. Fairhurst, Editor. Oxford: Pergamon. p. 113-171.
8. Rice, J.R. and M.P. Cleary 1976. Some basic stress diffusion solutions for fluid-saturated elastic porous media with compressible constituents. *Reviews of geophysics and space physics*. 14: 227-241.
9. Verruijt, A. 1969. Elastic storage of aquifers. in *Flow Through Porous Media* New York: Academic Press.
10. Wang, H.F. 2000. *Theory of Linear Poroelasticity with Applications to Geomechanics and Hydrogeology*. New Jersey: Princeton University Press.
11. Gutierrez, M. and R.L. Lewis 2001. Petroleum Reservoir Simulation Coupling Fluid Flow and Geomechanics. *SPE Reservoir Evaluation & Engineering*. 4: 164-171.
12. Gutierrez, M. and R.L. Lewis 2002. Coupling of Fluid Flow and Deformation in Underground Formations. *Journal of Engineering Mechanics*. 128.
13. Lewis, R.W. and B.A. Schrefler 1987. *The Finite Element Method in the Deformation and Consolidation of Porous Media*: John Wiley & Sons.

14. Lewis, R.W. and Y. Sukirman 1993. Finite Element Modelling of Three-Phase Flow in Deforming Saturated Oil Reservoirs. *International journal for Numerical and Analytical Methods in Geomechanics*. 17: 577-598.
15. Cheng, A.D.H., Y. Abousleiman and J.-C. Roegiers 1993. Review of some poroelastic effects in rock mechanics. *International journal of rock mechanics and mining sciences & geomechanics*. 30: 1119-1126.
16. Cheng, A.D.H. and E. Detournay 1988. A Direct Boundary Element Method for Plane Strain Poroelasticity. *International journal for Numerical and Analytical Methods in Geomechanics*. 12: 551-572.
17. Cui, L., A.H.D. Cheng and V.N. Kaliakin 1996. Finite Element Analyses of Anisotropic Poroelasticity: A Generalized Mandel's Problem and an Inclined Borehole Problem. *International Journal for Numerical Analysis Methods in Geomechanics*. 20: 381-401.
18. Skempton, A.W. 1954. The pore pressure coefficients A and B. *Geotechnique*. 4: 143-147.
19. Cryer, C.W. 1963. A comparison of the three-dimensional consolidation theories of Biot and Terzaghi. *Quarterly Journal of Mechanics & Applied Mathematics*. 16: 401-412.
20. Rodrigues, J.D. 1983. The Noordbergum effect and characterizaion of aquitards at the Rio Maior Mining Project. *Ground Water*. 21: 200-207.
21. Abousleiman, Y., A.H.-D. Cheng, L. Cui, E. Detournay and J.-C. Roegiers 1996. Mandel's problem revisited. *Geotechnique*. 46: 187-195.
22. Desai, C.S., M.M. Zaman, J.G. Fightner and H.J. Siriwardane 1984. Thin-layer element for interfaces and joints. *International Journal for Numerical and Analytical Methods in Geomechanics*. 8: 19-43.

3 BIOT'S THEORY FOR MULTI-PHASE FLUID FLOW

3.1 *Introduction*

The study of multi-phase immiscible flow behavior for production in hydrocarbon reservoirs has attracted researchers in petroleum engineering for more than forty years. In geotechnical engineering, fluid flow behavior in partially saturated soil has gained increased attention in recent years. Understanding the mechanics of immiscible fluid flow of fluids through soils has become an important research area in environmental engineering.

In this chapter, the fully-coupled Biot's theory is extended to two-phase fluid flow for deformable porous media which contains two immiscible fluids (e.g., water and vapor, and water and oil). Traditional two-phase fluid flow equations are derived using the rock compressibility term and it will later be used in the modular solution technique based on the updating the rock compressibility matrix. Throughout this chapter, constant temperature or isothermal condition is assumed. In case of fluid flow containing gas and liquid, gas is assumed to be not soluble (i.e., immiscible) in the liquid phase. Pore water pressure (i.e., wetting fluid) and pore gas (i.e., non-wetting fluid) pressure are chosen as the main variables in this chapter. The equations are therefore directly applicable to unsaturated soil mechanics. The choice of the pressures as the primary variables, in contrast to the use of fluid saturations or combinations of pressures and saturations, is appropriate in the

monolith, an modular solution method of the coupled equations. For hydrocarbon reservoirs, oil is typically the non-wetting fluid, and water is the wetting fluid.

3.2 Fluid Flow Properties

3.2.1 Capillary pressure

In a partially saturated soil, capillary phenomenon in a porous media involves a solid phase and at least two fluid phases. In solid-water-air system, water is said to be wetting phase and air is non-wetting phase. The pressure difference between these two phases is defined as a *capillary pressure*, p_c , and it can be expressed as;

$$p_c = p_g - p_w \quad (3.1)$$

where p_g , and p_w are gas pressure and water pressure, respectively

Capillary pressure is a fundamental factor in the study of multi-phase flow through porous media and it enables a dry soil to draw water through continuous pores to elevations above the phreatic line, or enables an initially saturated soil to keep the water at a certain elevation above the phreatic line in a draining process. In a two-phase situation, the amount of water and air in the voids are designated by the water saturation, $S_w = V_w / V_v$ and air saturation, $S_a = V_a / V_v$, respectively, where V_w is the volume of water, V_a is the volume of air, and V_v is the volume of voids. The relationship between, capillary pressure and saturation is represented by capillary pressure curve, and a typical shape of this curve is illustrated in Figure 3-1.

Capillary pressure is dependent on saturation and in general, two types of fluid displacement can occur, which are the imbibition and drainage process. The capillary pressure response follows the drainage curve for decreasing water saturation. On the other hand, the capillary pressure response follows the imbibition curve in case water displaces gas (i.e., increasing saturation). However, in a real situation, the direction of saturation change involves both processes and the boundary between two cases is not straightforward. Hence, the capillary pressure cannot be defined as either a drainage and an imbibition mode. Such phenomena are commonly known as *capillary hysteresis* and normally follow different paths between the imbibition and drainage curves. However, this is not taken into account in this chapter and an approximated identical capillary-saturation curve for both imbibition and drainage will be used. Irreducible saturations exist for both wetting and non-wetting phases in which one phase can no longer be displaced by applying the other phase's pressure gradient. Wetting and non-wetting phase irreducible saturations are denoted as S_{wc} , and S_{nc} respectively.

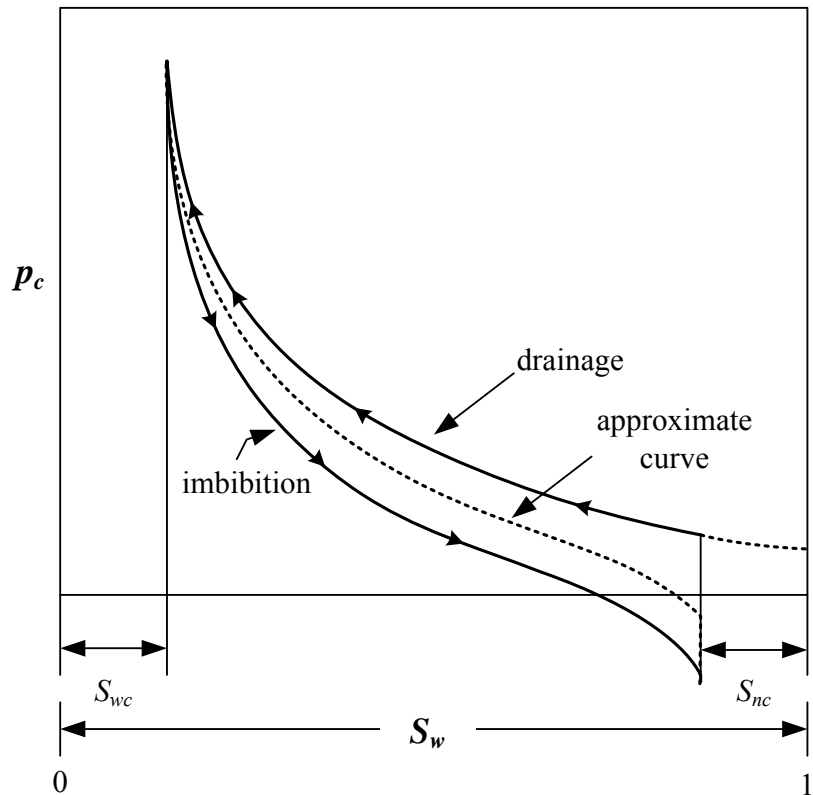


Figure 3-1 Typical capillary pressure vs. saturation curve

The time differential form of the capillary pressure can be written as:

$$\frac{\partial p_c}{\partial t} = \frac{\partial p_g}{\partial t} - \frac{\partial p_w}{\partial t} \quad (3.2)$$

The chain rule can be applied to equation (3.2) and which then results in;

$$\frac{\partial p_c}{\partial S_w} \frac{\partial S_w}{\partial t} = \frac{\partial p_g}{\partial t} - \frac{\partial p_w}{\partial t} \quad (3.3)$$

or in other form

$$\frac{\partial S_w}{\partial t} = S'_w \left(\frac{\partial p_g}{\partial t} - \frac{\partial p_w}{\partial t} \right) \quad (3.4)$$

where $S'_w = \partial S_w / \partial p_c$ is the slope of S_w vs. p_c curve

It is also assumed that the pore volume is completely filled by a combination of the fluids present. Therefore, the sum of the fluid phase saturations must equal unity as given below:

$$S_w + S_g = 1 \quad (3.5)$$

3.2.2 Relative permeability

In case of multi-phase flow in porous media, the ability of each fluid to move under an applied pressure gradient is a function of the relative permeability of that phase. The relative permeability is a dimensionless measure of the effective permeability of each phase and defined as the ratio of the permeability of porous media to the fluid at a given saturation to the permeability where 100 % saturated with the given fluid:

$$k_{ri} = \frac{k_i}{k} \quad (3.6)$$

where k_i is a phase permeability, and k is a permeability of the fully saturated medium in single-phase flow.

Typical curve of relative permeability against saturation is shown in Figure 3-2. It can be seen that each phase starts flow at irreducible saturation for both imbibition and drainage cycles. The relation among porosity, capillary pressure, and relative permeability are researched using theoretical methods as well as experimental results. These investigations

show that functional dependence of relative permeability with saturation can be approximated by:

$$k_{rw} = f(S_w) \quad (3.7)$$

$$k_{rg} = f(S_g) \quad (3.8)$$

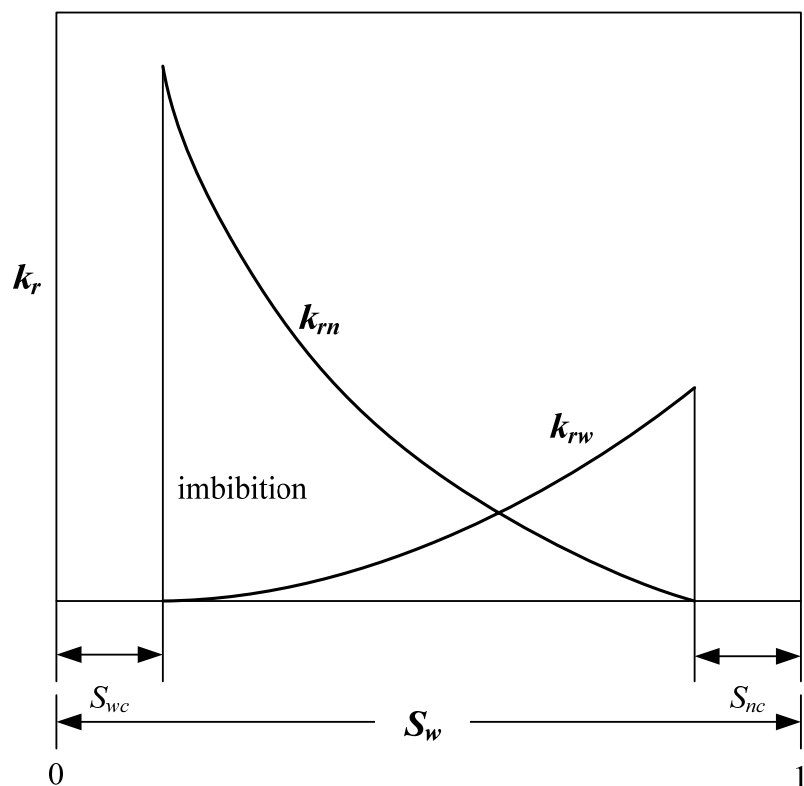


Figure 3-2 Typical relative permeability curve

3.3 Governing Equations

In this chapter, the equilibrium equations for the multi-phase flow in porous media are identical to the previous chapter except that the average pore pressure is used in the effective stress calculation for the multi-phase flow case. The average pore pressure has

been defined in different ways by several authors [1, 2]. In this thesis, the effective average pore pressure is calculated based on Lewis and Schrefler [3]:

$$p = S_w p_w + S_g p_g \quad (3.9)$$

Therefore, the effective stress law for two-phase fluids is given as:

$$\sigma'_{ij} = \sigma_{ij} + \delta_{ij} (S_w p_w + S_g p_g) \quad (3.10)$$

Differentiating equation (9) with respect to time yields;

$$\frac{\partial p}{\partial t} = S_w \frac{\partial p_w}{\partial t} + p_w \frac{\partial S_w}{\partial t} + S_g \frac{\partial p_g}{\partial t} + p_g \frac{\partial S_g}{\partial t} \quad (3.11)$$

Incorporating equation (3.1), (3.2), and (3.3) into equation (3.11) and then simplifying them, gives the following equation for the derivative of average pore pressure respective to the time in two-phase flow:

$$\frac{\partial p}{\partial t} = (S_w - p_w S'_w + p_g S'_w) \frac{\partial p_w}{\partial t} + (S_g + p_w S'_w - p_g S'_w) \frac{\partial p_g}{\partial t} \quad (3.12)$$

3.3.1 Continuity equation in the fully-coupled theory

In case of two-phase fluid flow, continuity equations for both air and water phase are needed. The equations can be derived in a similar manner to that applied for a single phase case that consists of combining the continuity equation with Darcy's law and the volume changes of materials (i.e., fluids and solid grains) due to the pore pressure and effective stresses. Each continuity equation conserves the mass balance of that phase within the

system for all time. With assumption of constant density of fluids, continuity equation of water phase can be expressed as below.

$$\nabla \cdot \frac{K_{ij} k_{rw}}{\mu_w} (\nabla p_w - \rho_w g) = \left(\delta_{kl} - \frac{\delta_{ij} D_{ijkl}}{3K_s} \right) \frac{\partial \varepsilon_{kl}}{\partial t} + S_w \left(\frac{1-\phi}{K_s} \right) \frac{\partial p}{\partial t} + S_w \frac{\phi}{K_w} \frac{\partial p_w}{\partial t} + \phi \frac{\partial S_w}{\partial t} \quad (3.13)$$

Details of the components of the rate of fluid accumulation term are as shown below:

- The rate of the soil matrix volume change due to the change of total strain

$$\frac{\partial \varepsilon_v}{\partial t} = \delta_{kl} \frac{\partial \varepsilon_{kl}}{\partial t} \quad (3.14)$$

- The rate of solid grain volume change due to average pore pressure changes

$$\frac{(1-\phi)}{K_s} \frac{\partial p}{\partial t} = \frac{(1-\phi)}{K_s} \left[(S_w - p_w S'_w + p_g S'_w) \frac{\partial p_w}{\partial t} + (S_g + p_w S'_w - p_g S'_w) \frac{\partial p_g}{\partial t} \right] \quad (3.15)$$

where K_s is the bulk modulus of the solid grain

- The rate of change of saturation

$$\phi \frac{\partial S_w}{\partial t} = \phi S'_w \frac{\partial p_c}{\partial t} \quad (3.16)$$

- The rate of water volume change due to pore water pressure change

$$\phi S_w \frac{\partial p_w}{\partial t} = \phi S_w \frac{\partial p_w}{\partial p} \frac{\partial p}{\partial t} = \frac{\phi S_w}{K_w} \frac{\partial p_w}{\partial t} \quad (3.17)$$

where K_w is the bulk modulus of water

- The change of solid grain size due to effective stress changes

$$-\frac{\delta_{ij}}{3K_s} \frac{\partial \sigma'_{ij}}{\partial t} \quad (3.18)$$

Incorporating of equation (3.15), (3.16) and (3.17) into equation (3.13) and then simplifying them, gives following continuity equation for water flow:

$$\nabla \cdot \frac{K_{ij}k_{rw}}{\mu_w} (\nabla p_w - \rho_w g) = \left[\frac{1-\phi}{K_s} S_w (S_w + p_g S'_w - p_w S'_w) + \frac{\phi S_w}{K_w} - \phi S'_w \right] \frac{\partial p_w}{\partial t} + \left[\frac{1-\phi}{K_s} S_w (S_w - p_g S'_w + p_w S'_w) + \phi S'_w \right] \frac{\partial p_g}{\partial t} + \left(\delta_{kl} - \frac{\delta_{ij} D_{ijkl}}{3K_s} \right) \frac{\partial \epsilon_{kl}}{\partial t} \quad (3.19)$$

The derivation of the continuity equation of the gas phase is essentially the same as that for the water flow equation and it can be formulated as:

$$\nabla \cdot \frac{K_{ij}k_{rg}}{\mu_g} (\nabla p_g - \rho_g g) = \left[\frac{1-\phi}{K_s} S_g (S_g - p_g S'_w + p_w S'_w) + \frac{\phi S_g}{K_g} - \phi S'_w \right] \frac{\partial p_g}{\partial t} + \left[\frac{1-\phi}{K_s} S_g (S_g + p_g S'_w - p_w S'_w) + \phi S'_w \right] \frac{\partial p_w}{\partial t} + \left(\delta_{kl} - \frac{\delta_{ij} D_{ijkl}}{3K_s} \right) \frac{\partial \epsilon_{kl}}{\partial t} \quad (3.20)$$

3.3.2 Continuity equation in the conventional multi-phase fluid flow formulation

The conventional continuity equation of multi-phase fluid flow has a different expression from the fully-coupled case on the right hand side terms. For example, the conventional fluid flow equation does not take into account of the more sophisticated volumetric changes due to effective stress changes and external load application. It assumes that volume changes are only related to porosity changes which only occur from the pore pressure changes. Also geomechanical effects on pore pressures are simplified through *pore*

compressibility, c_t , which relates the change in the pore volume of the rock to pore pressure change. The continuity equation of water phase is expressed as:

$$\nabla \cdot \frac{K_{ij}k_{rw}}{\mu_w} (\nabla p_w - \rho_w g) = \frac{\partial(\phi S_w)}{\partial t} \quad (3.21)$$

The right hand side of equation (3.21) can be expanded using chain rule:

$$\frac{\partial(\phi S_w)}{\partial t} = S_w \frac{\partial \phi}{\partial t} + \phi \frac{\partial S_w}{\partial t} = S_w \frac{\partial \phi}{\partial t} + \phi \frac{\partial S_w}{\partial p_c} \frac{\partial p_c}{\partial t} = S_w \frac{\partial \phi}{\partial t} + \phi S'_w \left(\frac{\partial p_g}{\partial t} - \frac{\partial p_w}{\partial t} \right) \quad (3.22)$$

Incorporating equation (3.9) into the time rate of change of porosity results in:

$$\frac{\partial \phi}{\partial t} = \frac{\partial \phi}{\partial p} \frac{\partial p}{\partial t} = \frac{\partial \phi}{\partial p} (S_w p_w + S_g p_g) = c_t (S_w p_w + S_g p_g) \quad (3.23)$$

where $c_t = \partial \phi / \partial p$ is the pore compressibility.

After inserting equation (3.11) into (3.23) and rearranging them, equation (3.22) can be reformulated with the use of equation (3.23) as:

$$\nabla \cdot \frac{K_{ij}k_{rw}}{\mu_w} (\nabla p_w - \rho_w g) = [c_t S_w (S_w + p_c S'_w) - \phi S'_w] \frac{\partial p_w}{\partial t} + [c_t S_w ((1 - S_w) - p_c S'_w) + \phi S'_w] \frac{\partial p_g}{\partial t} \quad (3.24)$$

Derivation of continuity equation for the gas phase is essentially same as those of the water phase, and it can be expressed as:

$$\nabla \cdot \frac{K_{ij}k_{rg}}{\mu_g} (\nabla p_g - \rho_g g) = [c_t S_g (S_g - p_c S'_w) - \phi S'_w] \frac{\partial p_g}{\partial t} + [c_t S_g (S_w + p_c S'_w) + \phi S'_w] \frac{\partial p_w}{\partial t}$$

(3.25)

3.4 Discretization of the Governing Equations

Finite Element method is used for the spatial discretization of the governing equations, and Finite Difference method is used for the time discretization with fully implicit integration scheme. Most of the procedures are essentially same as the ones described in Chapter 2. The basic variables are displacements, u , the water pressure, p_w , and the gas pressure p_g . The weighted residual method applied to these equations and the weighting functions are chosen as described in Chapter 2.

3.4.1 Equilibrium equation

The application of standard FE discretization procedure, after introduction of the effective stress principle (i.e., equation (3.10)), results in the following expression for the equilibrium equation:

$$\mathbf{K}_m \mathbf{u} + \mathbf{L}_{sw} \mathbf{p}_w + \mathbf{L}_{sg} \mathbf{p}_g = \mathbf{F}_u \quad (3.26)$$

where \mathbf{K}_m , and \mathbf{F}_u are the stiffness matrix and external load vector respectively, previously defined in Chapter 2. \mathbf{L}_{sw} and \mathbf{L}_{sg} are the coupling matrices between displacement and gas pressure, and between displacement and gas pressure, respectively. Details of these matrices are shown below:

$$\begin{aligned} \mathbf{L}_{sw} &= \int_{\Omega} \mathbf{B}^T S_w \mathbf{m} \mathbf{N}_p d\Omega \\ \mathbf{L}_{sg} &= \int_{\Omega} \mathbf{B}^T S_g \mathbf{m} \mathbf{N}_p d\Omega \end{aligned} \quad (3.27)$$

3.4.2 Continuity equation based on the fully-coupled theory

The spatial discretization of equations (3.19) and (3.20) and their boundary conditions is carried out exactly as for the continuity equation in the fully-saturated single phase case in Chapter 2. For the continuity equation of water, the discretization yields:

$$\mathbf{L}_{sw}^T \frac{\partial \mathbf{u}}{\partial t} - \mathbf{K}_{cw} \mathbf{p}_w + \mathbf{S}_{ww} \frac{\partial \mathbf{p}_w}{\partial t} + \mathbf{L}_{wg} \frac{\partial \mathbf{p}_g}{\partial t} = \mathbf{f}_w \quad (3.28)$$

and for the continuity equation of gas

$$\mathbf{L}_{sw}^T \frac{\partial \mathbf{u}}{\partial t} - \mathbf{K}_{cg} \mathbf{p}_g + \mathbf{S}_{gg} \frac{\partial \mathbf{p}_g}{\partial t} + \mathbf{L}_{gw} \frac{\partial \mathbf{p}_w}{\partial t} = \mathbf{f}_g \quad (3.29)$$

where

$$\begin{aligned} \mathbf{K}_{cw} &= \int_{\Omega} \left(\nabla \mathbf{N}_p \right)^T \left(\frac{\mathbf{K} k_{rw}}{\mu_w} \right) \nabla \mathbf{N}_p d\Omega \\ \mathbf{S}_{ww} &= \int_{\Omega} \left[\frac{1-\phi}{K_s} S_w \left(S_w + p_g S'_w - p_w S'_w \right) + \frac{\phi S_w}{K_w} - \phi S'_w \right] d\Omega \\ \mathbf{L}_{wg} &= \int_{\Omega} \left[\frac{1-\phi}{K_s} S_w \left(S_w - p_g S'_w + p_w S'_w \right) + \phi S'_w \right] d\Omega \\ \mathbf{f}_w &= \int_{\Omega} \left(\nabla \mathbf{N}_p \right)^T \frac{\mathbf{K} k_{rw}}{\mu_w} \rho_w \mathbf{g} d\Omega - \int_{\Gamma_w} \mathbf{N}_p^T \frac{q_w}{\rho_w} d\Gamma \\ \mathbf{K}_{cg} &= \int_{\Omega} \left(\nabla \mathbf{N}_p \right)^T \left(\frac{\mathbf{K} k_{rg}}{\mu_g} \right) \nabla \mathbf{N}_p d\Omega \\ \mathbf{S}_{gg} &= \int_{\Omega} \left[\frac{1-\phi}{K_s} S_g \left(S_g - p_g S'_w + p_w S'_w \right) + \frac{\phi S_g}{K_g} - \phi S'_w \right] d\Omega \\ \mathbf{L}_{gw} &= \int_{\Omega} \left[\frac{1-\phi}{K_s} S_g \left(S_g + p_g S'_w - p_w S'_w \right) + \phi S'_w \right] d\Omega \\ \mathbf{f}_g &= \int_{\Omega} \left(\nabla \mathbf{N}_p \right)^T \frac{\mathbf{K} k_{rg}}{\mu_g} \rho_g \mathbf{g} d\Omega - \int_{\Gamma_w} \mathbf{N}_p^T \frac{q_g}{\rho_g} d\Gamma \end{aligned} \quad (3.30)$$

3.4.3 Complete set of FE Biot's equation with two-phase fluid flow

Combining equations (3.26), (3.28) and (3.29) with a fully implicit Finite Difference time integration scheme results in the following incremental form of the two-phase fully coupled equation:

$$\begin{bmatrix} \mathbf{K}_m & \mathbf{L}_{sw} & \mathbf{L}_{sg} \\ \mathbf{L}_{sw}^T & \mathbf{S}_{ww} - \Delta t \mathbf{K}_{cw} & \mathbf{L}_{wg} \\ \mathbf{L}_{sg}^T & \mathbf{L}_{gw} & \mathbf{S}_{gg} - \Delta t \mathbf{K}_{cg} \end{bmatrix} \begin{Bmatrix} \Delta \mathbf{u} \\ \Delta \mathbf{p}_w \\ \Delta \mathbf{p}_g \end{Bmatrix} = \begin{Bmatrix} \Delta \mathbf{F}_u \\ \mathbf{F}_{ww} \\ \mathbf{F}_{gg} \end{Bmatrix} \quad (3.31)$$

where

$$\begin{aligned} \mathbf{F}_{ww} &= -\Delta t \mathbf{K}_{cw} \mathbf{p}_w^n + \Delta t \mathbf{f}_w \\ \mathbf{F}_{gg} &= -\Delta t \mathbf{K}_{cg} \mathbf{p}_g^n + \Delta t \mathbf{f}_g \end{aligned} \quad (3.32)$$

and superscript **n** represents the time step.

3.4.4 Conventional fluid flow equation

Since the conventional two-phase fluid flow equation does not involve the equilibrium equation, only equations (3.24) and (3.25) are discretized and the continuity equation of water is shown below,

$$-\mathbf{K}_{cw} \mathbf{p}_w + \mathbf{S} \mathbf{S}_{ww} \frac{\partial \mathbf{p}_w}{\partial t} + \mathbf{L} \mathbf{L}_{wg} \frac{\partial \mathbf{p}_g}{\partial t} = \mathbf{f}_w \quad (3.33)$$

and for the continuity equation of gas:

$$-\mathbf{K}_{cg} \mathbf{p}_g + \mathbf{S} \mathbf{S}_{gg} \frac{\partial \mathbf{p}_g}{\partial t} + \mathbf{L} \mathbf{L}_{gw} \frac{\partial \mathbf{p}_w}{\partial t} = \mathbf{f}_g \quad (3.34)$$

where

$$\begin{aligned}
 \mathbf{SS}_{\mathbf{ww}} &= \int_{\Omega} c_t S_w (S_w + p_c S'_w) - \phi S'_w d\Omega \\
 \mathbf{LL}_{\mathbf{wg}} &= \int_{\Omega} [c_t S_w ((1 - S_w) - p_c S'_w) + \phi S'_w] d\Omega \\
 \mathbf{SS}_{\mathbf{gg}} &= \int_{\Omega} [c_t S_g (S_g - p_c S'_w) - \phi S'_w] d\Omega \\
 \mathbf{LL}_{\mathbf{gw}} &= \int_{\Omega} [c_t S_g (S_w + p_c S'_w) + \phi S'_w] d\Omega
 \end{aligned} \tag{3.35}$$

Combining equations (3.33) and (3.34) with Finite Difference time integration results in:

$$\begin{bmatrix} \mathbf{SS}_{\mathbf{ww}} - \Delta t \mathbf{K}_{\mathbf{cw}} & \mathbf{LL}_{\mathbf{wg}} \\ \mathbf{LL}_{\mathbf{gw}} & \mathbf{SS}_{\mathbf{gg}} - \Delta t \mathbf{K}_{\mathbf{cg}} \end{bmatrix} \begin{Bmatrix} \Delta \mathbf{p}_w \\ \Delta \mathbf{p}_g \end{Bmatrix} = \begin{Bmatrix} \mathbf{F}_{\mathbf{ww}} \\ \mathbf{F}_{\mathbf{gg}} \end{Bmatrix} \tag{3.36}$$

It can be noted that equation (3.36) and the continuity relation in equation (3.31) have similar expressions except for the difference in the compressibility matrices (i.e., $\mathbf{SS}_{\mathbf{ww}}$, and $\mathbf{SS}_{\mathbf{gg}}$) and the displacement-pressure coupling matrix. Also, geomechanical effects in the continuity equation (3.36) are taken into account in the compressibility terms in equation (3.35).

3.5 Numerical procedures for multi-phase flow equations

The analysis of a multi-phase flow through a porous media requires a solution of nonlinear system of equation even in the case of linear elastic problems because of the dependency of the capillary pressure and relative permeability on saturation as shown in Figures 3-1 and 3.2. In an implicit time integration scheme, iterative procedures are usually performed within each time step to obtain the solution because several of the nonlinear coefficients are dependent on the unknowns. The method most commonly followed for dealing with the

nonlinearity is a scheme known generally as the *simultaneous solution* (SS) method. Because of the coupled nature of the governing equations, a simultaneous solution of the system seems to be the most applicable approach for solving the governing equations. However, alternative methods known as *implicit pressure – explicit saturation method* (IMPES) and *sequential method* (SEQ) may be used. In this thesis, the simultaneous solution method is employed to solve nonlinear flow equations. Brief discussions of IMPES and SEQ methods are also presented below.

3.5.1 Treatment of nonlinear terms

The mass balance parts of equations (3.31) and (3.36) represent a nonlinear system which requires special solution such as SS, IMPES and SEQ methods with different variable choices. Therefore, local linearization of the above systems is required prior to any solution effort. It implies that all the coefficient matrices which are functions of the primary unknowns should be updated in every time step. This may be carried out through either explicit or implicit method. Subsequently, the final linearized system may be solved through an iterative procedure if an implicit method is to be used, or through a direct procedure, if the explicit method is applied. Nonlinearity affects the final solution and the convergence rate, thus nonlinear term may be updated at different levels of time stepping.

Because material nonlinearity will be covered in Chapter 4, only nonlinearity of the fluid flow parts will be considered in this chapter. The nonlinear flow coefficient in equations (3.31) and (3.36) are relative permeability terms which are dependent on the unknowns (i.e., pressures and/or saturations). This dependency can be expressed in a general form as:

$$T = T_c f(S_i) \quad (3.37)$$

where T is a representative nonlinear flow coefficient, T_c is the constant part of the coefficient, and $f(S_i)$ is the variable part of the coefficient which is dependent on the phase saturation.

Aziz and Settari [4] classified the nonlinearity of fluid flow equations as weak nonlinearity and strong nonlinearity. A single-phase fluid flow in which all parameters are functions of pressure can be defined as weak nonlinearity. On the other hand, the coefficients that depend on saturation or capillary pressure can be called strong nonlinearity. These include the relative permeability, k_{ri} , and the saturation derivative, S'_i . In general, this case has a significant influence on the solution of the general nonlinear equations.

3.5.2 Simultaneous Solutions (SS)

This method is also known as the *implicit pressure-implicit saturation method* and requires the writing of the saturation time derivative of the flow equations in terms of pressure time derivatives and solving the resulting equations for pressure. It was originally proposed by Douglas et al. [5] and later extended by several researchers [6-9]. Figure 3-3 shows a schematic procedure of the simultaneous solution procedure for solving an implicit formulation within a single time step. It should be noted that all the nonlinear parameters are updated within each iteration level by using the most recent calculation for fluid pressures and saturations. In general, the SS method involves a complex programming effort, and high computational cost in terms of storage, and processing time. However, this

method is suitable for many difficult non-linear problems in which stability and the relatively larger time steps are essential.

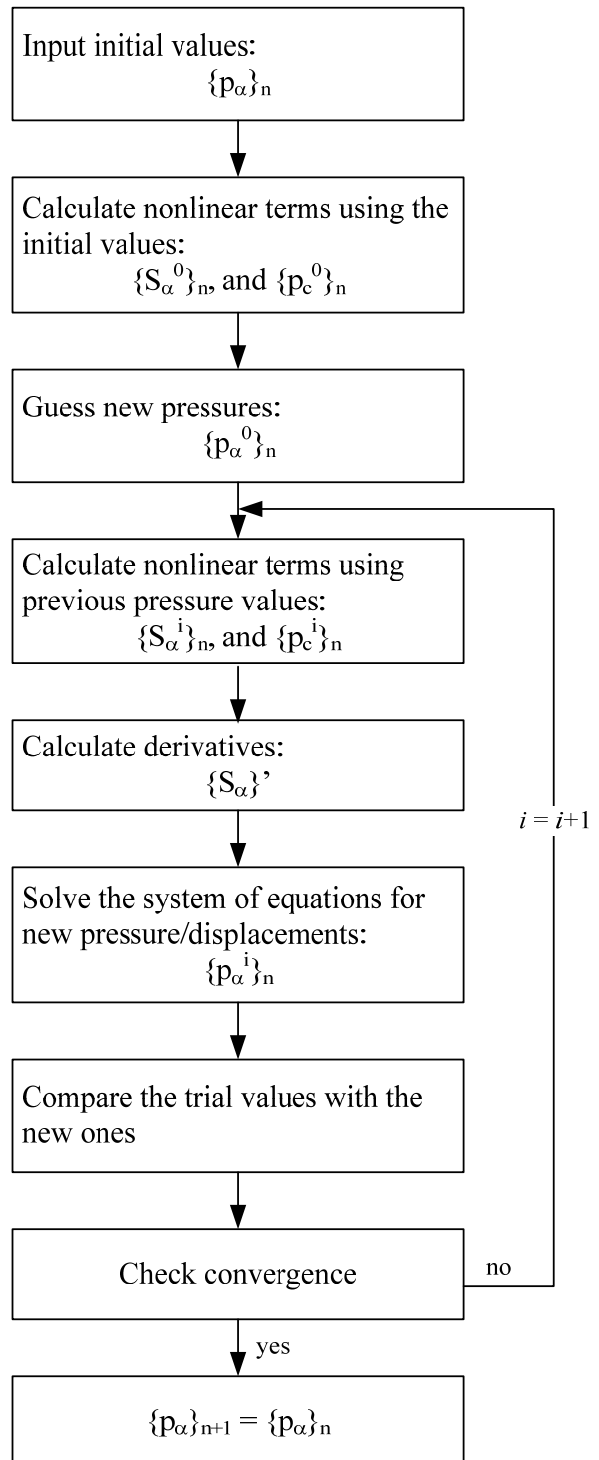


Figure 3-3 A schematic process of SS method

3.5.3 Implicit Pressure – Explicit Saturation method (IMPES)

This method was originally proposed by Sheldon et al. [10] and Stone and Gardner [11]. The basic idea of this method is to obtain a single multi-phase equation by a combination of the flow equations. After the pressure has been advanced in time, the saturations are updated explicitly. With a calculation of the saturations, new capillary pressure can be updated explicitly. The basic assumption of the IMPES method is that the capillary pressure does not change over a time step. It can be seen that the nonlinear terms in IMPES method are updated unevenly, as the capillary pressures are updated in terms of old pressure values while saturations are updated explicitly after the pressure has been advanced in time.

3.5.4 The Sequential Solution Method (SEQ)

This method was formulated by MacDonald and Coats [12] to improve the stability of the IMPES method by incorporating an implicit treatment of saturations. However, it does not solve pressures and saturations simultaneously. It obtains an implicit pressure by same manner as IMPES method then calculates saturations using linearized implicit relative permeabilities.

3.6 Validation of the Finite Element Formulations

The validation of the finite element formulations discussed above is carried out in terms of fluid flow in partially saturated soils. In case of multi-phase fluid flow in partially saturated soil, two types of analysis are possible. One is that the air flow in the partially saturated zone remains at atmospheric pressure, which is normally chosen as the reference pressure.

This approach is first used by Newman [13] for a rigid porous medium and the boundary between saturated and unsaturated zone is relatively well defined. Positive pore pressures are built in the saturated zone and negative pore pressures are built in the unsaturated zone. The free surface which separates the two zones is simply obtained as an isobar in which pore water pressure equals zero. The other type of analysis of partially saturated soil is that both water and air flow exists. This approach was used by several researchers [14, 15] and the gas phase continuity equation is always maintained.

Because no closed-form or exact solution exists of a two-phase flow in a deforming porous media experimental results by Liakopoulos [16] on a two-phase fluid flow in a column of Del Monte sand are used for the code validation. The experiment involves water drainage testing due to the gravitational load from a sand column and moisture tensions at various points along the column were measured during the drainage. As an initial condition, water was continuously added from the top and allowed to drain freely at the bottom through a filter, until uniform flow conditions were established. Before the start of draining, the water supply was ceased and tensiometer readings of the capillary pressures were recorded at several points along the column. This test problem has been solved previously by several researchers [15, 17-20].

The sand porosity and the dependence of water saturation and water permeability on water pressure were determined by Liakopoulos [16]. The original report by Liakopoulos did not include geomechanical effects on the analysis, however, linear elastic stress-strain relation with constant Young's modulus and Poisson's ratio are used in other references [15, 18].

Details of properties are shown in Table 3-1 and the geometry of the test problem with mechanical boundary conditions is shown in Figure 3-4.

Table 3-1 Material properties

Property	
Young's modulus, E	0.26 MPa
Poisson's ratio, ν	0.4
Solid grain density, ρ_s	2000 kg/m ³
Water density, ρ_w	1000 kg/m ³
Gas density, ρ_g	1.22 kg/m ³
Porosity, ϕ	0.2975
Intrinsic permeability, K	4.5 x 10 ⁻¹³ m ²
Water viscosity, μ_w	0.001 Pa s
Air viscosity, μ_g	1.8 x 10 ⁻⁵ Pa s
Gravitational acceleration, g	9.806 m/s ²
Atmospheric pressure, p_{atm}	1.01 x 10 ⁵ Pa

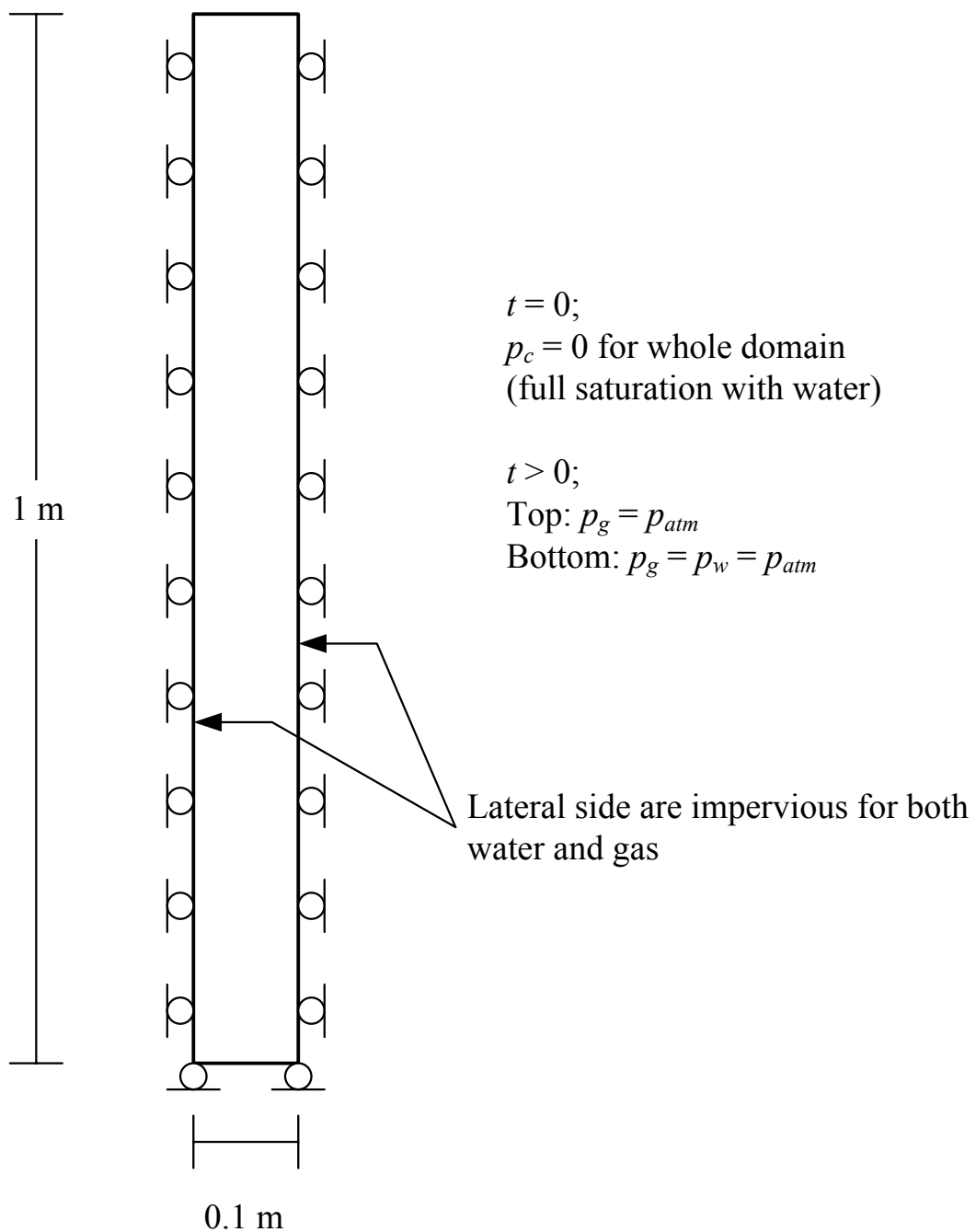


Figure 3-4 Mechanical boundary conditions of the Liakopoulos [16] test problem

The saturation-capillary pressure relation valid for $S_w > 0.92$ from Liakopoulos is shown in Figure 3-5. The relative permeability-saturation relations for both water and gas phases are assumed to be as given by Brooks and Corey [21, 22] and these are shown in Figure 3-6. These relations have the following forms:

$$S_w = 1.972 \times 10^{-11} p_c^{2.428}$$

$$k_{rw} = S_e^{\frac{(2+3\lambda)}{\lambda}}$$

$$k_{rg} = (1 - S_e)^2 \left(1 - S_e^{\frac{(2+\lambda)}{\lambda}} \right) \quad (3.38)$$

where $S_e = (S_w - S_{wc}) / (1 - S_{wc})$ is the effective saturation, S_{wc} is the irreducible water saturation, λ is the pore size distribution index. The proper values for S_{wc} , and λ are 0.2 and 3.0, respectively.

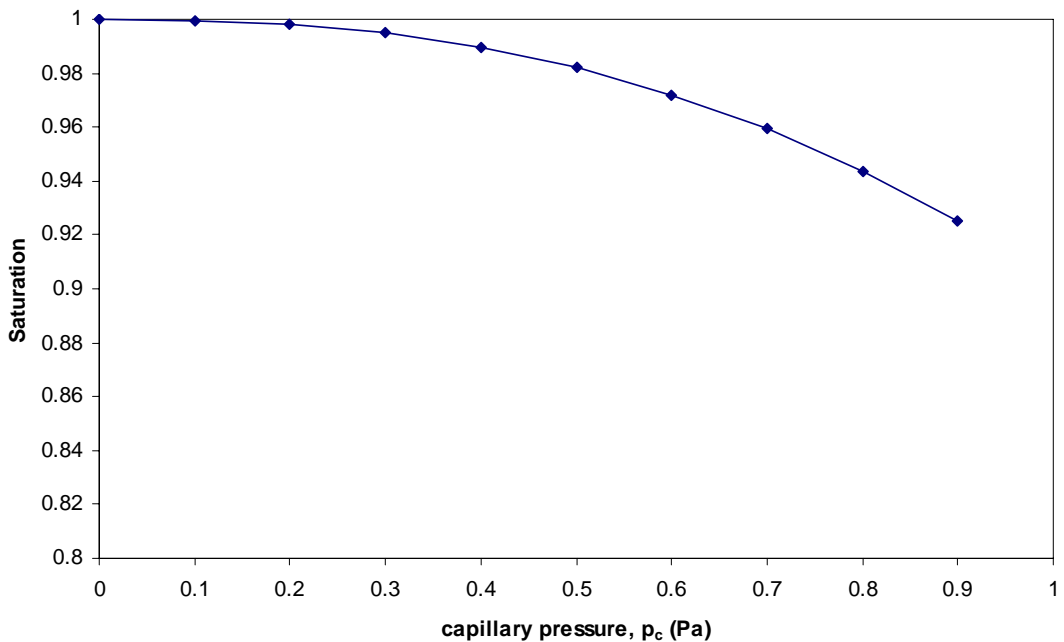


Figure 3-5 Saturation vs. capillary pressure

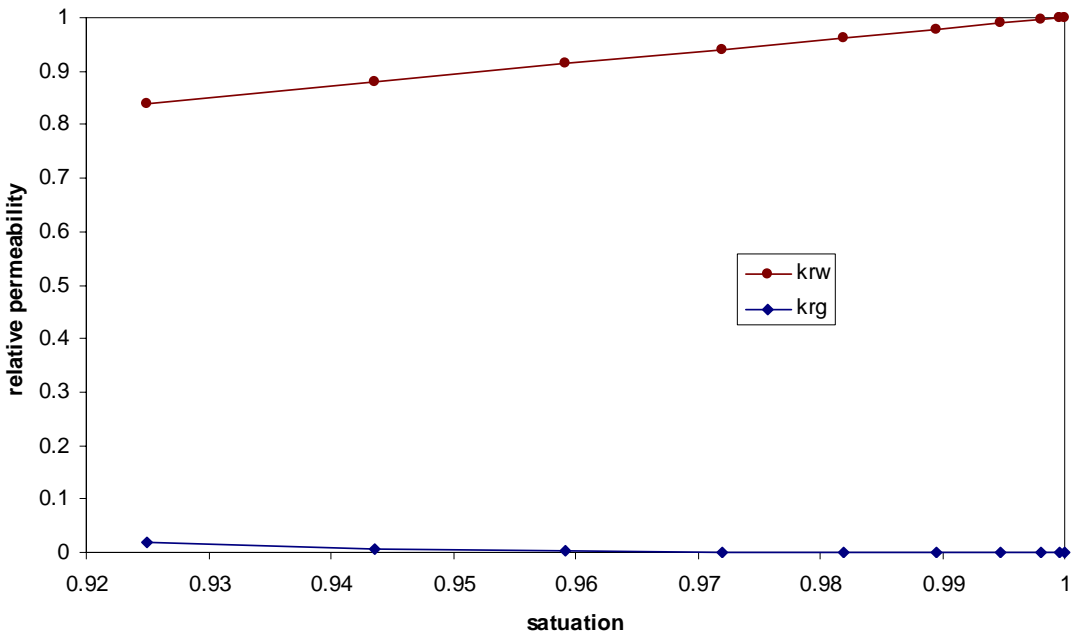


Figure 3-6 Relative permeability vs. saturation

In this problem, it is assumed that a small value of the gas relative permeability exists even for the fully saturated state. It implies that flow of gas exists for the fully-saturated state and can be obtained by appropriate modification to the capillary pressure–saturation relation and/or the relative permeability curve. Two-phase flow starts from zero capillary pressure which implies no gas flow with fully-saturated condition. In the simulation, the lower limit of the gas relative permeability is set to 0.0001. For the numerical calculations, the model is divided into 20 elements with 4-node quadrilateral isoparametric finite elements for displacements, water and gas. A constant 10 sec. of time increment is used for the simulations. Equation (3.31) is solved using the monolithic solution (solves variables simultaneously) method with implementation of SS method. Numerical simulation results are presented in Figures 3-7 to 3-11. Solid line represents the results of numerical solution,

and thick lines in Figure 3-7 represent the water pressure profile (i.e., $p_w - p_{atm}$) from the experimental result of Liakopoulos. It can be noted from Figure 3-7 that the computed values agree reasonably with the experimentally observed values after about 10 min. of start of the experiment. During the first 5 min. experimentally obtained water pressures are slightly higher than the numerical results. It can be inferred that no significant drainage occurred during the first 5 min., and the water was released from pores by a slight deformation of the soil skeleton and the fluid mass capacities of the volume elements are larger than they should be. Figure 3-8 presents gas pressure profiles and gas pressures are decreasing inside the specimen as water drains. Figure 3-9 shows the capillary pressure and it can be obtained with water and gas pressure values using equation (3.1). Figure 3-10 presents water saturation profiles and it does not decrease below assumed value (i.e., 0.92) in which equation (3.38) is applicable. Figure 3-11 shows displacements profile and calculated vertical displacement on the top of the specimen is about 0.007 m.

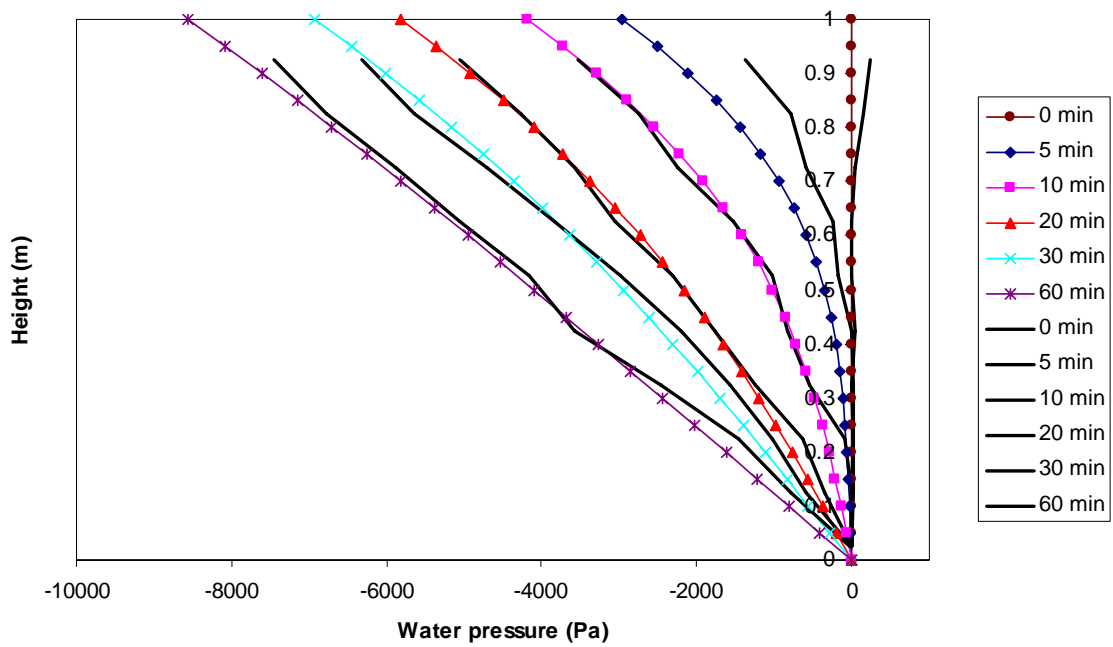


Figure 3-7 Comparison of water pressure profiles from numerical simulation and experimental results.

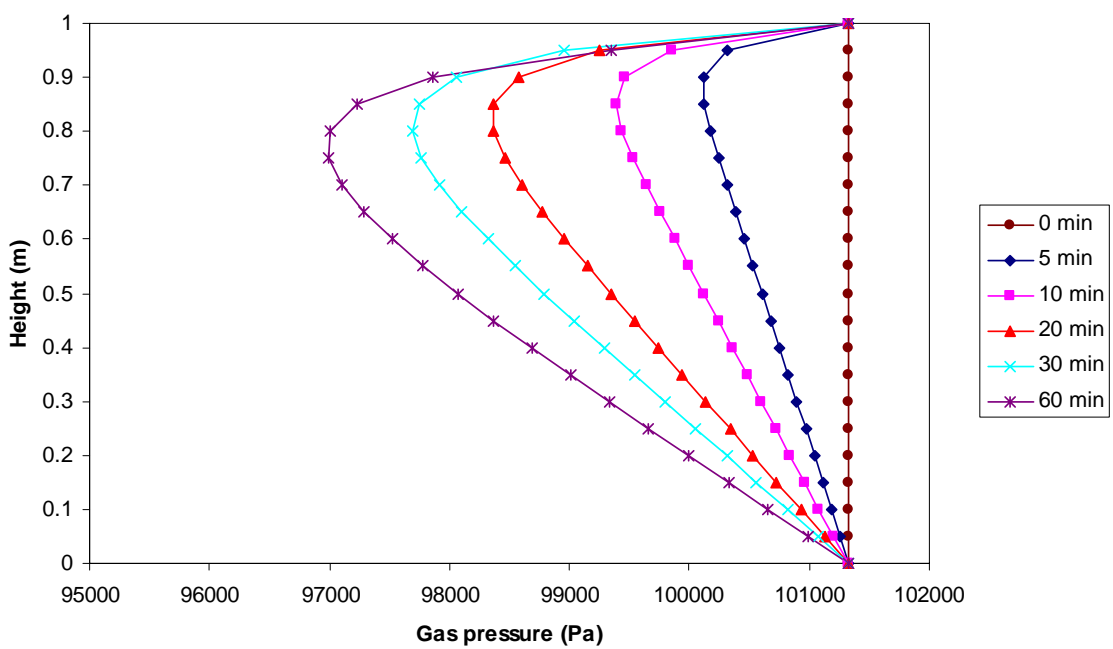


Figure 3-8 Gas pressure profiles

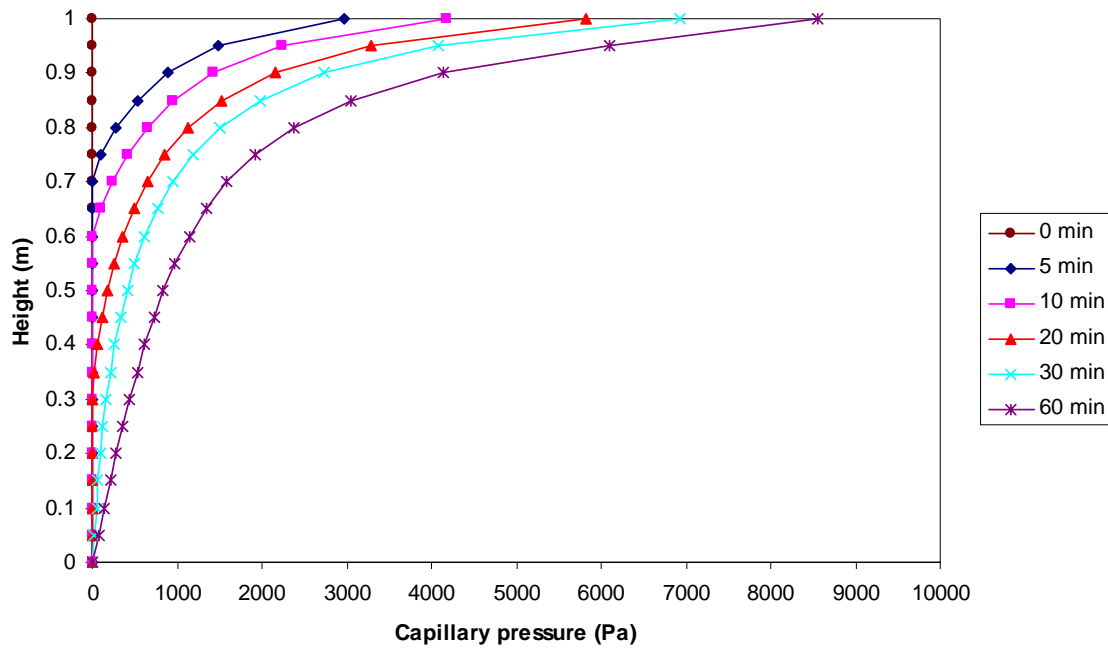


Figure 3-9 Capillary pressure profiles from numerical simulations

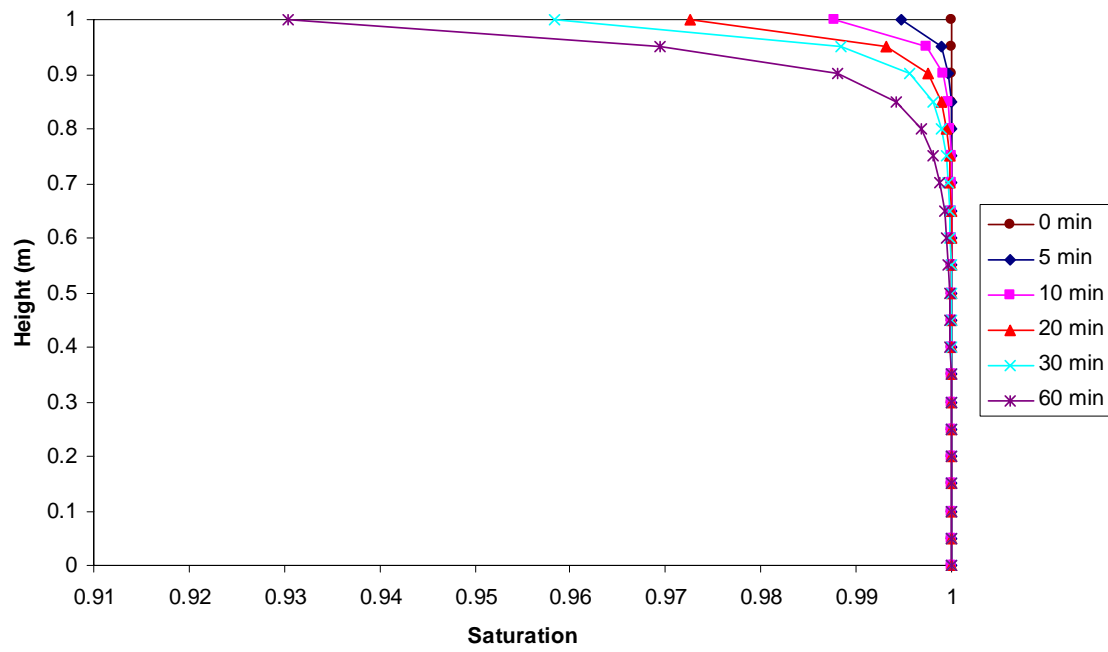


Figure 3-10 Saturation profiles from numerical simulations

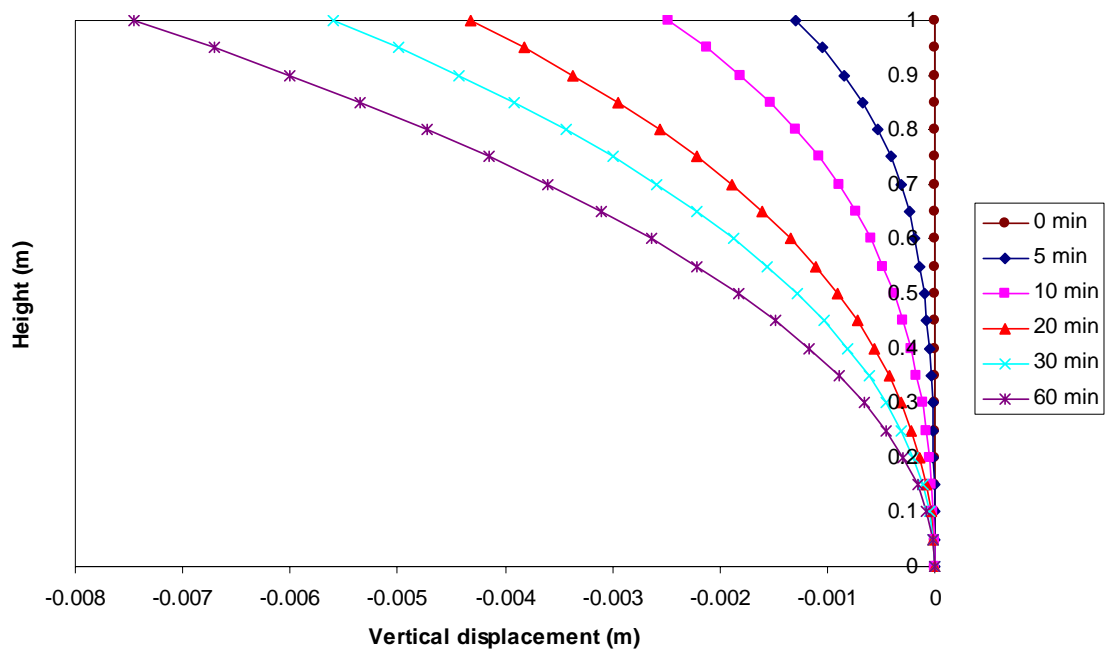


Figure 3-11 Vertical displacements profiles from numerical simulations

REFERENCES

1. Ertekin, T. and S.M. Farouq Ali 1979. Numerical Simulation of the Compaction Subsidence Phenomena in a Reservoir for Two-Phase Non-Isothermal Flow Conditions. in *Third International Conference on Numerical Method in Geomechanics*. Aachen.
2. Tortike, W.S. and S.M. Farouq Ali 1979. Modelling Thermal Three Dimensional Three-Phase Flow in a Deforming Soil. in *Third International Conference on Numerical Method in Geomechanics*. Aachen.
3. Lewis, R.W. and B.A. Schrefler 1987. *The Finite Element Method in the Deformation and Consolidation of Porous Media*: John Wiley & Sons.
4. Aziz, K. and A. Settari 1979. *Petroleum Reservoir simulation*. London: Applied Science Publishers Ltd.
5. Douglass, J., D.W. Peaceman and H.H. Rachford 1959. A Method for Calculating Multi-Dimensional Immiscible Displacement. *Trans. SPE of AMIE*. 216: 297-306.
6. Ghafouri, H.R., *Finite Element Modelling of Multi-phase Flow Through Deformable Fractured Porous Media*, in *Civil Engineering*. 1996, University of Wales: Swansea. p. 220.
7. Coats, K.H., R.L. Nielsen, M.H. Terhune and A.G. Weber 1967. Simulation of Three-Dimensional, Two-Phase Flow in Oil and Gas Reservoirs. *Society of Petroleum Engineers*. 240: 377-388.
8. Lewis, R.W. and Y. Sukirman 1993. Finite Element Modelling of Three-Phase Flow in Deforming Saturated Oil Reservoirs. *International journal for Numerical and Analytical Methods in Geomechanics*. 17: 577-598.
9. Sukirman, Y. and R.W. Lewis 1993. A Finite Element Solution of a Fully Coupled Implicit Formulation for Reservoir Simulation. *International Journal for Numerical and Analytical Methods in Geomechanics*. 17: 667-698.
10. Sheldon, J.W., B. Zondek and W.T. Cardwell 1959. One-Dimensional, Incompressible, Non-Capillary, Two-Phase Fluid Flow in a Porous Medium. *Trans. SPE of AMIE*. 216: 290-296.
11. Stone, H.L. and A.O. Gardner 1961. Analysis of Gas-Cap or Dissolved-Gas Reservoirs. *Trans. SPE of AMIE*. 222: 92-104.

12. MacDonald, R.C. and K.H. Coats 1970. Methods for Numerical Simulation of Water and Gas Coning. *SPE Journal*. 249: 425-436.
13. Newman, S.P., *Finite Element Computer Programs for Flow in Saturated-Unsaturated Porous Media*, in *Technion Isreal Institute*. 1972: Haifa.
14. Gawin, D. and B.A. Schrefler 1996. Thermo-Hydro-Mechanical Analysis of Partially Saturated Porous Materials. *Engineering Computations*. 13: 113-143.
15. Schrefler, B.A. and Z. Xiaoyong 1993. A Fully Coupled Model for Water Flow and Airflow in Deformable Porous Media. *Water Resources Research*. 29: 155-167.
16. Liakopoulos, A.C., *Transient Flow through Unsaturated Porous Media*. 1965, Univ. Calf. Berkely: Berkely.
17. Narasimhan, T.N. and P.A. Witherspoon 1978. Numerical Model for Saturated-Unsaturated Flow in Deformable Porous Media. 3, applications. *Water Resources Research*. 14: 1017-1034.
18. Gawiin, D., P. Baggio and B.A. Schrefler 1995. Coupled Heat, Water, and Gas Flow in Deformable Porous Media. *International Journal for Numerical Methods in Fluids*. 20: 969-987.
19. Schrefler, B.A. and L. Simoni 1988. *A Unified Approach to the Analysis of Saturated-Unsaturated Elastoplastic Porous Media*, in *Numerical Methods in Geomechanics*, G. Swoboda, Editor. Balkema: Rotterdam. p. 205-212.
20. Zienkiewicz, O.C., Y.M. Xie and B.A. Schrefler 1990. Static and Dynamic Behaviour of Soils: A Rational Approach to Quantitative Solutions, II. Semi-Saturated Problems. *Royal Society of London. Series A*. 429: 311-321.
21. Brooks, R.N. and A.T. Corey 1966. Properties of Porous Media Affecting Fluid Flow. *American Society of Civil Engineers Proceedings, Journal of the Irrigation and Drainage Division*. 92: 61-68.
22. Corey, A.T. 1994. *Mechanics of Immiscible Fluid in Porous Media*. Highlands Ranch, CO: Water Resources Publications.

4 NONLINEARITY OF THE CONSTITUTIVE RELATION

4.1 *Introduction*

In order to analyze realistic cases with numerical simulations, more rational representations of the stress-strain characteristics of the geomaterial are essential. The choice of an appropriate constitutive relation may have a significant influence on the numerical results. In general, geomaterials are characterized by nonlinear stress-strain response and the nonlinear behavior can be simulated using several approaches (e.g., nonlinear elastic models, and elasto-plastic models). This chapter contains a description of the types of constitutive models that are available for the geomaterials, and the basic principles of elasto-plastic constitutive relations are presented. Also, a critical state model is described and used in the numerical simulations of triaxial test. For the numerical code validation of the constitutive model, only fully-drained Modified Cam Clay model is tested and results are compared with analytical solutions. The implementation of the nonlinearity of constitutive relation into the fully-coupled model will be presented on the next chapter.

4.2 *Stress and Strain Invariants*

Stress/strain invariants are combination of stress/strain quantities which are independent of the orientation of the spatial reference axes. Since constitutive response is independent of the choice of reference axes, invariants are useful in formulating a constitutive model. Convenient choice of stress/strain invariants have been introduced as described below. The

various invariants which have been defined for two dimensional and three dimensional spaces are listed in the following Table 4-1.

Table 4-1 Stress/strain invariants

	2-D	3-D
Stress invariants	p, q	p, q, θ
Stress and strain increment invariants	$d\varepsilon_v, d\varepsilon_s$	$d\varepsilon_v, d\varepsilon_s, \theta_\varepsilon$

The stress invariants used in the following are the mean stress p , the deviator stress q , and the angular stress invariant θ (also known as Lode angle). The definition applies equally to effective stresses and total stress, however, stresses are assumed to be effective in this chapter.

$$p = \frac{1}{3}\sigma_{ij} = \frac{1}{3}(\sigma_{11} + \sigma_{22} + \sigma_{33}) \quad (4.1)$$

$$q = \sqrt{3J_2} = \sqrt{\frac{3}{2}s_{ij}s_{ij}} = \sqrt{\frac{1}{2}[(\sigma_{11} - \sigma_{22})^2 + (\sigma_{22} - \sigma_{33})^2 + (\sigma_{33} - \sigma_{11})^2 + 6(\tau_{12}^2 + \tau_{23}^2 + \tau_{13}^2)]} \quad (4.2)$$

$$\theta = \frac{1}{3}\sin^{-1}\left(-\frac{3\sqrt{3}J_3}{2J_2^{1.5}}\right) \quad (4.3)$$

where the three dimensional Cauchy stress tensor and the deviatoric stress tensor are defined as:

$$\sigma_{ij} = \begin{bmatrix} \sigma_{xx} & \tau_{xy} & \tau_{xz} \\ \tau_{xy} & \sigma_{yy} & \tau_{yz} \\ \tau_{xz} & \tau_{yz} & \sigma_{zz} \end{bmatrix} \quad (4.4)$$

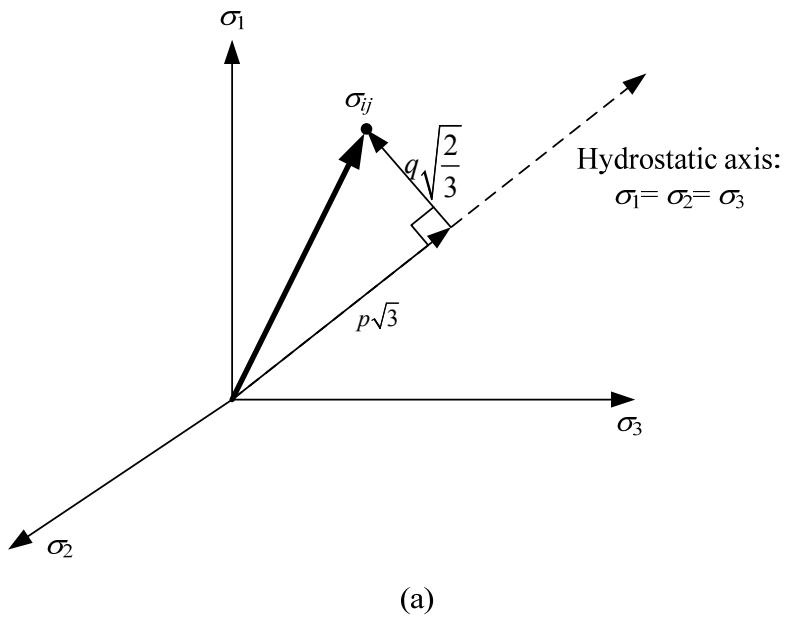
$$S_{ij} = \begin{bmatrix} \sigma_{xx} - p & \tau_{xy} & \tau_{xz} \\ \tau_{xy} & \sigma_{yy} - p & \tau_{yz} \\ \tau_{xz} & \tau_{yz} & \sigma_{zz} - p \end{bmatrix} \quad (4.5)$$

and J_2 and J_3 are themselves stress invariants, and are defined as:

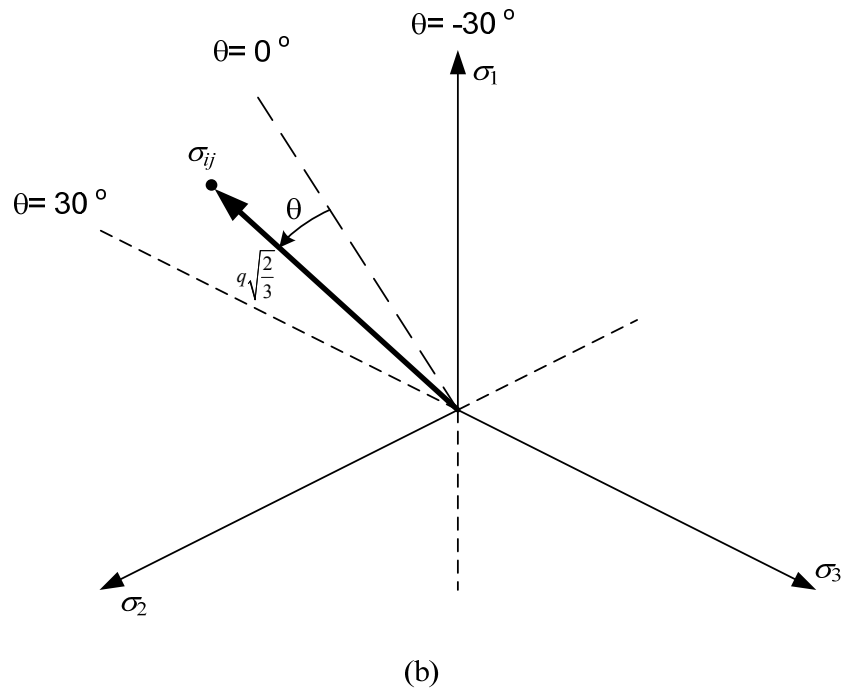
$$J_2 = \frac{1}{2} s_{ij} s_{ij} = \frac{1}{6} \left[(\sigma_{11} - \sigma_{22})^2 + (\sigma_{22} - \sigma_{33})^2 + (\sigma_{33} - \sigma_{11})^2 + 6(\tau_{12}^2 + \tau_{23}^2 + \tau_{13}^2) \right] \quad (4.6)$$

$$J_3 = \frac{1}{3} s_{ij} s_{jk} s_{kl} = |s_{ij}| \quad (4.7)$$

These stress invariants p , q , and θ are generally used to describe three dimensional elasto-plastic constitutive models for geomaterials and they are graphically shown in Figure 4-1.



(a)



(b)

Figure 4-1 Stress invariants in the principal stress space: (a) stress point in the principal stress space; (b) projection on the deviatoric plane (π -plane)

The choice of invariants is not arbitrary because the above quantities have geometric significance in principal stress space. The mean stress p is related to the distance from the origin of stress space along the hydrostatic axis ($\sigma_1 = \sigma_2 = \sigma_3$) to the current deviatoric plane (π -plane) in which the stress point is located. The deviatoric stress q is related to the distance from the hydrostatic axis to the current stress state on the deviatoric plane, and the magnitude of θ defines the orientation of the stress state within the deviatoric plane. The Lode angle shows the effect of the intermediate principal stress σ_2 . The stress in the deviatoric plane is constrained to lie between $\theta = -30^\circ$ and $\theta = 30^\circ$. These limiting values of θ corresponds for the triaxial compression conditions ($\sigma_1 > \sigma_2 = \sigma_3$) for a Lode angle $\theta = -30^\circ$; and for triaxial extension conditions ($\sigma_1 = \sigma_2 > \sigma_3$) and for a angle $\theta = 30^\circ$.

The corresponding three dimensional strain increment invariants are given by the incremental volumetric strain $d\varepsilon_v$, the incremental shear strain $d\varepsilon_s$, and Lode angle θ_ε . These invariants are defined as:

$$d\varepsilon_v = d\varepsilon_{ii} = d\varepsilon_{xx} + d\varepsilon_{yy} + d\varepsilon_{zz} \quad (4.8)$$

$$\begin{aligned} d\varepsilon_s &= \sqrt{\frac{3}{2} d\varepsilon_{ij} d\varepsilon_{ij}} \\ &= \sqrt{\frac{2}{9} \left[(d\varepsilon_{xx} - d\varepsilon_{yy})^2 + (d\varepsilon_{yy} - d\varepsilon_{zz})^2 + (d\varepsilon_{zz} - d\varepsilon_{xx})^2 + 6(d\gamma_{xy}^2 + d\gamma_{yz}^2 + d\gamma_{zx}^2) \right]} \end{aligned} \quad (4.9)$$

$$\theta_\varepsilon = \frac{1}{3} \sin^{-1} \left(-\frac{3\sqrt{3}J'_3}{2J'_2^{1.5}} \right) \quad (4.10)$$

where the three dimensional strain increment tensor and the deviatoric strain increment tensor are defined as:

$$d\boldsymbol{\varepsilon}_{ij} = \begin{bmatrix} d\varepsilon_{xx} & d\gamma_{xy} & d\gamma_{xz} \\ d\gamma_{xy} & d\varepsilon_{yy} & d\gamma_{yz} \\ d\gamma_{xz} & d\gamma_{yz} & d\varepsilon_{zz} \end{bmatrix} \quad (4.11)$$

$$de_{ij} = \begin{bmatrix} d\varepsilon_{xx} - \frac{1}{3}d\varepsilon_v & d\gamma_{xy} & d\gamma_{xz} \\ d\gamma_{xy} & d\varepsilon_{yy} - \frac{1}{3}d\varepsilon_v & \gamma_{yz} \\ d\gamma_{xz} & d\gamma_{yz} & d\varepsilon_{zz} - \frac{1}{3}d\varepsilon_v \end{bmatrix} \quad (4.12)$$

J'_2 and J'_3 are themselves strain increment invariants, and are defined as:

$$J'_2 = \frac{1}{2}de_{ij}de_{ij} = \frac{1}{6} \left[(d\varepsilon_{xx} - d\varepsilon_{yy})^2 + (d\varepsilon_{yy} - d\varepsilon_{zz})^2 + (d\varepsilon_{zz} - d\varepsilon_{xx})^2 + 6(d\gamma_{xy}^2 + d\gamma_{yz}^2 + d\gamma_{zx}^2) \right] \quad (4.13)$$

$$J'_3 = \frac{1}{3}de_{ij}de_{jk}de_{kl} = |de_{ij}| \quad (4.14)$$

where the angle θ_ε is analogous to the Lode angle θ in stress space.

The two dimensional stress invariants represent a special case of the three dimensional invariants, in which the Lode angle θ has a constant value corresponding to triaxial compression or triaxial extension conditions. For the simplicity, two dimensional stress and strain invariants are used in this report and they are defined as follow:

$$p = \frac{1}{2}\sigma_{ii} = \frac{1}{2}(\sigma_{xx} + \sigma_{yy}) \quad (4.15)$$

$$q = \sqrt{3J_2} = \sqrt{\frac{1}{2}s_{ij}s_{ij}} = \sqrt{\frac{1}{4}\left[\left(\sigma_{xx} - \sigma_{yy}\right)^2 + 4\tau_{xy}^2\right]} \quad (4.16)$$

$$d\varepsilon_v = d\varepsilon_{ii} = d\varepsilon_{xx} + d\varepsilon_{yy} \quad (4.17)$$

$$d\varepsilon_s = \sqrt{2de_{ij}de_{ij}} = \sqrt{\left(d\varepsilon_{xx} - d\varepsilon_{yy}\right)^2 + 4d\varepsilon_{xy}^2} \quad (4.18)$$

where the two-dimensional deviatoric strain increment tensor is defined as:

$$de_{ij} = \begin{bmatrix} d\varepsilon_{xx} - \frac{1}{2}d\varepsilon_v & d\gamma_{xy} \\ d\gamma_{xy} & d\varepsilon_{yy} - \frac{1}{2}d\varepsilon_v \end{bmatrix} \quad (4.19)$$

4.3 Linear Elastic Model

In case of isotropic linear elasticity, the two constants are required, which are usually Young's modulus E and Poisson's ratio ν . The general constitutive matrix relates increments of total stress to increments of strain are as follow:

$$\begin{bmatrix} \Delta\sigma_{xx} \\ \Delta\sigma_{yy} \\ \Delta\sigma_{zz} \\ \Delta\tau_{xy} \\ \Delta\tau_{yz} \\ \Delta\tau_{xz} \end{bmatrix} = \frac{E}{(1+\nu)(1-2\nu)} \begin{bmatrix} 1-\nu & \nu & \nu & 0 & 0 & 0 \\ \nu & 1-\nu & \nu & 0 & 0 & 0 \\ \nu & \nu & 1-\nu & 0 & 0 & 0 \\ 0 & 0 & 0 & \frac{1-2\nu}{2} & 0 & 0 \\ 0 & 0 & 0 & 0 & \frac{1-2\nu}{2} & 0 \\ 0 & 0 & 0 & 0 & 0 & \frac{1-2\nu}{2} \end{bmatrix} \begin{bmatrix} \Delta\varepsilon_{xx} \\ \Delta\varepsilon_{yy} \\ \Delta\varepsilon_{zz} \\ \Delta\gamma_{xy} \\ \Delta\gamma_{yz} \\ \Delta\gamma_{xz} \end{bmatrix} \quad (4.20)$$

sym

In some cases, it is convenient to characterize geomaterial behavior in terms of the elastic bulk modulus K , and the elastic shear modulus G . These moduli can be written using Young's modulus and Poisson's ratio:

$$K = \frac{E}{3(1-2v)}; G = \frac{E}{2(1+v)} \quad (4.21)$$

Equation (4.20) then becomes:

$$\begin{Bmatrix} \Delta\sigma_{xx} \\ \Delta\sigma_{yy} \\ \Delta\sigma_{zz} \\ \Delta\tau_{xy} \\ \Delta\tau_{yz} \\ \Delta\tau_{xz} \end{Bmatrix} = \begin{bmatrix} K + 4/3G & K - 2/3G & K - 2/3G & 0 & 0 & 0 \\ K + 4/3G & K - 2/3G & K - 2/3G & 0 & 0 & 0 \\ K + 4/3G & K + 4/3G & K + 4/3G & 0 & 0 & 0 \\ 0 & 0 & 0 & G & 0 & 0 \\ 0 & 0 & 0 & 0 & G & 0 \\ 0 & 0 & 0 & 0 & 0 & G \end{bmatrix} \begin{Bmatrix} \Delta\varepsilon_{xx} \\ \Delta\varepsilon_{yy} \\ \Delta\varepsilon_{zz} \\ \Delta\gamma_{xy} \\ \Delta\gamma_{yz} \\ \Delta\gamma_{xz} \end{Bmatrix} \quad (4.22)$$

For geotechnical related problem, plane strain conditions are frequently used. In this case, the length of the structure is much larger than the other two dimensions. The strains associated with length (i.e., the normal strain ε_{zz} , and the shear strain ε_{zx} , and ε_{zy} in case of the z -direction length) are negligible compared to the cross-sectional strain, and assumed to be zero. The strain tensor for that case and the corresponding stress tensor can be approximated by:

$$\varepsilon_{ij} = \begin{bmatrix} \varepsilon_{xx} & \gamma_{xy} & 0 \\ \gamma_{xy} & \varepsilon_{yy} & 0 \\ 0 & 0 & 0 \end{bmatrix}; \sigma_{ij} = \begin{bmatrix} \sigma_{xx} & \tau_{xy} & \tau_{xz} \\ \tau_{xy} & \sigma_{yy} & \tau_{yz} \\ \tau_{xz} & \tau_{yz} & \sigma_{zz} \end{bmatrix} \quad (4.23)$$

The linear elastic constitutive relation for the plane strain problem is as follows:

$$\begin{Bmatrix} \Delta\sigma_{xx} \\ \Delta\sigma_{yy} \\ \Delta\tau_{xy} \end{Bmatrix} = \frac{E}{(1+\nu)(1-2\nu)} \begin{Bmatrix} 1-\nu & \nu & 0 \\ \nu & 1-\nu & 0 \\ sym & & \frac{1-2\nu}{2} \end{Bmatrix} \begin{Bmatrix} \Delta\varepsilon_{xx} \\ \Delta\varepsilon_{yy} \\ \Delta\gamma_{xy} \end{Bmatrix} \quad (4.24)$$

or

$$\begin{Bmatrix} \Delta\sigma_{xx} \\ \Delta\sigma_{yy} \\ \Delta\tau_{xy} \end{Bmatrix} = \begin{Bmatrix} K + \frac{4}{3}G & K - \frac{2}{3}G & 0 \\ K - \frac{2}{3}G & K + \frac{4}{3}G & 0 \\ sym & & G \end{Bmatrix} \begin{Bmatrix} \Delta\varepsilon_{xx} \\ \Delta\varepsilon_{yy} \\ \Delta\gamma_{xy} \end{Bmatrix} \quad (4.25)$$

4.4 Nonlinear Elastic Models

Nonlinear elastic models attempt to simulate the nonlinear stress-strain behavior of geomaterials by making the elastic parameters (and consequently the stiffness) depend on stress state and/or accumulated strain. Several nonlinear elastic models have been used to simulate the behavior of geomaterials. Two of the more common nonlinear elastic models are the *K-G* model or the Barron-Sandler model [1], which is an extension of the bilinear model, and the hyperbolic model [2] , which is a variable elastic model. The original hyperbolic model was modified for Mohr-Coulomb strength parameters and applied to finite element analysis by Duncan and Chang [3]. Both models have simple hyper-elastic formulations in that the elastic parameters (e.g., bulk modulus, *K*, and shear modulus, *G*, for the *K-G* model, and tangent elastic modulus, E_t , and tangent Poisson's ratio, ν_t , for the Duncan-Chang model) are functions of only the stress state and model parameters. The coefficients used to determine the elastic moduli are functions of the failure criterion. The

Duncan-Chang model generally can provide a better fit to laboratory data than the $K-G$ model. The Duncan-Chang model allows critical values of deviator stress (i.e., peak strength and failure) and volume change (i.e., onset of dilatancy) to occur at different stages of the analysis, which is commonly observed in real geomaterials. Nonlinear elastic models are plagued by several shortcomings: (1) stress history and path dependency cannot be properly taken into account during analysis. Therefore, incremental strains are a function of the incremental stresses, rather than of the stress state at which the incremental stress are applied; (2) dilatant response during incremental compression loading (e.g., shear) cannot be simulated within the framework of nonlinear elasticity without the introduction of a negative Poisson's ratio; (3) unloading and other changes in loading direction cannot be properly simulated because the stiffness moduli are dependent only on stress and/or strain state.

4.5 Elasto-Plastic Models

Classical elasto-plastic constitutive models are formulated in this chapter and basic concepts and principles are described. Those basic concepts is described in this chapter includes coaxiality, yield function, plastic potential function, strain additivity, and plastic hardening/softening rule. Elasto-plastic models range from simple to complex. Examples of simple models are Tresca, von Mises, Mohr-Coulomb, and Drucker-Prager models which has linear elasticity and perfectly plasticity (i.e., constant plastic flow direction). The difference among these models is essentially in the shapes of the failure and plastic potential surfaces in the deviatoric plane. These models have suffered from several

limitations in representing behavior such as predicting unrealistic strength under triaxial extension condition. One of the most widely used elasto-plastic models is from the critical state soil mechanics including the Cam Clay models with a single yield surface. More complicated models incorporate yield surface evolution due to isotropic hardening and softening, stress state-dependent plastic flow, and stress-dependent elasticity. Additional complications can arise when kinematic hardening, multiple yield surfaces, multiple plastic potential surfaces, or bounding surfaces are introduced into the formulation. Later of this paper, critical state model (i.e., modified Cam Clay) is used to incorporate nonlinear stress-strain behavior into the fully-coupled analysis because it is considered simple enough to test the nonlinearity and realistic enough to represent soil behavior.

4.5.1 Coincidence of axes

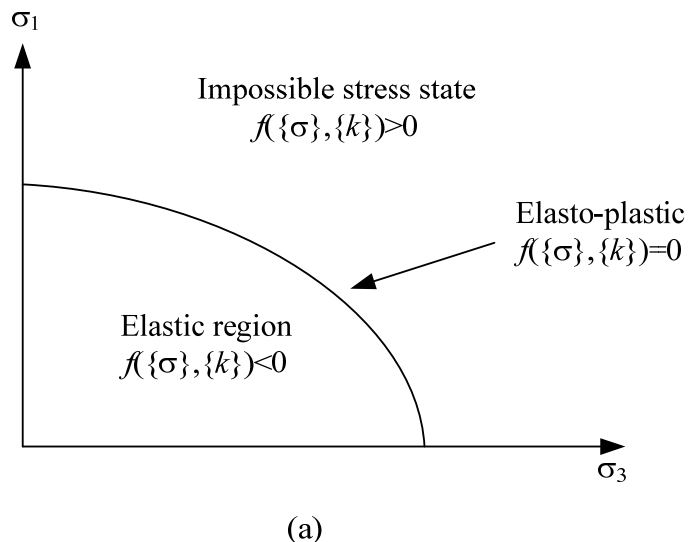
A fundamental assumption in the formulation of elasto-plastic models is the coaxiality postulate, which assumes that the principal directions of the accumulated stress and incremental plastic strain coincide. It is different from elastic behavior where the principal directions of incremental stress and incremental strain coincide.

4.5.2 Yield surface and yield function

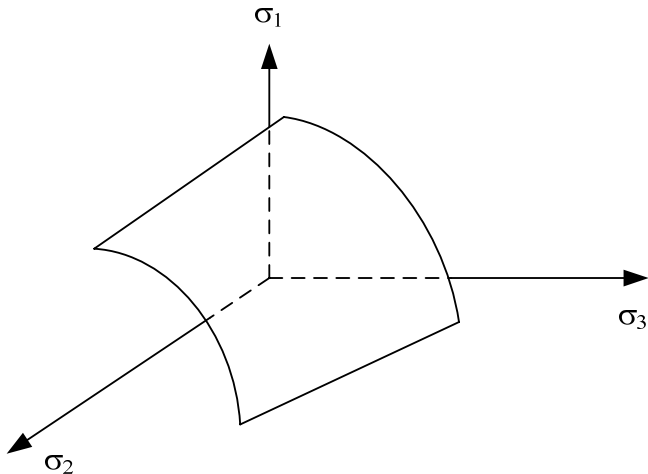
A yield function, f , separates purely elastic state from elasto-plastic state, and impermissible stress state (i.e., illegal stress state). In general it is defined with a scalar function of stress and plastic hardening parameters, \mathbf{k} .

$$f = f(\boldsymbol{\sigma}, \mathbf{k}) \quad (4.26)$$

The value of the yield function, f , is used to identify the type of material behavior. Purely elastic behavior occurs if $f < 0$ where a stress state is located inside of yield surface, and elasto-plastic behavior occurs if $f = 0$ where stress state is on the yield surface. In case of stress state is outside of yield surface, $f > 0$ and it is impossible. Depending on the particular constitutive model, the yield surface can be either fixed or the size, position and shape can change in stress space due to the plastic strain accumulation. Figure 4-2 shows a yield surface in stress space. A yield function can be expressed as a curve in two-dimensional stress space (see Figure 4-1a) with $\sigma_2=0$ and it forms a yield surface in three dimensional stress space (see Figure 4-1b).



(a)



(b)

Figure 4-2 Yield surface presentation; (a) two dimensional example; (b) segment of yield surface for three dimensional stress space

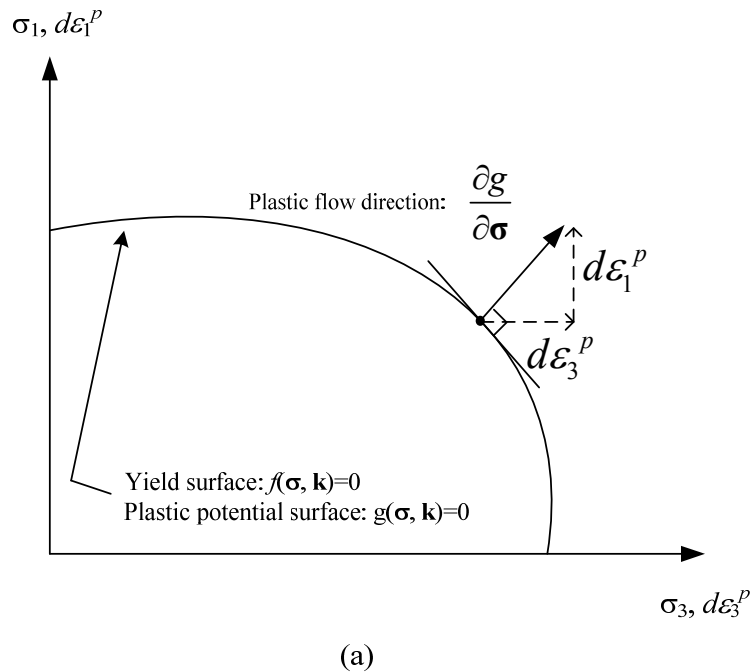
4.5.3 Plastic potential function

A plastic potential function determines the direction of plastic strain at every stress state during elasto-plastic loading and can be expressed as follows:

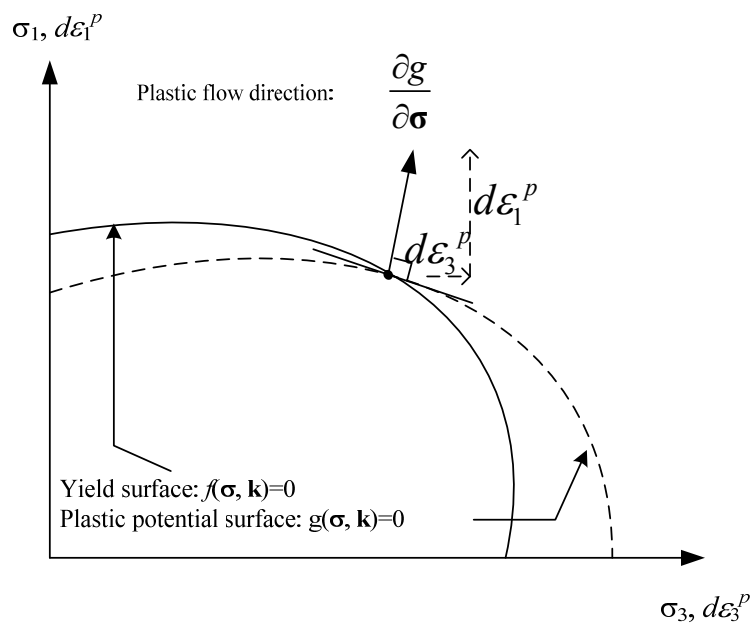
$$d\boldsymbol{\epsilon}^p = \varphi \frac{\partial g}{\partial \boldsymbol{\sigma}} \quad (4.27)$$

where $d\boldsymbol{\epsilon}^p$ represents the incremental plastic strain vector, g is the plastic potential function, and φ is a scalar plastic multiplier

Because of the assumption of coaxiality of principal directions of stress and incremental plastic strain, it is possible to plot incremental principal strains and principal stresses on the same axes. The outward vector normal to the plastic potential surface at the current stress state point has components which provide the relative magnitudes of the plastic strain increment components, and the magnitude of plastic strain is proportional to the plastic multiplier. In case the plastic potential surface equals to the yield surface ($f=g$), plastic flow rule is said to be associated. If the plastic potential surface is not coincided with the yield surface, flow is said to be non-associated. Figure 4-3 shows the plastic potential presentation for the associated and non-associated flow.



(a)



(a)

Figure 4-3 Plastic potential surface and plastic flow direction in two-dimensional stress space, for (a) associated flow; (b) non-associated flow

4.5.4 Incremental Elasticity

The generalized Hooke's Law relates the incremental stress ($d\sigma$) and the incremental strain ($d\epsilon^e$) using the elastic constitutive matrix (\mathbf{D}^e) or the elastic compliance matrix (\mathbf{C}^e).

$$d\sigma = \mathbf{D}^e d\epsilon^e \quad (4.28)$$

$$d\epsilon^e = \mathbf{C}^e d\sigma \quad (4.29)$$

The elastic constitutive matrix (\mathbf{D}^e) and the elastic compliance matrix (\mathbf{C}^e) are the inverses of each other: i.e., $\mathbf{D}^e = [\mathbf{C}^e]^{-1}$

4.5.5 Strain additivity

The elastic and plastic strain increments act independently of each other. Elastic strains accompany deformation in which the energy of deformation is stored such that the elastic deformation and energy of elastic deformation are fully reversible and may be recovered upon removal of the deformation-causing loads. Plastic strains accompany deformation in which the energy of deformation is dissipated, so the plastic deformation and energy of plastic deformation are not recovered when the loads are removed. A total strain increment $d\epsilon$ may be additively decomposed into its recoverable or elastic $d\epsilon^e$, and irrecoverable or plastic strain increments $d\epsilon^p$:

$$d\epsilon = d\epsilon^e + d\epsilon^p \quad (4.30)$$

4.5.6 Plastic hardening/softening rule

The hardening/softening rules determine the variation of the state parameter k with plastic strain. In case of the perfect plasticity, no hardening/softening occurs and the state

parameter \mathbf{k} is constant. For the materials exhibiting hardening/softening during plastic deformation, strain hardening rules are required to specify the change of the yield function. The state parameter \mathbf{k} , defines the size, position, and shape of the yield surface and the change in size of the yield surface can be related to either the accumulated plastic strain or plastic work.

4.6 Simple Critical State Model

The first critical state models for describing the behavior of soft soils such as clay, the original Cam Clay model as an elasto-plastic constitutive law, was presented by Roscoe and Schofield [4], and Schofield and Wroth [5]. Afterwards, Roscoe and Burland [6] proposed the modified Cam Clay model. Only the modified Cam Clay is reviewed briefly in this chapter because it will be used in the later for the numerical simulation. Critical state models enable to describe important the soil behavior such as strength, compression/dilatancy, and unlimited deformations without changing stresses. Both the Cam Clay and the modified Cam Clay models were originally developed for triaxial loading conditions. The model assumes that the relation between void ratio (or specific volume) and $\ln p'$ consists of a straight virgin consolidation line and swelling line, see Figure 4-4 when a soil sample is subjected to drained isotropic compression ($\sigma_1' = \sigma_2' = \sigma_3' = p'$). Initially, on first loading, the soil moves down the virgin consolidation line. If subsequently unloaded from point 'b', it moves up the swelling line 'bc'. If re-loaded, it moves back down this same swelling line until it reaches to point 'b' and it begins to move

down the virgin consolidation line again. The virgin consolidation line and the swelling lines are defined by the equation:

$$v = N - \lambda \ln p' \quad (\text{virgin consolidation line}) \quad (4.31)$$

$$v = v_s - \kappa \ln p' \quad (\text{swelling line}) \quad (4.32)$$

where values λ , κ , and N are characteristic properties of a particular soil. λ is the slope of the virgin consolidation line in $v - \ln p'$ space, while κ is the slope of swelling line in $v - \ln p'$ space. N is the specific volume of normal compression line at unit pressure that is dependent on the unit of stress.

The critical state condition is a state that no stress or volume change occurs during shearing of soils. The state at which a soil is undergoing distortion at constant state is characterized by the Critical State Line (CSL). The location of the CSL relative to the virgin consolidation is illustrated on Figure 4-5. The CSL line is parallel to the virgin consolidation line in $v - \ln p'$ space. The parameter Γ is the specific volume of the CSL at unit pressure that is analogous to the parameter N in the isotropic consolidation case.

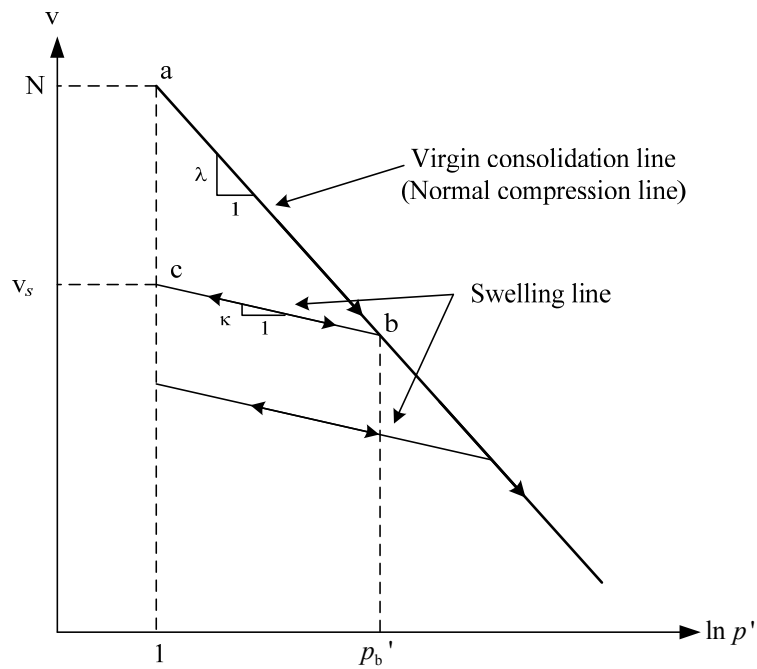


Figure 4-4 Behavior of soft soil under isotropic compression

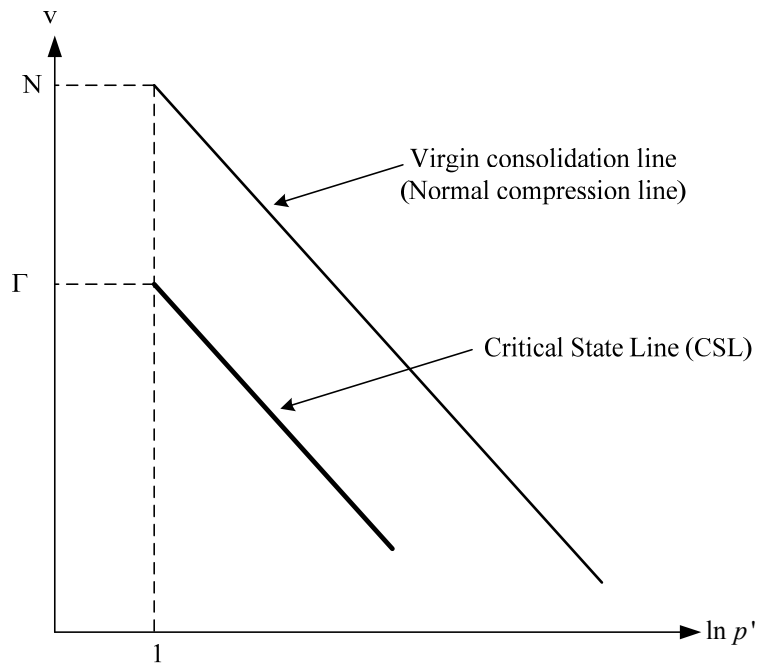


Figure 4-5 Location of CSL relative to virgin compression line

Under increasing triaxial loading condition, the Modified Cam Clay Model assumes yield function of the form:

$$f(\sigma, k) = \frac{q^2}{M^2} + p' (p' - p'_p) = 0 \quad (4.33)$$

where p' is the mean effective stress, q is the deviatoric stress, M equals to $\tan \phi$, and p'_p is the pre-consolidation pressure (see Figure 4-6). In this thesis p'_p is used to avoid confusion of expression for the capillary pressure which defined as p_c in chapter 3.

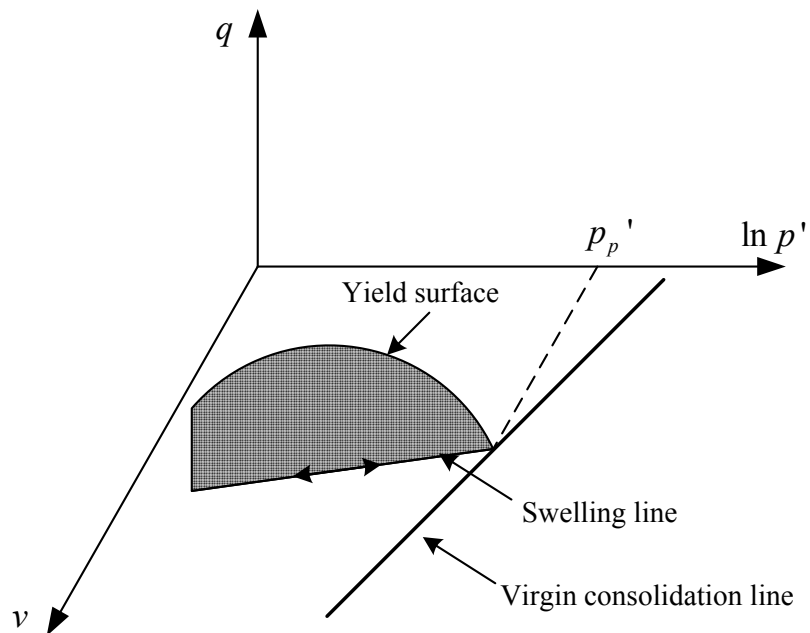


Figure 4-6 Yield surface

A projection of the yield surface onto $q-p'$ plane for the modified Cam clay model is shown in Figure 4-7. As it can be seen from Figure 4-7, if a soil yields at a point to the right of critical state point C (i.e., wet or subcritical), incremental plastic volumetric strains are positive (i.e., compressive), and soil is hardening. For a yielding occurs to the left of C (i.e., dry or supercritical), the incremental plastic volumetric strains are negative (i.e., dilatant).

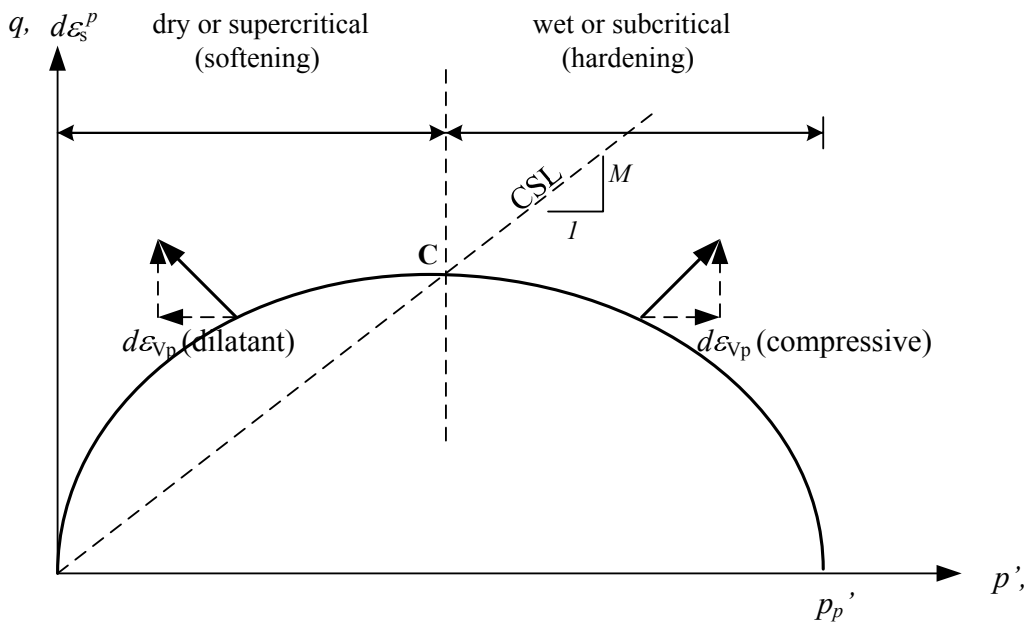


Figure 4-7 Projection of yield surface of modified Cam clay onto $q-p'$ plane

Isotropic hardening/softening behavior is controlled by the change in the pre-consolidation pressure p_p' and is related to the plastic volumetric strain $d\varepsilon_v^p$ by the following relationship which could be obtained from Figure 4.5.:

$$\frac{dp'_p}{p'_p} = d\varepsilon_v^p \frac{\nu}{\lambda - \kappa} \quad (4.34)$$

When yielding takes place on the subcritical or supercritical side, hardening or softening behavior occurs according to equation (4.34), respectively.

4.6.1 Elastic material properties for the Cam Clay and modified Cam Clay models

In elasticity modeling of geomaterials, shear modulus, G , and bulk modulus, K , are conveniently used because they allow the volumetric change and deviatoric change to be decoupled. The elastic bulk modulus for Cam clay and modified Cam clay can be determined from equation (4.33) since isotropic loading condition is assumed, and the behavior along the swelling line is elastic. Because of the linearity between specific volume and mean stress, the bulk modulus K increases linearly with mean stress and can be directly related to the slope of the swelling line κ as:

$$K = \frac{dp'}{d\varepsilon_v^e} = \frac{\nu p'}{\kappa} \quad (4.35)$$

The elastic shear modulus in the original critical state formulation assumed a constant Poisson's ratio, ν , which results in a shear modulus G , also proportional to effective mean stress p' :

$$G = \frac{3(1-2\nu)}{2(1+\nu)} \frac{\nu p'}{\kappa} \quad (4.36)$$

Zytinski et al. [7] demonstrated that the above expressions for K and G , with K linearly dependent on p' and constant G , is not conservative especially for cyclic loading conditions. Wroth and Houlsby [8] proposed conservative elastic shear modulus proportional to effective mean stress and proportional to the hardening parameter.

4.7 FE Solution Procedure for Nonlinear Materials

In general, four basic conditions need to be satisfied to analyze any boundary value stress-strain problem, and these are: equilibrium, compatibility, constitutive relation, and boundary condition. Material nonlinearity introduced by the constitutive behavior causes the governing finite element equations to be reduced to the following incremental form:

$$\mathbf{K}_m^i \Delta \mathbf{u}^i = \Delta \mathbf{F}_u^i \quad (4.37)$$

where \mathbf{K}_m is the incremental stiffness matrix, $\Delta \mathbf{u}$ is the incremental nodal displacement vector, $\Delta \mathbf{F}_u$ is the incremental nodal force vector, and i is the incremental number

Due to the nonlinear constitutive relation, \mathbf{K}_m is dependent on the current stress state and it varies incrementally during loading. The final solution is obtained by summing the results of each increment. Many algorithms and methods are available for the nonlinear stress-strain relation and several methods will be briefly described below. In particular, detailed explanations of Newton-Raphson method with implicit and explicit constitutive integration will be shown in this chapter.

4.7.1 Tangent stiffness method

The tangent stiffness method, otherwise known as the variable stiffness method is the simplest solution strategy. In this approach, the incremental stiffness matrix, \mathbf{K}_m , in equation (4.37) is assumed to be constant over each increment and is calculated using the current stress state at the beginning of each increment. The tangent stiffness method uses a piece-wise approximated linearization of the nonlinear constitutive relation. Unless very small loading increments are used, the method may produce inaccurate results and the simulated results may drift from the true stress-strain relation. In case of plastic behavior the method may result in an illegal stress state which violates the constitutive model. Especially in case that the increment size used is too large for plastic elements, it may results the solution to violate the equilibrium condition as well as the constitutive model.

4.7.2 Visco-plastic method

This method for integrating constitutive models was originally developed for linear elastic visco-plastic (i.e., time dependent) material behavior but was later used to calculate the nonlinear, elasto-plastic, time independent materials [9, 10]. In this method, the material can be represented by a network of the simple rheological units which consists of elastic (e.g., represented by a spring) and a visco-plastic (e.g., represented by a dashpot with a slider) component. In this approach, the external load can be purely supported by the springs, but time-dependent strains also can be occurred not only due to the springs, but also due to movement of the dashpot. When load is removed, strains from the springs are recoverable, but ones from the dashpot are permanent.

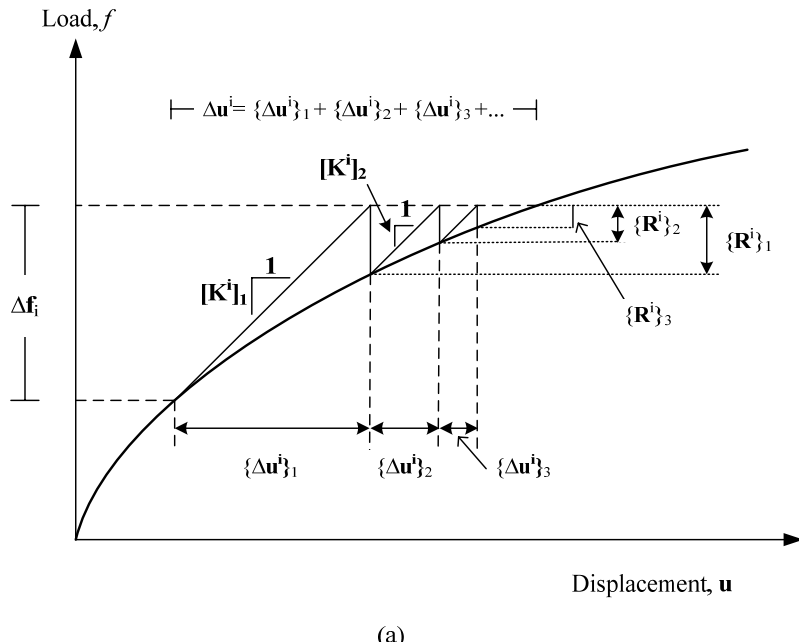
4.7.3 Newton-Raphson method

The Newton-Raphson method uses an iterative technique to solve the nonlinear equation (4.37). In the first iteration in a load increment, the linearized incremental relation given in equation (4.37) predicts increment displacement which contains error due to drift from the true stress-strain relation. The error due to the difference from the predicted and the true stress-strain relation is called the *force residual*. Equation (4.37) can be expressed in terms of residual load \mathbf{R} , vector as:

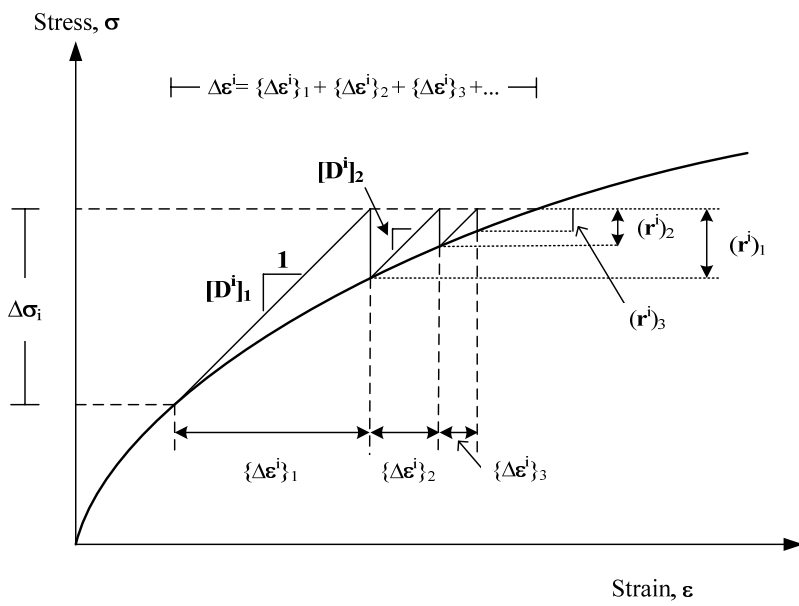
$$\mathbf{K}_m^i \{\Delta \mathbf{u}^i\}_j = \{\mathbf{R}^i\}_j \quad (4.38)$$

where the subscript ‘ j ’ is the iteration number (e.g., $\{\mathbf{R}^i\}_0 = \Delta[11]^i$)

This procedure is repeated until the force residual is small enough to satisfy certain tolerance value. The incremental displacement equals to the sum of the iterative displacement ($\Delta \mathbf{u}^i = \Delta \mathbf{u}_1^i + \Delta \mathbf{u}_2^i + \Delta \mathbf{u}_3^i + \dots$). This method is illustrated on Figure 4-8 for the simple uniaxial loading condition.



(a)



(b)

Figure 4-8 Examples of Newton-Raphson method for the uniaxial loading of nonlinear material in a) load-displacement space; and b) stress-strain space

In Newton-Raphson method, it is essential to calculate the force residual vector during each iteration. That is handled by integration of constitutive model along the incremental strain paths to obtain an estimate of the stress changes. The objective of an integration procedure is to use the incremental constitutive relations to obtain finite increments of the unknown quantities for finite increments of the known quantities (i.e., $\Delta\sigma = [\mathbf{D}] \Delta\epsilon$). Integration of constitutive relations in elasto-plasticity (e.g., implicit and explicit algorithms) is described in the following sections. Since the constitutive behavior changes over the increment (i.e., iteration) Newton-Raphson method is dependent on the constitutive integration. The original Newto-Raphson method uses a variable stiffness matrix \mathbf{K}^i on the each increment (i.e., stiffness matrix is calculated based on the latest estimate of the stresses and strains obtained from the previous iteration). If a constant stiffness matrix equal to the initial value in each load increment is used, it is called the modified Newton-Raphson method.

4.7.3.1 Elastic predictor-plastic corrector method (stress return method)

According to the constitutive relations of elasto-plasticity, the elastic and plastic components of an elasto-plastic loading step may be evaluated independently and then summed, using the operator split technique described by Simo and Ortiz [12, 13]. When this approach is used, the loading step is first assumed to be fully elastic, and the initial estimate for the solution uses the fully elastic constitutive matrix. If the resulting fully elastic stress increment (i.e., the predictor) causes the trial stress state to locate outside the initial yield surface, the loading step is then known to be elasto-plastic and a second (i.e., plastic) stress increment is added to the first (i.e., the corrector). This method treats the stress increment as if it was a two-step process, with an elastic component followed by a

plastic component. The elastic predictor-plastic corrector method uses a return algorithm, in which the initial estimate of the function (based on a fully elastic stress increment) is corrected by returning the stress point to the yield surface to meet the requirements for the solution. In the case of the elasto-plastic loading problem, this means that the final stress point must locate on the final yield surface.

Borja and Lee [14], and Borja[15, 16] presented one-step implicit type return algorithms. In this approach, the plastic strains over the increment are calculated from the stress conditions corresponding to the end of the increment. Due to the implicit nature of the scheme, these stress conditions are not known and a sophisticated iterative sub-algorithm to transfer these stress back to the yield surface is needed. Therefore, the objective of the iterative sub-algorithm is to satisfy the constitutive relation, albeit with the assumption that the plastic strains over the increment are based on the plastic potential at the end of the increment. The basic assumption in these approaches is that the plastic strains over the increment can be evaluated from the stress state at the end of the increment as shown in Figure 4-9. This may be theoretically incorrect because the plastic response (i.e., plastic flow direction) needs to be determined by the current stress state. The plastic flow direction should be consistent with the stress state at the beginning of the increment and should evolve as a function of the changing stress state, such that at the end of the increment is consistent with the final stress state.

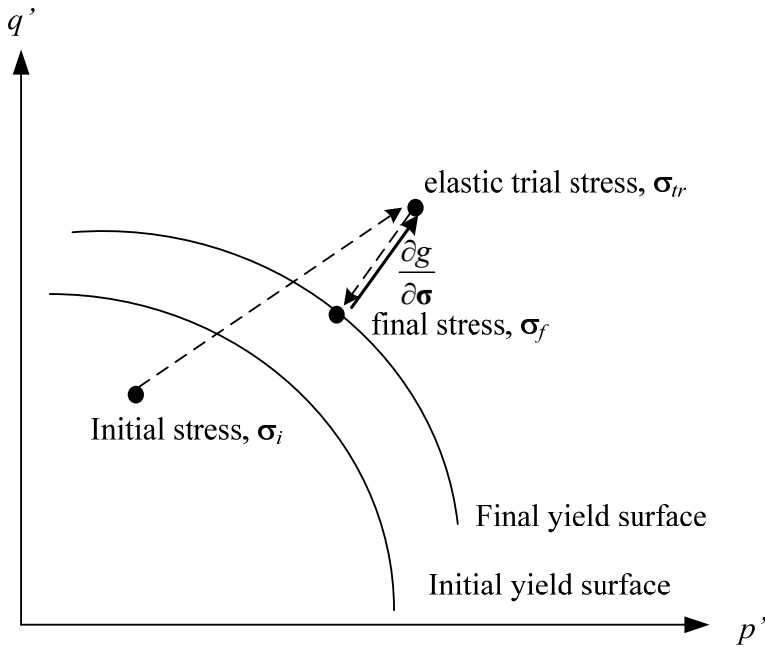


Figure 4-9 Illustration of elastic predictor-plastic corrector (implicit method)

Implicit algorithms which use the Euler method are called backward Euler algorithms.

When implicit methods are used, a solution is implicitly assumed to exist and a solution should be obtained for any step size. This method is theoretical incorrect because the plastic flow direction is a function of the current stress state in the plastic response. The plastic flow direction should be consistent with the stress state at the beginning of the solution increment and should evolve as a function of the changing stress state, such that at the end of the increment it is consistent with the final stress state.

Explicit algorithms use the forward Euler algorithms. The explicit method evaluates the solution increment for the initial yield conditions in which the stress point starts elasto-plastic behavior (See Figure 4-10). When explicit methods are used, the values of the

variables are known, since the initial stresses and strains are known. The value of the function can be calculated only by changing the value of the plastic multiplier until the consistency condition is satisfied. However, a solution is not assumed or known to exist when using explicit methods. These methods may exhibit divergence for highly nonlinear functions. Explicit methods also theoretically incorrect because they assume that the solution increment is a function of the stress state at the beginning of the solution increment.

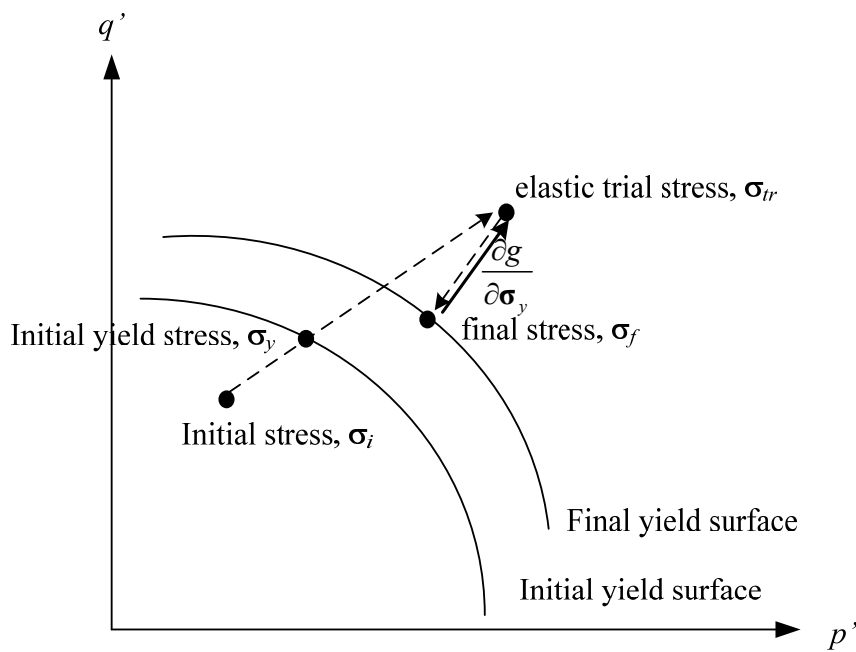


Figure 4-10 Illustration of elastic predictor-plastic corrector (explicit method)

4.7.3.2 Explicit sub-stepping method

In this method, the incremental strains are assumed known as divided into a number of sub-steps, and loading in each sub-step is proportional to the incremental strains. Since the

stresses and hardening parameter are known at the beginning of the load increment, elasto-plastic constitutive matrix \mathbf{D}^{ep} , can be calculated before a loading step using Euler, modified Euler or Runge-Kutta scheme. The size of each sub-step can vary and is determined by setting an error tolerance on the numerical integration. Sloan [17] presented the sub-stepping stress point algorithm and simple graphical strategy is shown in Figure 4-11.

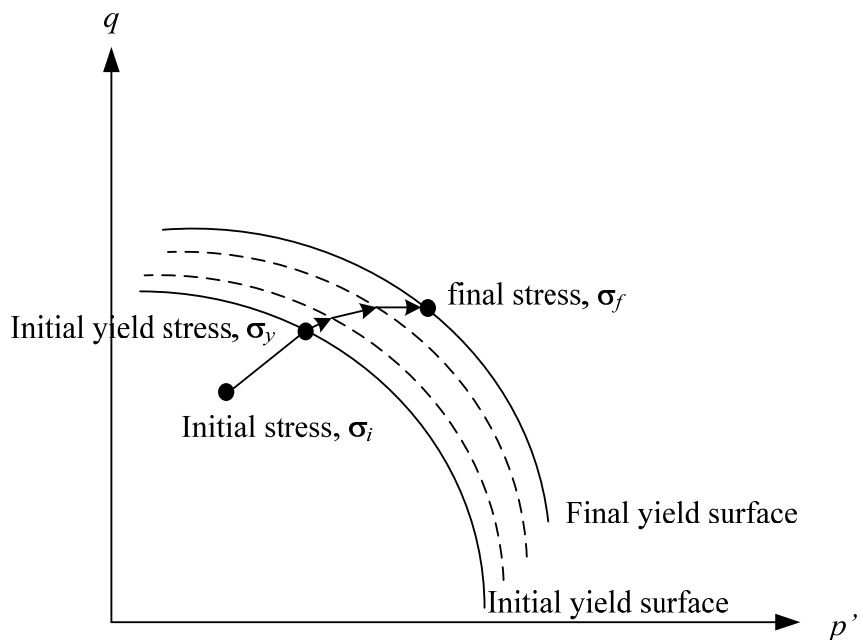


Figure 4-11 Illustration of sub-stepping method

The basic assumption in the sub-stepping approaches is that the strains vary in proportional over the load increment. However, this assumption may not be true and an error can be introduced, such that the magnitude of the error is dependent on the size of the increment.

Also, the stress increment calculated using the elasto-plastic constitutive matrix may not lie on the final yield surface due to drift or nonlinearity in the stress-strain behavior which is not taken into account during calculation of \mathbf{D}^{ep} . Therefore, the final stress point calculated using this method may need to be corrected to the final yield surface to satisfy the consistency condition.

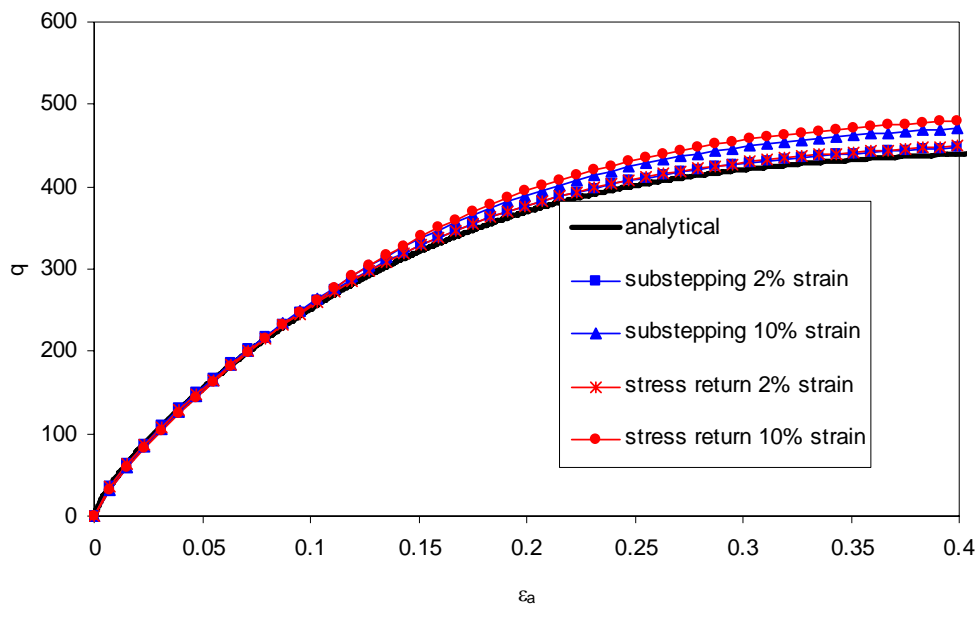
4.8 Uniform Compression Test for the Modified Cam Clay Soils

The Newton-Raphson method with stress return algorithm proposed by Boja [15, 16] and the sub-stepping algorithm by Sloan [17] are tested for the idealized consolidated-drained (CD) triaxial test of the modified Cam Clay soils. Finite Element analysis is performed using the Matlab platform under two dimensional plane strain condition. Four-noded isoparametric elements with four Gaussian integration points are used and strain control technique is employed for the boundary value problem. The soil sample is assumed to be isotropically normally consolidated to a means effective stress p' of 200 KPa with zero excess pore pressure. Elastic bulk modulus is assumed constant and independent of the mean effective stress changes, and the elastic shear modulus is calculated using a constant Poisson's ratio. Soil properties used in the analysis are shown in Table 4-2. In case of undrained triaxial test, the fully-coupled approach can be implemented for the pore pressure calculations as well as stresses/strains calculations, which will be presented on the next chapter.

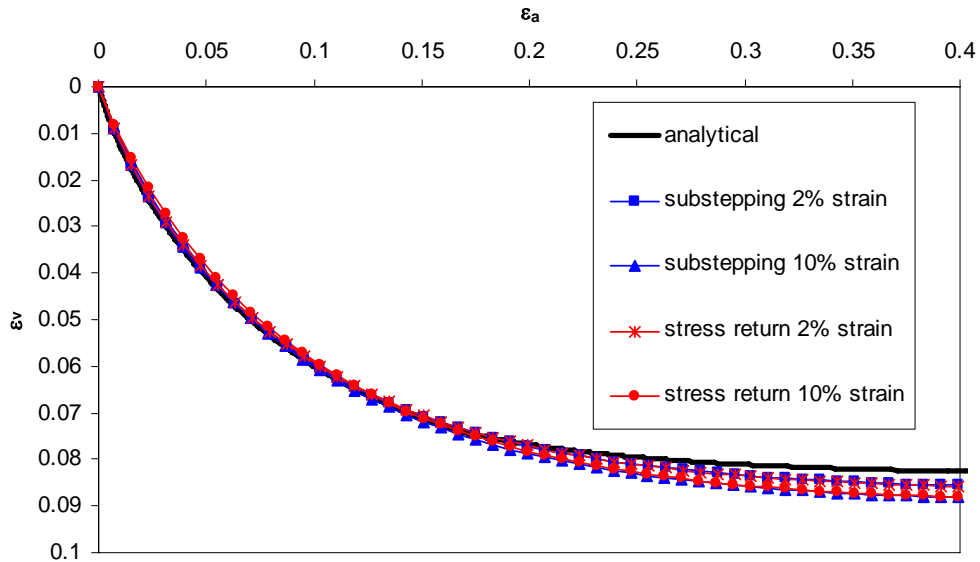
Table 4-2 Soil parameters for the modified Cam clay model

Parameter	
Over consolidation ratio, OCR	1.0 for N.C. clay 10 for O.C. clay
Specific volume, v_1	1.788
Slope of virgin consolidation line, λ	0.066
Slope of swelling line, κ	0.0077
Slope of critical state line, M	0.693
Poisson's ratio, ν	0.26

Results from the Newton-Raphson method drained triaxial test analyses are compared with the analytical solution in Figure 4-12. Analytical solution is obtained based on the incremental formulation with use of very small axial strain increments ($\varepsilon_a=10^{-6}$). Results from both sub-stepping and stress return constitutive integration method for the normally consolidated soil (OCR=1) and the over consolidated soil (OCR=10) are agree well with the analytical solution. For this specific boundary problem, the stress return method is more sensitive for the effect of incremental size and requires less computational times than the sub-stepping method. Table 4-3 and 4-4 shows the computational times of the both methods for the N.C. and O.C. clay. The incremental formulations of triaxial test for Modified Cam Clay model are presented in the Appendix-B.

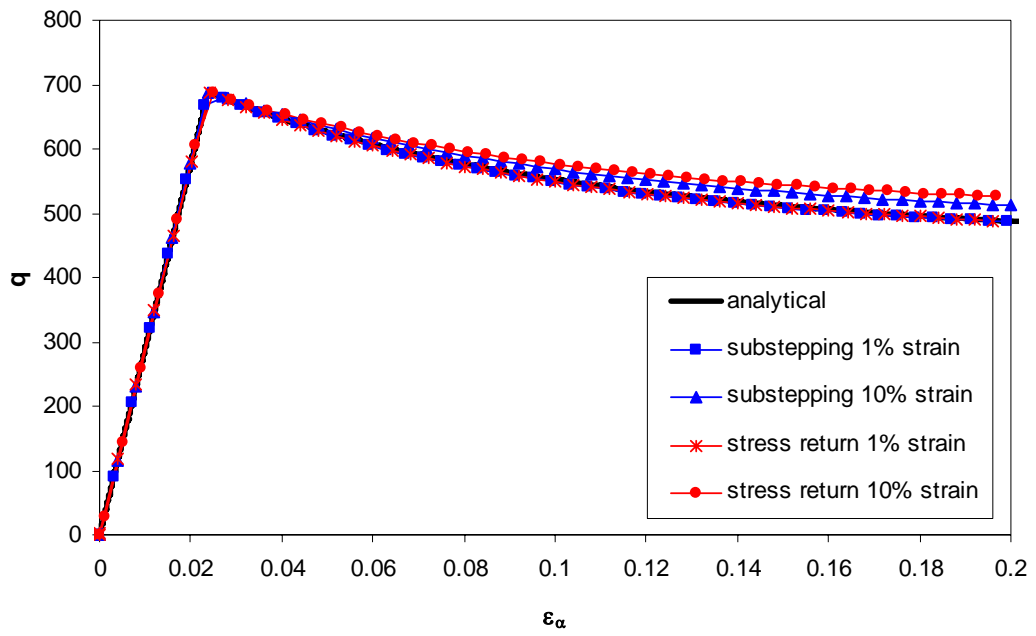


(a)

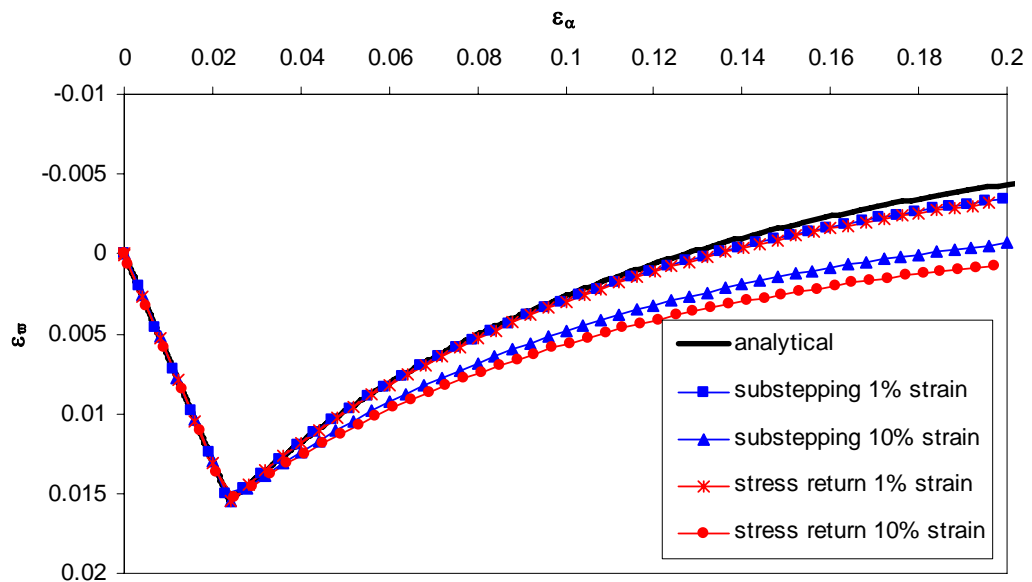


(b)

Figure 4-12 Idealized drained triaxial test for N.C. clay in (a) q vs. ε_a , and (b) ε_v vs. ε_a



(a)



(b)

Figure 4-13 Idealized drained triaxial test for O.C. clay in (a) q vs. ϵ_a , and (b) ϵ_v vs. ϵ_a

Table 4-3 Results and CPU times for the idealized drained triaxial test analyses (N.C. clay)

N.C.	% strain	No. of increments	p' (KPa)	q (KPa)	Vol. strain (%)	CPU sec
Analytical			640.1	440.1	8.26	n/a
Sub-stepping	2	2000	647.21 (1.1 %)	447.21 (1.6 %)	8.56 (3.5 %)	105
	10	400	670.63 (4.5 %)	470.63 (6.5 %)	8.83 (6.5 %)	54
Stress return	2	2000	650.45 (1.6 %)	450.45 (2.3 %)	8.56 (3.5 %)	62
	10	400	680.11 (5.8 %)	480.11 (8.3 %)	8.812 (6.3 %)	28

Table 4-4 Results and CPU times for the idealized drained triaxial test analyses (O.C. clay)

O.C.	% strain	No. of increments	p' (KPa)	q (KPa)	Vol. strain (%)	CPU sec
Analytical			687.8	487.8	-0.44	n/a
Sub-stepping	1	2000	686.0 (-0.3 %)	486.0 (-0.4 %)	-0.34 (23 %)	103
	10	200	712.6 (3.4 %)	512.6 (4.8 %)	0.07 (116 %)	33
Stress return	1	2000	687.4 (-0.1 %)	487.4 (-0.1 %)	-0.33 (25 %)	78
	10	200	725.0 (5.1 %)	525.0 (7.1 %)	0.06 (113 %)	14

REFERENCES

1. Naylor, D.J., G.N. Pande, B. Simpson and R. Tabb 1981. *Finite Elements in Geotechnical Engineering*. Swansea, Wales, U. K.: Pineridge Press.
2. Kondner, R.L. 1963. Hyperbolic Stress-Strain Response: Cohesive Soil. *ASCE Journal of Soil Mechanics and Foundation Engineering Division*. 189(SM1): 115-143.
3. Duncan, J.M. and C.-Y. Chang 1970. Nonlinear analysis of stress and strain in soils. *ASCE Journal of the Soil Mechanics and Foundation Engineering Division*. 96(SM5): 1629-1653.
4. Roscoe, K.H., A.N. Schofield and A. Thurairajah 1963. Yielding of clays in states wetter than critical. *Geotechnique*. 13: 211-240.
5. Schofield, A.N. and C.P. Wroth 1968. *Critical State Soil Mechanics*. New York: McGraw-Hill.
6. Roscoe, K.H. and J.B. Burland 1968. *On the generalized stress-strain behaviour of 'wet clay'*, in *Engineering Plasticity*, L.F.A. Heyman J., Editor. Cambridge University Press: Cambridge. p. 535-609.
7. Zytinski, M. 1978. On Modelling the Unloading-reloading Behavior of Soils. *Int. J. Num. Anal. Meth. Geomech.* 2: 87-93.
8. Wroth, C.P. and G. Houlsby 1985. Soil mechanics - property characterization and analysis procedure. in *11th International Conference on Soil Mechanics and Foundation Engineering*. Sanfrancisco.
9. Zienkiewicz, O.C. and I.C. Cormeau 1974. Visco-Plasticity, Plasticity and Creep in elastic Solids - A Unified Numerical Solution Approach. *International Journal for Numerical Methods in Engineering*. 8: 821-845.
10. Owen, D.R.J. and E. Hinton 1980. *Finite Elements in Plasticity: Theory and Practice*. Swansea, UK: Peneridge Press.
11. Nakagawa, H., M. Murakami, S. Fujiwara and M. Tobita 2000. Land subsidence of the northern Kanto plains caused by ground water extraction detected by JERS-1 SAR interferometry. *International Geoscience and Remote Sensing Symposium (IGARSS)*. 5: 2233-2235.
12. Simo, J.C. and M.A. Ortiz 1985. A unified approach to the finite deformation elastoplastic analysis based on the use of hyper elastic constitutive equations. *Computer Methods in Applied Mechanics and Engineering*. 49: 221-245.
13. Simo, J.C. and R.L. Taylor 1985. Consistent Tangent Operators for Rate-Independent Elastoplasticity. *Computer Methods in Applied Mechanics and Engineering*. 48: 101-118.
14. Borja, R.I. and S.R. Lee 1990. Cam-caly Plasticity, Part I: Implicit Integration of Elasto-plastic Constitutive Relatios. *Communications in Numerical Methods in Engineering*. 78: 49-72.

15. Borja, R.I. 1991. One-step and Linear Multistep Methods for Nonlinear Consolidation. *Computer Methods in Applied Mechanics and Engineering*. 85: 239-272.
16. Borja, R.I. 1991. Cam-clay Plasticity, Part II: Implicit Integration of Constitutive Equation Based on a Nonlinear Elastic Stress Predictor. *Computer Methods in Applied Mechanics and Engineering*. 88: 225-240.
17. Sloan, S.W. 1987. Sup-stepping Schemes for the Numerical Integration of Elastoplastic Stress-Strain Relations. *International Journal for Numerical and Analytical Methods in Geomechanics*. 24: 893-911.

5 SOLUTION TECHNIQUES FOR THE DISCRETIZED BIOT'S EQUATIONS

5.1 *Introduction*

The discretized fully-coupled Biot's equations presented in the preceding chapters can be solved using various solution methods such as monolithic, partitioned, porosity coupling, and modular approaches. The monolithic method solves the full set of equations simultaneously in one time step. Partitioned solution methods involve the rearrangement and splitting of the discretized Biot's equation into mechanical part and fluid flow part. The monolithic and partitioned methods produce most rigorous and consistent solutions. Modular approach exploits separate geomechanical and fluid flow simulators based on various coupling strategies (e.g., porosity coupling, permeability coupling, and updating compressibility matrix method). In some approaches involving modular solutions neglect or simplify the effects of coupling between fluid flow and mechanical response.

The objective of this chapter is to develop a rigorous partitioned and modular solution of the discretized Biot's equation. The modular solutions will be based on the updating of the full compressibility matrix or porosity updating with including an additional source term on the continuity equations also, implementing the effective stress law in the equilibrium equation. The modular approaches are flexible and has an advantage of using the latest developments in existing commercial simulators with relatively small modification and is still based on the fully-coupled theory.

In general, the Finite Element method is widely used in geomechanical analysis and Finite Difference method is popular in fluid flow analysis. Therefore, it is beneficial to develop efficient solution techniques to couple FE geomechanics and FD fluid flow codes, as well as FE geomechanics and FE fluid flow codes. In this chapter, numerical solution strategies including monolithic, partitioned and modular approaches such as a porosity coupling method, and updating compressibility matrix (FE-FE, and FE-FD) will be presented. Description for each method starts from the simple linear stress-strain relation with single-phase flow model which was described in Chapter 2. Throughout this chapter, the methods will be expanded to more complicated elasto-plastic stress-strain relation with multi-phase fluid flow. For simplicity, detailed explanations of solution procedure will be presented for the single-phase fluid flow case. For multi-phase fluid flow, the coupling procedures between geomechanics and fluid flow fields are essentially same as the single-phase flow case, and therefore will be shown only briefly on following sections.

5.2 Monolithic Solution

Since the monolithic method for linear elastic stress-strain model with single-phase flow was already described in Chapter 2, this chapter begins with nonlinear stress-strain case with single-phase flow. In order to incorporate nonlinear stress-strain analysis, numerical method (e.g., Newton-Raphson method) is required for solving the full set of FE discretized Biot's equation which is shown below as:

$$\begin{bmatrix} \mathbf{K}_m & \mathbf{L} \\ \mathbf{L}^T & \mathbf{S} - \Delta t \mathbf{K}_c \end{bmatrix} \begin{Bmatrix} \Delta \mathbf{u}^i \\ \Delta \mathbf{p}^i \end{Bmatrix} = \begin{Bmatrix} \Delta \mathbf{R}_u^{i-1} \\ \Delta \mathbf{R}_p^{i-1} \end{Bmatrix} \quad (5.1)$$

where superscript i is the iteration counter in Newton-Raphson procedure. The residual vector, \mathbf{R} , for both mechanical and fluid flow parts are given as:

$$\begin{aligned}\Delta\mathbf{R}_u^i &= \Delta\mathbf{F}_u^{\text{ext}} - \Delta\mathbf{F}_u^{\text{int}} - \mathbf{L}\Delta\mathbf{p} \\ \Delta\mathbf{R}_p^i &= \Delta\mathbf{F}_p^{\text{ext}} - \mathbf{L}\Delta\mathbf{u} - \mathbf{S} + \Delta t\mathbf{K}_c\Delta\mathbf{p}\end{aligned}\quad (5.2)$$

A flow chart for the numerical implementation of the monolithic method for nonlinear stress-strain analysis is shown in Figure 5-1. The implementation solves the displacements and the pressure variables simultaneously in equation (5.1) with iterations when it is necessary. The Newton-Raphson approach is an iterative method which requires small residual vector under a specific criterion for convergence to a correct solution. Internal stresses can be calculated using various existing methods to numerically integrate the constitutive relations [1-5].

The monolithic method is straightforward and produces the most rigorous results, however, it may not be the most efficient method in terms of computational cost. For example, it requires the solution of a large system of simultaneous to solve multiple variables (e.g., displacements and fluid pressures) simultaneously. Also, in many reservoir problems where the porous domain is surrounded by the impermeable material, the monolithic method still requires full discretizations for the fluid flow part as well as geomechanical domain. In this case, analysis of the only part of the problem domain corresponding to the fluid flow domain (i.e., permeable porous media) is more cost effective, although mechanical part still uses full discretized domain to take into account boundary effects on porous media (e.g., stiffness effects of overburden and side burden). In addition, the monolithic method is not

flexible and it is cumbersome to incorporate in conjunction with sophisticated existing simulators (i.e., uncoupled commercial flow and geomechanical simulators).

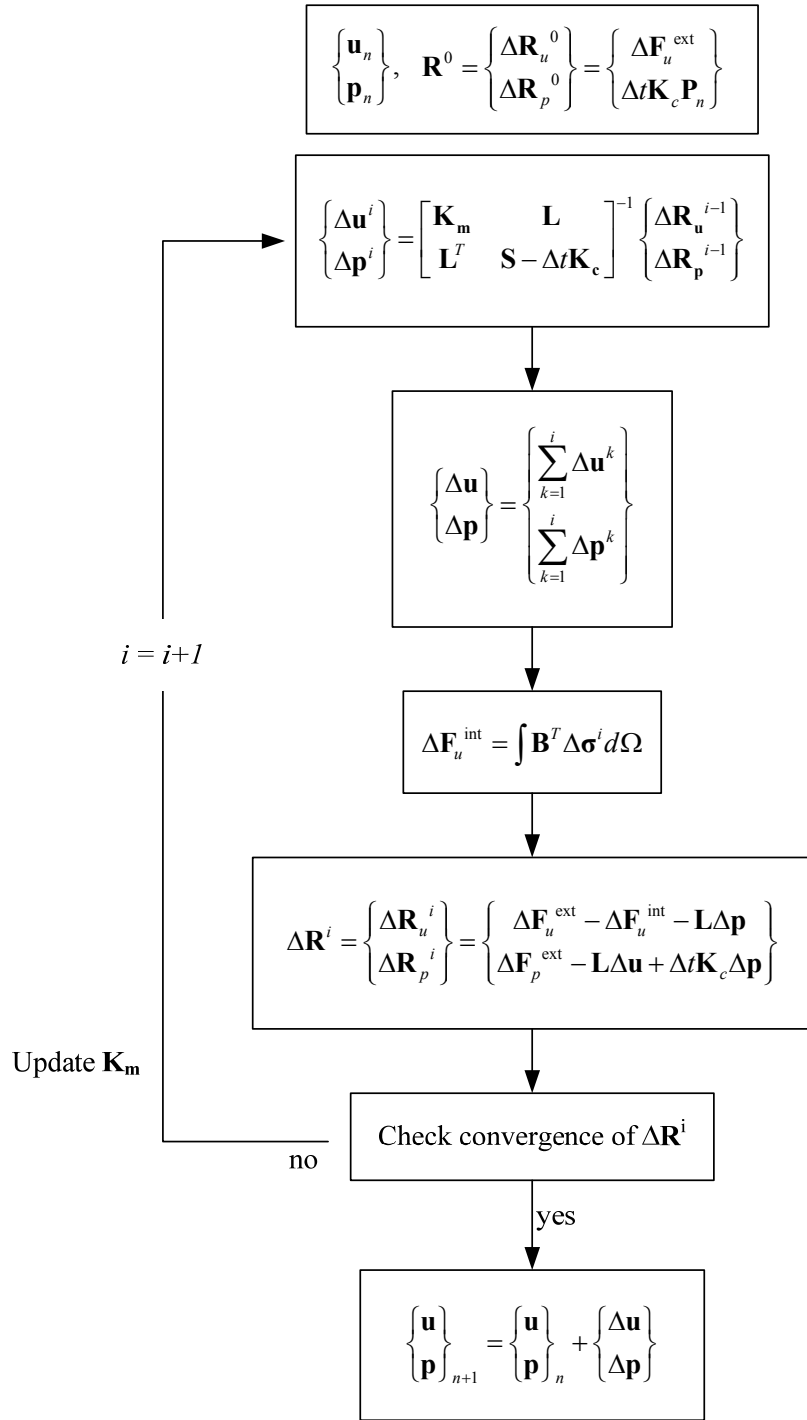


Figure 5-1 A schematic flow chart for the monolithic method with incorporation of nonlinear stress-strain analysis

5.3 Partitioned Solution Methods

5.3.1 Partitioned approach with direct solution method

The basic idea of the partitioned method starts from the rearrangement of the fully-coupled monolithic solution expressed in FE formulations. In order to derive the partitioned solution, the full set of the fully-coupled Biot's system of equations needs to be separated into the mechanical equilibrium part and the fluid flow continuity equation part. Using a linear elastic stress-strain model, the separate equations can be written as:

$$\mathbf{K}_m \Delta \mathbf{u} + \mathbf{L} \Delta \mathbf{p} = \Delta \mathbf{F}_u \quad (5.3)$$

$$\mathbf{L}^T \Delta \mathbf{u} + (\mathbf{S} - \Delta t \mathbf{K}_c) \Delta \mathbf{p} = \Delta \mathbf{F}_p \quad (5.4)$$

Solving for $\Delta \mathbf{u}$ in equation (5.3), inserting the solution into equation (5.4) and rearranging in terms of the pore pressure increment vector yields:

$$[\mathbf{L}^T \mathbf{K}_m^{-1} \mathbf{L} - \mathbf{S} + \Delta t \mathbf{K}_c] \Delta \mathbf{p} = -\Delta t \mathbf{K}_c \mathbf{p}_n + \mathbf{L}^T \mathbf{K}_m^{-1} \Delta \mathbf{F}_u \quad (5.5)$$

$$\Delta \mathbf{u} = \mathbf{K}_m^{-1} (\Delta \mathbf{F}_u - \mathbf{L} \Delta \mathbf{p}) \quad (5.6)$$

During the solution procedure, the calculated pore pressure increment vector from equation (5.5) is re-inserted to calculate the displacement increment vector using equation (5.6). First, a trial displacement vector assuming no pore pressure change (using equation (5.6)) is used to calculate the incremental pore pressure vector using equation (5.5). Then the corrected incremental displacement vector including the pore pressure term is calculated using equation (5.6). In case of linear elasticity, a trial displacement vector is not needed and and,

both equations (5.5 and 5.6) do not require iteration because the pore pressure equation contains external force vector instead of incremental displacement vector. However, iteration cannot be avoided for nonlinear stress-strain relations solved by Newton-Raphson method. A schematic flow chart of the partitioned solution method which can be implemented in nonlinear stress-strain relation is presented in Figure 5-2. It is noted that the partitioned method separates the FE formulation of Biot's equation into geomechanical part and fluid flow part within an identical discretized domain. Therefore, it is worth noting that the partitioned approach gives possibilities of the modular approach based on the fully-coupled analysis. However, it may still not be most efficient method in case that the discretized domain for the geomechanical analysis of the no fluid flow region is included in the analysis.

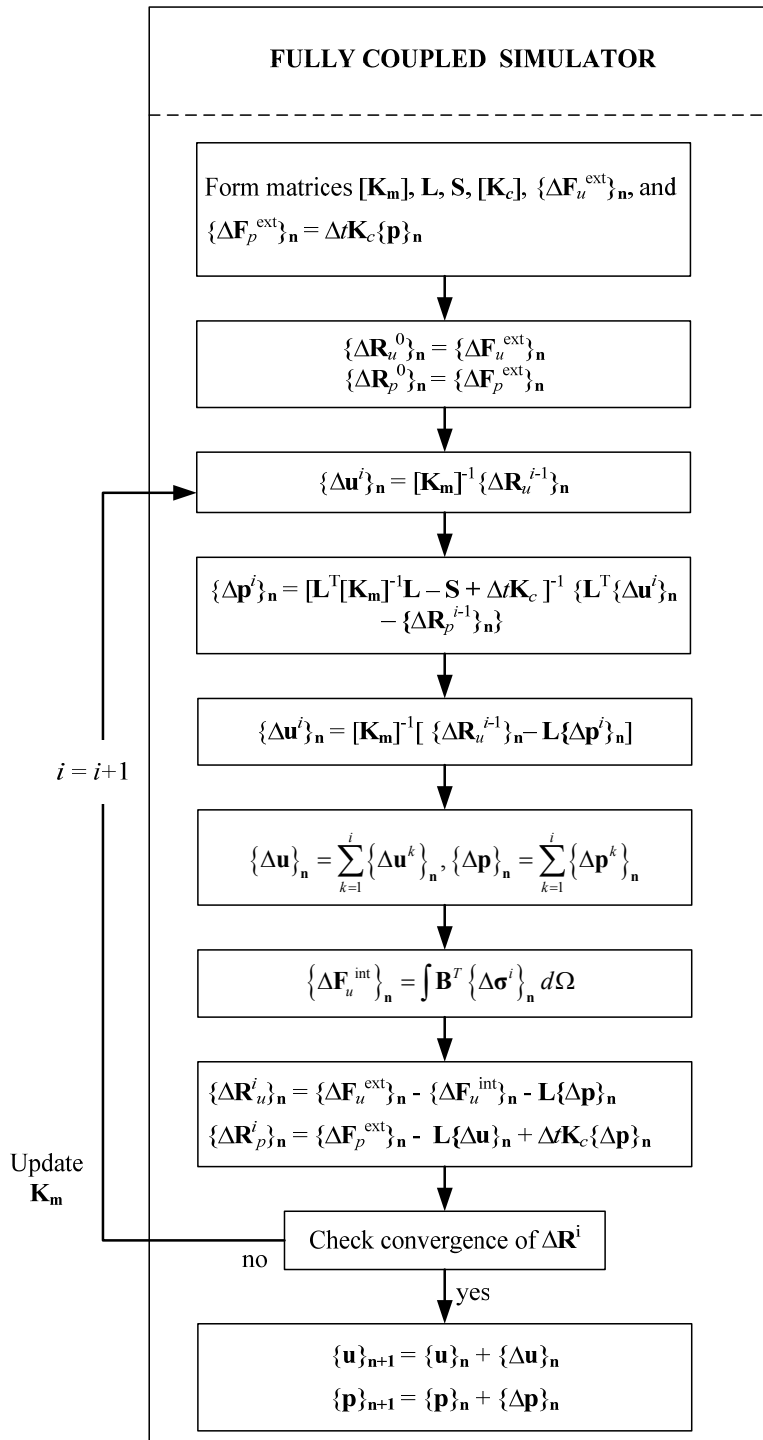


Figure 5-2 A schematic flow chart of the partitioned Method with incorporation of nonlinear stress-strain analysis

5.3.2 Partitioned approach with iterative solution method

Several iterative methods have been introduced for a linear and non-linear partitioned system of equations [6-9]. Also, Elman [10] introduced several iterative methods with applications in incompressible fluid dynamics. In case of iterative methods, preconditioners may be used to accelerate convergence and a possible candidate for the preconditioner is the symmetric positive definite fluid permeability matrix, \mathbf{K}_c , in the system of equations. Brief descriptions of various methods are presented below and these methods are modified to be applicable for the partitioned Biot's system of equations. Detailed algorithms for each method are presented in the Appendix-C.

- Conjugate Gradient Method

A conjugate Gradient method was developed by Hestenes [11] for symmetric positive definite matrices. Prevost [12] presented an implicit unconditionally stable staggered solution procedure for coupled problems using an iterative staggered preconditioned conjugate gradient method (PPCG). This method generates a sequence of conjugate (or orthogonal) vectors that are equal to the residuals in each iteration.

- MINRES Method

The minimum residual method (MINRES) derived by Paige [13]. This method is applicable to any symmetric system and it is an effective algorithm for indefinite coefficient matrices as well as positive-definite matrix system. In the MINRES method, the sequence of orthogonal vectors are computed, combined and updated through a least-squares solution procedure.

- Bi-Conjugate Gradient Method

Bi-Conjugate gradient method is applicable to non-symmetric matrices and produces the same iterations as conjugate gradient method [14]. This method generates two conjugate gradient sequences of vectors, one based on a system with the original coefficient matrix, and the other based on the transpose of the coefficient matrix. In case of the symmetric positive definite system, the method is equivalent to the minimization principle for conjugate gradient method, however, it requires two more matrix vector operations per iteration step.

5.4 Modular Approaches

5.4.1 Updating of the compressibility matrix

Similar to the partitioned solution method, the modular approach solves the basic equations for the geomechanics and fluid flow field independently. In this section, modular approach by updating the compressibility matrix is presented. This method is based on external coupling and that information between two simulators is exchanged through a coupling module in a necessary number of iteration on time steps. Information provided by fluid flow simulator is the pressure increment, and stress/strain is calculated by geomechanics simulator using calculated pressure from fluid flow simulator. In the geomechanics simulator, pressure values from fluid flow simulator are treated as external loads in the calculations of displacements. After the displacements calculation, stresses and strains can be obtained using the displacement-strain compatibility relation and stress-strain constitutive relation.

5.4.1.1 Geomechanics (FE) – Fluid Flow (FE) coupling

- Single-phase fluid flow

Geomechanics (FE) – fluid flow (FE) coupling starts with modifying the FE fluid flow equation which was shown in earlier chapters. In the conventional uncoupled fluid flow equation, it is generally assumed that compressibility is the only function of pore pressure, which is associated with the change in mean total stresses (i.e., traditional compressibility term is either a scalar or diagonal matrix). However, it is well known fact that not only mean stresses can cause volumetric stress but also shear stresses can cause volumetric strain in geomaterials due to dilatancy. Therefore, instead of a scalar relationship between volumetric change and the pore pressure change, the full compressibility matrix needs to be used to take into account effects of full tensorial relations between stresses and strains. Also, bulk volume change needs to be considered to satisfy continuity equations. In this section, the fully-coupled modular solution is developed, which is based on updating the compressibility term with full tensorial matrix and bulk volume change calculated from geomechanics simulator. Conventional FE formation of the fluid flow equation using fully implicit FD time discretization is given by the following equation:

$$[\mathbf{c}_t \mathbf{M} + \Delta t \mathbf{K}_c] \mathbf{p}_{n+1} = \mathbf{c}_t \mathbf{M} \mathbf{p}_n \quad (5.7)$$

where \mathbf{c}_t is the diagonal compressibility matrix, and \mathbf{M} is the mass matrix.

In comparison, the continuity equation from the fully-coupled equation (i.e., equation (5.5)) can be reformulated by replacing $\Delta \mathbf{p}$ with $(\mathbf{p}_{n+1} - \mathbf{p}_n)$ and rearrange terms:

$$[\mathbf{C}_m + \Delta t \mathbf{K}_c] \mathbf{p}_{n+1} = \mathbf{C}_m \mathbf{p}_{n+1} + \mathbf{L}^T \mathbf{K}_m^{-1} \Delta \mathbf{F}_u \quad (5.8)$$

where \mathbf{C}_m ($= \mathbf{L}^T \mathbf{K}_m^{-1} \mathbf{L} - \mathbf{S}$) is the full compressibility matrix

It can be noted that those equations (5.7) and (5.8) have similar forms. Important differences between two equations are the compressibility terms (i.e., $\mathbf{c}_t \mathbf{M}$ in equation (5.7) and $\mathbf{C}_m = \mathbf{L}^T \mathbf{K}_m^{-1} \mathbf{L} - \mathbf{S}$ in equation (5.8)) on both hand sides of the equation, and the bulk volume change which can be treated as an additional source term (i.e., $\mathbf{L}^T \mathbf{K}_m^{-1} \Delta \mathbf{F}_u$) on the right hand side of equation (5.8). Therefore, it is possible to obtain fully-coupled effects using the conventional fluid flow equation by updating compressibility term and adding additional fluid source or sink vector. It means that it is possible to implement fully-coupled approach in the conventional FE based fluid flow simulator with aid of existing geomechanics simulator. This simple strategy applicable for the linear elasticity is shown in Figure 5-3.

$$\begin{aligned} & \left[\mathbf{L}^T \mathbf{K}_m^{-1} \mathbf{L} - \mathbf{S} + \Delta t \mathbf{K}_c \right] \mathbf{p}_{n+1} = (\mathbf{L}^T \mathbf{K}_m^{-1} \mathbf{L} - \mathbf{S}) \mathbf{p}_n + \mathbf{L}^T \mathbf{K}_m^{-1} \Delta \mathbf{F}_u \\ & \mathbf{C}_t = \mathbf{L}^T \mathbf{K}_m^{-1} \mathbf{L} - \mathbf{S} \\ & \rightarrow [\mathbf{c}_t \mathbf{M} + \Delta t \mathbf{K}_c] \mathbf{p}_{n+1} = \mathbf{c}_t \mathbf{M} \mathbf{p}_n \end{aligned}$$

Additional source

Figure 5-3 A simple scheme of updating fluid flow equation based on the Biot's theory

Once pore pressure has been calculated, displacements can be calculated using equation (5.6). In this approach, it is possible to use separate discretization domains such that fluid-flow simulation can use a discretization domain only over the permeable porous media, and it is not required to have the full domain which may include impermeable domain. The

basic flow chart of partitioned FE-FE coupling method applicable to linear and nonlinear stress-strain relations is shown in Figure 5-4.

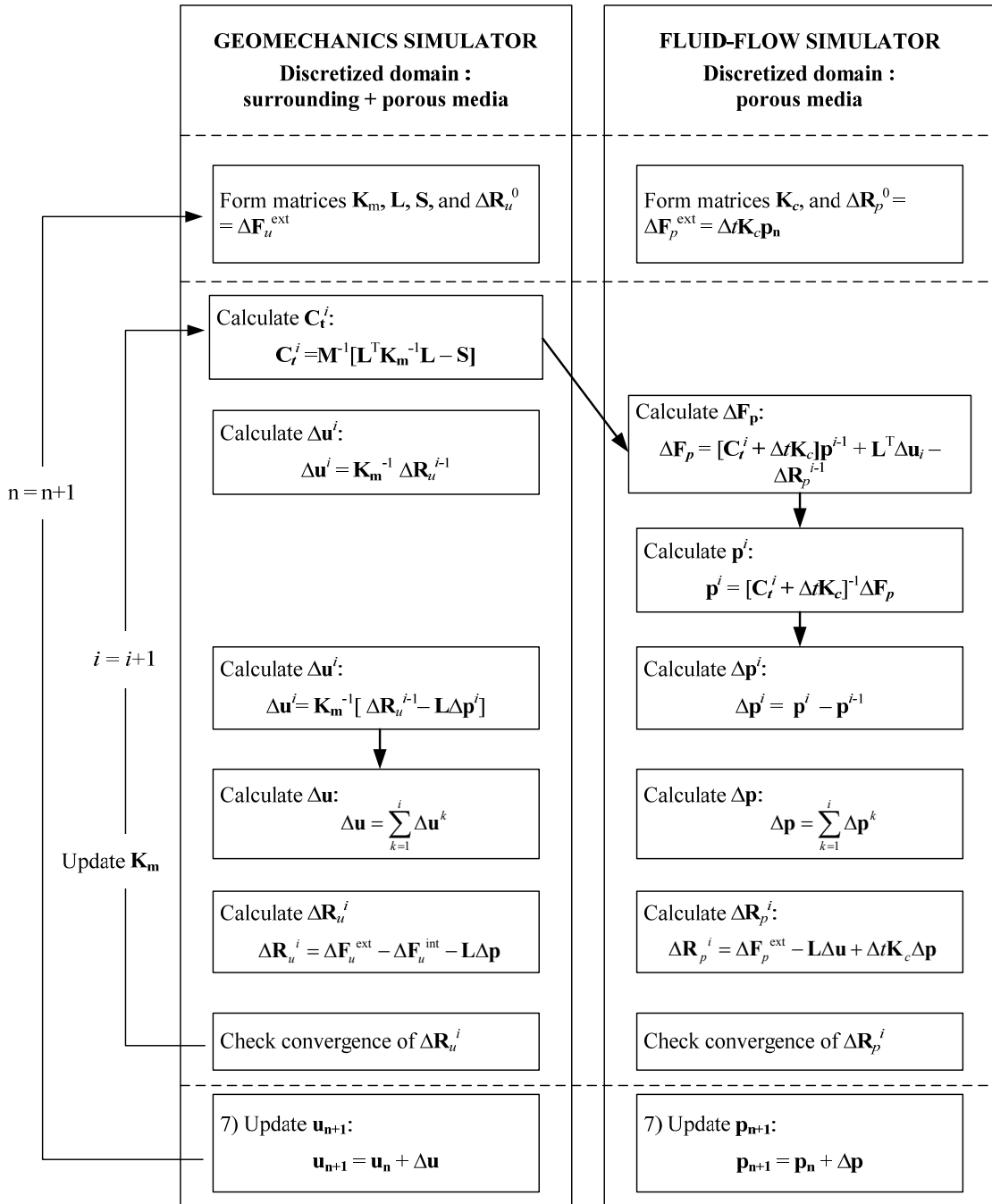


Figure 5-4 A schematic flow charts for modular approach: geomechanics (FE) – fluid-flow (FE) coupling with incorporation of nonlinear stress-strain analysis

- **Two-phase fluid flow**

The modular approach based on the updating of the compressibility matrix for two-phase flow is essentially same as single-phase flow case described earlier. In this section, only the FE-FE partitioned solution will be briefly described. In multi-phase fluid flow case, additional iteration is required for solving the nonlinear fluid continuity equations using various methods (e.g., SS method, IMPES and SEQ method as discussed in Chapter 3). In this thesis, the SS method is chosen because it contains pressure variables instead of saturation and it is relatively easy to implement than other methods. Continuity equations for the two-phase flow described in the previous chapter can be reformulated as;

$$\begin{bmatrix} \mathbf{C}_t \mathbf{S}_{ww1} - \mathbf{S}_w' - \Delta t \mathbf{K}_{ew} & \mathbf{C}_t \mathbf{S}_{wg1} + \mathbf{S}_w' \\ \mathbf{C}_t \mathbf{S}_{gw1} + \mathbf{S}_w' & \mathbf{C}_t \mathbf{S}_{gg1} - \mathbf{S}_w' - \Delta t \mathbf{K}_{eg} \end{bmatrix} \begin{Bmatrix} \Delta \mathbf{p}_w \\ \Delta \mathbf{p}_g \end{Bmatrix} = \begin{Bmatrix} \mathbf{F}_{ww} \\ \mathbf{F}_{gg} \end{Bmatrix} \quad (5.9)$$

where

$$\begin{aligned} \mathbf{SS}_{ww1} &= \int_{\Omega} S_w (S_w + p_c S_w') d\Omega \\ \mathbf{LL}_{wg} &= \int_{\Omega} [S_w ((1 - S_w) - p_c S_w')] d\Omega \\ \mathbf{SS}_{gg} &= \int_{\Omega} [S_g (S_g - p_c S_g')] d\Omega \\ \mathbf{LL}_{gw} &= \int_{\Omega} [S_g (S_w + p_c S_w')] d\Omega \\ \mathbf{S}_w' &= \int_{\Omega} [\phi S_w'] d\Omega \end{aligned} \quad (5.10)$$

Expression for the compressibility matrix is identical to the single-phase flow and it is presented in equation (5.8). After the fluid pressure calculation, displacements can be obtained using equation (5.6) in the same manner as in single phase flow case. It should be

noted that pore pressures used in the geomechanical simulation are average value of the fluid pressures as defined in Chapter 3.

5.4.2 Geomechanics (FE) – Fluid Flow (FD) coupling

Fully-coupled solution of geomechanics (FE) – fluid flow (FD) based on the updating of the compressibility matrix starts from revisiting the global matrix formation of FD transient flow equation shown as following:

$$[\mathbf{V}_b \mathbf{c}_t + \Delta t \mathbf{H}_c] \mathbf{p}_{n+1} = \mathbf{V}_b \mathbf{c}_t \mathbf{p}_n \quad (5.11)$$

where \mathbf{H}_c is global FD conductivity matrix and \mathbf{V}_b is a diagonal global bulk volume matrix. It can be noted that equation (5.11) has a similar format as the FE equation (5.8) except the FD equation has a conductivity matrix, \mathbf{H}_c , different from \mathbf{K}_c in FE equation. Therefore, a similar modular approach is possible by updating compressibility matrix. Also the effect of bulk volume change needs to be added on the right hand side of equation (5.11) as an additional source term to satisfy the continuity relation. In order to implement the modular approach based on the fully-coupled equation, the compressibility matrix needs to be updated with $\mathbf{M}^{-1} \mathbf{c}_t$ in the FD fluid-flow equation and an additional source term $\mathbf{V}_b \Delta \epsilon_v$ can be added as shown in Figure 5-5. The other steps are identical with the FE-FE modular approach, and the basic flow chart for nonlinear stress-strain relation FE-FD modular approach is shown in Figure 5-6.

$$\begin{aligned}
 & \left[\mathbf{L}^T \mathbf{K}_m^{-1} \mathbf{L} - \mathbf{S} + \Delta t \mathbf{K}_c \right] \mathbf{p}_{n+1} = \left(\mathbf{L}^T \mathbf{K}_m^{-1} \mathbf{L} - \mathbf{S} \right) \mathbf{p}_n + \mathbf{L}^T \mathbf{K}_m^{-1} \Delta \mathbf{F}_u \\
 & \mathbf{C}_t = \mathbf{L}^T \mathbf{K}_m^{-1} \mathbf{L} - \mathbf{S} \\
 & \rightarrow \left[\mathbf{V}_b \mathbf{c}_t + \Delta t \mathbf{H}_c \right] \mathbf{p}_{n+1} = \mathbf{V}_b \mathbf{c}_t \mathbf{p}_n
 \end{aligned}$$

Additional source

Figure 5-5 A simple scheme of updating compressibility matrix on FD equation

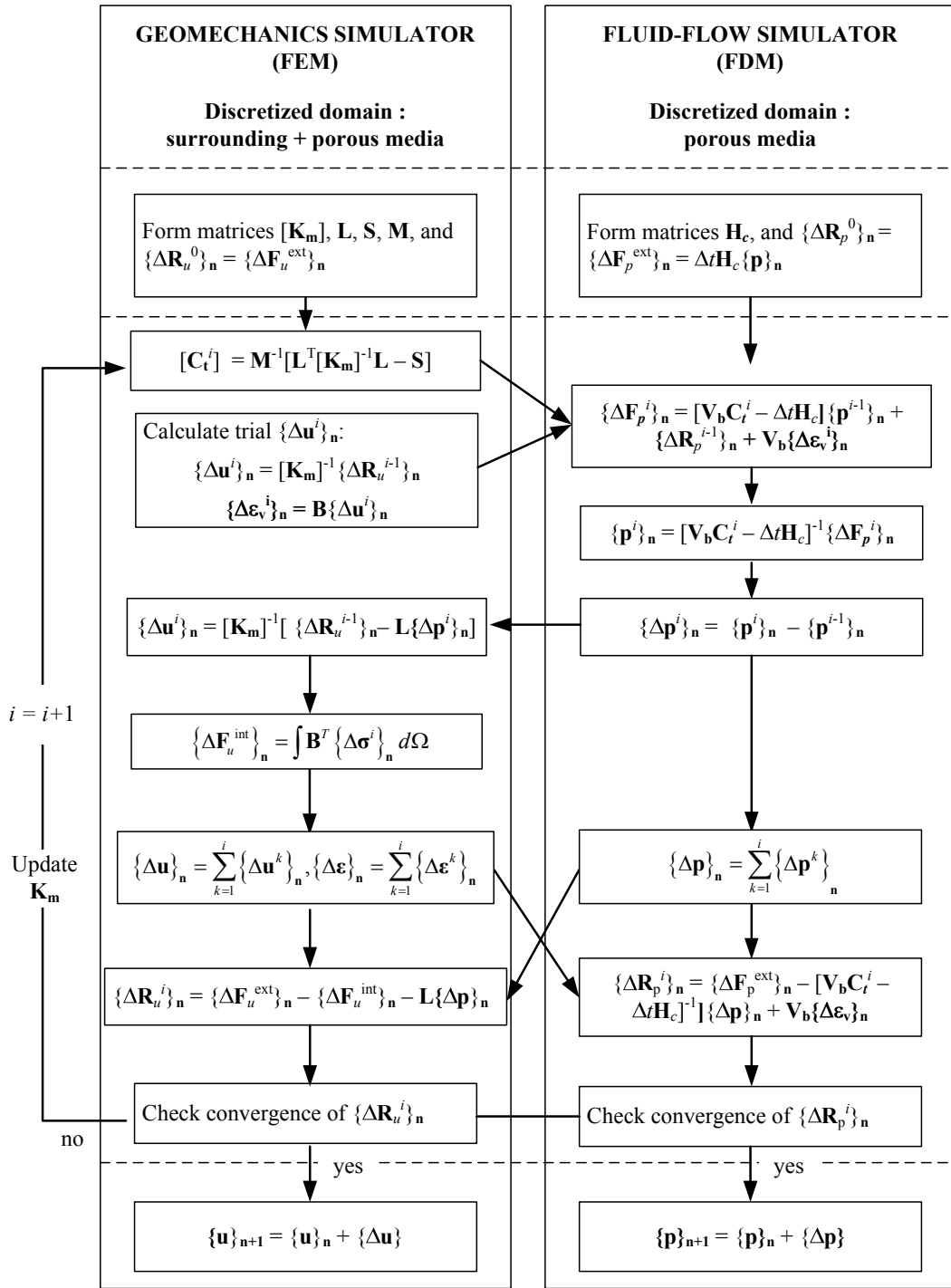


Figure 5-6 A schematic flow charts of geomechanics (FE) – fluid-flow (FD) coupling with incorporation of nonlinear stress-strain analysis

The final FD equation for the fluid-flow simulation is given as:

$$[\mathbf{V}_b \mathbf{c}_t + \Delta t \mathbf{H}_c] \mathbf{p}_{n+1} = \mathbf{V}_b \mathbf{c}_t \mathbf{p}_n + \mathbf{V}_b \Delta \boldsymbol{\varepsilon}_v \quad (5.12)$$

In general, two different grid systems such as a block-centered, and a point-distributed grid are available for the FD method. In a block-centered grid, the dependent variables are calculated at the center of the block and there are no points on the boundary. It is generally used with a Newman-type boundary condition, which specifies flow across the boundary.

Further details of this grid are shown in Figure 5-7.

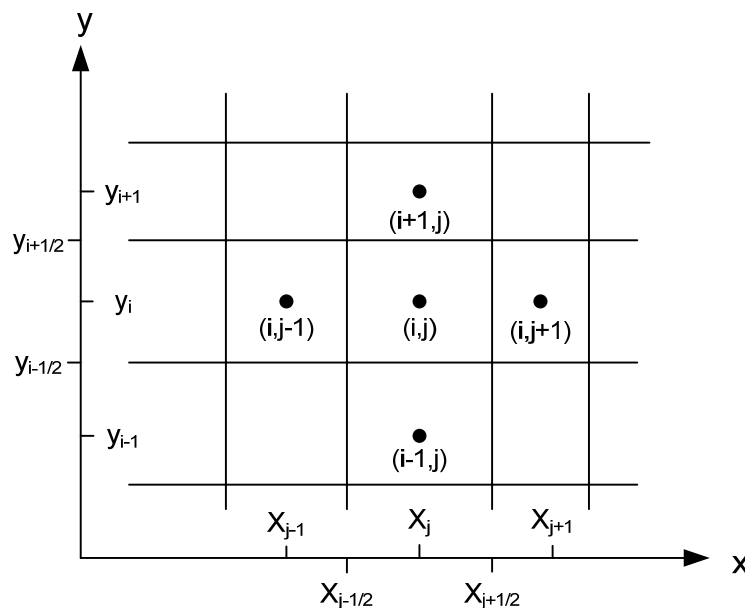


Figure 5-7 Details of block-centered grid for 2D case

In point-distributed grid, the dependent variables are calculated at the intersection of the grid lines and points are located on the boundary. It is generally used for a Dirichlet-type boundary which specifies the values on the boundary. Further details of this grid are shown

in Figure 5-8. In case of impermeable boundary, both grids systems utilize a set of fictitious points located either one half-interval or one interval outside of the rectangular element.

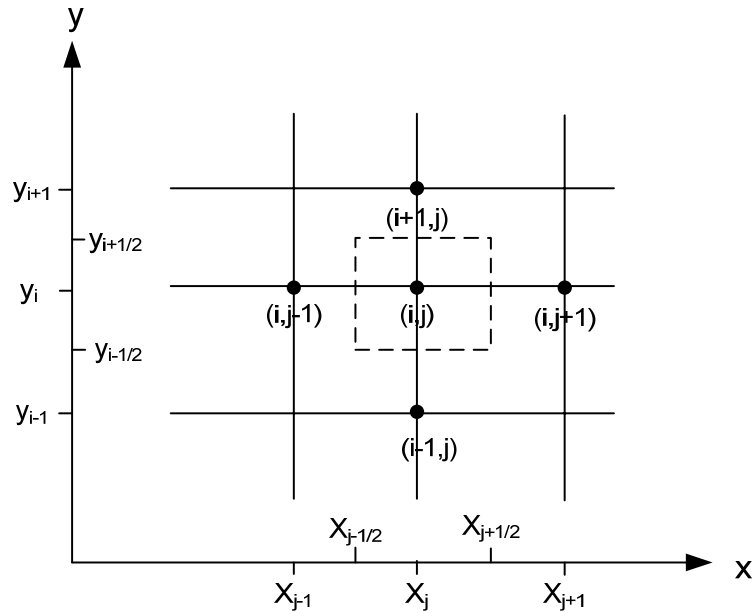


Figure 5-8 Details of point-distributed grid for 2D case

In order to implement the updated full compressibility matrix, both geomechanics (FE) and fluid-flow (FD) need to share nodes over the discretized domain. Figure 5-9 shows possible grid scheme for the modular approach and solid line and dashed line represent FE grid and FD grid, respectively. The left figure shows a simple element sharing scheme (i.e., FE and FD with a block-centered grid system), and the other one shows node sharing grid (i.e., FE and FD with a point-distributed grid system) between geomechanics and fluid flow domain. For the proposed modular approach, the latter is an appropriate domain discretization scheme for the fluid flow analysis because the element sharing scheme, the full-

compressibility matrix from geomechanics model (FE) cannot be implemented into the fluid flow model (FD). For instance, the size of the full compressibility matrix for the 4-nodes quadrilateral single element in FE model is a 4x4 matrix. In case of node sharing grid model, FD model has 4-nodes element and the size of the permeability matrix, \mathbf{H}_c , is 4x4 matrix, too. However, FD model in the element sharing grid has only one node which is scalar while full compressibility matrix from geomechanics model (FE) is still a 4x4 matrix.

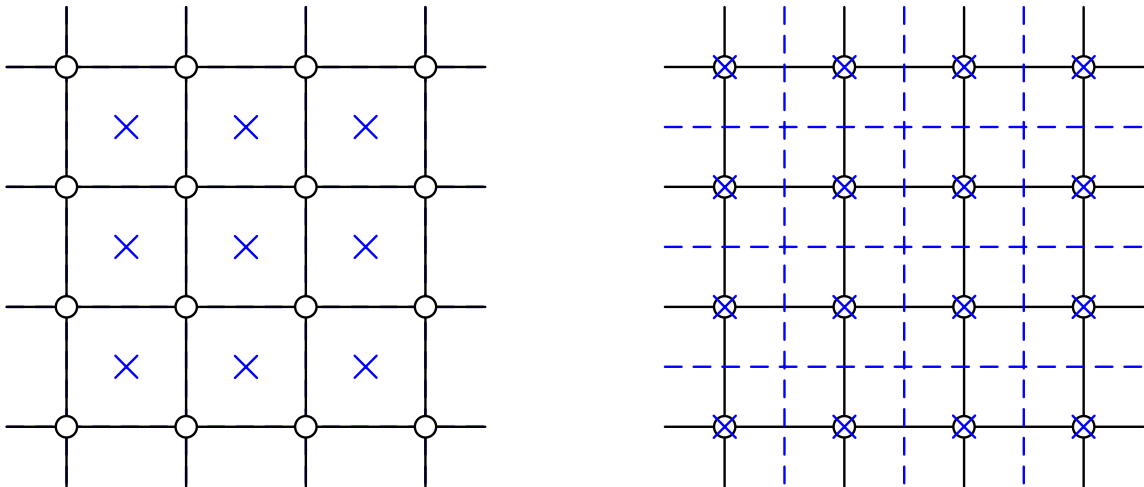


Figure 5-9 Element sharing grid (left) and node sharing grid (right)

5.4.2.1 Mass lumping

In order to implement the full tensorial compressibility matrix into a FD fluid flow simulator, the inverse mass matrix is needed from the geomechanics simulator. The mass matrix, \mathbf{M} , derived from the governing equation is called the consistent mass matrix, and it is symmetric, positive-definite, and non-diagonal. The computational time may be saved by reformulating a mass matrix as a diagonal matrix form. There are several ways of

constructing diagonal mass matrices known as lumped mass matrices. The row-sum and diagonal scaling method are briefly discussed here.

- Row-sum lumping: The sum of the elements of each row of the consistent mass matrix is used as the diagonal element.

$$\mathbf{M}_{ii} = \int_{\Omega} \mathbf{N}_i \rho \mathbf{N}_j d\Omega = \int_{\Omega} \rho \mathbf{N}_i d\Omega \quad (5.13)$$

- Diagonal scaling: The diagonal elements of the lumped mass matrix are proportional to the diagonal elements of the consistent matrix while total mass of the element are conserved.

$$\mathbf{M}_{ii} = \alpha \int_{\Omega} \rho \mathbf{N}_i^T \mathbf{N}_i d\Omega \quad (5.14)$$

$$\text{where } \alpha = \left(\int_{\Omega} \rho d\Omega \right) / \left(\sum_{i=1}^n \int_{\Omega} \rho \mathbf{N}_i^T \mathbf{N}_i d\Omega \right)$$

5.4.3 Porosity coupling

Besides proposed updating compressibility matrix approach based on fully-coupled Biot's theory, iterative coupling is one of the popular methods of incorporating geomechanical effects into the fluid flow equations. In iterative coupling, the geomechanics and fluid flow fields are coupled through coupling terms (e.g., porosity, and permeability) within the iteration for each time step. The biggest advantage is the flexibility and it also enables the use of conventional geomechanical simulator (an FE code) and fluid flow simulator (usually an FD code). Porosity is usually used as the key coupling parameter between the two fields and several different expressions of porosity as a function of pressure, temperature, mean stress, and volumetric strain have been proposed by many researchers

[15-19]. In earlier days, porosity function is based on the pore compressibility which is only applicable for the limited stress path condition. Nowadays, various porosity functions have been published by several researchers [15-17, 19-21]. The simplest formula for porosity is a linear model developed directly from the definition of pore compressibility and the porosity is a function of only the pore pressure as in conventional reservoir simulators. However, more rigorous porosity expression can be obtained as a function of volumetric strain, mean stress, and pore pressure. Various expressions of porosity are shown in the Table 5-1.

Table 5-1 Published porosity expressions

Paper	Porosity expression
Mainguy, M. et al. (2002)	$\Delta\phi = [\phi_0 c_p + (\phi_0 - b)c_s] \frac{\partial p}{\partial t} - b \frac{\partial \epsilon_v}{\partial t}$ $\Delta\phi = \phi_0 c_p \frac{\partial p}{\partial t} - \frac{\partial \phi}{\partial t}$ $\Delta\phi = [\phi_0 (c_p + c_s) - bc_b] \frac{\partial p}{\partial t} - (c_b - c_s) \frac{\partial \sigma_m}{\partial t}$
Settari, A. et al. (2005)	$\phi = \phi_0 [1 + c_R (p - p_0)]$
Chin, L. et al. (2003)	$\phi = \phi_0 + (e^{\epsilon_v} - 1)$
Tran, D. (2004)	$\phi_{n+1} = \phi_n + \phi_0 c_p \Delta p + \Delta \Phi_l$ $c_p = \frac{c_\phi (1 - \epsilon_v) + (c_b - c_s) \phi_n}{\phi_0}$ $c_\phi = c_b (1 - \phi_n) - c_s$ $\Delta \Phi = -[c_\phi (1 - \epsilon_v) + c_b \phi_n] \Delta \sigma_m$

where b is a Biot's coefficient $\left(1 - \frac{K_d}{K_s}\right)$, c_p is a pore compressibility $\left(= \frac{1}{\phi_0} \frac{\partial \phi}{\partial p}\right)$, c_s is a solid grain compressibility $\left(= \frac{1}{K_s}\right)$, c_b is a drained compressibility $\left(= \frac{1}{K_d}\right)$, c_R is a rock compressibility, and it is explicitly calculated by assuming a specific stress-strain path.

In this chapter, a new porosity formulation presented and it is based on the fully-coupled Biot's theory and it will be developed in appropriate formulation to apply to the iterative coupling scheme. In order to develop the porosity formulation, the linkage between the continuity equations between conventional reservoir simulator and fully-coupled system need to be investigated. A single-phase continuity equation in the conventional reservoir simulator assuming no fluid density change as:

$$\nabla \cdot \left[\frac{K_{ij}}{\mu} \nabla (p - \rho_f gh) \right] + q = \frac{\partial \phi}{\partial t} \quad (5.15)$$

A single-phase continuity equation based on the Biot's theory assuming no fluid density change as:

$$\nabla \cdot \left[\frac{K_{ij}}{\mu} (\nabla p - \rho_f gh) \right] + q = \left(\delta_{kl} - \frac{\delta_{ij} D_{ijkl}}{3K_s} \right) \frac{\partial \varepsilon_{kl}}{\partial t} + \left(\frac{\phi}{K_f} + \frac{1-\phi}{K_s} - \frac{\delta_{ij} D_{ijkl} \delta_{kl}}{(3K_s)^2} \right) \frac{\partial p}{\partial t} \quad (5.16)$$

The main idea of this partially-coupled scheme is to change porosity expression in the conventional reservoir simulator with that of fully-coupled equation. Equalizing the right-hand side of both continuity equation (5.15) and (5.16) yields:

$$\frac{\partial \phi}{\partial t} = \left(\delta_{kl} - \frac{\delta_{ij} D_{ijkl}}{3K_s} \right) \frac{\partial \varepsilon_{kl}}{\partial t} + \left(\frac{\phi_0}{K_f} + \frac{1-\phi_0}{K_s} - \frac{\delta_{ij} D_{ijkl} \delta_{kl}}{(3K_s)^2} \right) \frac{\partial p}{\partial t} \quad (5.17)$$

After a discretization of equation (5.17), an updated porosity expression in terms of pore pressure and strain variations is:

$$\Delta\phi = \left(\mathbf{m}^T - \frac{\mathbf{m}^T \mathbf{D}}{3K_s} \right) \Delta\varepsilon + \left[\frac{\phi_0}{K_f} + \frac{1-\phi_0}{K_s} - \frac{1}{(3K_s)^2} \mathbf{m}^T \mathbf{D} \mathbf{m} \right] \Delta p \quad (5.18)$$

Simple flow chart for partial coupling is shown in Figure 5-10. Reservoir simulator calculates pressures in a required number of iterations and these pressures are sent to the geomechanical simulator for the calculation of displacements as well as stresses/strains. These updated stresses and strains with pore pressure values are used to update the porosity. New pore pressures can be calculated using the updated porosity and steps are repeated until convergence is achieved. During the iteration, approximated pore pressure values (i.e., \mathbf{p}^1 , and $\Delta\mathbf{p} = \mathbf{p}^1 - \mathbf{p}^0$, where the superscripts 1 and 0 refer to two successive iterations) is used to calculate displacement increments (i.e., $\Delta\mathbf{u}$) and strain increments (i.e., $\Delta\varepsilon$) in the geomechanics simulator. Then porosity increment (i.e., $\Delta\phi$) is calculated based the equation (5.18). Updated pore pressure values can be calculated using the updated porosity ($\phi^1 = \phi^0 + \Delta\phi$) in the reservoir simulator, and this procedure continues until convergence is achieved. The convergence can be checked by taking the norm of $\mathbf{p}^{i+1} - \mathbf{p}^i$.

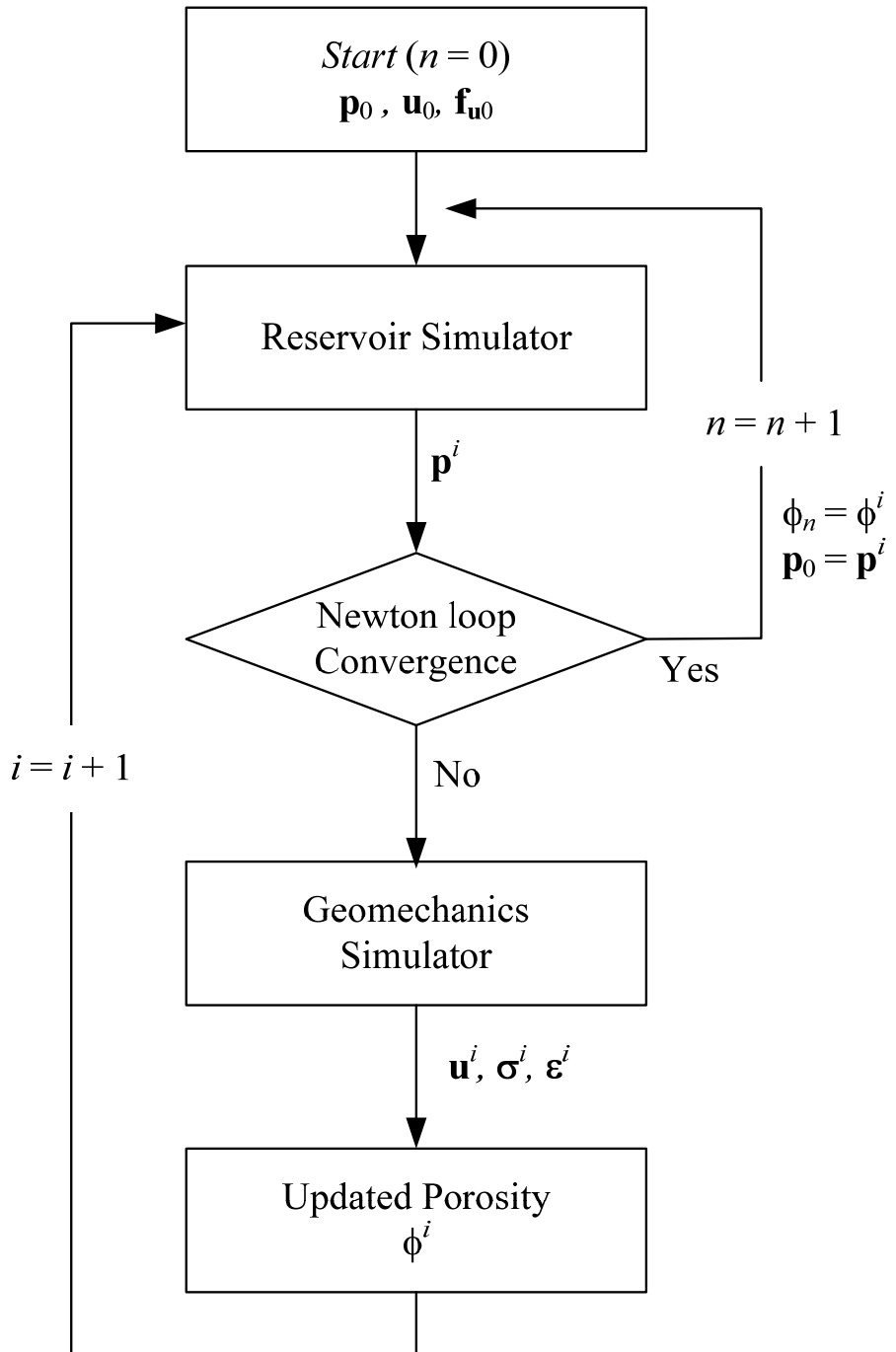


Figure 5-10 Flow chart of partially-coupled analysis

It can be noted that the equation (5.15) is a nonlinear problem because the pressure values on the left hand side is dependent on the porosity values on the right hand side even for the single-phase flow. In order to solve nonlinear problem in the fluid flow simulation, a special solution technique is needed. The Finite Difference discretized nonlinear system of equations given by equation (5.15) can be written as:

$$\mathbf{F}^{n+1} = \mathbf{H}_c \mathbf{p}^{n+1} - \frac{1}{\Delta t} [\phi^{n+1} - \phi^n] = 0 \quad (5.19)$$

A nonlinear system of equations of the form given above may be solved by Newton's method [22] as defined below:

$$\mathbf{p}^i = \mathbf{p}^{i-1} - [\mathbf{J}^{i-1}]^{-1} \mathbf{F}^{i-1} \quad (5.20)$$

where \mathbf{J} is the Jacobian matrix of the vector function of \mathbf{F} :

$$\mathbf{J}^i = \left(\frac{\partial \mathbf{F}}{\partial \mathbf{p}} \right)^i = \mathbf{H}_c - \frac{1}{\Delta t} \left[\frac{\partial \phi^i}{\partial \mathbf{p}^i} - \frac{\partial \phi_n}{\partial \mathbf{p}^i} \right] \quad (5.21)$$

and it is the vertical extension of derivative used in the classical Newton's method for single equation.

Insert equation (5.16) and (5.21) into equation (5.20) leads;

$$\mathbf{p}^i = \mathbf{p}^{i-1} - \left[\mathbf{H}_c - \frac{1}{\Delta t} \left[\frac{\partial \phi^{i-1}}{\partial \mathbf{p}^i} - \frac{\partial \phi_n}{\partial \mathbf{p}^i} \right] \right]^{-1} \left[\mathbf{H}_c \mathbf{p}^{i-1} - \frac{1}{\Delta t} [\phi^{i-1} - \phi_n] \right] \quad (5.22)$$

Equation (5.22) is implemented in the fluid flow simulator in Figure 5-10. In case of the linear stress-strain constitutive model in the geomechanics simulator, Newton's method

shows fast convergence and modular approach based on the porosity coupling can be achieved (e.g., Mandel's problem is solved using porosity coupling and it is shown in the following section). However, in case of analyzing strain hardening/softening elasto-plastic constitutive model in the geomechanics simulators, Newton method in the fluid flow simulator may not converge. For example, calculated pore pressure vector, \mathbf{p}^1 , equals zero ($\frac{\partial \phi^0}{\partial \mathbf{p}^i} = \frac{\partial \phi_n}{\partial \mathbf{p}^i}$, and $\phi^0 = \phi_n$) in the first iteration. It causes pore pressure increment to the same magnitude as initial pore pressure value except negative sign and those pore pressure increments leads effective stress increase. Then geomechanics simulator calculates displacements and volumetric strains (e.g., porosity) based on the effective stresses increments, and that information is sent back to the fluid flow simulator. On the next iteration, the fluid flow simulators calculates pore pressure values somewhere between initial value and first iteration (i.e., increment pore pressure is positive for the pore pressure dissipation case, $0 < \mathbf{p}^2 < \mathbf{p}^1$) and it causes decrease effective stresses. In the geomechanics simulator, decrease effective stresses lead the unloading condition along the stress-strain path. Since it follows unloading stress-strain path, calculated displacements and strains (i.e., porosity) are not correct. Therefore, more rigorous numerical algorithms in the fluid flow simulator are required to implement the porosity coupling techniques otherwise, special treatment in the geomechanics simulator is necessary for the analysis of the stress hardening/softening constitutive model in the geomechanics simulator.

5.5 Code Validations and Applications

In order to test the various solution techniques described above, five problems are solved in the following sections. Because not all of problems have analytical or closed-form solutions, results of several problems are compared with available numerical solution or experimental results. Table 5-2 summarizes the important elements of each problem.

Table 5-2 Summary of test problems

Problem	Problem type	Constitutive relation	Fluid flow type	Coupling solution techniques	Available solution
Simplified Ekofisk Field	Pressure extraction	Linear elastic	Single-phase	Monolithic Partitioned	Numerical
Mandel (1953)	Consolidation	Linear elastic	Single-phase	Monolithic Modular (FE-FE & FE-FD, porosity coupling)	Closed-form
Schiffman et al. (1969)	Consolidation	Linear elastic	Single-phase	Modular (FE-FE & FE-FD)	Closed-form
Borja (1991)	Consolidation	Linear elastic Elasto-plastic	Single-phase	Modular (FE-FE & FE-FD)	Numerical
Liakopoulos (1965)	Water drainage	Linear elastic	Two-phase	Monolithic Modular (FE-FE)	Experimental data

5.5.1 Simplified model of the Ekofisk Field subsidence

Over several years from 1971 up to the present, the Ekofisk field, a rich oil field in the Norwegian sector of the North Sea, has been under production. The Ekofisk reservoir is known as a compaction drive reservoir in that the basic mechanism controlling the reservoir pressure, and consequently the production rate, is the compaction of the producing

formation. The compaction is also transferred to the overburden layers where it causes seabed subsidence. Discussions of the issues related to the interaction between rock deformation and multiphase fluid flow behavior in the Ekofisk reservoir and comparisons between coupled and uncoupled analyses of the Ekofisk reservoir are presented by Gutierrez [23, 24].

In this study, the efficiency in terms of computational efforts of monolithic and partitioned methods with various solution techniques (e.g., CG, MINRES, and BiCG) is compared. The FE simulations have been performed for a 14 years production by specifying prescribed pressures in the Finite Element nodes corresponding to the production wells within the reservoir. Initial pore pressure values for the whole region are 48 MPa and the prescribed pressure for the production wells is 24 MPa with assumption that pressure is controlled during the production over 14 years. A simplified West-East cross-section of the Ekofisk through the approximate center of the field is shown in Figure 5-11 is analyzed with 612 Q4 isoparametric elements for displacements and pore pressure values. The geometry is based on Gutierrez [23]. The total number of time steps used in the simulations is 140 and the material properties used in the simulation are shown in Table 5-3.

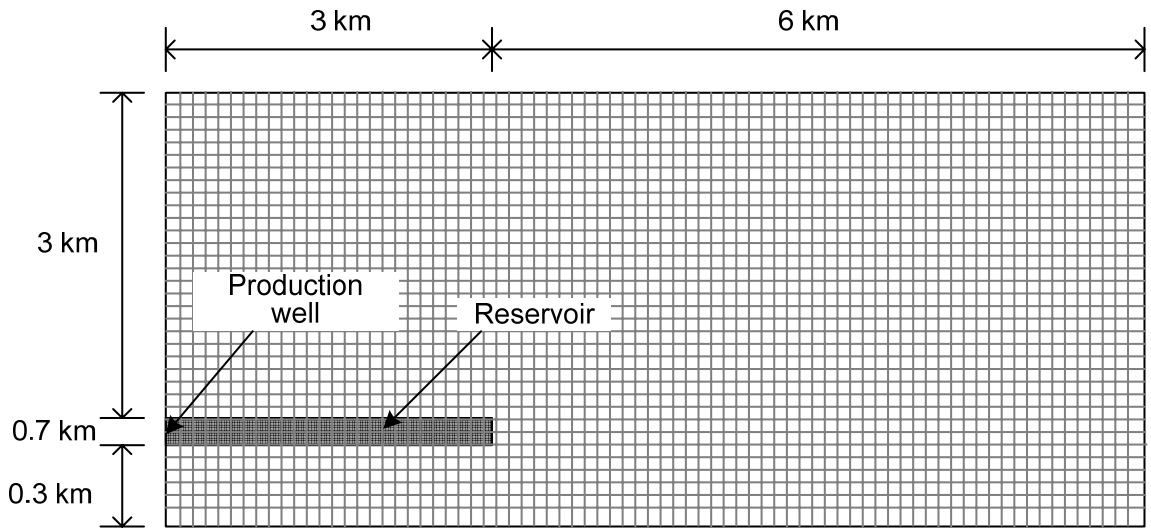


Figure 5-11 Simplified 2D FE model of West-East section of the Ekofisk Field

Table 5-3 Material properties of simplified Ekofisk problem

Property	Surrounding rock	Reservoir rock
Young's modulus, E (GPa)	2.5	0.05
Poisson's ratio,	0.45	0.25
Absolute permeability, k (md)	0	150

Rock displacements after 14 years of production and pore pressure profiles calculated along the center of the reservoir are shown in Figure 5-12 and Figure 5-13 respectively. The calculated maximum subsidence is about 6 m and it is worth noting that the pore pressure increased near the reservoir flanks to about 52 MPa, which is higher than the initial pressure of 48 MPa despite continuous production. This result is close to that from Gutierrez [23], which involved a fully coupled simulation taking into account porosity and pore compressibility as stress dependent components in the reservoir simulation.

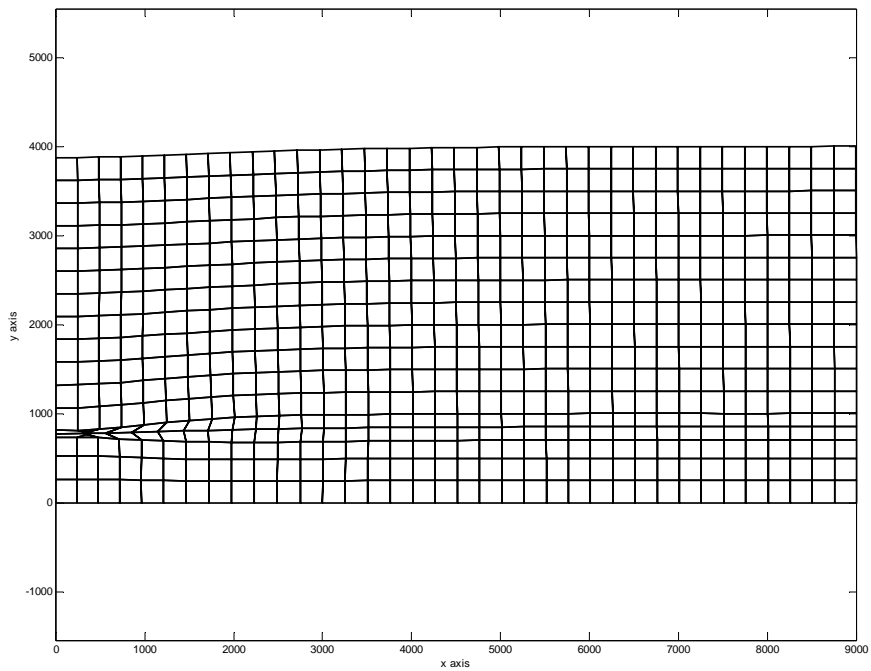


Figure 5-12 Rock deformations after 14 years production magnified 20 times

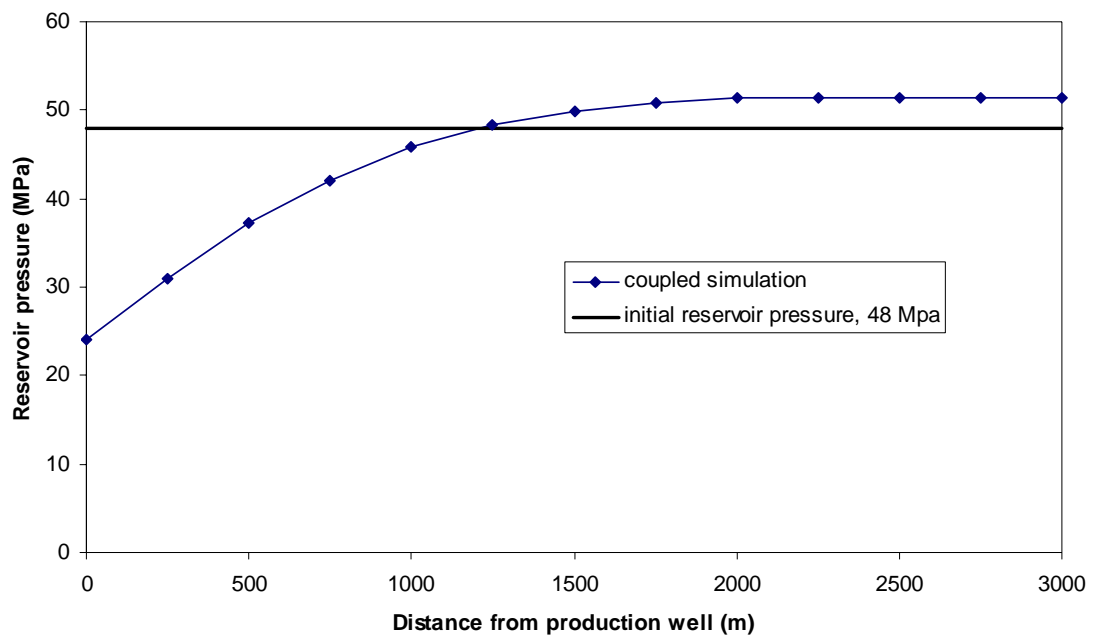


Figure 5-13 Reservoir pressures profile after 14 years

A summary of the comparison of different solution techniques is shown in Table 5-4. The same number of time steps was used for all methods, and the tolerance for the all iterative methods was set to 10^{-3} . As can be seen from the table, the different methods produced nearly identical results and the partitioned CG method was most efficient method for the simulation in terms of the computational cost (i.e., least time consuming for the simulation). Pre-conditioners were not used in the simulations.

Table 5-4 Comparison among different solution techniques for the simplified Ekofisk case

Result	Monolithic Method	Partitioned Direct method	Partitioned CG method	Partitioned MINRES method	Partitioned BiCG method
Max. surface subsidence (m)	5.915	5.915	5.915	5.9150	5.9149
Max. pore pressure in the reservoir (MPa)	51.49	51.49	51.491	51.491	51.491
No. of time step	140	140	140	140	140
Tolerance (δ_{tol})	n/a	n/a	10^{-3}	10^{-3}	10^{-3}
Total no. of iteration	n/a	n/a	5675	13798	5821
Average no. of iteration for each time step	n/a	n/a	40.5	98.6	41.6
Elapse time for the simulation (sec.) *	552	566	431	17600	14407

- Single machine with CPU of Intel Pentium4 3.0 GHz and 1GB of ram memory were used for FE simulations.

5.5.2 Mandel's problem

The original Mandel's problem, as described in Chapter 2, is solved using various solution methods including the monolithic method, the modular approach by updating compressibility, and porosity coupling. The results are compared with analytical solution given in [25, 26]. Problem descriptions are identical to the one given in Chapter 2 and an elastic impermeable layer with relatively high modulus (e.g., modulus ratio between the overburden and the saturated porous media is 10^7) is placed on the top of a permeable porous media. Figures 5-14 and 5-15 show the Finite Element meshes for the numerical analyses. It can be noted that fluid flow simulation in the modular approaches (e.g., methods based on pore compressibility updating and porosity coupling) only requires a discretized domain for a permeable porous material.

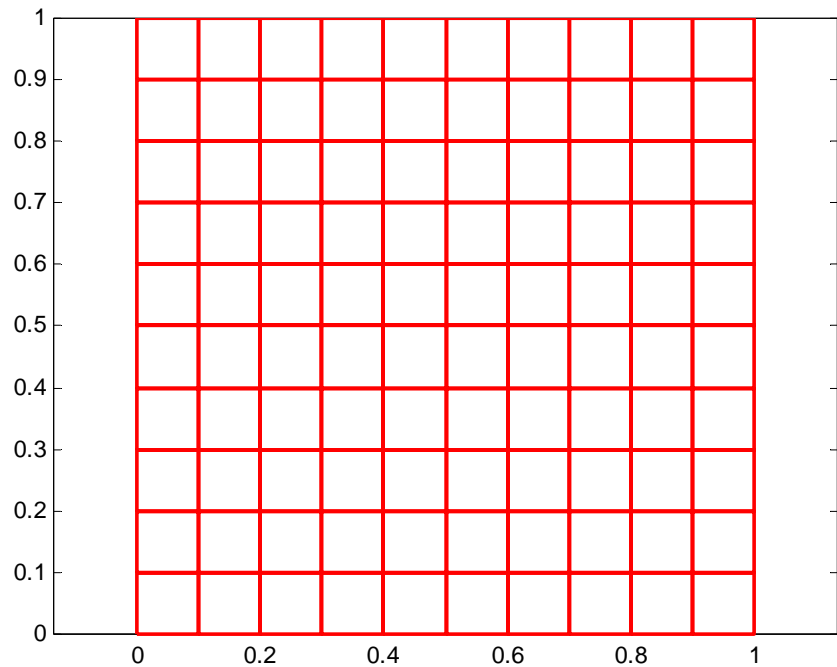


Figure 5-14 FE mesh for the geomechanical domain of a partitioned solution method and the full domain of a monolithic solution method

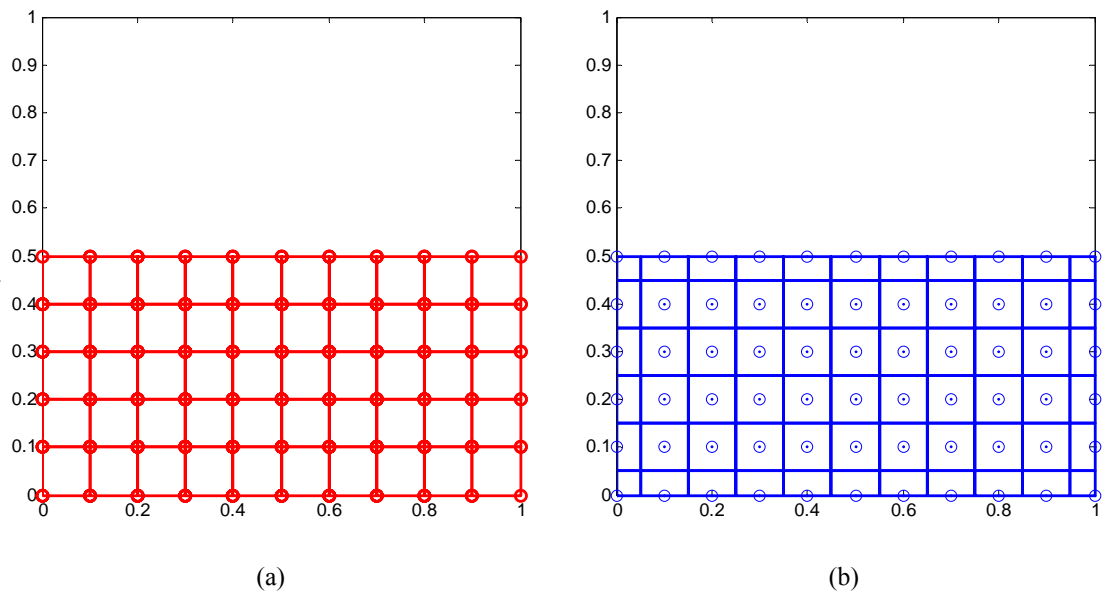


Figure 5-15 Meshes for the fluid-flow domain (i.e., permeable porous media); (a) Finite Element, and (b) Finite Difference

In order to generate the most pronounced Mandel-Cryer effect, the Poisson's ratio is set to zero for this problem. Figure 5-16 shows the pore pressure profiles at the center of the permeable porous material as function of time from the analytical and numerical solutions. Figure 5-17 presents the pore pressure profiles along the center line of the permeable porous media with different time. As can be seen, all tested solution methods show good agreements with analytical solution. Discrepancies between analytical solution and numerical solutions can be reduced by refining the mesh, and/or using smaller time steps. In this specific problem, the most efficient solution method in terms of computational time is the FE-FE modular solution method because a constant stiffness matrix to a constant compressibility matrix in case of linear stress-strain relation. Porosity coupling required the most computational time because it requires iterations for porosity calculations and updates in every time step.

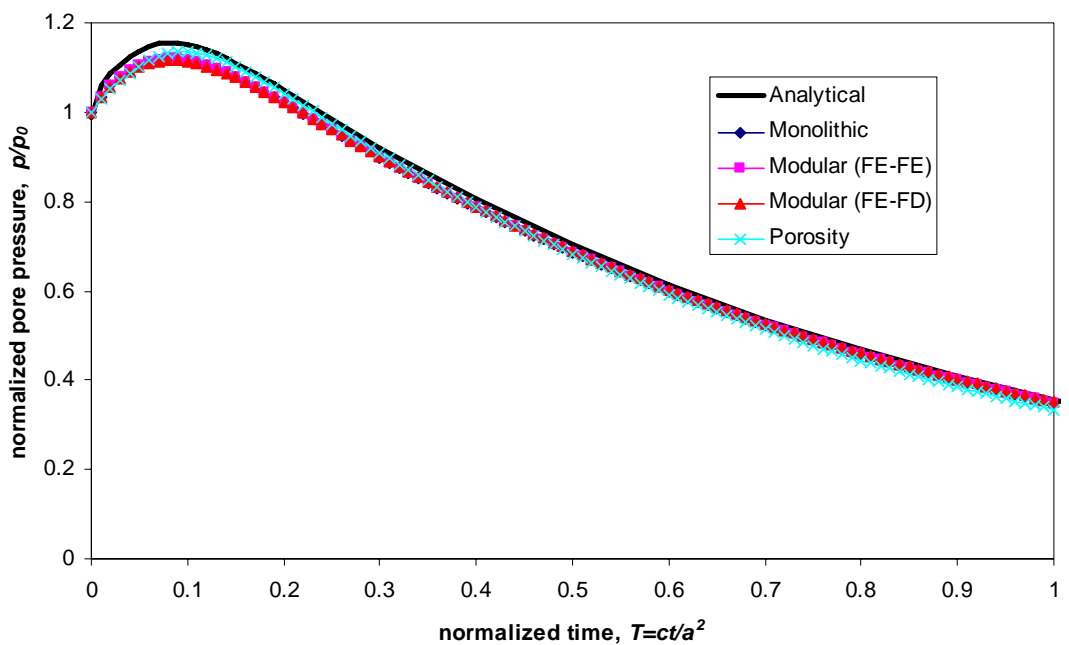
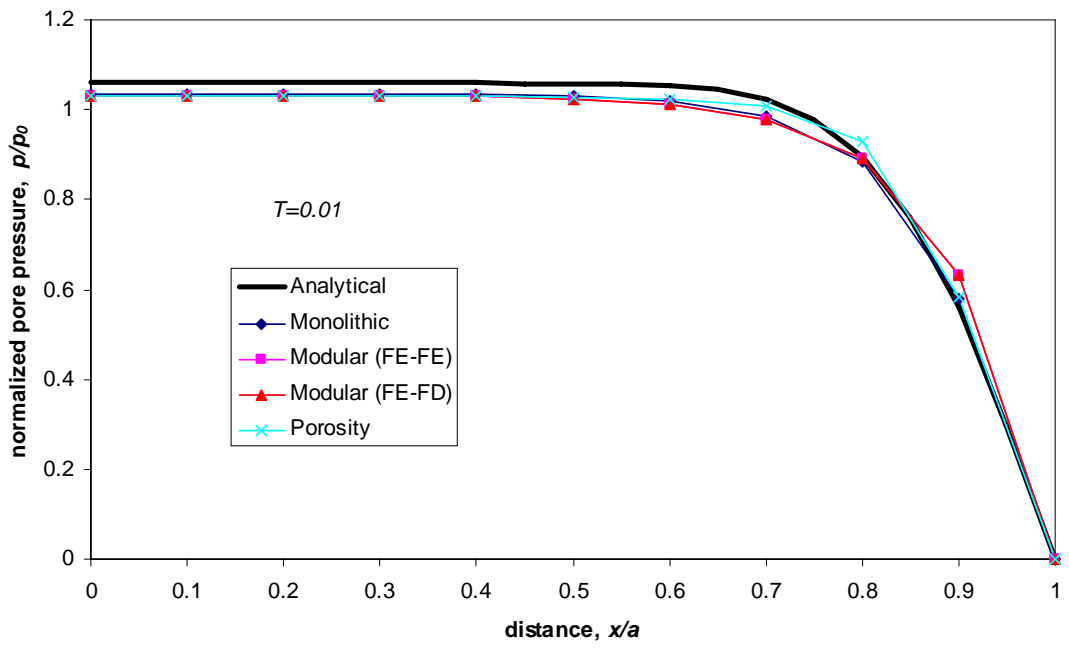


Figure 5-16 Pore pressure profile at point 'A'



(a)

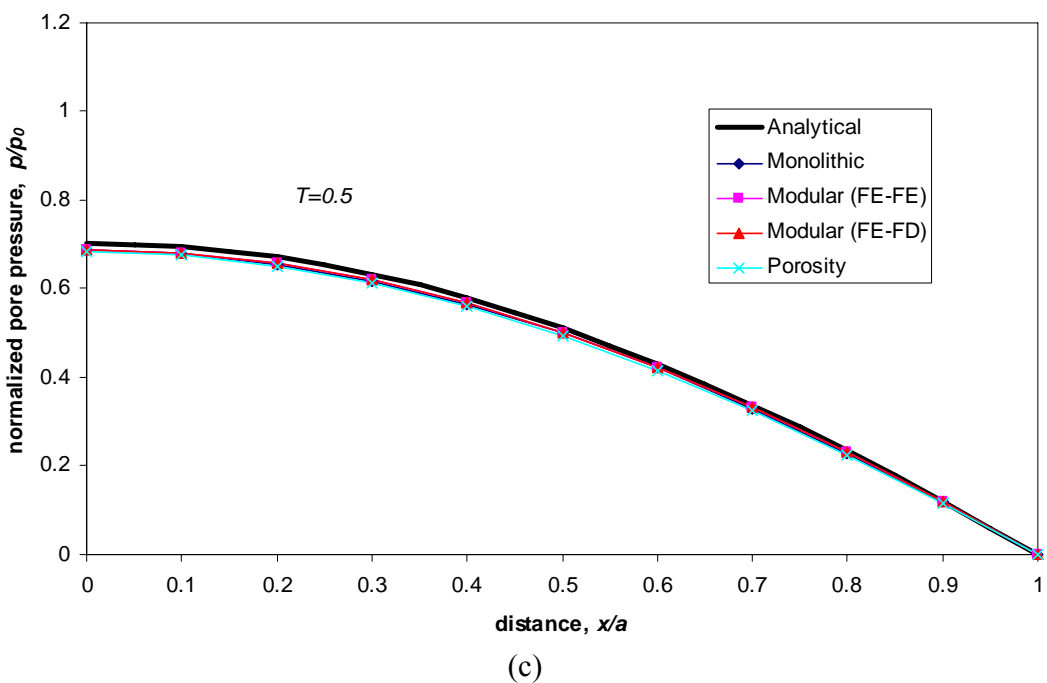
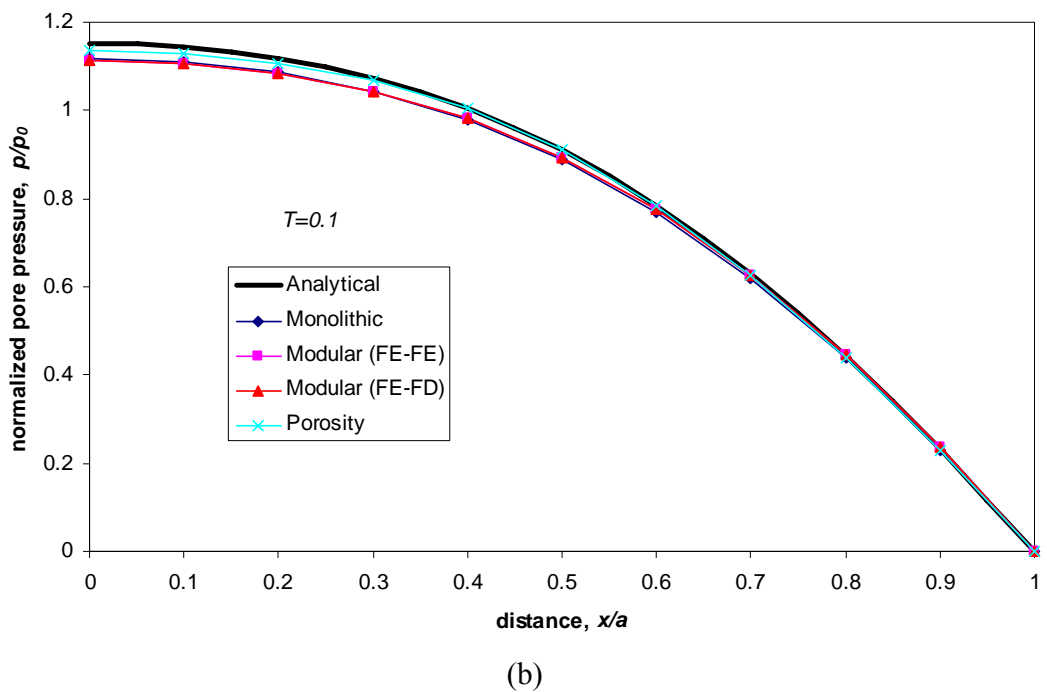


Figure 5-17 Pore pressure distributions along horizontal line; (a) $T=0.01$, (b) $T=0.05$, and (c) $T=0.5$

5.5.3 Linear elastic consolidation by Schiffman et al.

Schiffman et al. [27] proposed a closed-form solution for the plane strain consolidation problem of an elastic half-space subjected to a uniform strip load. To test the numerical procedures, numerical simulations were carried out for a strip load of $w=120$ kPa applied instantly during $\Delta t=1$ day at the ground surface (i.e., it can be assumed that the load is applied instantaneously since $\Delta t=1$ is small compared to $t=10,000$ days required to reach complete consolidation). The load is then held constant while the soil consolidates. Figure 5-18 gives a brief description of the problem. Soil behaves as linear elastically and the material properties used in the numerical simulation are shown in Table 5-5. The soil elements are assumed to be initially stress-free. A normalized time factor $T = ct/a^2$, where $c = 2Gk/\gamma_w$, G is the shear modulus, and t is the elapsed time since the beginning of the consolidation and it is used to describe the solution in the time domain. Figure 5-19 shows the mesh for the numerical analysis. Figure 5-20 shows the excess pore pressure profile of point ‘A’ as function of time. It can be noted that both the closed-form and numerical solutions exhibit the Mandel-Cryer effect which is a characteristic feature of the fully-coupled solution. The numerical solutions agree with the closed-form solution, but they are not identical particularly at the early time of the consolidation because of: 1) the limitation of the numerical models to represent an infinite half-space, 2) Differences in solution approaches between FE and FD methods, and 3) the use of a finite time increment to impose the embankment load, among other factors. Figure 5-21 illustrates the isochrones of excess pore pressure along the center line at different times. It can be noted that the FE-FD

modular solution produces larger pore pressure values at the early time of drainage in comparison with FE-FD modular solution.

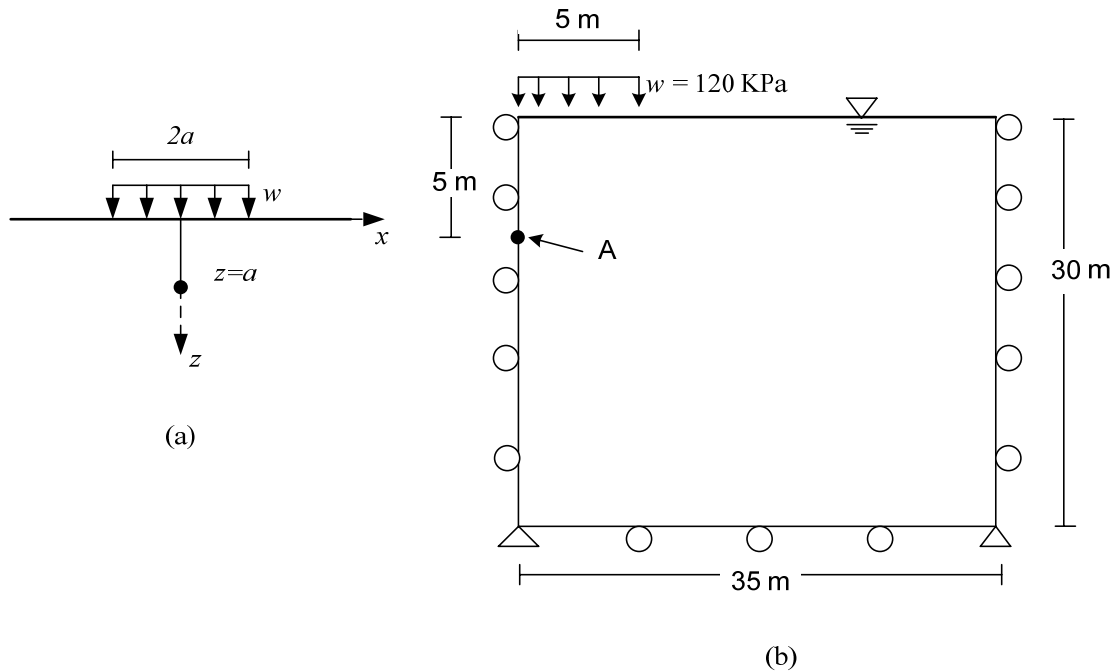


Figure 5-18 Plane strain linear elastic consolidation; (a) Normally loaded half-plane, and (b) Numerical model with boundary conditions

Table 5-5 Numerical input for the linear elastic consolidation problem

Parameter	
E (Young's modulus)	500 kPa
ν (Poisson's ratio)	0
k_{11} , and k_{22} (isotropic soil permeability, $k_{12}=k_{21}=0$)	8.64×10^{-4} m/day
w (strip load)	120 kPa
Δt (time step)	1 day

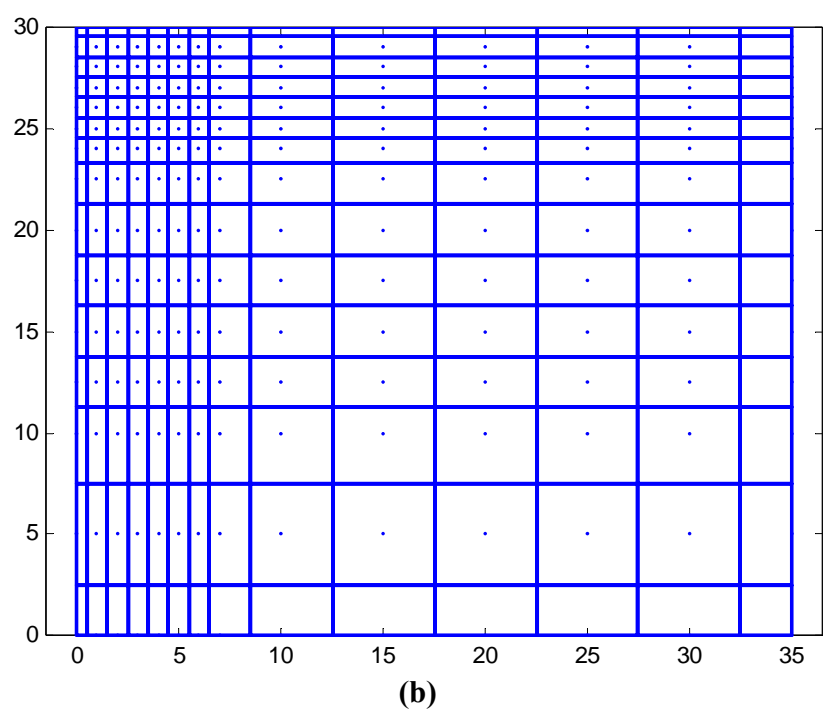
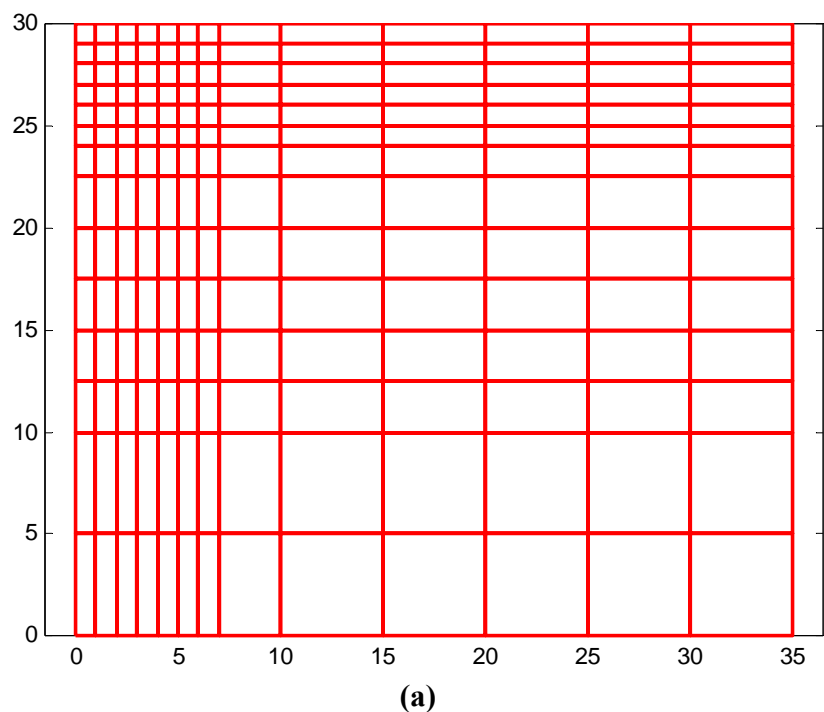


Figure 5-19 Meshes for numerical analysis; (a) FEM, and (b) FDM

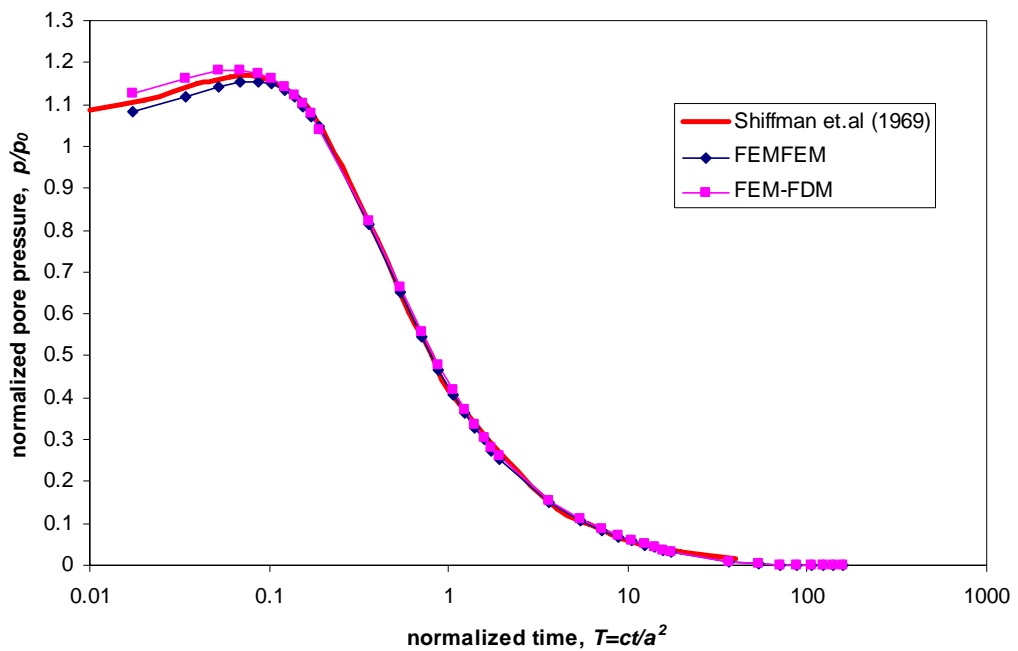


Figure 5-20 Excess pore pressure variation of center line at depth $z=a$ with time

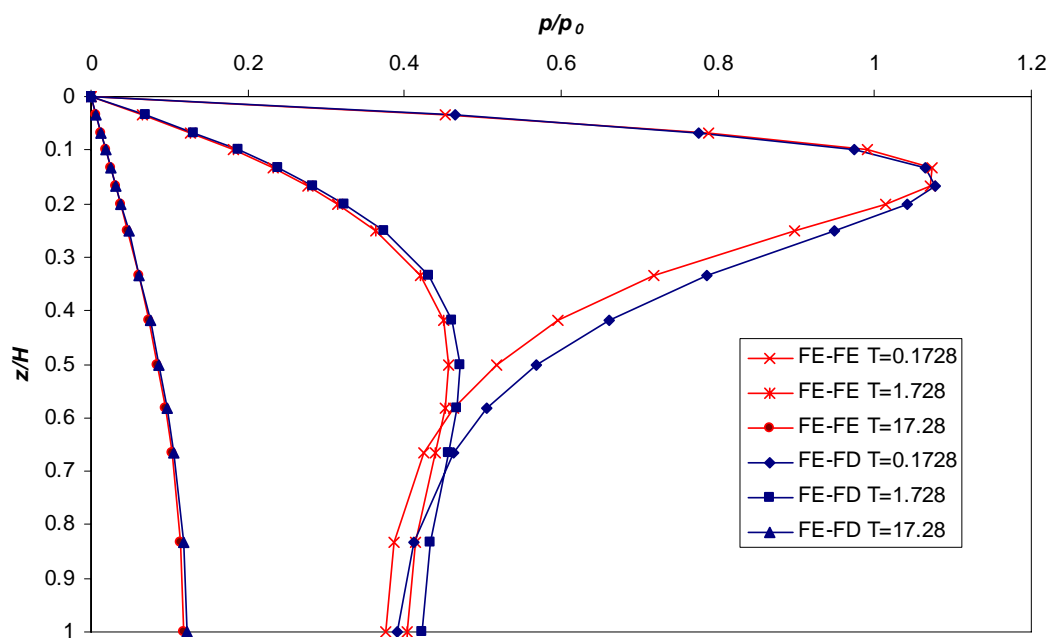


Figure 5-21 Isochrones of excess pore pressure along center line

5.5.4 Borja's example consolidation problem

Borja [28] proposed a linear multi-step method to solve the non-linear stress-strain case in a fully-coupled system as well as the linear stress strain case. In this chapter, a two-dimensional flexible strip footing on a porous soil under plane strain condition is analyzed for linear elastic and elasto-plastic materials. The strip load is applied linearly with time over a period of T_0 as shown in Figure 5-22. Drainage is assumed to occur at the ground surface. The exact solution to this semi-discrete problem is not available in closed form even for the linear case. Therefore, numerical results are compared to the ones from Borja's. The discretizations used for the numerical analyses are shown in Figure 5-23.

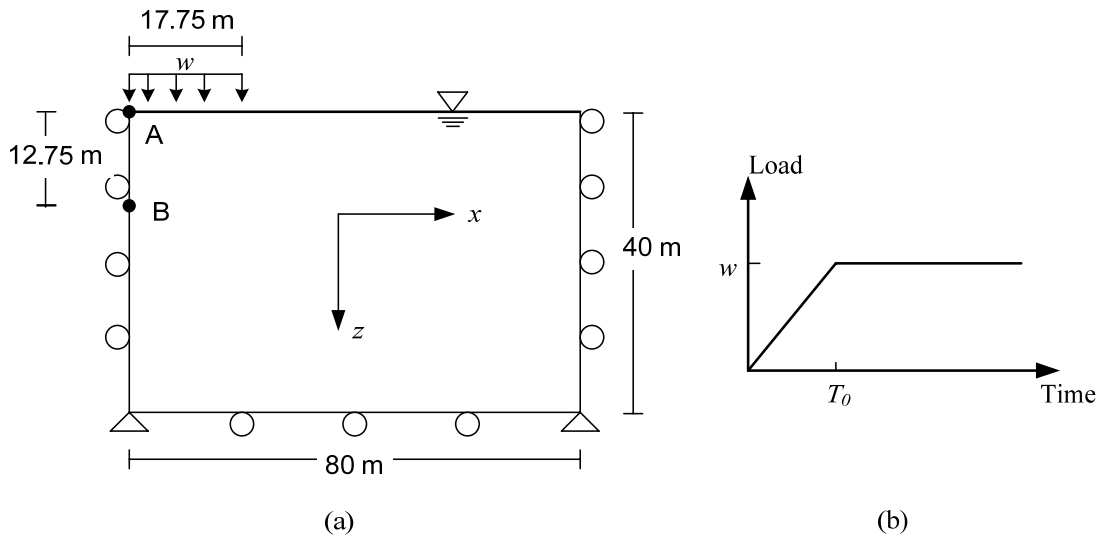
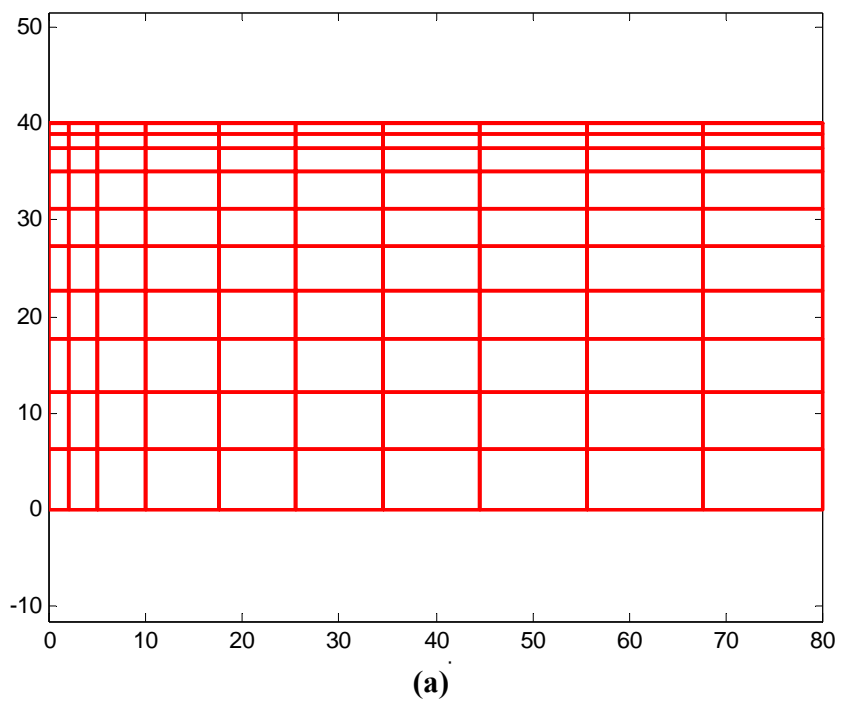
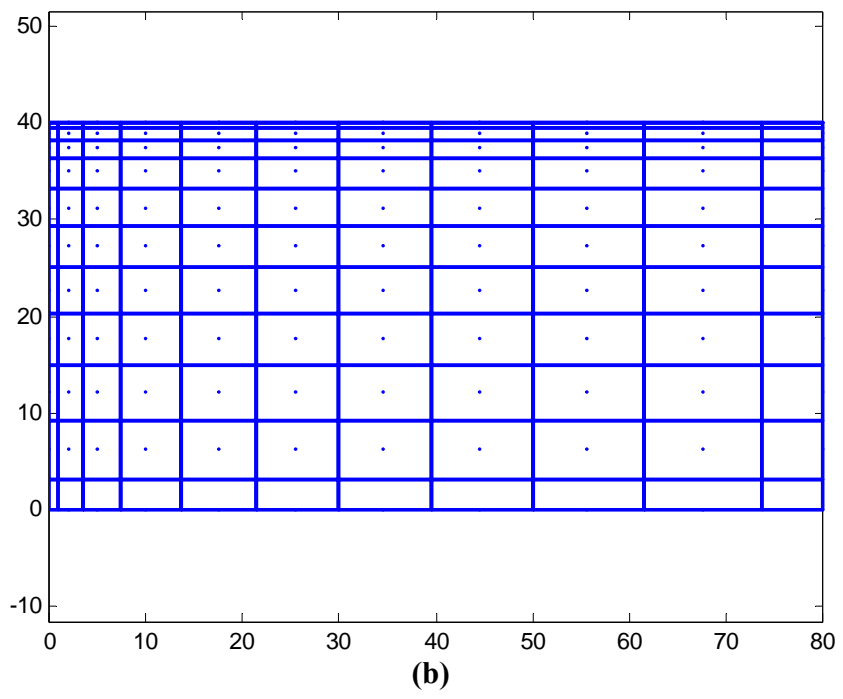


Figure 5-22 Illustration of consolidation problem in Borja's paper; (a) Geometry for linear elastic and elasto-plastic consolidation problem, and (b) Load application scheme



(a)



(b)

Figure 5-23 Meshes for numerical analysis; (a) FE, and (b) FD

- **Linear elastic consolidation**

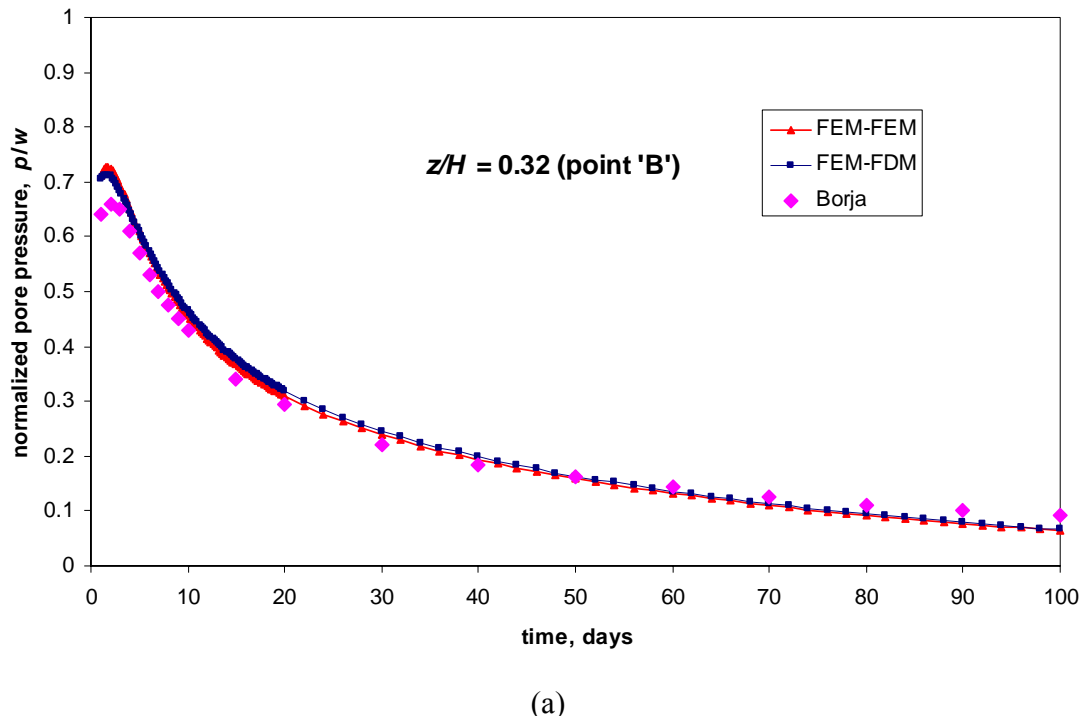
In this problem, the soil skeleton is assumed to be a linearly elastic material and all elements are assumed to be initially stress-free. A strip load is applied linearly with time over a T_0 . The model parameters used are listed in Table 5-6.

Table 5-6 Model parameters for the linear elastic consolidation problem

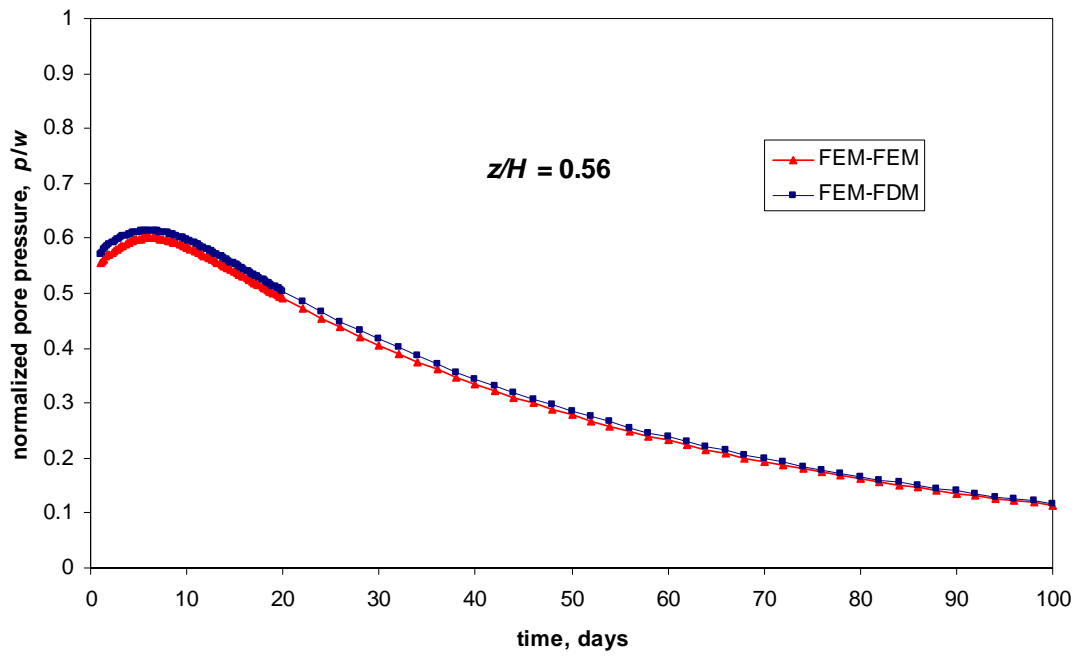
Parameter	
E (Young's modulus)	10^4 kPa
ν (Poisson's ratio)	0
k_{11} , and k_{22} (isotropic soil permeability, $k_{12}=k_{21}=0$)	0.01 m/day
w (strip load)	10^3 kPa
T_0 (time for linear strip load)	1.0 day
Δt (time step)	0.2 day

Excess pore pressure profiles at various depths are presented in Figure 5-24. Borja's result is only available at point 'B' ($z/H = 0.32$) and it can be seen that Borja's result shows smaller initial pore pressure values from the external lamp load than the proposed modular approaches solutions. However, results from FE-FE and FE-FD methods are in good agreement with Borja's results in general. Differences among solutions are attributed to: 1) different FE elements used (i.e., Borja uses 8-node serendipity elements), and 2) Inaccurate measurement of location for point 'B' since exact depth is not available in the published paper. It can be noted that magnitude of Mandel-Cryer effects are more significant (i.e., p/p_0 where p_0 is excess pore pressure after external load), and the peak of pore pressure increases at slower rate with increasing depth. These differences can be explained by the

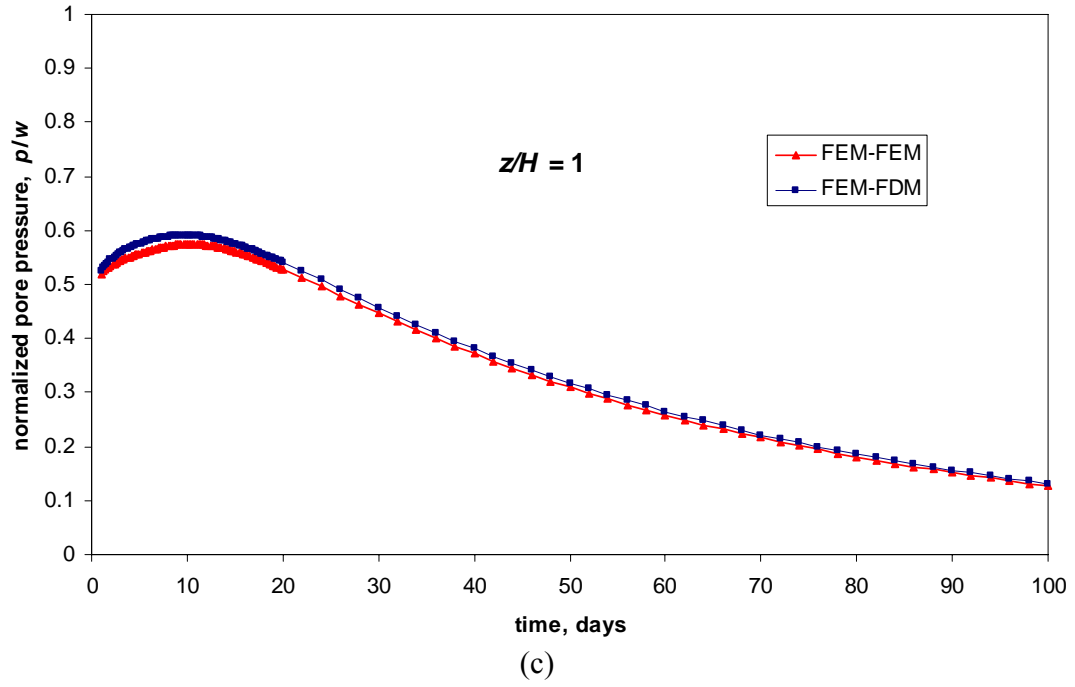
stiffness effects of overburden and drainage length since more pronounced Mandel-Cryer effects are expected as the overburden stiffness is increased. Settlement profile is shown in Figure 5-25 with Borja's results and it predicts larger settlements than the ones from modular approaches. The differences may be due to inaccurate plotting of the results from Borja since it exceeds fully-drained settlement (e.g., uncoupled solution). Final deformed meshes are presented in Figure 5-26.



(a)



(b)



(c)

Figure 5-24 Pore pressure profiles of various depths; (a) $z/H=0.32$, (b) $z/H=0.56$, and (c) $z/H=1$

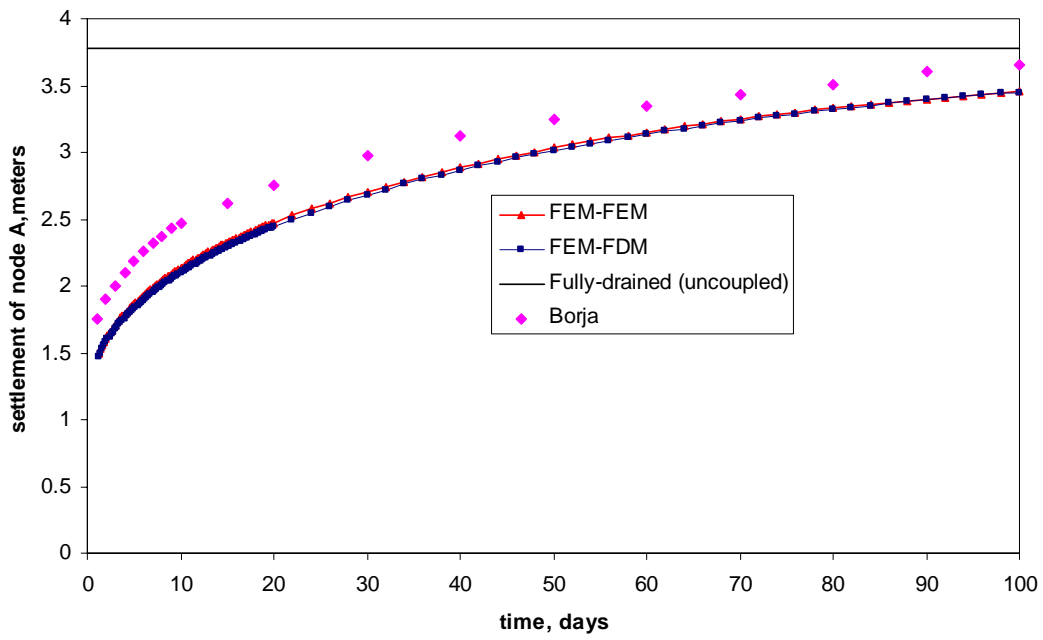


Figure 5-25 Settlement profile at point A

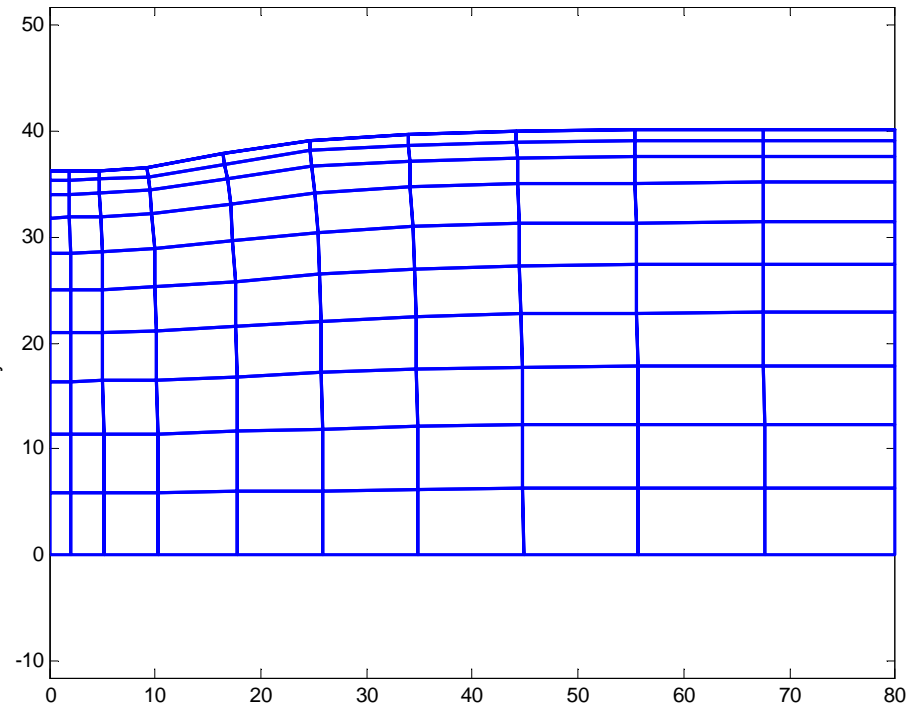


Figure 5-26 Final deformation of linear elastic consolidation problem

- **Elasto-plastic consolidation**

In this problem, soil is assumed to behave as an elasto-plastic material according to the modified Cam-Clay model with associative flow rule. Accurate, stable, and efficient algorithms for the integration of the rate constitutive equation for this model are available and the sub-stepping method by Sloan [5] is used in this analysis. This method was described in previous Chapter. Cam-Clay parameters and other model properties used in the analysis are shown in Table 5-7. Although soil permeabilities are high for the clay, these values are assumed by Borja to investigate the cases where pore pressure generation and dissipation occur at reasonable rates and times.

Table 5-7 Material properties for the nonlinear elasto-plastic (Modified Cam Clay) consolidation problem

Parameter	
κ (swelling index)	0.054
λ (virgin compression index)	0.37
M (slope of critical state line)	1.40
e_0 (reference void ratio)	2.54
γ_b (effective soil unit weight)	10 KN/m ³
w (strip load)	10 kPa
T_0 (time for linear strip load)	10 day
Δt (time step)	0.1 day
k_{11} , and k_{22} (isotropic soil permeability, $k_{12}=k_{21}=0$)	0.2 m/day
Over consolidation ratio (OCR) for whole domain	1

The elements are assumed to be initially under a K_0 -condition. In order to represent the initial conditions, small isotropic compressive stresses are generated at each integration

point because non-zero initial compressive stresses are required as input to get the solution started and then gravity loads, corresponding to the self weight of the soils, are applied. Since the elastic moduli are proportional to the volumetric effective stress p' in the Cam Clay model and the elastic moduli are treated explicitly in the sub-stepping method. Figure 5-27 presents the pore pressure profiles at node B as function of consolidation time. The figure shows the temporal variations of excess pore pressure and settlement due to the strip load of $w=10$ kPa applied linearly with time over a period of 10 days. The results of the simulation using FD for the fluid-flow predict about 10 % higher pore pressures during the external load at $t=10$ days compared to the FE solution. Consequently, less settlements are predicted with consolidation time as can be seen in Figure 5-28. Differences with Borja's results are attributed that different elements for FE geomechanics simulation (i.e., Borja used 8-nodes serendipity elements) and different constitutive integration algorithms for the elasto-plastic Modified Cam Clay model (i.e., Borja uses stress-return algorithm with consistent tangent stiffness). Isochrones of excess pore pressure at different times are shown in Figure 5-29.

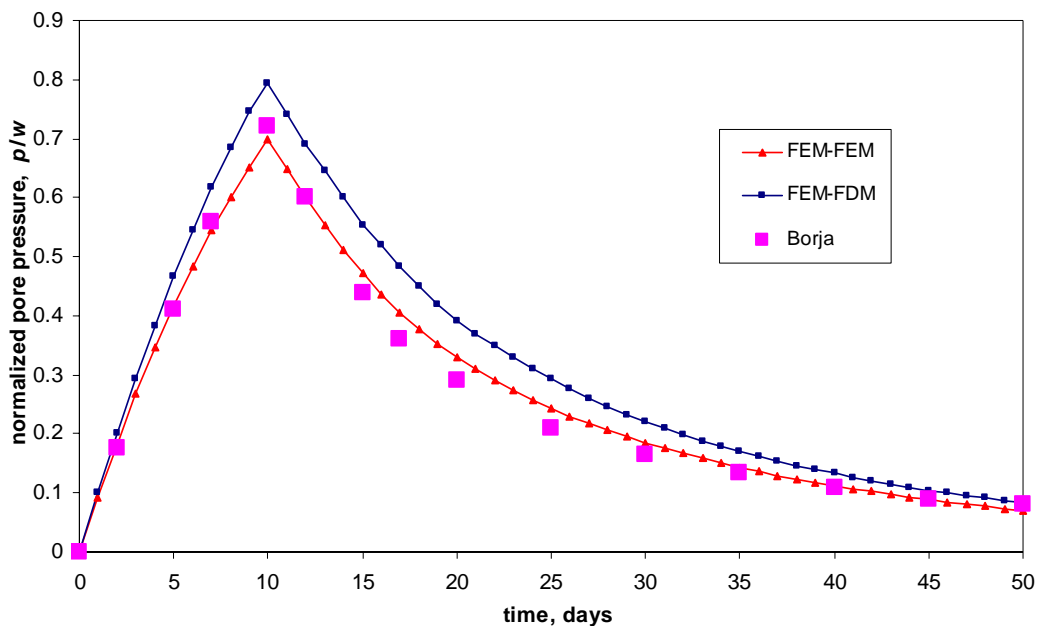


Figure 5-27 Excess pore pressure profiles at point B for nonlinear consolidation problem

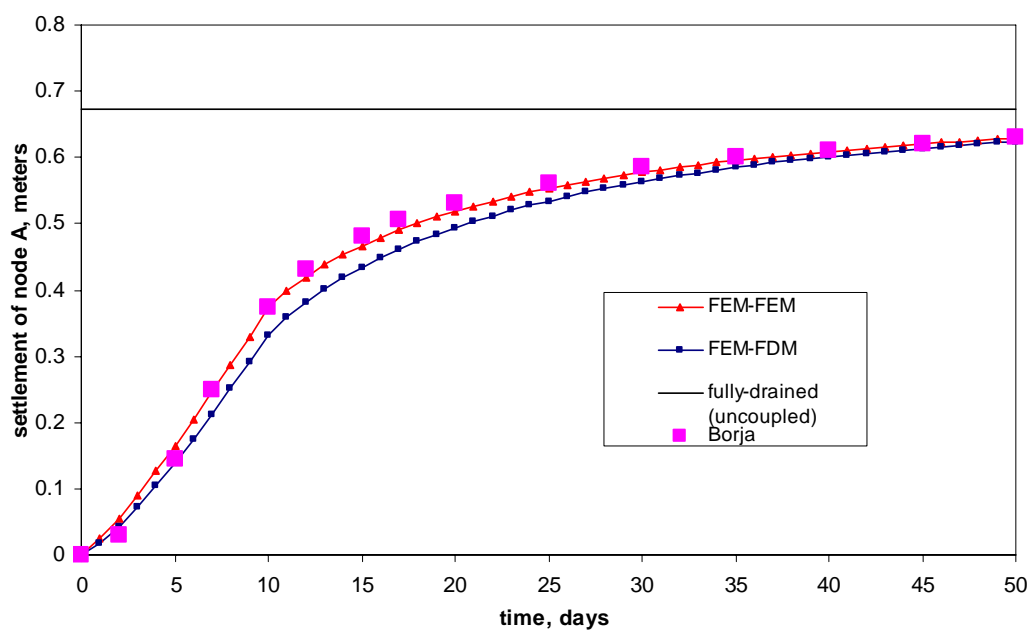


Figure 5-28 Settlement profile at point A for nonlinear consolidation problem

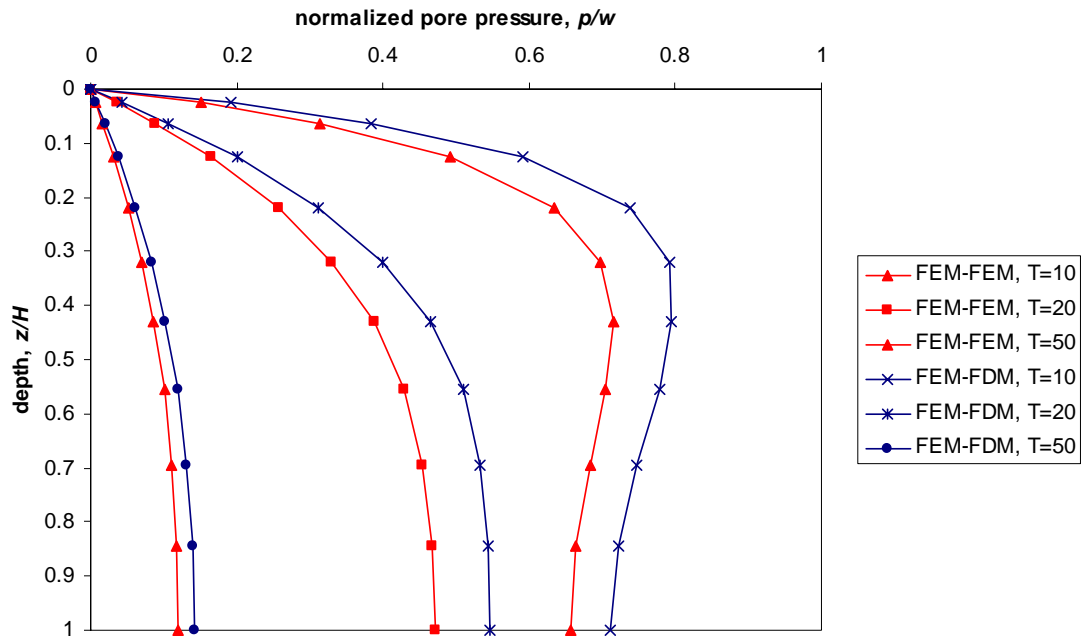


Figure 5-29 Isochrones of pore pressure along depth

5.5.5 Liakopoulos's drainage test

Liakopoulos's drainage test problem is re-analyzed using the both monolithic, and the FE-FE modular approaches. Other parameters and problem descriptions are identical to the ones in Chapter 3. Since experimental results from Liakopoulos were presented in Chapter 3, only the monolithic solution results are compared with the FE-FE partitioned modular approach results in Figures 5-30 to 5.34. Solid lines and dashed line represent results of monolithic solution, and FE-FE modular approach, respectively. It can be seen that the modular approach produces identical results comparing to the monolithic solution.

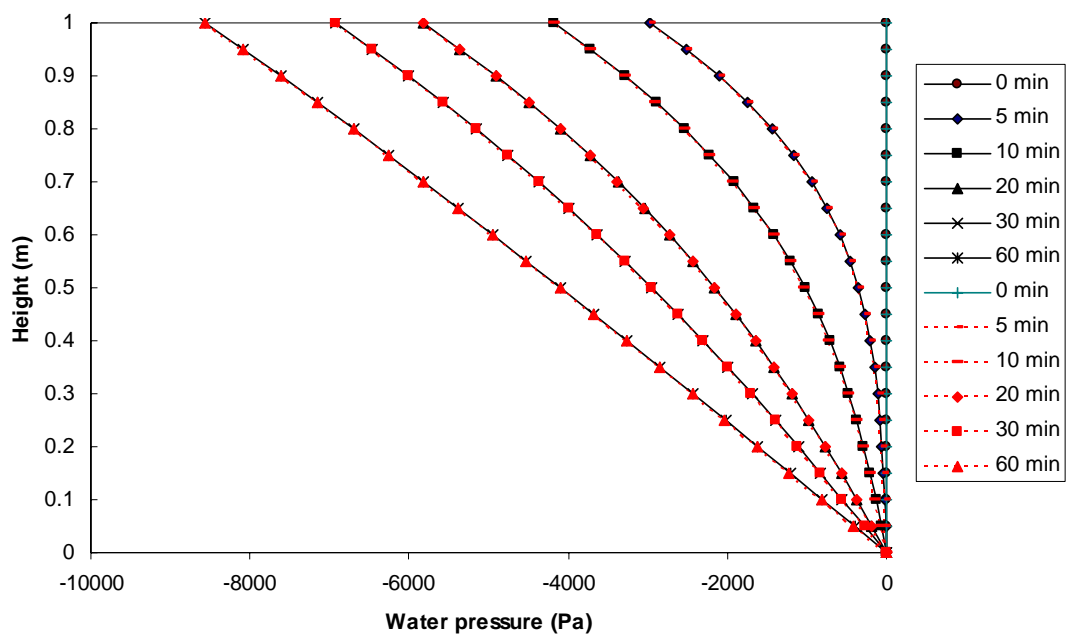


Figure 5-30 Water pressure profiles

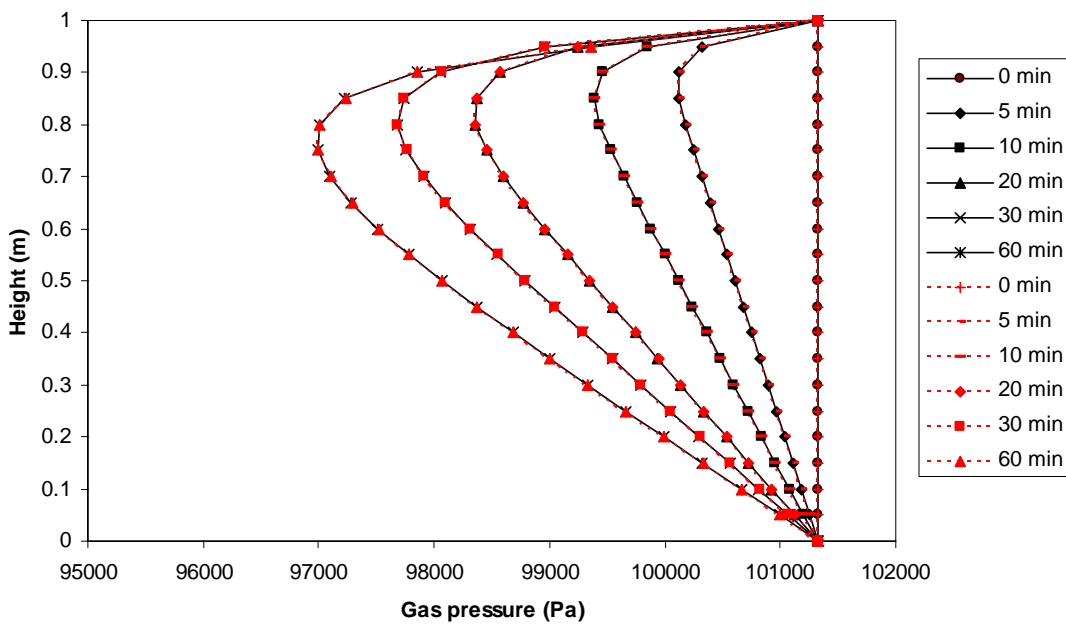


Figure 5-31 Gas pressure profiles

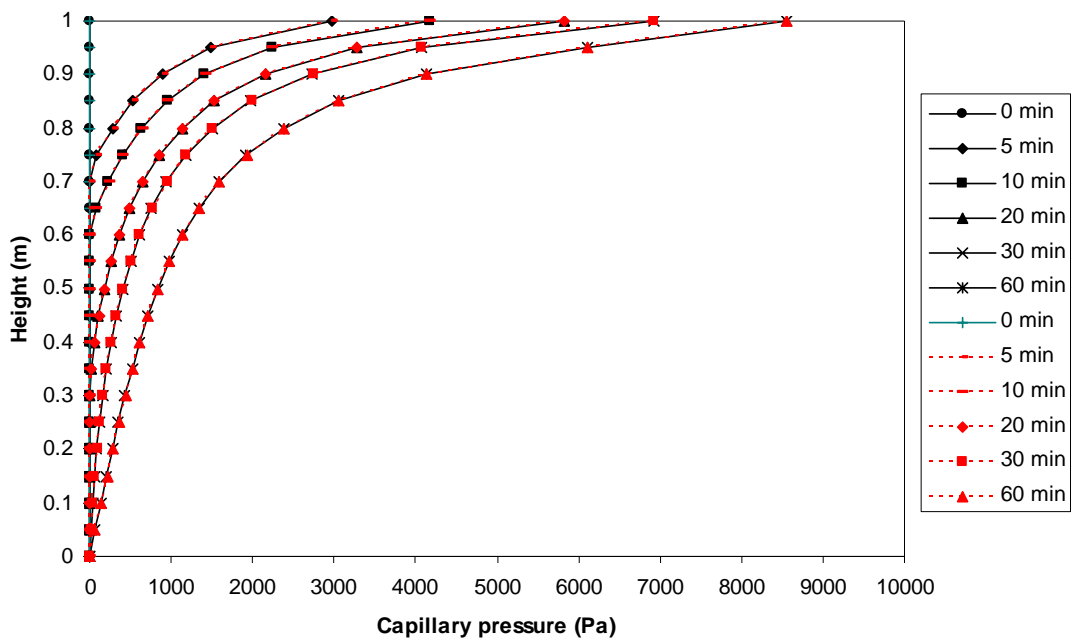


Figure 5-32 Capillary pressure profiles

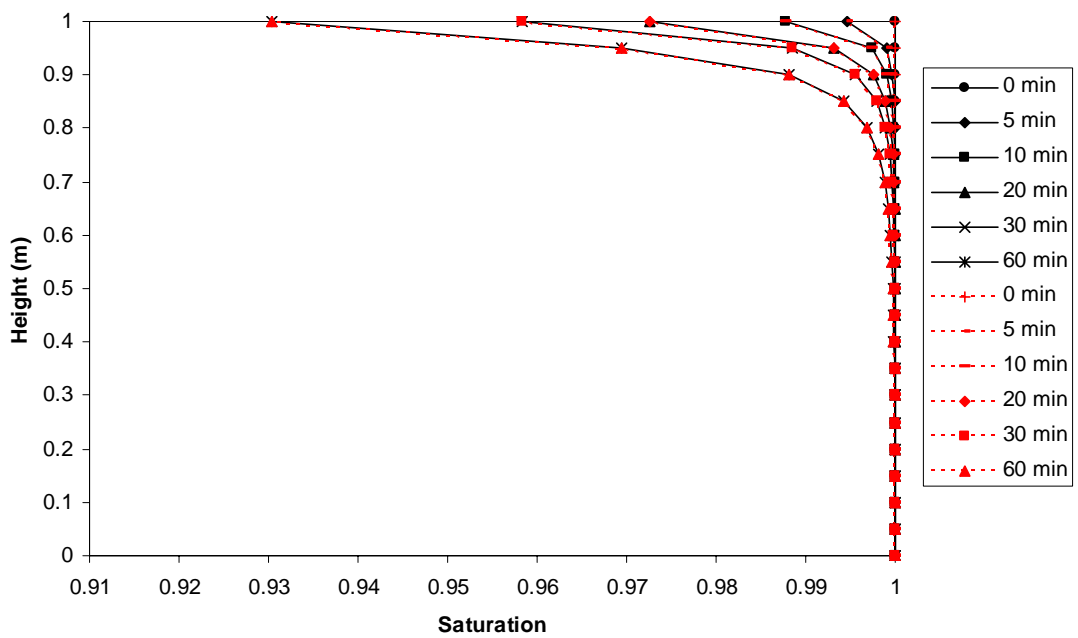


Figure 5-33 Saturation profiles

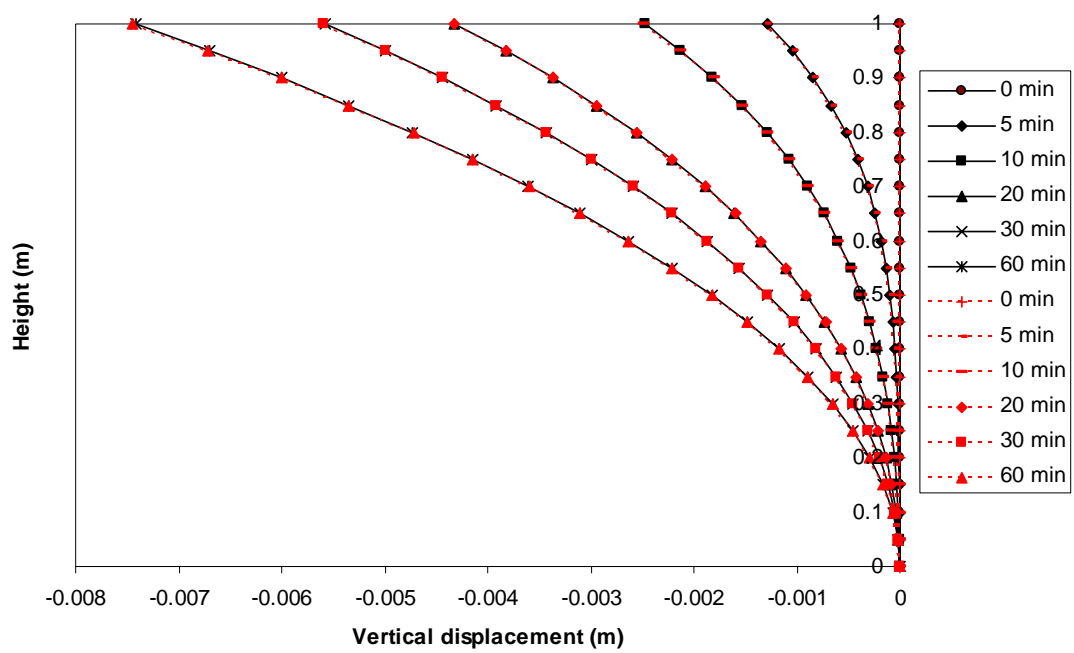


Figure 5-34 Vertical displacement profiles

REFERENCES

1. Borja, R.I. 1989. linearization of Elasto-Plastic Consolidation Equations. *Engineering Computations*. 6: 163-168.
2. Borja, R.I. and S.R. Lee 1990. Cam-caly Plasticity, Part I: Implicit Integration of Elasto-plastic Constitutive Relatios. *Communications in Numerical Methods in Engineering*. 78: 49-72.
3. Simo, J.C. and M.A. Ortiz 1985. A unified approach to the finite deformation elastoplastic analysis based on the use of hyperelastic constitutive equations. *Computer Methods in Applied Mechanics and Engineering*. 49: 221-245.
4. Simo, J.C. and R.L. Taylor 1985. Consistent Tangent Operators for Rate-Independent Elastoplasticity. *Computer Methods in Applied Mechanics and Engineering*. 48: 101-118.
5. Sloan, S.W. 1987. Sup-stepping Schemes for the Numerical Integration of Elastoplastic Stress-Strain Relations. *International Journal for Numerical and Analytical Methods in Geomechanics*. 24: 893-911.
6. Barrett, R., M. Berry, T.F. Chan, J. Demmel, J. Donato, J. Dongarra, V. Eijkhout, R. Pozo and C. Romine 1994. *Templates for the solution of linear systems: building blocks or iterative methods*. Philadelphia: Society for industrial and applied mathematics.
7. Chan, R.H. and T.F. Chan, eds. *Iterative Methods in Scientific Computing*. ed. G.H. Golub. 1997, Springer: Singapore.
8. Hageman, L.A. and D.M. Young 1981. *Applied Iterative Methods*. Vol. 1. New York: Academic Press.
9. Kelly, C.T. 1995. *Iterative Methods for Linear and Nonlinear Equations*. Philadelphia: Society for Industrial and Applied Mathematics.
10. Elman, H., D. Silvester and A. Wathen 2005. *Finite Elements and Fast Iterative Solvers with applications in incompressible fluid dynamics*. Oxford: Oxford science publications.
11. Hestenes, M.R. and E. Stiefel 1954. Methods of conjugate gradients for solving linear systems. *United States Bureau of Standards -- Journal of Research*. 49: 109-436.

12. Prevost, J.H. 1997. Partitioned Solution Procedure for Simultaneous Integration of Coupled-Field Problems. *Communications in Numerical Methods in Engineering*. 13: 239-247.
13. Paige, C. and M. Saunders 1975. Solution of sparse indefinite systems of linear equations. *SIAM Journal of Numerical Analysis*. 12: 617-629.
14. Barrett, R., M. Berry, T.F. Chan, J. Demmel, J. Donato, J. Dongarra, V. Eijkhout, R. Pozo, C. Romine and H. Van der Vorst 1994. *Templates for the Solution of Linear Systems: Building Blocks for Iterative Method*. 2nd ed. Philadelphia: Society for Industrial Mathematics.
15. Tran, D., A. Settari and L. Nghiem 2004. New iterative coupling between a reservoir simulator and a geomechanics module. *SPE Journal*. 9: 362-369.
16. Settari, A. and F.M. Mourits 1994. Coupling of geomechanics and reservoir simulation models. *Computer Methods and Advances in Geomechanics*. 2151-2158.
17. Minkoff, S., C.M. Stone, J. Guadalupe-Arguello, S. Bryant, J. Eaton, M. Peszynska and M. Wheeler 1999. Staggered in Time Coupling of Reservoir Flow Simulation and Geomechanical Deformation: Step 1 - One-Way Coupling. in *Proc. 15th SPE Symp. Reservoir Simulation*. Houston, Texas.
18. Thomas, L.K., L.Y. Chin, R.G. Pierson and J.E. Sylte 2003. Coupled geomechanics and reservoir simulation. *SPE Journal*. 8: 350-358.
19. Longuemare, P., M. Mainguy, P. Lemonnier, A. Onaisi, C. Gerard and N. Kotsabeloulis 2002. Geomechanics in Reservoir Simulation: Overview of Coupling Methods and Field Case Study. *Oil & Gas Science and Technology*. 57: 471-483.
20. Chin, L.Y., L.K. Thomas, J.E. Sylte and R.G. Pierson 2002. Iterative Coupled Analysis of Geomechanics and Fluid Flow for Rock Compaction in Reservoir Simulation. *Oil & Gas Science and Technology*. 57: 485-497.
21. Settari, A. and D.A. Walters 1999. Advances in Coupled Geomechanical and Reservoir Modeling with Applications to Reservoir Compaction. in *SPE Reservoir Simulation Symposium*. Houston, Texas.
22. Aziz, K. and A. Settari 1979. *Petroleum Reservoir simulation*. London: Applied Science Publishers Ltd.
23. Gutierrez, M. and R.L. Lewis 2001. Petroleum Reservoir Simulation Coupling Fluid Flow and Geomechanics. *SPE Reservoir Evaluation & Engineering*. 4: 164-171.

24. Gutierrez, M., N. Barton and A. Makurat 1995. Compaction and subsidence in North Sea hydrocarbon fields. in *International Workshop on Rock Foundations of Large Structures*.
25. Cheng, A.D.H. and E. Detournay 1988. A Direct Boundary Element Method for Plane Strain Poroelasticity. *International journal for Numerical and Analytical Methods in Geomechanics*. 12: 551-572.
26. Mandel, J. 1953. Consolidation des sols. *Geotechnique*. 3: 287-299.
27. Schiffman, R.L., A.T. Chen and J.C. Jordan 1969. An Analysis of Consolidation Theories. *International Journal of Soil Mechanics Foundation Divisioin SM-1*: 285–312.
28. Borja, R.I. 1991. One-step and Linear Multistep Methods for Nonlinear Consolidation. *Computer Methods in Applied Mechanics and Engineering*. 85: 239-272.

6 APPLICATION OF THE MODEL

6.1 Ekofisk Hydrocarbon Field

Numerical modeling of the behavior of the production induced subsidence in the Ekofisk field was performed using the proposed coupled modular approach (FE-FE) described in the preceding Chapter. The primary objectives of the simulation are: 1) to show the rigorousness of the developed code, and 2) to understand the fully-coupled behavior of compacting and subsiding hydrocarbon reservoir. The nonlinear behavior of the reservoir rock, which is chalk, was modeled by the Modified Cam Clay model. The validity of using the Modified Cam Clay model to represent the constitutive behavior of the Ekofisk chalk has been shown by Gutierrez and Hickman [1].

Two-phase fluid flow (i.e., oil and water system) conditions, with the gas phase dissolved in the oil phase, were assumed. Simulations were therefore carried only for reservoirs pressures below “blowdown” conditions at which the dissolved gas was released from the oil phase and at which point the reservoir became a three-phase fluid system. The reservoir chalk is water wet and, thus, water is the wetting fluid. Although the present simulation is not a fully comprehensive analysis of the field due to the limitations of the code and lack of published input data, it may serve as a pilot study to establish for a more comprehensive study in the future.

The Ekofisk field is located in the south of the Norwegian sector of the North Sea (see Figure 6-1). The sea depth in the area is about 70 to 75 meters. The field is an anticline

structure with its fold axis in the North-South direction. Locally, the Ekofisk is an elliptical dome-like structure which serves as the geological hydrocarbon trap. It was discovered in 1961, and from the early 1970s up to the present, the Ekofisk field, one of the most important oil fields in the North Sea, has been under production by Phillips Petroleum Company. Facing a lower oil production rate due to a gradual decline of the reservoir pressure from the production, oil companies have been conducted extensive studies to increase the efficiency and productivity of the reservoir. As a solution to raise the reservoir pressure, water injection was operated in 1984.

In the mid 1980s, the Ekofisk field was found to be suffering from an unexpected high degree of subsidence. Detailed investigations concluded that the subsidence was a result of the compaction of the chalk formation which is a main material of the reservoir. The Ekofisk field is called *compaction drive* reservoir in that the basic mechanism controlling the reservoir pressure and consequently the production rate is the compaction of the producing formation. However, the compaction of the reservoir can be transferred to the overburden layers and lead to the seabed subsidence. This is the case for Ekofisk were subsidence is currently (2008) at almost 10 m.

In order to achieve a reasonable estimation of the reservoir behavior, several numerical studies of the Ekofisk subsidence have been performed in the past [2-6]. Most of them utilized uncoupled models or simple geomaterial constitutive models (i.e., linear elastic model). In this chapter, the proposed modular approach based on the fully-coupled Biot's theory, described in the previous Chapter, was implemented to predict the behavior of the Ekofisk field including pressure estimations, reservoir compaction, and surface subsidence

under the first production phase (i.e., before pressure blowdown conditions). Throughout the present study, the reservoir is assumed to behave as a Modified Cam clay model. The validity of using the Modified Cam Clay Model to model the compaction of the Ekofisk Chalk has been amply demonstrated by Hickman and Gutierrez [1].

The surrounding layers (e.g., overburden, sideburden, and underburden) consist of very low permeability shale. The surrounding layers are included in the simulations to obtain more rigorous interactions effects between geomechanics and pore pressures, and between the producing and non-pay rocks. No fluid flow conditions and elastic behavior are assumed for the surrounding rocks. Initial numerical simulation data in the present study are mostly based on the three previous studies by Chin et al. [4], Ghafouri [2], and Gutierrez et al [5], throughout this chapter.

In order to minimize the size of the model and the computational efforts, symmetry with respect to the North-South axis was assumed. This assumption is not far from reality as can be seen in Figure 6-2. Although the real Ekofisk reservoir is be elliptically shaped in plan view, the numerical region is assumed to be a rectangular shaped for simplicity as can be seen in Figure 6-3. Simplified cross sectional area with respect to the North-South axis was assumed in the 2-D numerical simulation and it is shown in Figure 6-4.



Figure 6-1 Location of the Ekofisk field in the North Sea (from Conocophillips.com
http://www.conocophillips.com/about/worldwide_ops/country/europe/norway.htm)

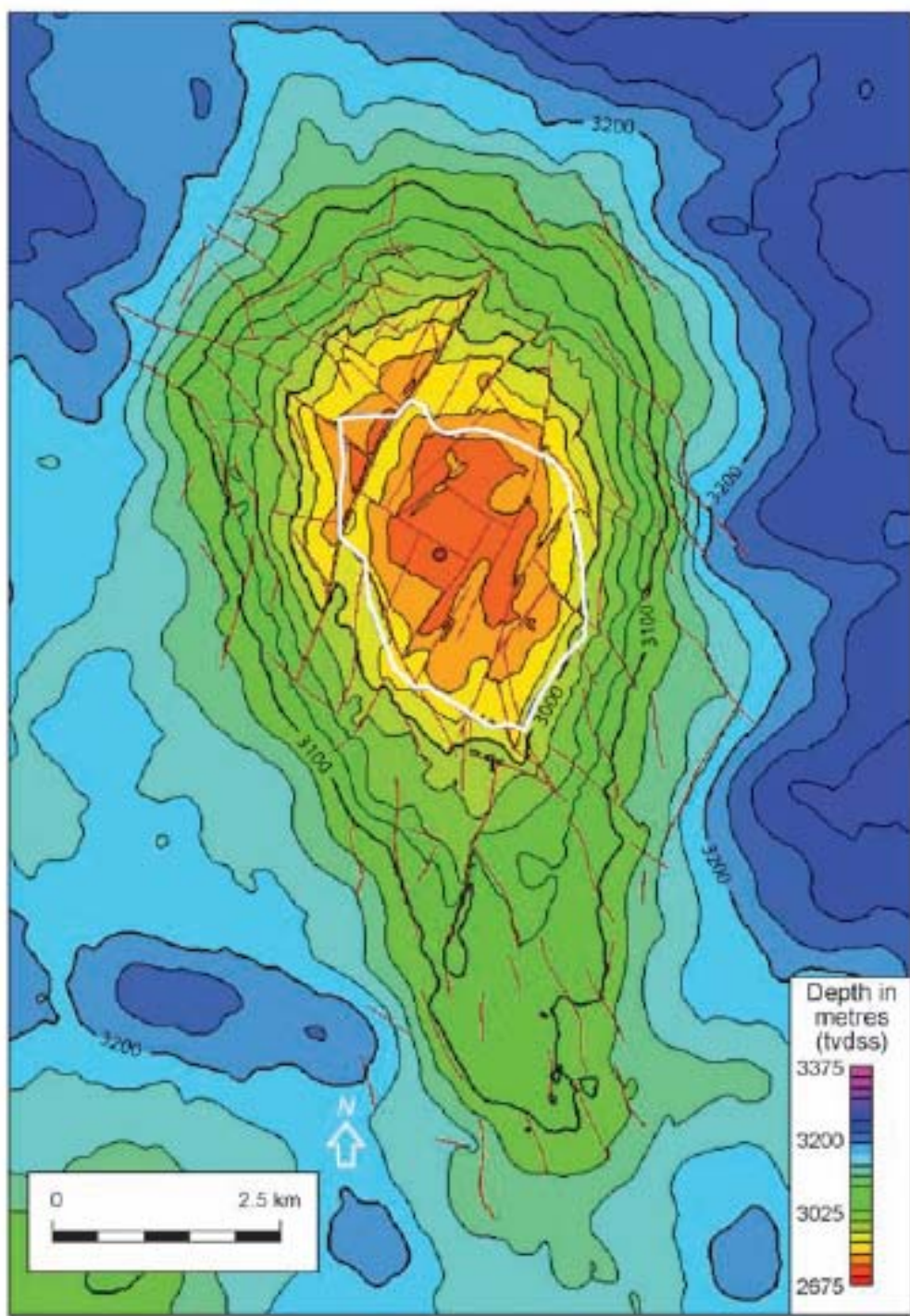


Figure 6-2 Ekofisk Field: depth map of the top of the Ekofisk Formation (by Spencer et al. [7])

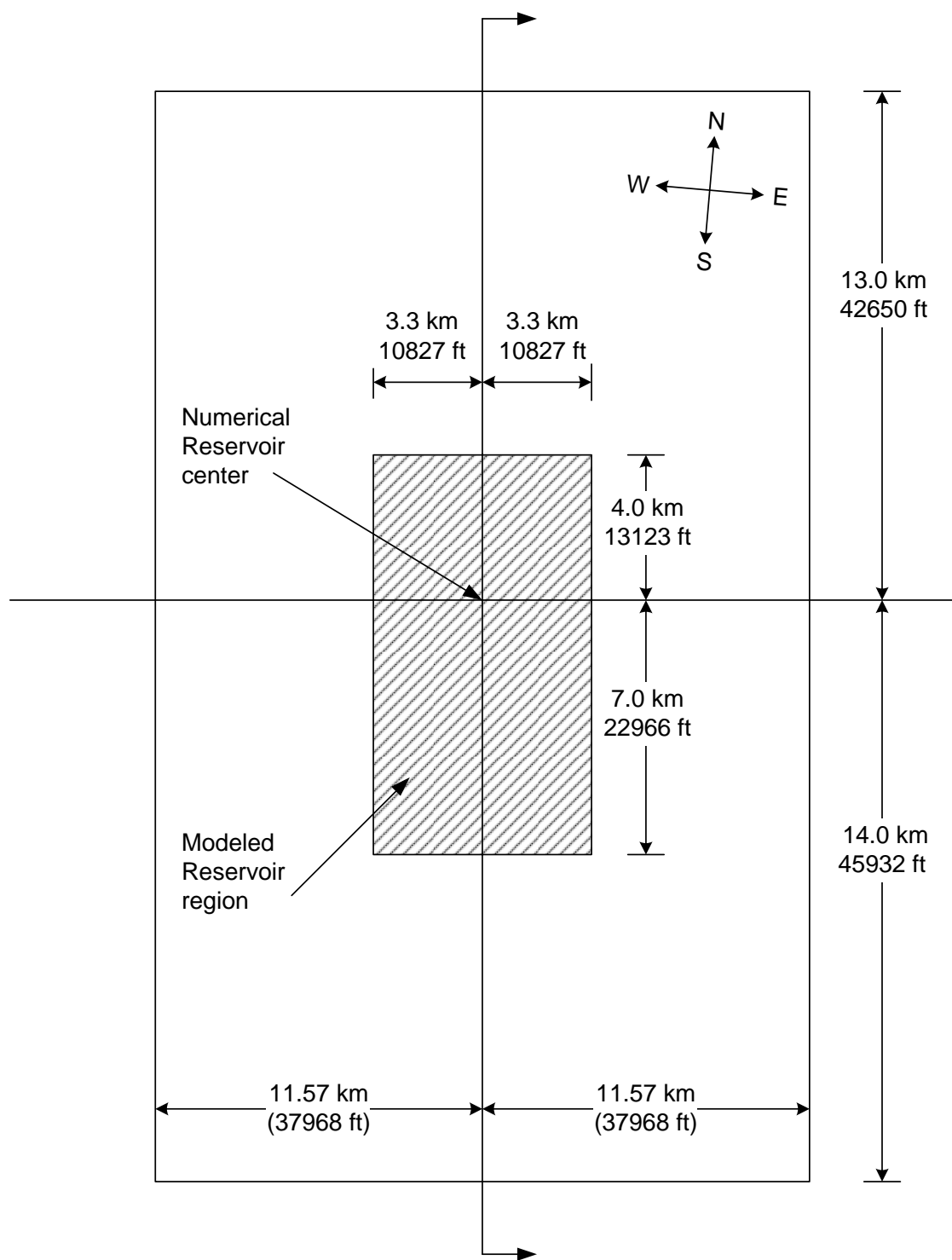


Figure 6-3 Plan view of the numerical modeled region for the Ekofisk field

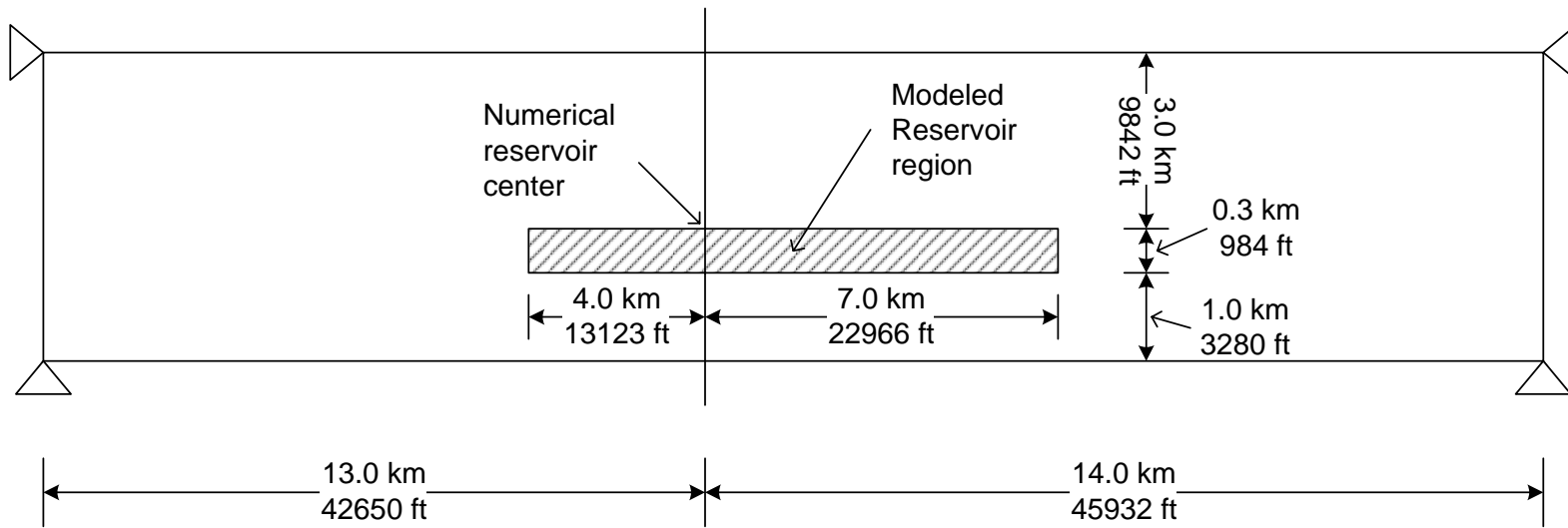


Figure 6-4 Cross section (North-South) of the numerical modeled region for the Ekofisk field

Figure 6-5 shows porosity distribution and the initial water saturations, which is close to 0.2 in the entire reservoir. The initial absolute permeability value of the chalk layers in the reservoir zone is 150 md as given by Gutierrez et al. [6]. As noted above in the initial simulation, only two-phase flow (i.e., water, and oil) was assumed due to absence of a free gas component in the Ekofisk reservoir. Saturation vs. relative permeability and saturation vs. capillary pressure curves used in the simulation are presented in Figure 6-6 and Figure 6-7. Typical values for the fluid properties were assumed based on the Ghafouri [6]. Table 6-1 shows the fluid properties used in the simulation.

Material properties used in the previous numerical simulations of the Ekofisk vary among the different researchers because of the lack of laboratory test data on surrounding materials. Chin [5] assumed overburden to be a homogeneous material with specific gravity of 2.13. The overburden was assumed to respond mechanically as an elasto-plastic solid and Drucker-Prager yield criterion was used in the numerical simulation. Elastic properties of the overburden material were described using a Young's modulus of 345 MPa and a Poisson's ratio of 0.42. Identical material properties in the underburden and sideburden were assumed as a homogeneous linear-elastic solid with a specific gravity of 2.22, a Young's modulus of 14 GPa and a Poisson's ratio of 0.25.

Gutierrez et al. [6] assumed homogeneous linear elasticity through the whole region with different properties between reservoir and surrounding layers. Elastic Young's modulus of the reservoir rock is 50 MPa and the Poisson's ratio is 0.25. For the surrounding non-pay rock, the Young's modulus and Poisson's ratio are, respectively, equal to 2.5 GPa and 0.25.

Ghafouri [2] assumed homogeneous linear elasticity with various elastic properties along the different layers of the overburden. Elastic modulus of the overburden varied from 0.3 MPa for the top layer to 14 MPa to the layer just above the reservoir. The Young's modulus for the underburden varied from 1.0 MPa to 1.3 MPa. Poisson's ratio was assumed 0.25 throughout the whole surrounding rocks.

For the reservoir rocks, the moduli values can be obtained using the stress-strain curves shown in Figures 6-8 and 6-9. These figures are from Chin et al. [4] and are based on the results of uniaxial strain or K_0 compression tests on Ekofisk chalk. The main reservoir has two distinct layers separated by a thin and very low permeability called the "tight zone." The upper layer and lower layer of chalk show different strength properties according to their quartz content (e.g., the upper portion of chalk is stronger than the lower portion of chalk). It may be noted that once pore-collapse occurs in the chalk, it is irreversible and the slope of stress-strain curve increases (i.e., shows more stiff material behavior). In the simulations, it is assumed that the reservoir consists of a single chalk material because Modified Cam Clay parameters are not available for each of different chalk layer. Modified Cam Clay parameters used in the simulations are based on Gutierrez et al. [8] with 40 % of porosity in the reservoir. The initial effective vertical stress of the reservoir was assumed to be 14 MPa and K_0 condition was assumed with value of 0.2. Detailed material properties used in the simulations are shown in Table 6-2 and Table 6-3.

Table 6-1 Fluids properties of reservoir

Parameter	
Reservoir absolute permeability, K	150 md (10^{-15} m^2)
Oil viscosity, μ_o	0.29 cp (mPa s)
Water viscosity, μ_w	0.31 cp (mPa s)

Table 6-2 Linear elastic parameters of surrounding materials

	Overburden	Sideburden	Underburden
Young's modulus, E (GPa)	10	10	10
Poisson's ratio, ν	0.45	0.45	0.45

Table 6-3 Modified Cam Clay parameters of reservoir materials

Parameters	Porosity (%)		
	40	35	30
Young's modulus, E (MPa)	250	550	1200
Poisson's ratio, ν	0.25	0.25	0.25
Initial void ratio, e_0	0.67	0.55	0.43
Slope of virgin consolidation line, λ	0.45	0.42	0.42
Slope of swelling line, κ	0.05	0.05	0.05
Slope of critical state line, M	0.46	0.46	0.46
Pre-consolidation pressure, p'_p	17	25	50

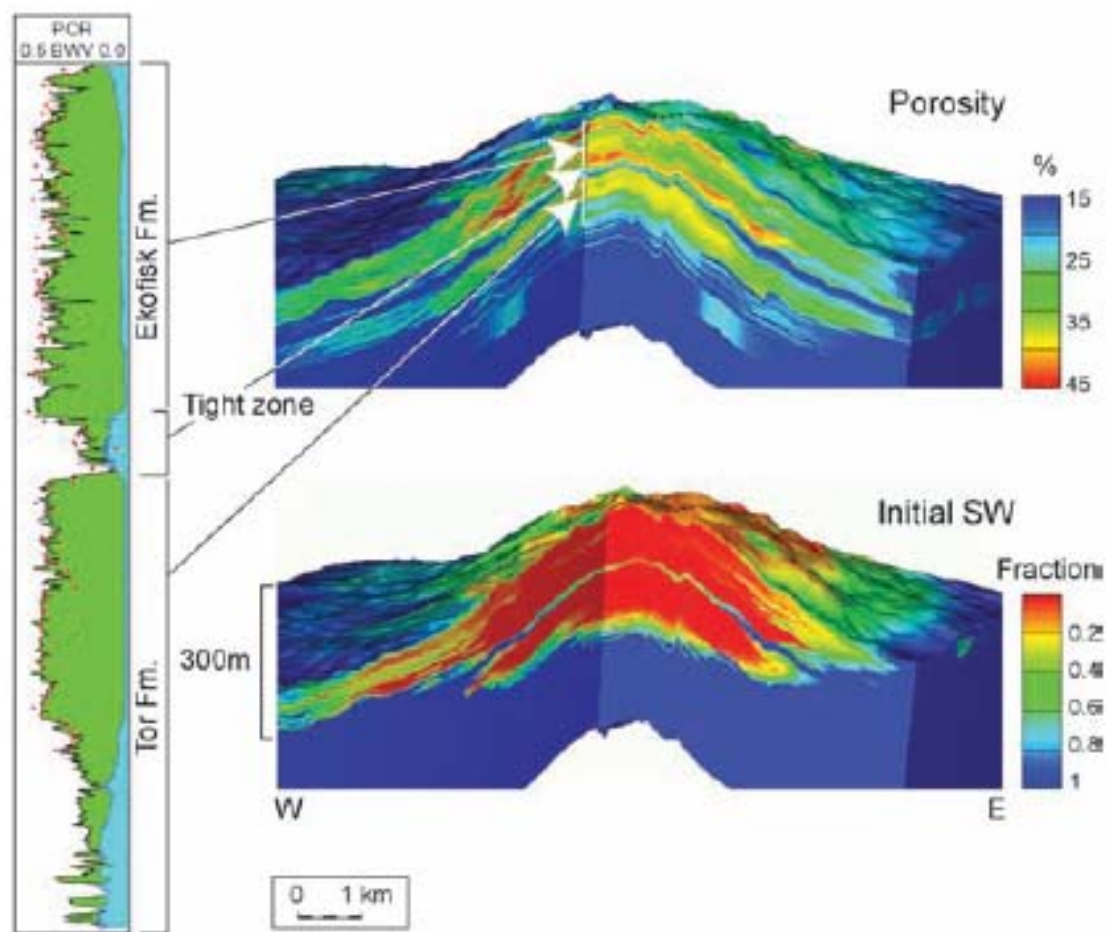


Figure 6-5 Cross section of the Ekofisk reservoir showing porosity and initial water saturation (by Spencer et. al [7])

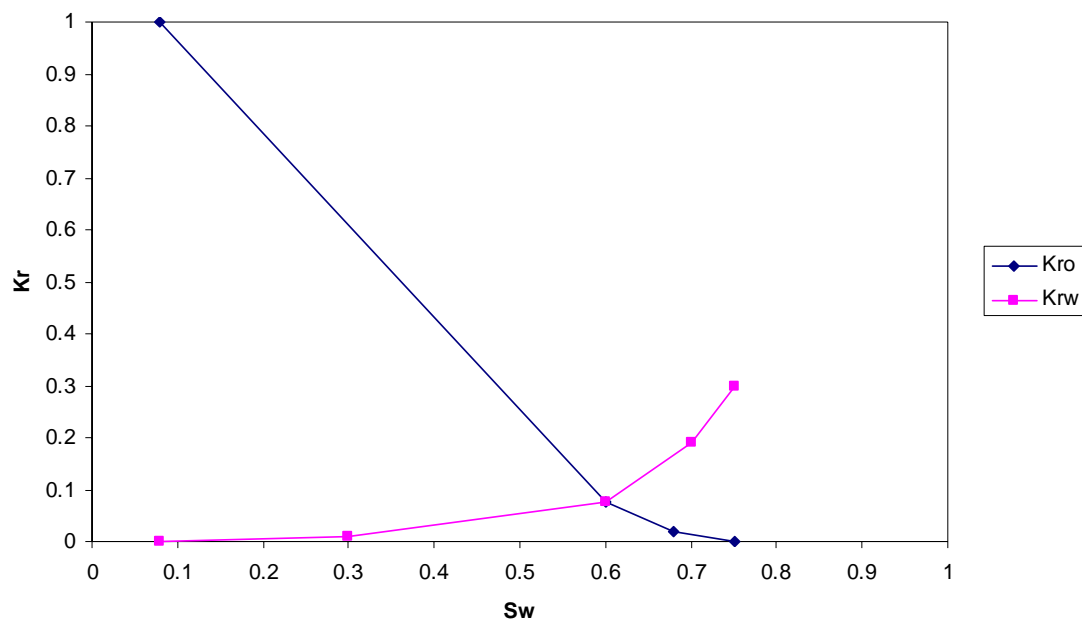


Figure 6-6 Saturation vs. relative permeabilities in the oil-water system (similar to Ghafouri [2])

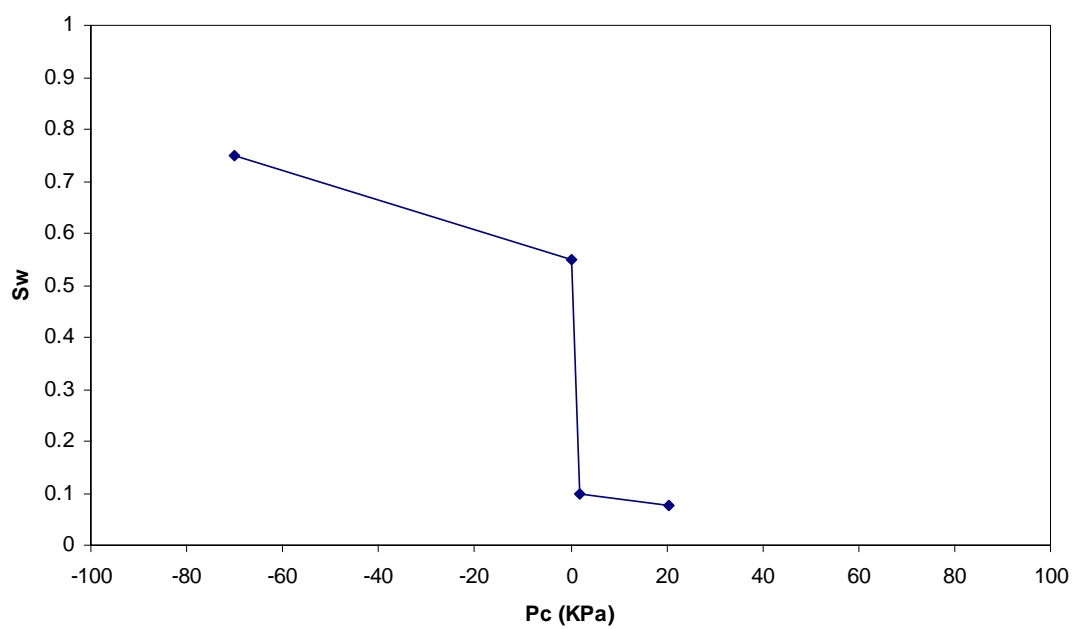


Figure 6-7 Capillary pressure vs. water saturation in the oil-water system (similar to Ghafouri [2])

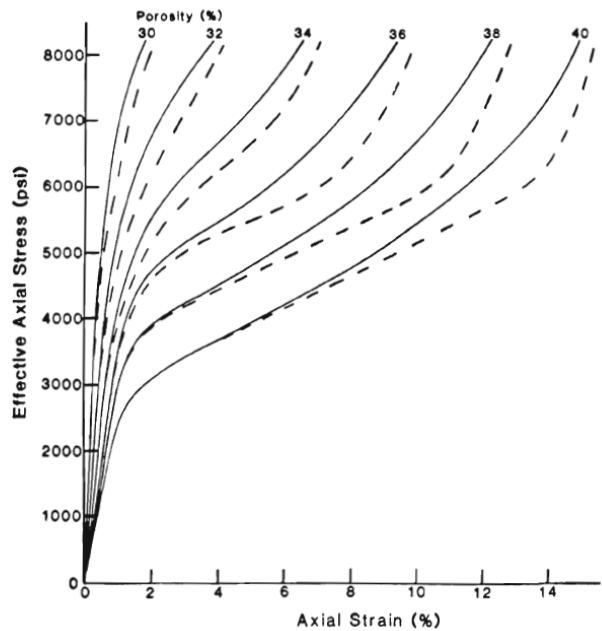


Figure 6-8 Stress-strain curves for Low-Quartz-Content reservoir chalk
Dashed curves illustrate the effect of long-term creep (by Chin et al. [4])

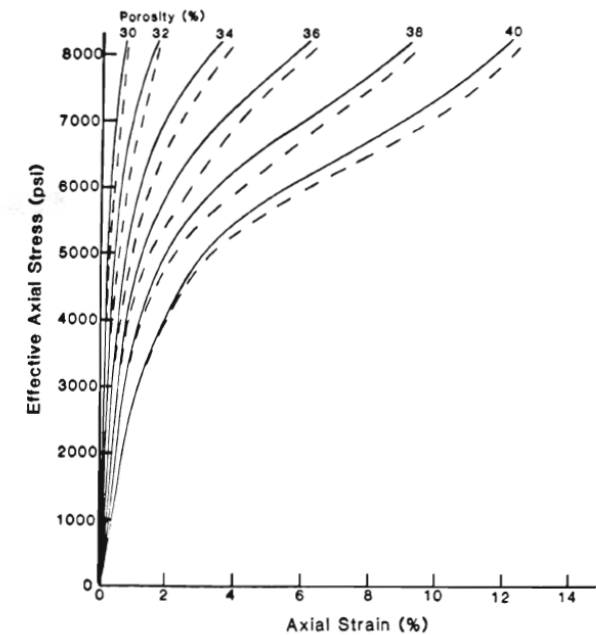


Figure 6-9 Stress-strain curves for High-Quartz-Content reservoir chalk
Dashed curves illustrate the effect of long-term creep (by Chin et al. [4])

Figure 6-10 and 6-11 shows the historical water production and oil production, respectively [9] and the average reservoir pressure vs. time plot is created based on the production histories. Only a primary recovery phase is simulated from 1971 to 1985 and the initial and the final average pressure values in the simulations were assumed 48 MPa and 24 MPa, respectively at the well points. In order to produce the average pressure history, it was assumed that cumulative productions are directly related to the pressures at the well (e.g., more production leads more pressure down). Those pressure values are used to specify the pressure on the well points (i.e., center of the reservoir) in the FE simulations. Since only average pressure data is available, the saturation data is needed to specify each pressure (e.g., oil and water) values on the well points because the primary variables for the fluid flow simulator are pressures. In case of using prescribed pressure values on the boundary, assumed saturation values are implemented according to the capillary pressure – saturation relation. In the simulations, saturation values are assumed varying from 0.2 as an initial state to 0.5 as a final state. Variation of the water saturation may be achieved based on the production history because saturation is directly related to the capillary pressure.

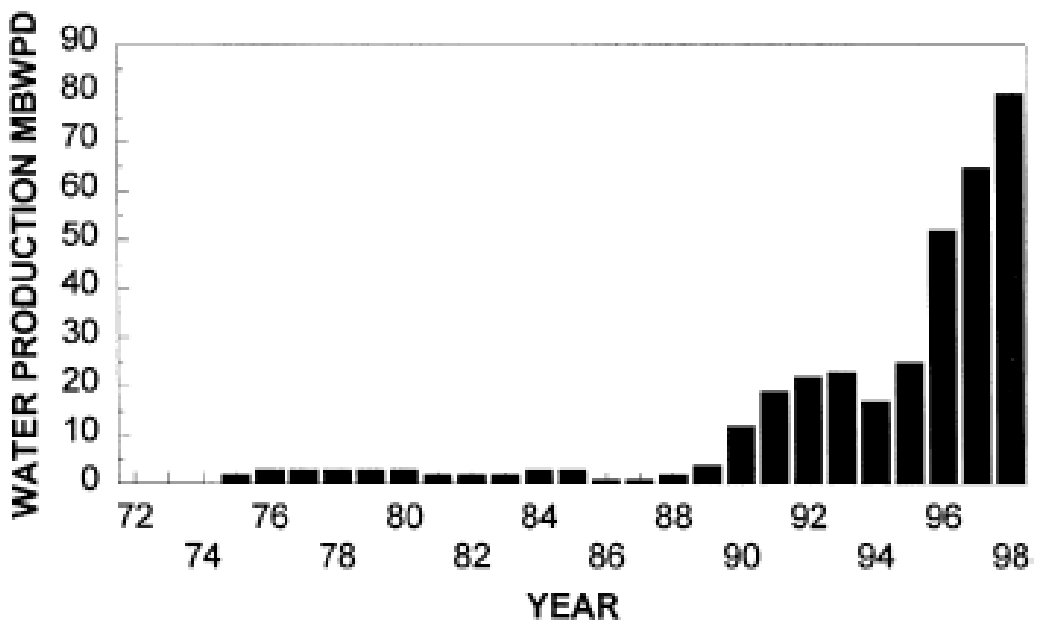


Figure 6-10 Ekofisk water production (by Hermnsen, H. et al. [9])

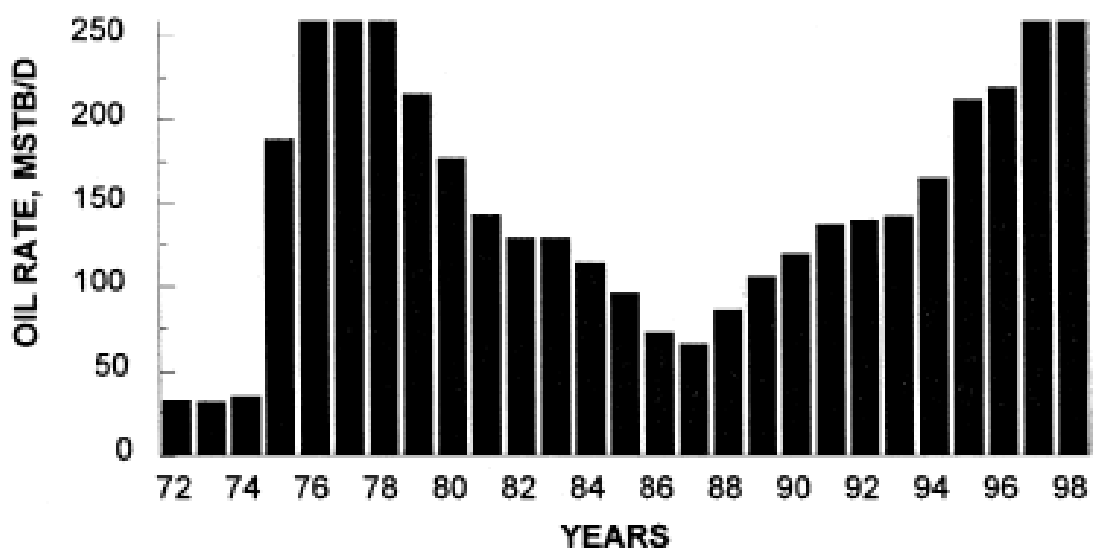


Figure 6-11 Ekofisk oil production (by Hermnsen, H. et al. [9])

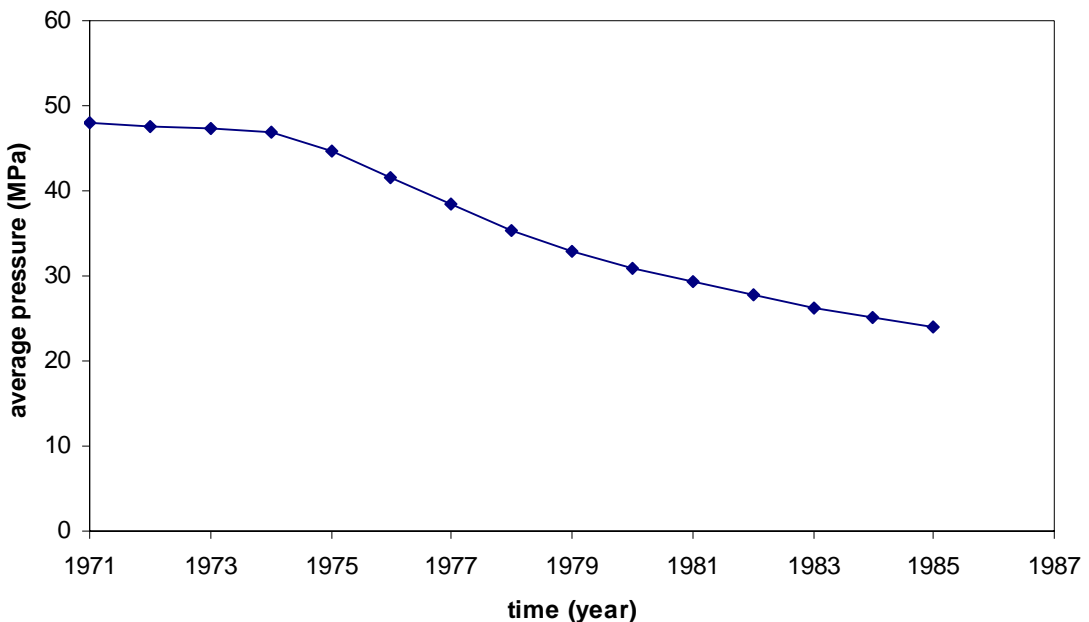


Figure 6-12 Average pressure history on the well point

The FE mesh is used for the entire 2-D model including the reservoir and its surrounding area. Quadrilateral 4-noded elements are used for both the geomechanics and fluid flow simulations. Figure 6-13 shows the initial FE mesh with the surrounding area, and the shaded area represents the reservoir region. There are eight layers of elements in the mesh, two passing through the reservoir, four through the overburden, and two through the underburden. In the lateral direction, the mesh contains thirty five rows in the North-South direction containing twenty two rows for the reservoir region.

It should be noted that only the reservoir area in which fluid flow occurs are included in the two-phase fluid flow simulator in the FE-FE modular approach. The total number of elements for the geomechanic simulation is 280 and the total system of degree of freedom

number is 648. On the other hand, total number of elements for the reservoir simulation is 44, and total system degree of freedom number is 69.

In this particular boundary problem, the modular approach requires less system degree of freedom in the comparison to other solution schemes. The surrounding region is not discretized because it is assumed to be impermeable. The monolithic solution requires full domain for the fluid simulation (although permeability of the impermeable zone sets to zero) results 280 element numbers with 648 system degree of freedoms. Although the efficiency of modular approach was not directly compared with the monolithic solution because only the FE-FE modular approach was developed for cases of nonlinear stress-strain and two-phase fluid flow, it can be suspected that modular approach is more efficient because it needs smaller size of the system of equations.

Figure 6-14 shows final nodal deformed mesh after 14 years of production and it illustrates the general displacement profiles including surface subsidence and reservoir compaction due to the oil production. Figure 6-15 shows subsidence and compaction profiles along the North-South cross-section. The calculated *subsidence-compaction ratio*, S/C , at the center of the subsidence bowl was 0.83. Figure 6-16 gives a plot of the subsidence and compaction profiles as function of the production time. More significant vertical displacements in the reservoir (i.e., compaction) were calculated than on the surface (i.e., surface subsidence) because the relatively chalk material is relatively softer than the overburden material.

Figure 6-17 and 6-18 present the water and oil pressure profiles of the reservoir region along the mid depth of the reservoir after the production. Although it is not the real distribution, due to the assumed hypothetical spatial distribution of the fluid pressures along the boundary, it may serve to give an idea about the general reservoir behavior. It may be noted that Mandel-Cryer effects are observed at the edge of the reservoir (i.e., average pressure is 52 MPa) and average pressures build up above the initial pressures (i.e., average pressure is 48 MPa) due to the interaction between overburden and reservoir. Figure 6-19 shows water saturation profiles. Although saturation varies from 0.2 to 0.5, it does not affect much on the calculated pressure values because the magnitude of capillary pressure for the saturation change (approximately 2 KPa) is small comparing to the average pressure value change (24 MPa).

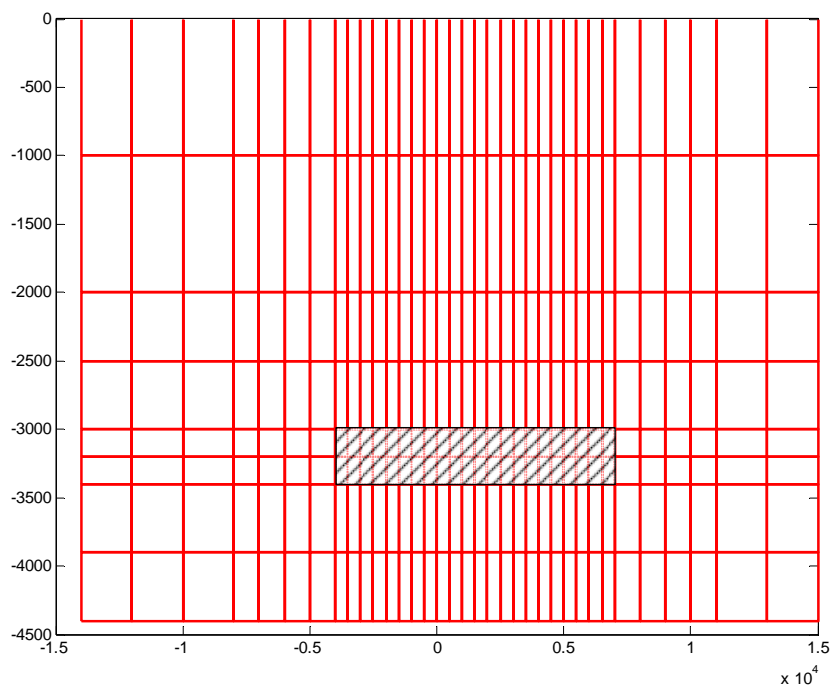


Figure 6-13 Initial FE mesh with surrounding area (shaded area represents reservoir field)

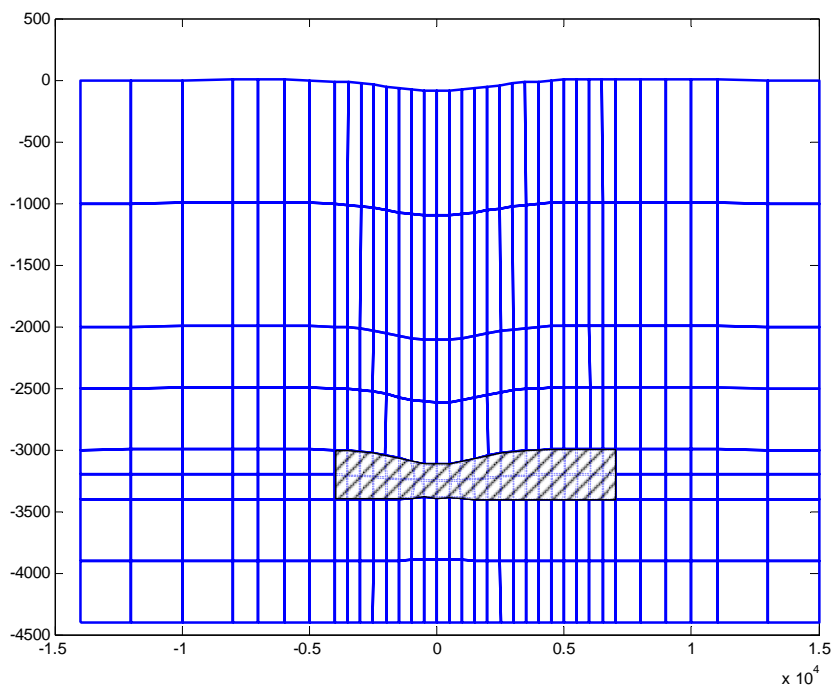


Figure 6-14 Final displacements profile after 14 years production with magnified 10 times
(shaded area represents reservoir field)

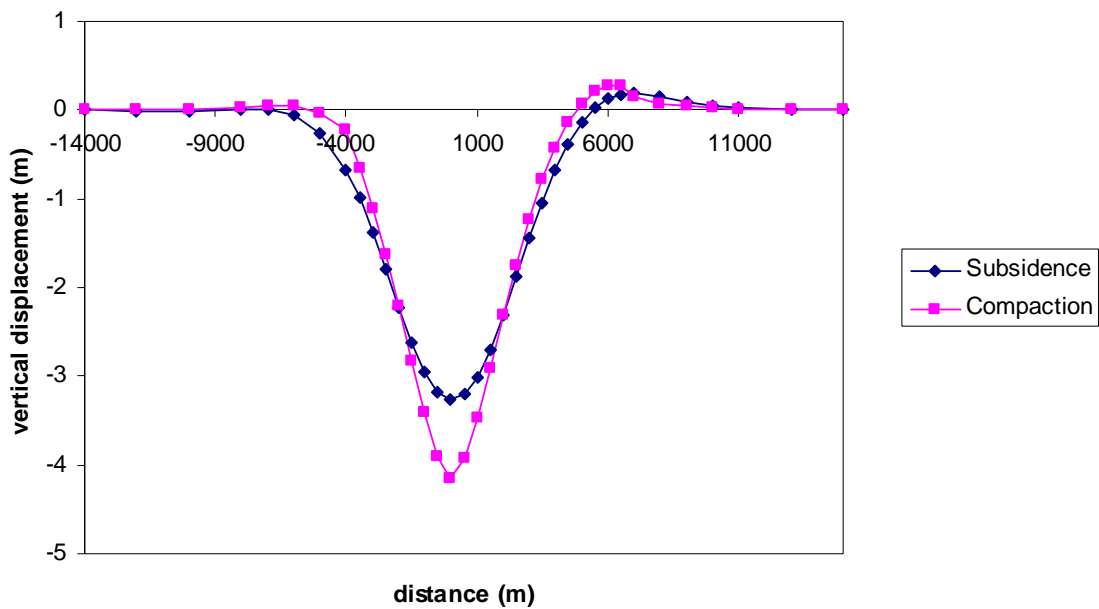


Figure 6-15 Final subsidence and compaction profiles along the North-South cross-section

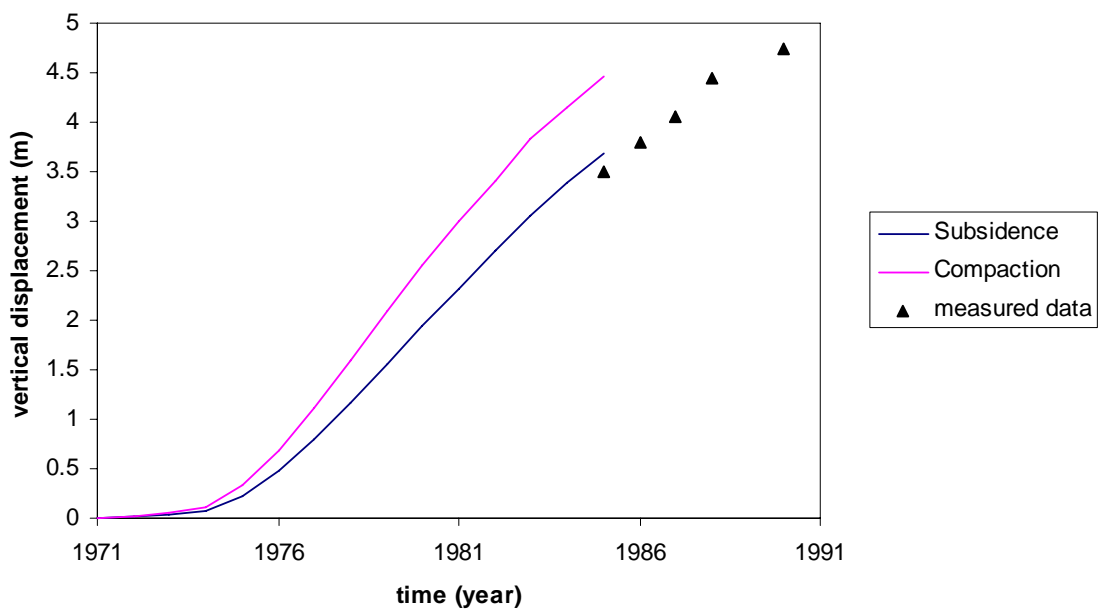


Figure 6-16 Subsidence and compaction profiles at the center along the production time

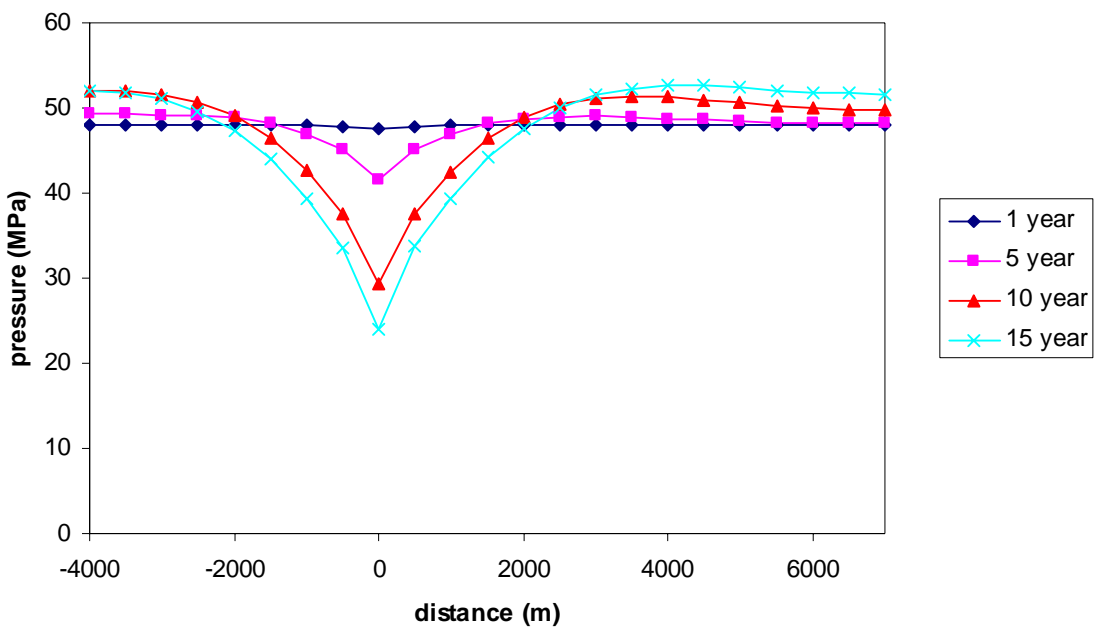


Figure 6-17 Water pressure profiles in the Ekofisk reservoir region along the mid depth

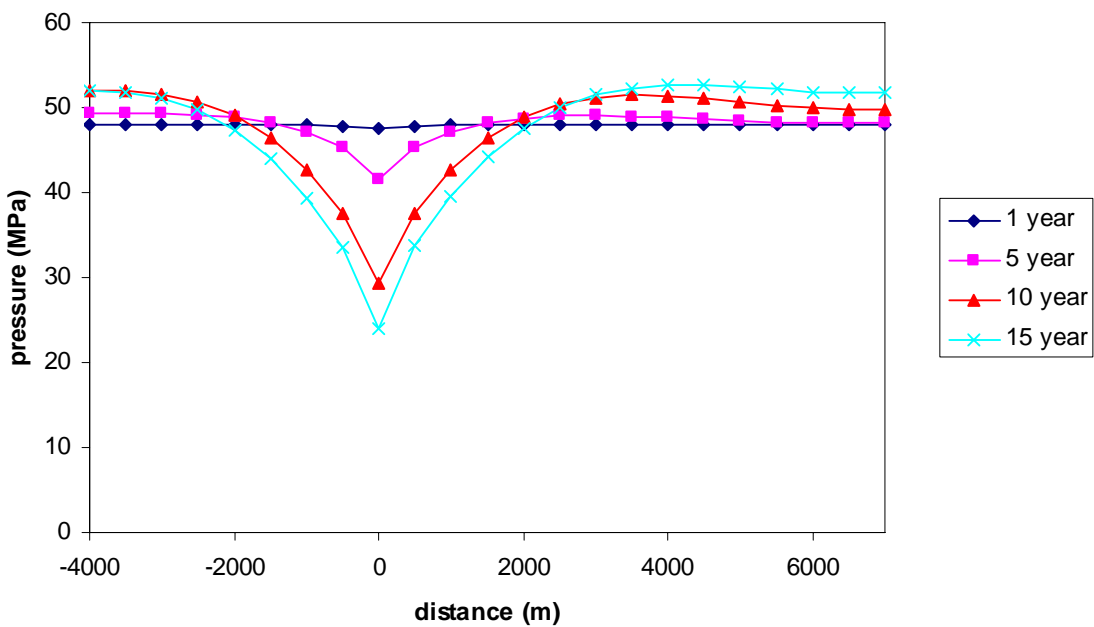


Figure 6-18 Oil pressure profiles in the Ekofisk reservoir region along the mid depth

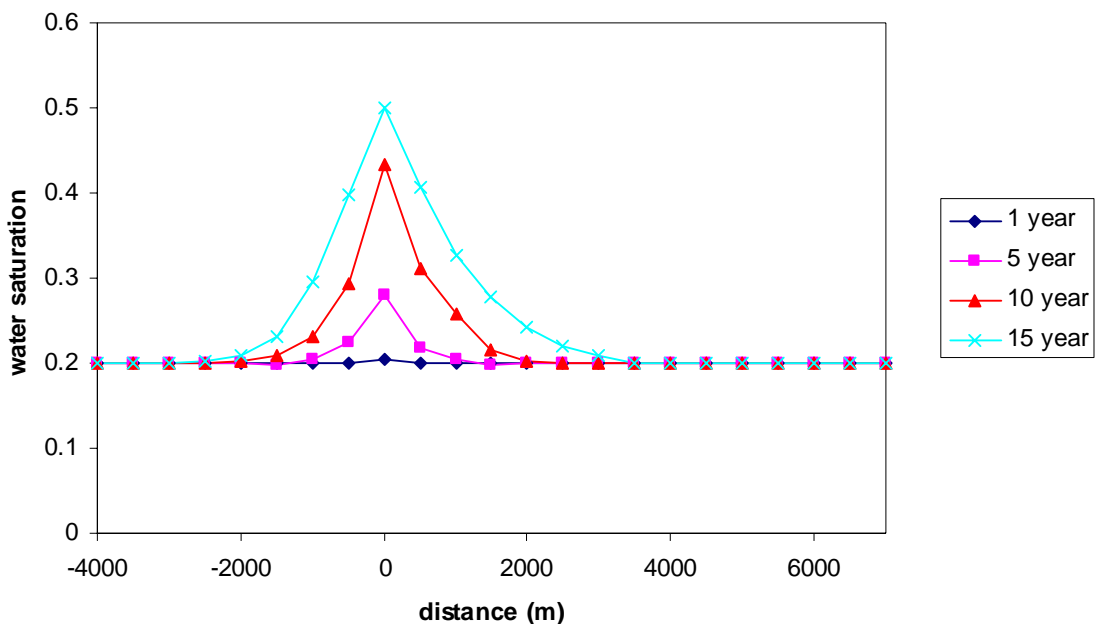


Figure 6-19 Water saturation profiles in the Ekofisk reservoir region along the mid depth

REFERENCES

1. Hickman, R.J. and M.S. Gutierrez 2007. Formulation of a three-dimensional rate-dependent constitutive model for chalk and porous rocks. *International Journal for Numerical and Analytical Methods in Geomechanics*. 31: 583-605.
2. Ghafouri, H.R., *Finite Element Modelling of Multi-phase Flow Through Deformable Fractured Porous Media*, in *Civil Engineering*. 1996, University of Wales: Swansea. p. 220.
3. Lewis, R.W. and Y. Sukirman 1993. Finite Element Modelling of Three-Phase Flow in Deforming Saturated Oil Reservoirs. *International journal for Numerical and Analytical Methods in Geomechanics*. 17: 577-598.
4. Chin, L. and R.R. Boade 1990. Full-Field, 3-D, Finite Element Subsidence Model for Ekofisk. in *3rd Northsea Chalk Symposium*.
5. Gutierrez, M., N. Barton and A. Makurat 1995. Compaction and subsidence in North Sea hydrocarbon fields. in *Intl. Workshop on Rock Foundations of Large Structures*.
6. Gutierrez, M. and H. Hansteen, *Fully-Coupled Analysis of Reservoir Compaction and Subsidence*, in *SPE 28900*. 1994: London.
7. Spencer, A., P.I. Briskeby, L.D. Christensen, M. Kjolleberg, E. Kvadsheim, I. Knight, M. Rye-Larsen and J. Williams 2008. Petroleum Geoscience in Norden-Exploration, Production and Organization. *Episodes* 31: 115-124.
8. Gutierrez, M., L. Tunbridge and H. Hansteen 1992. Discontinuum Simulation of Fractured Chalk Reservoir Behavior - Ekofisk. in *Fourth Northsea Chalk Symposium*. Deaville, France.
9. Hermansen, H., G.H. Landa, J.E. Sylte and L.K. Thomas 2000. Experiences after 10 years of waterflooding the Ekofisk Field, Norway. *Journal of Petroleum Science & Engineering*. 26: 11-18.

7 CONCLUSIONS AND RECOMMENDATIONS

Summary

The focus of this dissertation has been to develop effective computational schemes for coupled deformation and fluid flow problems in fluid saturated deformable porous media.

The developed schemes are based on the fully-coupled Biot's theory, which is known as the general three-dimensional consolidation theory. Numerical discretizations of the original Biot equations are made using the Finite Element (FE) method, the Finite Difference (FD) method and combinations of both methods. Computer codes based on the FE and FD discretization are developed for two-dimensional plane strain condition. The computer codes are extended to cover more general cases involving nonlinear stress-strain relations and multi-phase fluid flow.

Coupling effects can be observed in many engineering fields such as consolidation in soils, groundwater extraction, hydrocarbon production, contaminant transportation, and in biological field (e.g., tissues and bones). Due to the complexity of the problem, coupling effects have been usually neglected or simplified in many engineering problems. For instance, in the traditional fluid flow problem in hydrogeology and petroleum engineering, geomechanical effects on fluid flow are oversimplified through use of a scalar compressibility term, leading to uncoupled or partially coupled system. These oversimplifications may not properly take into account the rigorous geomechanical effects on the fluid flow behaviors and result in the incorrect prediction of the response of the fluid

saturated porous medium. Therefore, proper understanding of the coupled mechanisms between fluid flow and stress-strain is of great importance.

Chapter 2 reviewed the basic governing equations of the fully-coupled poroelasticity theory. The understanding of a fluid flow behavior in a saturated deformable porous media starts from revisiting of Biot's theory. Finite Element implementation of the complete set of Biot's equation containing both static equilibrium and fluid flow continuity equations was presented. The original Mandel's problem was used to validate the FE numerical solution, and numerical results are compared with analytical solutions. In addition, the effects of the rigidity of the material surrounding the porous layer in Mandel's problem were analyzed via a parametric study. Simple equations to predict the Mandel-Cryer effect as function of the rigidity of the surrounding impermeable material was proposed based on the numerical results.

Chapter 3 presented an extension of Biot's theory to multi-phase fluid flow. Multi-phase fluid flow is also essential in situations where more than one fluid in the porous medium such as in petroleum engineering and in unsaturated soil mechanics. The multi-phase fluid flow equations contain nonlinear terms in which the state coefficients are dependent on the state variables. Numerical discretizations using the Finite Element method was presented. Different numerical solution methods of nonlinear fluid flow problem were reviewed with more details given to the *Simultaneous Solution* (SS) method. Discretized two-phase fluid flow equations were implemented in the fully-coupled system as an extension of Biot's theory.

Chapter 4 gave a description of nonlinear stress-strain constitutive relation with particular emphasis on the elasto-plasticity theory. Brief reviews of nonlinear stress-strain constitutive models and current integration procedures for elasto-plasticity, including implicit return algorithm methods and explicit sub-stepping methods were presented. The Modified Cam Clay model was implemented in the fully-coupled system using a Newton-Raphson iteration method. Numerical results were compared with results from the incremental formulation of triaxial test.

Chapter 5 presented different numerical algorithms of the fully-coupled equations including proposed modular approaches. Monolithic solution solves the displacement and pressure variables simultaneously and is most the straightforward among techniques for the rigorous solution of Biot's theory. However, it requires relatively large computational efforts. Partitioned solutions may be considered as rearrangements of the monolithic solution, but they may serve as the starting point for the development modular solution approaches. Modular approaches involve separate simulations solutions of the main unknown variables (e.g., geomechanical and fluid flow simulations) by the use of proper algorithm to provide communication between each of the main variables. A modular coupling algorithm which uses the compressibility matrix as a key coupling factor was developed. The proposed method was tested in single-phase FE and FD fluid flow codes coupled with a FE geomechanical code and the numerical results were compared with analytical solutions and published results.

Chapter 6 was devoted to the verification of both the proposed coupling algorithm and the code developed throughout this study. The Ekofisk oil field in the Norwegian Sector of the

North Sea was analyzed as a field application of the proposed modular solution strategies and the corresponding computer code. Although the numerical results may not predict exact behavior of the Ekofisk due to the simplicity of the model, and the limitations of the code, it may serve as a pilot study of coupling of geomechanical and fluid flow behavior in hydrocarbon reservoirs.

Conclusions

The main conclusions obtained from the work presented in this dissertation are summarized as follows:

- Biot's theory is a general three-dimensional consolidation theory based on a poroelasticity. It consists of both static equilibrium and fluid flow continuity relations required to achieve the fully-coupled effects between geomechanics and fluid flow fields. The original Biot's theory can be extended into the more general/complex conditions such as those that involve nonlinear stress-strain relation and multi-phase fluid flow.
- Fluid flow behavior in a deformable porous media needs to take into account the geomechanical effects based on the Biot's fully-coupled theory. Conventional uncoupled fluid flow solutions cannot consider the geomechanical effects rigorously because the geomechanical terms in the fluid flow equations are oversimplified. For example, Mandel-Cryer effect, in which fluid pressures may be increased more than its initial values during fluid extraction, without external force can only be properly predicted by a fully-coupled system.

- Rigidity or stiffness of the surrounding material has significant effects on the fluid flow behavior. It is shown using modified Mandel's problem that as stiffness of the impermeable materials surrounding the deformable porous material increases more pronounced Mandel-Cryer effect is predicted. Simple equations were proposed to predict the Mandel-Cryer effect in porous media as function of the stiffness of the surrounding materials. These equations may be useful to predict the impact of Mandel-Cryer effects during fluid extraction in underground formations.
- More efficient algorithms in terms of computational effort can be implemented in separate simulators based on the fully-coupled theory. Rigorous updating of the compressibility matrix in an uncoupled fluid flow simulator with an aid of geomechanical simulator enables one to predict fluid flow behavior more correctly based on the Biot's theory.

Recommendations for Future Work

Although the work in this dissertation represents an important step in the ability to understand the mechanism of geomechanics-fluid flow coupling and in the development of numerical solution methods, there are further research that needs to be performed. Future developments should be conducted to improve the mathematical model and upgrading the developed code. The main recommendations for the future extensions of the study presented in this thesis are summarized as follows:

- The developed FE and FD based computer codes in this dissertation are based on two-dimensional plane strain condition. In general, plane strain condition is not

sufficient to represent more realistic field conditions which require three dimensional models. However, extension from two-dimensional cases to three dimensional cases requires significant work in cases where both geomechanical and fluid flow parts are involved.

- The solution techniques presented in the thesis can utilize both linear elastic and a Modified Cam Clay model as the constitutive law governing the geomaterial behavior. In order to have the capability of representing various geomechanical constitutive models, other commonly used constitutive models such as Druck-Prager, Mohr-Coulomb, and NGI cap plasticity model may need to be included.
- The present model can only be used for the case of isothermal condition. However, in a real practice of petroleum engineering, a constant temperature assumption is not valid. Thus, the present model can be further developed to include the effect of temperature variation in the case of a non-isothermal problem.
- The multi-phase fluid flow uses SS method with simple iteration. SS method has an advantage of easy implementation, however, it is strongly dependent on size of time step and convergence is not always guaranteed. Therefore, more rigorous numerical approaches that achieve efficiency and/or high convergence rate are needed on fluid flow simulation.
- One of the advantages of proposed modular approach is that it enables to exploit existing commercial codes with relatively small modifications. Thus, proposed algorithm needs to be implemented using separate existing commercial codes (e.g.,

geomechanics and fluid flow codes) and tested. Successful implementation of compressibility matrix updating scheme may solve other limitations described above.

APPENDIX-A

Analytical Solution of Mandel's Problem

The analytical expressions for the displacement in x direction, u_x , and y -direction, u_y , were derived by Mandel [4] as:

$$u_x = \left[\frac{Fv}{2Ga} - \frac{Fv_u}{Ga} \sum_{i=1}^{\infty} \frac{\sin \alpha_i \cos \alpha_i}{\alpha_i - \sin \alpha_i \cos \alpha_i} \exp(-\alpha_i^2 ct/a^2) \right] x + \frac{F}{G} \sum_{i=1}^{\infty} \frac{\cos \alpha_i}{\alpha_i - \sin \alpha_i \cos \alpha_i} \sin \frac{\alpha_i x}{a} \exp(-\alpha_i^2 ct/a^2) \quad (1)$$

$$u_y = \left[-\frac{F(1-v)}{2Ga} + \frac{F(1-v_u)}{Ga} \sum_{i=1}^{\infty} \frac{\sin \alpha_i \cos \alpha_i}{\alpha_i - \sin \alpha_i \cos \alpha_i} \exp(-\alpha_i^2 ct/a^2) \right] y \quad (2)$$

where B is Skempton's pore pressure coefficient which is the ratio of induced pore pressure to variation of confining pressure under undrained conditions, v and v_u are drained and undrained Poisson's ratio, c is the general consolidation coefficient :

$$c = \frac{2kB^2G(1-v)(1+v_u)^2}{9(1-v_u)(v_u-v)} \quad (3)$$

t is time, and $\alpha_i, i = 1, \infty$, are the roots of the equation:

$$\tan \alpha_i = \frac{1-v}{v_u-v} \alpha_i \quad (4)$$

Since rigid vertical displacement are assumed, horizontal displacement, u_x , is independent of vertical direction, y , while vertical displacement, u_y , is independent of horizontal direction, x .

Pore pressure expression, normal total stresses, σ_{xx} and σ_{yy} , and shear stress were derived by Mandel [4], and Cheng and Detournay [16] as:

$$p = \frac{2FB(1+\nu_u)}{3a} \sum_{i=1}^{\infty} \frac{\sin \alpha_i}{\alpha_i - \sin \alpha_i \cos \alpha_i} \left(\cos \frac{\alpha_i x}{a} - \cos \alpha_i \right) \exp(-\alpha_i^2 ct / a^2) \quad (5)$$

$$\sigma_{xx} = 0 \quad (6)$$

$$\begin{aligned} \sigma_{yy} &= -\frac{F}{a} - \frac{2F(\nu_u - \nu)}{a(1-\nu)} \sum_{i=1}^{\infty} \frac{\sin \alpha_i}{\alpha_i - \sin \alpha_i \cos \alpha_i} \cos \frac{\alpha_i x}{a} \exp(-\alpha_i^2 ct / a^2) \\ &\quad + \frac{2F}{a} \sum_{i=1}^{\infty} \frac{\sin \alpha_i \cos \alpha_i}{\alpha_i - \sin \alpha_i \cos \alpha_i} \exp(-\alpha_i^2 ct / a^2) \end{aligned} \quad (7)$$

$$\sigma_{xy} = 0 \quad (8)$$

Drainage is allowed on the lateral sides and vertical force is applied on rigid frictionless plate, the discharge has only a horizontal component. Therefore, the pore pressure, stress and strain fields are independent of the y -direction. Also, horizontal total stress, σ_{xx} , and shear stress, σ_{xy} , are zero for all time. The degree of consolidation, D , in the vertical and horizontal directions are identical:

$$\begin{aligned}
D &= \frac{u_x(a,t) - u_x(a,0)}{u_x(a,\infty) - u_x(a,0)} = \frac{u_y(b,t) - u_y(b,0)}{u_y(b,\infty) - u_y(b,0)} \\
&= 1 - \frac{4(1-\nu_u)}{1-2\nu} \sum_{i=1}^{\infty} \frac{\cos \alpha_i \sin \alpha_i}{\alpha_i - \sin \alpha_i \cos \alpha_i} \exp(-\alpha_i^2 ct/a^2)
\end{aligned} \tag{9}$$

APPENDIX-B

Incremental formulations of the modified Cam clay

- **Elastic strains**

2-D plane strain condition

$$d\varepsilon_v^e = \frac{1}{K + 1/3G} dp, \text{ and } d\varepsilon_d^e = \frac{1}{G} dq \quad (1)$$

3-D condition

$$d\varepsilon_v^e = \frac{1}{K} dp, \text{ and } d\varepsilon_d^e = \frac{1}{3G} dq \quad (2)$$

- **Plastic strains**

Associated plasticity is assumed, with the yield function, f , and plastic potential function, g , both given by:

$$f(\sigma, k) = g(\sigma, k) = \frac{q^2}{M^2} + p' (p' - p'_p) = 0 \quad (3)$$

where p' is the mean effective stress, q is the deviatoric stress, M is a clay parameter, and p'_p is the hardening parameter (see Figure 4-6)

The plastic flow directions and yield function gradients are obtained by differentiating equation (3)

$$\begin{aligned}\frac{\partial f(\sigma, k)}{\partial p'} &= \frac{\partial g(\sigma, k)}{\partial p'} = 2p' - p_p' \\ \frac{\partial f(\sigma, k)}{\partial q} &= \frac{\partial g(\sigma, k)}{\partial q} = \frac{2q}{p' p_p' M^2}\end{aligned}\tag{4}$$

In case the stresses are in the plastic state, the consistency condition needs to be satisfied as follows:

$$df(\sigma, k) = \frac{\partial f(\sigma, k)}{\partial p'} dp + \frac{\partial f(\sigma, k)}{\partial q} dq + \frac{\partial f(\sigma, k)}{\partial p_p'} dp_p' = (2p' - p_p') dp + \frac{2q}{M^2} dq - p' dp_p' = 0\tag{5}$$

Rearrangement of equation (5) gives:

$$\frac{dp_p'}{p_p'} = \left(\frac{2}{p_p'} - \frac{1}{p'} \right) dp + \frac{2q}{p' p_p' M^2} dq\tag{6}$$

Hardening is assumed to be isotropic and dependent on the plastic volumetric strain, ε_v^p as:

$$\frac{dp_p'}{p_p'} = \xi d\varepsilon_v^p\tag{7}$$

$$\text{where } \xi = \frac{v}{\lambda - \kappa}, \text{ and } v = v_1 - \lambda \ln(p')$$

Inserting equation (7) into equation (6) and rearranging gives:

$$d\varepsilon_v^p = \frac{1}{\xi} \left[\left(\frac{2}{p_p'} - \frac{1}{p'} \right) dp + \frac{2q}{p' p_p' M^2} dq \right]\tag{8}$$

The gradients to the plastic potential function give plastic strain increments as:

$$d\boldsymbol{\varepsilon}_v^p = \varphi \frac{\partial g}{\partial p'} = \varphi (2p' - p_p') \quad (9)$$

$$d\boldsymbol{\varepsilon}_d^p = \varphi \frac{\partial g}{\partial q} = \varphi \frac{2q}{M^2} \quad (10)$$

Equation (9) enables the determination of the scalar plastic multiplier, φ , as;

$$\varphi = \frac{1}{2p' - p_p'} d\boldsymbol{\varepsilon}_v^p \quad (11)$$

Inserting equation (11) into equation (10) gives an expression of a plastic deviatoric strain increment given by:

$$d\boldsymbol{\varepsilon}_d^p = \frac{2q}{\xi(2p' - p_p')M^2} \left[\left(\frac{2}{p_p'} - \frac{1}{p'} \right) dp + \frac{2q}{p' p_p' M^2} dq \right] \quad (12)$$

APPENDIX-C

The numerical iteration algorithms of the different strategies for the staggered solution of the fully-coupled Biot's equation

- **Staggered Conjugate Gradient Method (PCG)**

This method is applicable to symmetric positive-definite matrix system. The proposed algorithm for the partitioned conjugate gradient is shown as a pseudo-program below.

Assume $\Delta\mathbf{p}^0$

$$\begin{aligned}\Delta\mathbf{u}^0 &= \mathbf{K}_m^{-1} [\Delta\mathbf{F}_u - \mathbf{L}\Delta\mathbf{p}^0] \\ \mathbf{r}_p^0 &= \Delta\mathbf{F}_p - \mathbf{L}^T \Delta\mathbf{u}^0 - [\mathbf{S} - \Delta t \mathbf{K}_e \Delta\mathbf{p}^0]\end{aligned}$$

for $i = 1, 2, 3, \dots$

solve $\mathbf{z}_p^{i-1} = \mathbf{M}^{-1} \mathbf{r}_p^{i-1}$

$$\mathbf{p}_p^{i-1} = \mathbf{r}_2^{(i-1)T} \mathbf{z}_p^{i-1}$$

if $i = 1$

$$\mathbf{p}_p^1 = \mathbf{z}_p^0$$

else

$$\beta^{i-1} = \rho_p^{i-1} / \rho_p^{i-2}$$

$$\mathbf{p}_p^i = \mathbf{z}_p^{i-1} + \beta^{i-1} \mathbf{p}_p^{i-1}$$

end

$$\begin{aligned}
\mathbf{p}_u^i &= -\mathbf{K}_m^{-1} \mathbf{L} \mathbf{p}_p^i \\
\mathbf{q}_p^i &= \mathbf{L}^T \mathbf{p}_u^i + [\mathbf{S} - \Delta t \mathbf{K}_c] \mathbf{p}_p^i \\
\alpha^i &= \rho_p^{i-1} / (\mathbf{p}_p^{iT} \mathbf{q}_p^i) \\
\Delta \mathbf{p}^i &= \Delta \mathbf{p}^{i-1} + \alpha^i \mathbf{p}_p^i \\
\Delta \mathbf{u}^i &= \Delta \mathbf{u}^{i-1} + \alpha^i \mathbf{p}_u^i \\
\mathbf{r}_p^i &= \mathbf{r}_p^{i-1} - \alpha^i \mathbf{q}_p^i
\end{aligned}$$

Check convergence; continue if necessary

end

where \mathbf{M} is a pre-conditioner

- **Staggered MINRES method**

This method is applicable to any symmetric system and it is a robust algorithm for indefinite coefficient matrices as well as symmetric positive-definite matrix system. The proposed algorithm for the partitioned MINRES method is shown as a pseudo-program below.

Initialize:

$$\begin{aligned}
\mathbf{V}_p^0 &= \mathbf{0} \\
\mathbf{W}_p^0 &= \mathbf{W}_p^1 = \mathbf{0} \\
\mathbf{W}_u^0 &= \mathbf{W}_u^1 = \mathbf{0}
\end{aligned}$$

Assume $\Delta \mathbf{p}^0$

$$\begin{aligned}
\Delta \mathbf{u}^0 &= \mathbf{K}_m^{-1} [\Delta \mathbf{F}_u - \mathbf{L} \Delta \mathbf{p}^0] \\
\mathbf{V}_p^0 &= \Delta \mathbf{F}_p - \mathbf{L}^T \Delta \mathbf{u}^0 - [\mathbf{S} - \Delta t \mathbf{K}_c] \Delta \mathbf{p}^0
\end{aligned}$$

$$\text{Solve } \mathbf{Z}_p^1 = \mathbf{M}^{-1} \mathbf{V}_p^1$$

$$\gamma_1 = \sqrt{(\mathbf{Z}_p^{-1}, \mathbf{V}_p^{-1})}$$

$$\begin{aligned}\eta &= \gamma_1 \\ s_0 &= s_1 = 0 \\ c_1 &= c_0 = 1\end{aligned}$$

Iteration:

For $i=1, 2, 3, \dots$

$$\begin{aligned}\mathbf{Z}_p^i &= \mathbf{Z}_p^{-1} / \gamma_i \\ \mathbf{Z}_u^i &= -\mathbf{K}_m^{-1} \mathbf{L} \mathbf{Z}_p^i \\ (\mathbf{A} \mathbf{Z}_p)^i &= \mathbf{L}^T \mathbf{Z}_u^i + [\mathbf{S} - \Delta t \mathbf{K}_c] \mathbf{Z}_p^i \\ \delta_i &= ((\mathbf{A} \mathbf{Z}_p)^i, \mathbf{Z}_p^i) \\ \mathbf{V}_p^{i+1} &= \mathbf{A} \mathbf{Z}_p^i - (\delta_i / \gamma_i) \mathbf{V}_p^i - (\gamma_i / \gamma_{i-1}) \mathbf{V}_p^{i-1}\end{aligned}$$

$$\text{Solve } \mathbf{Z}_p^{i+1} = \mathbf{M}^{-1} \mathbf{V}_p^{i+1}$$

$$\gamma_{i+1} = \sqrt{(\mathbf{Z}_p^{i+1}, \mathbf{V}_p^{i+1})}$$

$$\alpha_0 = c_i \delta_i - c_{i-1} s_i \gamma_i$$

$$\alpha_1 = \sqrt{\alpha_0^2 + \gamma_{i+1}^2}$$

$$\alpha_2 = s_i \delta_i + c_{i-1} c_i \gamma_i$$

$$\alpha_3 = s_{i-1} \gamma_i$$

$$c_{i+1} = \alpha_0 / \alpha_1$$

$$s_{i+1} = \gamma_{i+1} / \alpha_1$$

$$\mathbf{W}_u^{i+1} = (\mathbf{Z}_u^i - \alpha_3 \mathbf{W}_u^{i-1} - \alpha_2 \mathbf{W}_u^i) / \alpha_1$$

$$\mathbf{W}_p^{i+1} = (\mathbf{Z}_p^i - \alpha_3 \mathbf{W}_p^{i-1} - \alpha_2 \mathbf{W}_p^i) / \alpha_1$$

$$\Delta \mathbf{u}^i = \Delta \mathbf{u}^{i-1} + c_{i+1} \eta \mathbf{W}_u^{i+1}$$

$$\Delta \mathbf{p}^i = \Delta \mathbf{p}^{i-1} + c_{i+1} \eta \mathbf{W}_p^{i+1}$$

Check convergence, and continue if necessary

end

- **Staggered Preconditioned Bi-Conjugate Gradient Method (PPBiCG)**

The bi-conjugate gradient method is applicable to non-symmetric matrices and produces the same iterations as conjugate gradient method. The proposed algorithm for the partitioned bi-conjugate gradient method is shown as a pseudo-program below.

Assume $\Delta\mathbf{p}^0$

$$\begin{aligned}\Delta\mathbf{u}^0 &= \mathbf{K}_m^{-1} [\Delta\mathbf{F}_u - \mathbf{L}\Delta\mathbf{p}^0] \\ \mathbf{r}_p^0 &= \Delta\mathbf{F}_p - \mathbf{L}^T \Delta\mathbf{u}^0 - [\mathbf{S} - \Delta t \mathbf{K}_c] \Delta\mathbf{p}^0 \\ \tilde{\mathbf{r}}_p^0 &= \mathbf{r}_p^0\end{aligned}$$

for $i = 1, 2, 3, \dots$

solve $\begin{aligned}\mathbf{z}_p^{i-1} &= \mathbf{M}^{-1} \mathbf{r}_p^{i-1} \\ \tilde{\mathbf{z}}_p^{i-1} &= \mathbf{M}^{T-1} \tilde{\mathbf{r}}_p^{i-1}\end{aligned}$

$$\rho_p^{i-1} = \mathbf{z}_p^{(i-1)T} \tilde{\mathbf{r}}_p^{i-1}$$

if $i = 1$

$$\begin{aligned}\mathbf{p}_p^1 &= \mathbf{z}_p^0 \\ \tilde{\mathbf{p}}_p^1 &= \tilde{\mathbf{z}}_p^0\end{aligned}$$

else

$$\begin{aligned}\beta^{i-1} &= \rho_p^{i-1} / \rho_p^{i-2} \\ \mathbf{p}_p^i &= \mathbf{z}_p^{i-1} + \beta^{i-1} \mathbf{p}_p^{i-1} \\ \tilde{\mathbf{p}}_p^i &= \tilde{\mathbf{z}}_p^{i-1} + \beta^{i-1} \tilde{\mathbf{p}}_p^{i-1}\end{aligned}$$

end

$$\begin{aligned}
\mathbf{p}_u^i &= -\mathbf{K}_m^{-1} \mathbf{L} \mathbf{p}_p^i \\
\tilde{\mathbf{p}}_u^i &= -[\mathbf{K}_m]^{T-1} \mathbf{L} \tilde{\mathbf{p}}_p^i \\
\mathbf{q}_p^i &= \mathbf{L}^T \mathbf{p}_u^i + [\mathbf{S} - \Delta t \mathbf{K}_c] \mathbf{p}_p^i \\
\tilde{\mathbf{q}}_p^i &= \mathbf{L}^T \tilde{\mathbf{p}}_u^i + [\mathbf{S} - \Delta t \mathbf{K}_c]^T \tilde{\mathbf{p}}_p^i \\
\alpha^i &= \rho_p^{i-1} / \left(\tilde{\mathbf{p}}_p^{iT} \mathbf{q}_p^i \right) \\
\Delta \mathbf{p}^i &= \Delta \mathbf{p}^{i-1} + \alpha^i \mathbf{p}_p^i \\
\Delta \mathbf{u}^i &= \Delta \mathbf{u}^{i-1} + \alpha^i \mathbf{p}_u^i \\
\mathbf{r}_p^i &= \mathbf{r}_p^{i-1} - \alpha^i \mathbf{q}_p^i \\
\tilde{\mathbf{r}}_p^i &= \tilde{\mathbf{r}}_p^{i-1} - \alpha^i \tilde{\mathbf{q}}_p^i
\end{aligned}$$

Check convergence, and continue if necessary

end